

Heat Transfer and Fluid Flow Analysis in Rotor-Stator Combination of Canned Motor Pump

Submitted in partial fulfillment of the requirements

of the degree of

Master of Technology

by

Sanit Prashant Bhatkar

(Roll No.173109003)

Supervisor:

Prof. Rajendra P. Vedula



Department of Mechanical Engineering

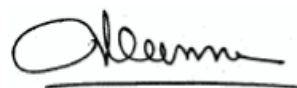
INDIAN INSTITUTE OF TECHNOLOGY BOMBAY

2020

Dissertation Approval

The dissertation entitled **Heat Transfer and Fluid Flow analysis in Rotor-Stator Combination of Canned Motor Pump** by **Sanit Prashant Bhatkar** is approved for the degree of **Mater of Technology**.

Examiners:

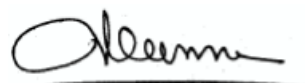


July 3, 2020

Supervisor:



Chairperson:



Date: 03/07/2020

Place: Mumbai

Declaration

I declare that this written submission represents my ideas in my own words and where others ideas or words have been included, I have adequately cited and referenced the original sources. I also declare that I have adhered to all principles of academic honesty and integrity and have not misrepresented or fabricated or falsified any idea/data/fact/source in my submission. I understand that any violation of the above will be cause for disciplinary action by the Institute and can also evoke penal action from the sources which have thus not been properly cited or from whom proper permission has not been taken when needed.

Date: 03/07/2020

Sanit Prashant Bhatkar

Roll No. 173109003

A handwritten signature in black ink, appearing to read "Sanit".

Abstract

Canned motor pump uses electric induction motor to drive the centrifugal pump. The rotor in the canned motor pump, unlike the normal motor, is sealed in a protective envelope as the windings are cooled by liquid coolant unlike the normal motor. The elimination of the fan, couplings and mechanical seal makes the canned motor pump a suitable application in chemical and nuclear industries where the leaking of the working fluid can be hazardous and noise generation is also reduced. The literature survey suggested that the main mechanism of noise generation is unsteady interactions with the pump casing. The mechanism of unsteady interactions is studied for the centrifugal pump so that conventional design of the pump can be improved. Design approach for the induction motor, impeller and volute casing is given in the dissertation for designing the components from in the absence of experimental data. Characteristic curves for centrifugal pump are reproduced by simulation in Ansys® CFX for the designed impeller geometry by following the frozen rotor approach. Unsteady simulations were carried out for investigating the turbulent flow interaction with volute casing by using sliding mesh approach.

Another challenge with the canned pump is excess heat generation in the rotor stator gap. Taylor number governs the behaviour of the flow in narrow gap geometry by introducing the instability in the flow. The flow is termed as Taylor-Couette-Poiseuille flow. The average Nusselt number data reported in the literature is discussed and compared in the dissertation through simulation. It is concluded that the presence of the instability enhances the heat transfer in the rotor stator gap thereby increasing the effectiveness of the cooling system. The methodology for estimating the flow, and heat transfer characteristics in the gap along with the estimate of noise generation frequency of the pump in the harmonic space is given in the dissertation.

Keywords : Instability, Taylor-Couette-Poiseuille flow, Centrifugal pump, Canned motor pump, Mean-line design, Impeller, Vane development, Noise generation, Unsteady pressure fluctuations, Acoustics, Blade pass frequency.

Contents

Abstract.....	i
List of Figures.....	ix
List of Tables.....	xv
Chapter 1 Introduction	1
1.1 Canned Motor Pump.....	1
1.1.1 Introduction	1
1.1.2 Components	1
1.1.3 Advantages and limitations	3
1.2 Induction motor.....	4
1.2.1 Basic definitions	4
1.3 Centrifugal Pump.....	6
1.3.1 Introduction	6
1.3.2 Basic definitions	7
1.4 Impeller basics	12
1.4.1 Geometry details.....	12
1.4.2 Velocity triangle	14
1.4.3 Velocity slip at the blade outlet	15
1.5 Volute Casing	16
1.5.1 Nomenclature used for volute geometry	16
1.6 : Acoustics: Theory	16
1.6.1 Basic Definitions	17

1.6.2	Types of sound measurement	18
1.6.3	Governing equations.....	19
1.6.4	Solution of the wave equation	20
1.6.5	Kirchhoff- Helmholtz integral	21
1.7	Types of noise sources	21
1.7.1	Introduction	21
1.7.2	Monopole.....	21
1.7.3	Volume velocity	23
1.7.4	Dipole	24
1.7.5	Quadrupole	26
1.8	Lighthill acoustic analogy	27
Chapter 2 Survey of Literature	28
2.1	Introduction.....	28
2.2	Flow structure in Stator-Rotor gap	29
2.2.1	Introduction	29
2.2.2	Flow structure for Couette flow	30
2.2.3	Flow structure for Taylor-Couette flow	31
2.2.4	Flow structure in Taylor-Couette-Poiseuille Flow	35
2.3	Heat transfer characteristics in Rotor-Stator gap	36
2.3.1	Basic definitions	37
2.3.2	Heat transfer in Taylor-Couette flow	37
2.3.3	Heat transfer in Taylor-Couette-Poiseuille flow	41
2.4	Effect of TCPF on the pressure drop	44
2.5	Centrifugal Pump.....	45
2.5.1	Introduction	45

2.5.2	1D Preliminary Impeller design	46
2.5.3	Blade shaping	46
2.5.4	Volute Design.....	47
2.6	Performance prediction.....	47
2.6.1	Throughflow method	48
2.6.2	Slip and loss analysis	50
2.7	Steady state pump simulation	51
2.8	Unsteady state pump simulation and noise.....	53
2.9	Objective and Present work	60
	Chapter 3 Design of Components of Canned Motor Pump.....	61
3.1	Design of basic dimensions of the impeller.....	61
3.1.1	Efficiencies	61
3.1.2	Impeller suction diameter	64
3.1.3	Shaft and hub diameter	64
3.1.4	Impeller inlet diameter.....	65
3.1.5	Inlet Velocity Triangle.....	66
3.1.6	Impeller outlet dimensions	69
3.1.7	Slip factor	71
3.1.8	Outlet Velocity Triangle	72
3.1.9	Commercial software.....	73
3.2	Shaping of the blades	73
3.2.1	Meridional section basic dimensions.....	73
3.2.2	Meridional section shaping.....	74
3.2.3	Blade shape in front view	77
3.2.4	Commercial software.....	80

3.3	Design of basic dimensions of the volute	81
3.3.1	Throat diameter.....	81
3.3.2	Volute inlet width	82
3.3.3	Volute wall thickness	82
3.3.4	Volute throat angle	83
3.4	Shaping of the volute	83
3.4.1	Volute cross section shaping	83
3.4.2	Average flow velocity in casing	83
3.4.3	Area variation at different cross sections	83
3.4.4	Relative distance from cutwater	84
3.5	Empirical design of an Induction motor	85
3.5.1	Introduction	85
3.5.2	Dimensions of the Stator	85
3.5.3	Dimensions of the rotor	85
Chapter 4 Numerical Simulation	87
4.1	Flow structure in Stator-Rotor gap	87
4.1.1	Turbulent Couette flow.....	87
4.1.2	Taylor-Couette flow	89
4.1.3	Taylor-Couette-Poiseuille flow	95
4.2	Heat transfer characteristics in Stator-Rotor gap	95
4.2.1	Taylor-Couette flow	95
4.2.2	Taylor-Couette-Poiseuille flow	103
4.2.3	Minimum flow rate.....	107
4.3	Centrifugal pump simulation work flow.....	109
4.4	Performance prediction.....	111

4.4.1	Pump characteristics prediction by Throughflow method.....	111
4.4.2	Pump characteristics prediction by slip and loss analysis	112
4.5	Impeller and volute pre-processing.....	113
4.5.1	General work flow	113
4.5.2	Impeller and volute geometry	114
4.5.3	Impeller and volute CFD mesh.....	114
4.5.4	Impeller and Volute boundary conditions	117
4.6	Steady state simulation	118
4.6.1	Comparison with literature	118
4.6.2	Comparison with real pump	121
4.7	Unsteady state simulation	126
4.7.1	Ansys setup for unsteady case	126
4.7.2	Results and discussions	126
4.8	Acoustics simulations	132
4.8.1	Basic sources	132
4.8.2	Basic sound source simulation on COMSOL.....	132
4.8.3	Multiple monopole sources	132
4.8.4	Sound radiation by baffled piston.....	136
Chapter 5 Conclusion and Future scope	139
Appendix A Design of Single Stage Centrifugal Pump Impeller	141
A.1	Design Specifications	141
A.2	Basic Calculations.....	142
A.3	Inlet velocity triangle	143
A.4	Outlet dimensions	145

A.5	Slip factor and Head verification	146
A.6	Outlet velocity triangle	147
A.7	Complete final dimensions	147
Appendix B Design of volute		149
B.1	Design Specifications	149
B.2	Volute shaping	150
Appendix C First cell height estimation for turbulent flow		151
C.1	Y plus calculation	151
C.2	Shear stress calculation	152
Appendix D Bezier curves		153
Appendix E Numerical validation of laminar plane Couette and Poiseuille flow		155
E.1	Couette flow	155
E.1.1	Numerical simulation for laminar flow	155
E.1.2	Boundary conditions	157
E.2	Poiseuille flow	157
E.2.1	Numerical simulation for laminar flow	158
Appendix F Solution for baffled piston		159
F.1	Acoustic radiation by a 2D ring	159
F.1.1	Solution for 2D Annular ring	159

F.1.2	Far-field pressure solution	161
F.1.3	Near-field pressure solution.....	161
Appendix G UDF For Fully Developed Flow At The Inlet		162
G.1.1	UDF code.....	163
Appendix H MATLAB codes.....		164
H.1	Meanline design of the Impeller	164
H.1.1	Main code: Impeller_scratch.m	164
H.1.2	Shaft diameter calculation function.....	168
H.1.3	Efficiency Calculation function.....	168
H.1.4	Blockage factor calculation function	170
H.1.5	Velocity triangle calculation function	170
H.1.6	Slip factor calculation function.....	170
H.1.7	Head verification function	171
H.2	Meridional section	171
H.2.1	Main code: meridional_section.m	171
H.2.2	Bezier curve calculation function	174
H.3	Front view profile generation code Kaplan method	175
H.4	Vane development in front view by Srinivasan[24]	179
H.5	Volute basic dimensions and shaping	182
H.6	Slip and Loss analysis.....	183
H.7	FFT code	186
H.8	Basic sound sources	188

References.....	191
Design Drafts.....	197
Canned Motor Pump parts.....	197
Canned Motor Pump flow path.....	198
Impeller geometry.....	199
Volute geometry.....	200
Centrifugal Pump Assembly.....	201
Centrifugal pump cross-sections.....	202

List of Figures

Figure 1.1 Schematic diagram of the canned motor pump	2
Figure 1.2 Schematic of the conventional pump with mechanical seal (Shown in purple colour) Elsey[1].....	2
Figure 1.3 Schematic diagram of centrifugal pump Oilfield[4]	6
Figure 1.4 Schematic of the general pumping system.....	8
Figure 1.5 Cross-section view of the impeller and casing a) without b) with balance hole Gülich[5].....	10
Figure 1.6 Schematic diagram of the impeller in A) front view and B) Side view.....	12
Figure 1.7 Details of the impeller dimensions in the Meridional passage.	13
Figure 1.8 Velocity triangles with usual notations.	14
Figure 1.9 Velocity slip at the blade outlet.....	15
Figure 1.10 Basic volute geometry and different cross-sections.....	15
Figure 1.11 Propagation of sound through medium by compression and rarefaction.....	16
Figure 1.12 A vibrating body with arbitrary shape and surface area S in an infinite volume S with sound source at distance r_o	20
Figure 1.13 Schematics of acoustic sources	22
Figure 1.14 Schematic of dipole source reproduced from Manik[6]	25
Figure 1.15 Schematic of a quadrupole source reproduced from Manik[6].....	26
Figure 2.1 Schematic diagram of simplified Stator-Rotor assembly.....	29
Figure 2.2 Mean velocity distribution in turbulent plane Couette flow a) One wall moving b) Walls moving in opposite direction Bech et al.[7]	30
Figure 2.3 Schematic of Taylor-Couette flow Fénot et al.[9]	31
Figure 2.4 Influence of annular gap thickness on the transition to Taylor instability Fénot et al.[9].....	33
Figure 2.5 Gardiner and Sabersky[13] parameter for different gap thickness	33
Figure 2.6 Axial wavelength for Taylor vortices	34
Figure 2.7 Flow regimes for Taylor-Couette-Poiseuille Flow Fénot et al.[9]	35
Figure 2.8 Comparison of different values of average Nusselt numbers reported by authors Fénot et al.[9].....	38

Figure 2.9 Schematic a) Two-dimensional rib roughness b) Three-dimensional protrusion Gilchrist et al.[17].....	38
Figure 2.10 Change in Nusselt number with modified Taylor number for the paper A) Becker and Kaye[14] $Re = 2015$ B) Gilchrist et al.[17] $Re = 2080$ C) Jakoby et al.[18] $Re = 4000$...	39
Figure 2.11 Effect of fluid properties on heat transfer in the annular gap. Gardiner and Sabersky[13].....	40
Figure 2.12 Variation of fanning friction factor $f = \lambda$ with rotating Reynolds number for different values of $e/R_1 = s/R_1$ Yamada[12].....	41
Figure 2.13 Composite of data for Nusselt number for combined rotation and axial flow Becker and Kaye[14].....	42
Figure 2.14 Temperature contours for mechanical seal type and canned type pumps Lim et al.[19].....	43
Figure 2.15 Pressure drop along the length of the rotor for the annular gap with no rotation. Nouri-Borujerdi and Nakhchi[20]	44
Figure 2.16 Canned motor pump with a secondary impeller cooling arrangement designed in SOLIDWORKS	45
Figure 2.17 S1 and S2 surfaces in blade row Wu[33]	48
Figure 2.18 Computational grid used for Throughflow calculations Ansys®[35].....	49
Figure 2.19 Throughflow calculation algorithm	49
Figure 2.20 Pump impeller simulation for different turbulence models simulated by Kaewnai et al.[39].....	51
Figure 2.21 Comparison between regular and optimized impeller Kim et al.[41].....	52
Figure 2.22 Effect of outlet blade angle on pump performance Tan et al.[43]	53
Figure 2.23 Measured pressure pulsation at volute throat Timouchev and Tourret[45]	54
Figure 2.24 Unsteady pressure measurement points for Majidi[46] geometry	54
Figure 2.25 Pressure fluctuations for a) $Q < Q_d$ b) $Q = Q_d$ c) $Q > Q_d$ d) Volute throat Majidi[46]	55
Figure 2.26 Pressure fluctuations at volute throat for different flow rates Si et al.[47].....	56
Figure 2.27 Monitor points used for recording the pressure fluctuation data by Si et al.[47]..	57
Figure 2.28 Pressure coefficient fluctuation in the frequency domain Si et al.[47]	57
Figure 2.29 Sound Pressure Level distribution for the pump Chen et al.[49].....	58

Figure 2.30 Sound Pressure Level variation from the pump for different rotational speed Guo et al.[53].....	58
Figure 2.31 Sound fluctuation power variation with outlet blade angle A. Yang et al.[54]	59
Figure 3.1 Hydraulic efficiency variation with specific speed for a single stage, single entry radial pump at different flow rates	63
Figure 3.2 Normalized suction specific speed as a function of flow angle the outer streamline of the impeller reproduced from Gülich[5]	65
Figure 1.4 Simplified geometry triangle at the blade inlet	67
Figure 3.4 Variation of dimensionless head developed by the pump with dimensionless velocity parameter	71
Figure 3.5 Design parameters for Meridional section taken from Gülich[5]	73
Figure 3.6 Flow velocity and relative velocity variation from inlet to outlet of the impeller blade	74
Figure 3.7 Basic definition for Kaplan error triangle in Meridional section.....	75
Figure 3.8 Meridional section generated by Bezier curve.....	76
Figure 3.9 Six blade impeller viewed in Front view	77
Figure 3.10 Blade profile generated by Kaplan error triangle method with 5 streamlines and 201 points viewed in front view	78
Figure 3.11 Blade profile generated by Kaplan error triangle method with 5 streamlines and 201 points viewed in top view	78
Figure 3.12 Vane development by point by point method Srinivasan[24].....	79
Figure 3.13 Airfoil generated by point by point method for static head $H = 13.8$ m and discharge $Q = 16$ lps with 101 points used for numerical integration.....	80
Figure 3.14 3D CAD profile of Impeller generated by Ansys BladeGen	81
Figure 3.15 Volute constant data taken from Stepanoff[25]	82
Figure 3.16 Relative distance from volute throat (Figure not to scale)	84
Figure 4.1 Comparison of DNS model of Bech et al.[7]and Numerical simulation models for turbulent flow.	88
Figure 4.2 Grid independence study for the turbulent flow through parallel plates for Bech et al.[7] geometry.....	89
Figure 4.3 Numerical simulation results A) Geometry details B) Velocity contours for $T_a = 500$ C) Velocity contours for $T_a = 5000$	90

Figure 4.4 Numerical simulation results A) Velocity streamline plot B) Velocity vectors for Ta = 5000 for plane (1) of Figure 4.3.A C) Velocity vectors for Ta = 5000 for plane (2) of Figure 4.3.A	91
Figure 4.5 Radial velocity profile variation at R = 0.041 m with axial distance.....	93
Figure 4.6 Axial velocity profile variation at R = 0.029 m with axial distance	93
Figure 4.7 Velocity contours for unsteady simulation of Taylor-Couette-Poiseuille flow at the square root of $Ta^* = 1474$ and A) Re = 500 B) Re = 28.8 for the geometry of Kataoka et al.[58].....	94
Figure 4.8 Grid independence study for Local Nusselt number variation along the length of the stator at $Ta \sim 24828$ using two different meshes.....	97
Figure 4.9 Nusselt number variation with axial direction for two different working fluids, Air and Water.....	99
Figure 4.10 Nusselt number variation with axial direction for the $Ta \sim 24900$ compared with Kataoka[59]	100
Figure 4.11 Nusselt number variation with axial direction for the $Ta \sim 99300$ compared with Kataoka[59]	101
Figure 4.12 Temperature variation for the Taylor-Couette (Top) flow and the Couette flow (Bottom).	101
Figure 4.13 Comparison of Nusselt number variation for Couette flow for rotational Reynolds number $R = 60$ and Taylor-Couette flow $R = 200$ and 400 referred from Kataoka[59].	102
Figure 4.14 Nusselt variation for horizontal and vertical configuration of the rotor.	102
Figure 4.15 Variation of Mass/Heat transfer on the stator with Reynolds number Kataoka et al.[58].....	103
Figure 4.16 Fully developed velocity profile at the inlet of concentric cylinder for Re = 500 and geometry of Kataoka et al.[58]	104
Figure 4.17 Simulation results for variation heat transfer for Kataoka et al.[58] geometry ..	105
Figure 4.18 Local Nusselt number variation reported by Kataoka et al.[58]	105
Figure 4.19 Simulation results for variation heat transfer for Kataoka et al.[58] geometry ..	106
Figure 4.20 Velocity contours for unsteady simulation of Taylor-Couette-Poiseuille flow at square root of $Ta = 1474$ and Re = 500 for geometry of Kataoka et al.[58]	106
Figure 4.21 General process flow for centrifugal pump simulation.....	108

Figure 4.22 Average pressure comparison between Throughflow method and CFX results meaured from inlet to outlet of Kaewnai et al.[39] impeller for design flow rate $Q = 528 \text{ m}^3/\text{hr}$	109
Figure 4.23 Contour plot of flow velocity calculated by Throughflow method with 3D solution A. CFX solution B. Throughflow solution at Meridional plane for Kaewnai et al.[39] impeller.....	110
Figure 4.24 Average pressure comparison between Throughflow method and CFX results meaured from inlet to outlet of Kaewnai et al.[39] impeller for design flow rate $Q = 360 \text{ m}^3/\text{hr}$	111
Figure 4.25 Head vs Discharge characteristics for Win[32] geometry	112
Figure 4.26 Head and Efficiency variation with flow rate for Win[32] geometry	113
Figure 4.27 Flow chart for impeller and volute design with ANSYS	114
Figure 4.28 Assembly of impeller and volute generated by ANSYS.....	115
Figure 4.29 Assembly of impeller generated by ANSYS and volute generated by SOLIDWORKS for Si et al.[47] pump geometry	115
Figure 4.30 Impeller CFD mesh generated by TurboGrid for all the cases of the literature..	116
Figure 4.31 Volute CFD mesh generated by ANSYS	116
Figure 4.32 Blade geometry used by Kim et al.[41] for simulation.....	118
Figure 4.33 Head vs Discharge characteristics comparison for our simulation with the Kim et al.[41] pump.	119
Figure 4.34 Head vs Discharge characteristics comparison for our simulation with the Kaewnai et al.[39] pump.	120
Figure 4.35 Hydraulic efficiency vs Discharge characteristics comparison for our simulation with the Kaewnai et al.[39] pump.	120
Figure 4.36 Head vs Discharge comparison for simulation and Hydrodyne Pump data.....	122
Figure 4.37 Velocity contours for the simulation of the Hydrodyne pump	123
Figure 4.38 Pressure variation for the Meridional cross-section of the Hydrodyne pump	123
Figure 4.39 Pressure variation from inlet to outlet along the mean streamline in the Meridional view for the Hydrodyne pump. (Chart generated in Ansys).....	124
Figure 4.40 Pressure contours for the pump at the cut-section taken at the midplane.	124
Figure 4.41 Hydrodyne pump pressure contours for A) Complete pump assembly B) At different sections C)At the blade leading edge D) Blade trailing edge.....	125

Figure 4.42 Pressure fluctuations for fully developed flow for one rotation of the impeller.	128
Figure 4.43 Pressure variation at throat point in frequency domain	128
Figure 4.44 Coefficient of pulsation comparison with Si et al.[47] at different design points	129
Figure4.45 Vorticity variation for the simulated pump.....	129
Figure 4.46 Pressure fluctuation at different monitor points plotted in frequency domain....	130
Figure 4.47 Pressure contours for different rotation angles of the impeller (Varying from 0 to 90° taken at 15° interval)	131
Figure 4.48 Far-field pressure distribution A. Monopole B. Dipole C. Qudrapole D. Linear Quadrapole.....	133
Figure 4.49 Comparison of far-field pressure on the sphere at a distance = 1m from the source	133
Figure 4.50 Comparison of far-field SPL on the sphere at a distance = 1m from the source	134
Figure 4.51 Geometry details for the dipole simulation in COMSOL	134
Figure 4.52 Multiple monopole sources simulated in COMSOL.....	135
Figure 4.53 Sound pressure level radiation pattern for multiple monopole sources	135
Figure 4.54 Schematic diagram for a baffled piston surface	136
Figure 4.55 Baffled piston geometry created in COMSOL.....	137
Figure 4.56 Acoustic pressure contours due to vibrating baffled piston	137
Figure 4.57 Sound pressure level comparison for COMSOL model with Analytic solution.	138
Figure 1 Geometry details for the designed impeller.	143
Figure 2 Bezier curves for different location of the control points	153
Figure 4 Comparison of Numerical and Analytic solution.....	156
Figure 3 Couette Flow through two parallel plates	156
Figure 5 Schematic diagram of Plane Poiseuille Flow.....	157
Figure 6 Numerical solution results and grid independence study for the velocity profile in plane Poiseuille flow	158
Figure 7 Schematic diagram of 2D annular ring vibrating at harmonic velocity excitation ..	160

List of Tables

Table 1 Equations for acoustic quantities of monopole	24
Table 2 Expressions used for Eq.1.29	25
Table 3 Equations for acoustic quantities of a dipole source	25
Table 4 Head losses described in Win[32] paper	50
Table 5 Inlet Velocity Triangle calculations	68
Table 6 Outlet Velocity Triangle calculation	72
Table 7 Suction pipe diameter versus volute wall thickness	82
Table 8 Design dimensions for 30kW ac induction motor from the empirical relations	86
Table 9 Simulated domain from Bech et al.[7]	87
Table 10 Grid details for Turbulent Couette flow	88
Table 11 Numerical simulation for Taylor-Couette flow	89
Table 12 Numerical simulation for Adebayo and Rona[57] geometry	92
Table 13 Numerical simulation for Taylor-Couette-Poiseuille flow	95
Table 14 Mesh used for grid independence study	97
Table 15 Details of the cases simulated in Ansys Fluent	98
Table 16 Letter grades for thermal insulation used in motor	107
Table 17 Temperature change from inlet to outlet on rotor for flow through annulus.....	108
Table 18 Design details given by Kim et al.[41].....	118
Table 19 Design details given Kaewnai et al.[39].....	119
Table 20 Pump data for the canned motor pump provided by Hydrodyne Pumps	121
Table 21 Design details for the case simulated by Si et al.[47].....	127
Table 22 Grid details for Poiseuille flow	158
Table 23 Geometry and Co-ordinate details of annular ring	160

Chapter 1

Introduction

1.1 Canned Motor Pump

1.1.1 Introduction

The canned motor pump is a centrifugal pump in which the rotor of an electric motor is hermetically sealed in a stainless steel can and mounted on the same shaft as the pump impeller. The pump generates less noise compared to conventional pump due to the elimination of the cooling fan and the use of a Rotodynamic bearing. It is a zero-leak device and is therefore well suited for pumping of hot fluids, hazardous chemical fluids etc.

1.1.2 Components

The schematic diagram of the canned motor pump is shown in Figure 1.1. It consists of a centrifugal pump, induction motor, hydrodynamic bearing and a casing. The schematic of the conventional pump with mechanical seal is given in Figure 1.2.

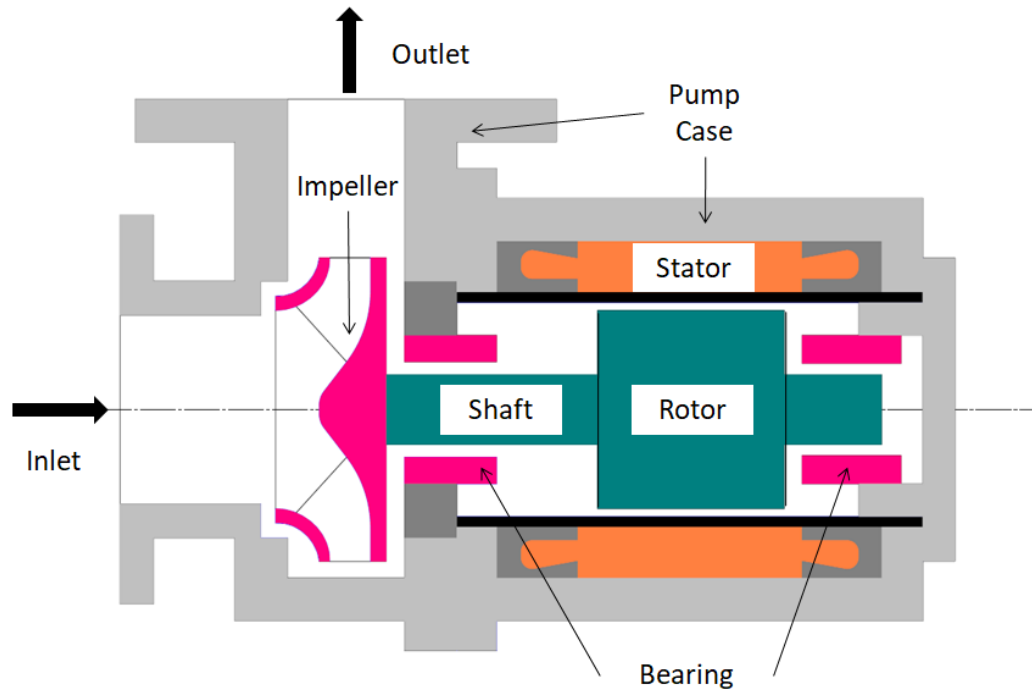


Figure 1.1 Schematic diagram of the canned motor pump

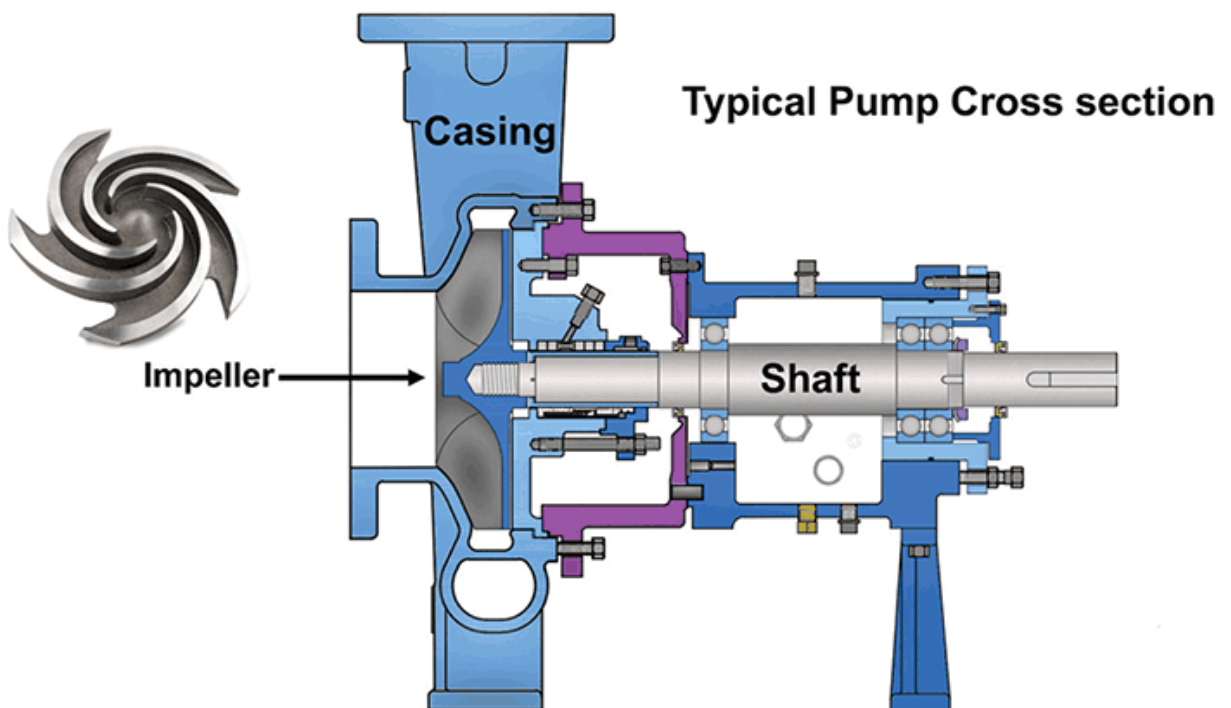


Figure 1.2 Schematic of the conventional pump with mechanical seal (Shown in purple colour) Elsey[1].

1.1.2.1 Induction motor

Induction motor works on the principle of electromagnetic induction. When the current is passed through the copper coils of the stator, the induced magnetic field produces a torque on the rotor. An alternating current is used for driving the rotor at different speeds required as per the application.

1.1.2.2 Centrifugal pump

Centrifugal pump is a hydraulic machine used to convert mechanical energy to hydraulic energy. It consists of a series of impeller blades which generate the centrifugal force on the fluid such that the fluid flows in radially outward direction from inlet to the outlet of the pump.

1.1.2.3 Hydrodynamic bearing

Hydrodynamic bearing supports the shaft of impeller and rotor and is designed to withstand both the radial and the thrust load. The bearing uses the working fluid itself for lubrication and a suitable design obviates the need to be cooled by some external coolant for smooth operation.

1.1.3 Advantages and limitations

1.1.3.1 Advantages

In a centrifugal pump, there is a small gap between the impeller and the casing of the pump through which the working fluid can leak. In order to avoid the leakage, a mechanical seal is provided for the pump. The leakage reduces the volumetric efficiency of the pump and adversely affects the performance of the pump. In some applications, the leakage is not desirable due to environmental hazards or due to the cost of the fluid. The centrifugal pump is driven by an electric motor which is connected by a coupling. The electric motor is cooled by a fan. The fan and coupling generate noise which is undesirable for some applications. In a canned motor pump, both the impeller of the centrifugal pump and the rotor are placed on the same shaft which eliminates the need for the coupling. The entire assembly is hermetically

sealed making, the pump a leak-free machine. The fluid from the impeller and casing cavity is used for cooling the rotor of the induction motor, thereby eliminating the use of an external cooling fan.

1.1.3.2 Limitations

The rotor coils are encased in a stainless steel jacket because the fluid which is passing over the rotor of the induction motor can come in contact with the copper coils of the rotor, thereby corroding them. This increases the gap between the stator and the rotor of the motor. The increased gap results in reduced magnetic induction, and the torque on the rotor. In order to get the desired torque, more current has to be passed through the stator coils at the expense of more heat generation in the windings. The fluid from the impeller cavity is primarily used for cooling the rotor-stator arrangement and this reduces the volumetric efficiency of the pump.

1.2 Induction motor

1.2.1 Basic definitions

1.2.1.1 Synchronous speed

A canned motor pump can be driven by a three-phase induction motor. The induction motor has different number of poles which decide the synchronous speed of the motor at full load condition. Synchronous speed is the speed at which the magnetic field rotates which drives the rotor at some speed. The synchronous speed N_s can be calculated by Eq.1.1. The rotor runs at a slightly lesser speed than the synchronous speed due to presence of slip and friction losses. The motor of canned motor pump referred from Kirloskar[2] catalogue runs at 2850 rpm for two pole motor and 1450 rpm for four pole induction motor. Frequency F of the alternating current is 50 Hz.

$$N_s = F \cdot \frac{2}{poles} \cdot 60 \quad (1.1)$$

1.2.1.2 Phase angle

The phase angle is the angle through which the sinusoidal wave is shifted from a certain reference point in the horizontal direction. It is denoted by symbol φ .

1.2.1.3 Power factor

Power factor is the ratio of actual power used to do work with the power applied to the electric circuit. The mathematical definition is given by cosine of the phase angle φ .

1.2.1.4 Specific electric loading

The total number of ampere conductors around the periphery is known as electric loading (Sawhney[3]), and it is measured in Ampere. The loading sets the limit on the current without exceeding the working temperature. The electric loading is given by the product of the number of conductors to the current per conductor. Specific electric loading is the ratio of electric loading per peripheral area at the air gap. It is denoted by symbol q and the unit is A/m^2 .

1.2.1.5 Specific magnetic loading

The total flux in the air gap of the electrical machine is called as magnetic loading (Sawhney[3]), and the unit is Weber. The loading sets the limit on working flux without saturation. The magnetic loading is given by the product of a number of poles to the flux per pole. Specific magnetic loading is a ratio of magnetic loading per peripheral area in the armature of the machine. It is denoted by symbol B_{av} and the unit Wb/m^2 .

1.2.1.6 Loading efficiency

Loading efficiency is defined as the ratio of the output power to the input power. It is denoted by the symbol η .

1.2.1.7 Winding factor

The winding factor is the multiplication factor used for evaluating the RMS voltage in such a way that the output torque and the voltage does not consist of any harmonics. Presence of harmonics reduces the efficiency of the motor. The winding factor is denoted by the symbol K_w .

1.3 Centrifugal Pump

1.3.1 Introduction

The centrifugal pump is used for many industrial applications for transporting liquids at a specified flow rate and pressure. It consists of an impeller mounted on a shaft, and a volute casing which has one inlet called eye end and one outlet called discharge end. Figure 1.3 shows the schematic diagram of a centrifugal pump.

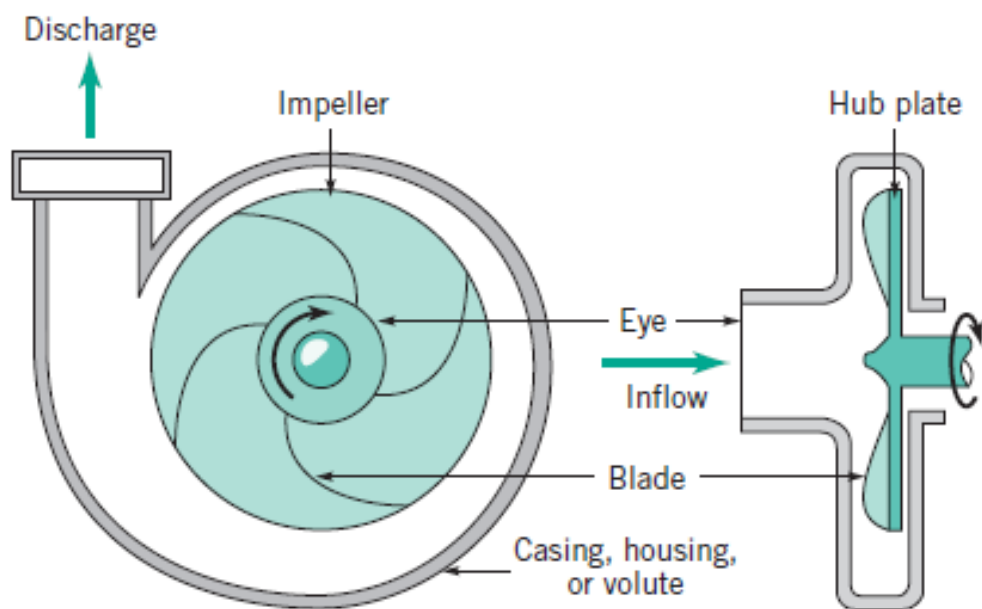


Figure 1.3 Schematic diagram of centrifugal pump Oilfield[4]

The liquid flows from the inlet to outlet of the impeller as it is accelerated and pushed in the radially outward direction by rotating impeller blades. The static pressure rises in the impeller blade gap due to the centrifugal action, and further rises towards discharge end by slowing down of the fluid in the volute casing.

1.3.2 Basic definitions

The pump is characterized by three basic parameters like discharge Q , total head H_t , and power P which are defined below. The schematic of a general pumping system is shown in Figure 1.4. The fluid is sucked from the sump and pushed to the discharge reservoir.

1.3.2.1 Discharge

The total volume of the fluid passing per unit time is called discharge, and it is represented by symbol Q .

1.3.2.1 Total head

Total head defined by Eq.1.3 is the net rise in energy of the fluid from the sump to the discharge reservoir. It is calculated by adding the static, datum and the dynamic head rise along with the friction loss encountered in the pumping system shown in Figure 1.4. Static head is the difference in elevation of the highest point where the fluid has to be delivered and the sump where the suction pipe is immersed. The first and the second term of the Eq.1.2 are static and datum head respectively, and they are constant parameters which do not change with the flow rate. The friction head has to be calculated after knowing the pipe material and the velocity in the pipe. All the friction losses such as suction pipe, discharge pipe, bend loss, entrance and exit losses are to be considered in order to get the friction head. The pipe diameter is constant and thus it can be said that $C_F = C_2$ and $C_A = C_1$. The velocities C_1 and C_2 are calculated from the inlet and outlet velocity triangle.

$$H_t = \frac{(P_F - P_A)}{\rho g} + (Z_2 - Z_1) + \frac{(C_2^2 - C_1^2)}{2g} \quad (1.2)$$

$$H_t = \frac{(P_F - P_A)}{\rho g} + (Z_2 - Z_1) + \frac{(C_2^2 - C_1^2)}{2g} + H_{friction} \quad (1.3)$$

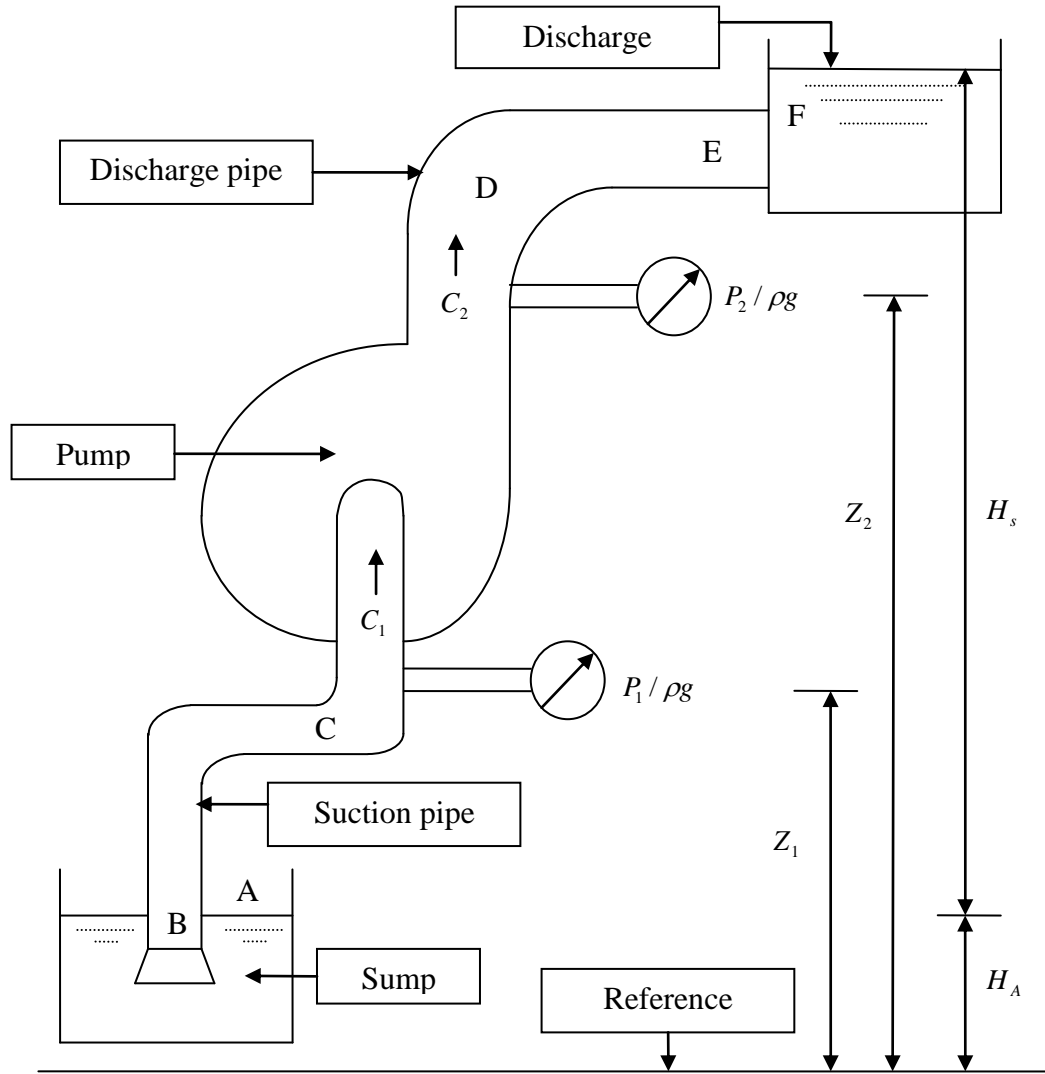


Figure 1.4 Schematic of the general pumping system

1.3.2.2 Specific speed

Specific speed is a parameter used for comparing the performance of two geometrically similar pumps and it is calculated at maximum efficiency point. It is defined in SI units by the Eq.1.4. For the non-dimensional form, the head H in the denominator is replaced with the product of gravitational acceleration g and the head.

$$N_s = \frac{N\sqrt{Q}}{H^{3/4}} \quad (1.4)$$

1.3.2.3 Net positive suction head

When the liquid pressure drops below the vapour pressure, the liquid evaporates. This can damage the blade at the inlet, and the phenomenon is called cavitation. Net positive suction head (NPSH_r) is the head required at the inlet to avoid cavitation. Suction specific speed N_{ss} is also calculated by substituting $H = NPSH_r$ in Eq.1.4.

1.3.2.4 Hydraulic power

Hydraulic power is defined as the amount of work done by the pump on the fluid to raise the fluid to the specified head. Hydraulic power is given by the

$$P = \rho g Q H \quad (1.5)$$

1.3.2.5 Hydraulic loss and efficiency

The theoretical head H_{th} developed at the discharge is reduced due to the friction, circulation and the secondary flow. The hydraulic efficiency given by Eq.1.7 is the ratio of actual head to the theoretical head and it is calculated at the design flow rate.

$$\Delta H = H_{th} - H_{actual} \quad (1.6)$$

$$\eta_h = \frac{H_{actual}}{H_{th}} = 1 - \frac{\Delta H}{H_{th}} \quad (1.7)$$

The hydraulic losses in the pump reduce the useful head generated by the pump. For calculation of the head, the hydraulic efficiency η_h is either assumed or calculated from the statistical data fitted from the known performance data of the similar pump. Friction losses and mixing are dependent on the flow rate and the specific speed of the pump. If the flow rate

Q and specific speed N_s are known, correlation for estimating head loss and the hydraulic efficiency η_h can be used. This empirical approach is often used in design procedures.

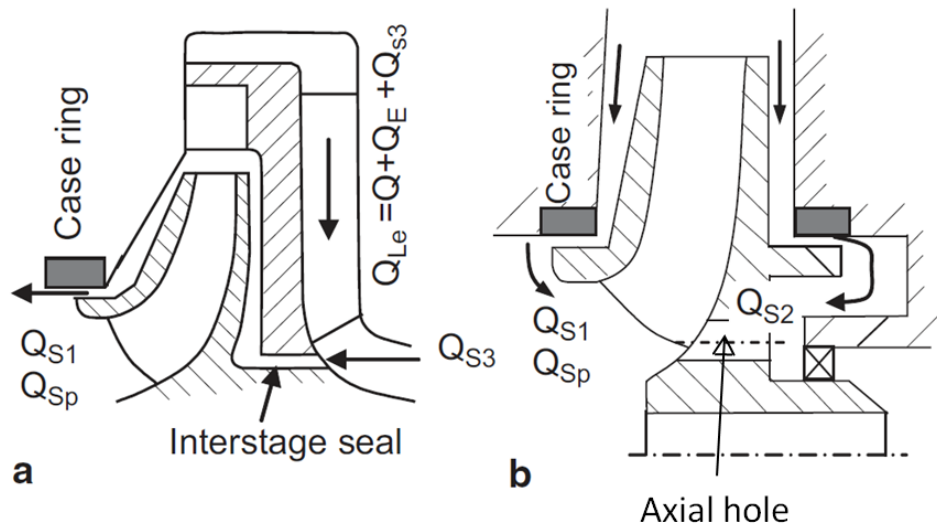


**Figure 1.5 Cross-section view of the impeller and casing a) without b) with balance hole
Gülich[5]**

1.3.2.6 Nomenclature of Figure 1.5

Q	Flow rate without leakage
Q_{sp}	Leakage through pipe
Q_{s1}	Leakage through impeller seal
Q_{s2}	Leakage through balance hole
Q_{s3}	Leakage through multistage connection
Q_{le}	Required flow rate at impeller exit

1.3.2.7 Volumetric loss and efficiency

The impeller smoothly rotates inside the stationary casing due to the small clearance gap provided at the inlet, and the outlet near the case rings shown in Figure 1.5. The pressure at

the outlet of the blade is more than the pressure at the inlet. Due to the higher pressure at the outlet the pump, part of the fluid leaks through the clearance of the impeller and the casing into the inlet of the impeller. This leakage is denoted by Q_{s1} in the Figure 1.5. In some cases, the axial hole (refer Figure 1.5.b) is provided on the impeller to balance the axial thrust. The fluid leakage through axial hole is denoted by Q_{s2} in the Figure 1.5. If the multiple stages of the impeller are connected, some of the higher pressure fluid from the next stage leaks back into the previous stage. This leakage is denoted by Q_{s3} in the Figure 1.5. The leakage Q_{sp} can also occur in the flanges where the pipes and pump are connected. The flow leakage has to be considered for the optimum design of the pump. The volumetric efficiency given in the Eq.1.9 is the ratio of the actual discharge to the theoretical discharge. The value of the actual discharge is calculated after adding all the additional leakages to the theoretical value of the discharge.

$$\Delta Q = Q_{th} - Q_{actual} \quad (1.8)$$

$$\eta_v = \frac{Q_{actual}}{Q_{th}} = 1 - \frac{\Delta Q}{Q_{th}} \quad (1.9)$$

1.3.2.8 Mechanical loss and efficiency

The energy loss in bearing, disc friction loss and loss due to mechanical seal come under mechanical losses. The mechanical efficiency is denoted by the symbol η_m .

1.3.2.9 Overall efficiency

Overall efficiency is the product of all the efficiencies, and it is given by Eq.1.10.

$$\eta_{overall} = \eta_h \times \eta_v \times \eta_m \quad (1.10)$$

1.3.2.10 Blade pass frequency (BPF)

BPF is frequency at which noise generated in a pump is maximum and it is given by the product of rotational frequency and number of blades.

1.4 Impeller basics

1.4.1 Geometry details

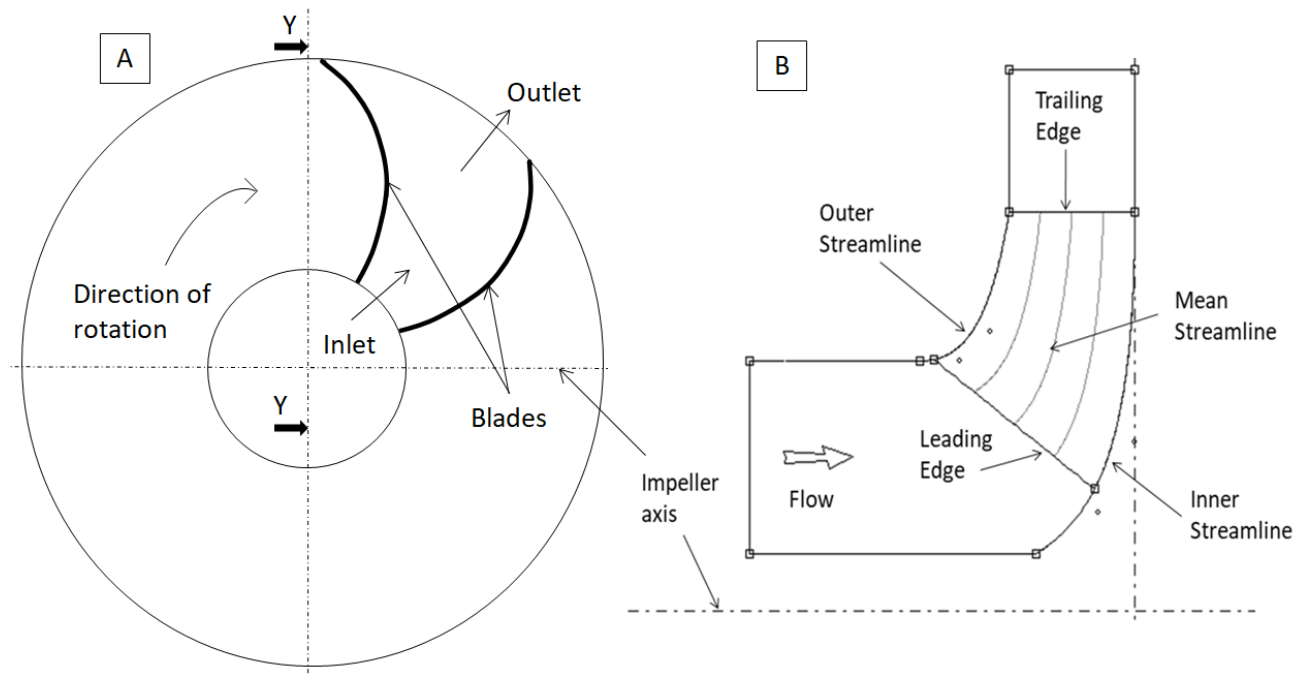


Figure 1.6 Schematic diagram of the impeller in A) front view and B) Side view.

The schematic diagram of the impeller when viewed from the front and the side is given in the Figure 1.6. The side view is obtained when the section of front view is taken along the Y-Y line. This view of the impeller is called as Meridional passage. The Meridional passage is divided in different number of streamlines shown in Figure 1.6 b. For the impeller design, the geometric quantities like diameter, blade angles, and the flow quantities like velocity are represented by a specific suffix assigned to them. The details of the suffix are given on the following page.

- 0 Quantities at the impeller eye before the leading edge
- 1 Quantities on the impeller leading edge
- 2 Quantities on the impeller trailing edge
- 3 Quantities at the impeller eye after the trailing edge

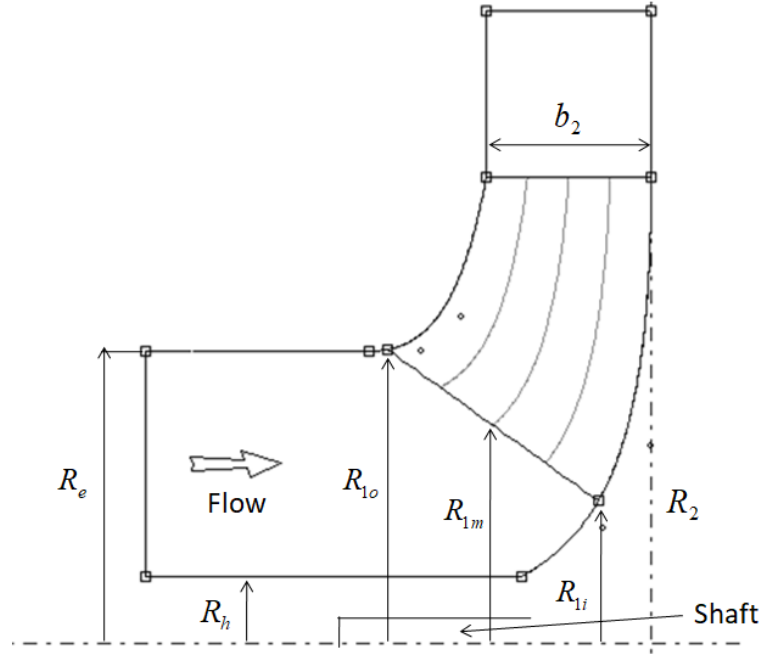


Figure 1.7 Details of the impeller dimensions in the Meridional passage.

The impeller is constructed using free hand curves or Bezier curves to join inlet and outlet sections. The outer streamline is called as shroud and the inner streamline is called as hub. The calculation for velocities is done only for one of the streamlines and other streamline values are interpolated. The dimensions of the impeller at different streamlines are represented in Figure 1.7. The details of the suffix for impeller dimensions associated with different streamlines are given below. From the notations below, the diameter of the shroud at the blade leading edge will be represented by D_{1o} and at the blade trailing by D_{2o} .

- o Quantities at the outer streamline
- i Quantities at the inner streamline
- m Quantities at the mean streamline
- h Quantities at the impeller hub
- e Quantities at the impeller eye
- b Width of the blade

1.4.2 Velocity triangle

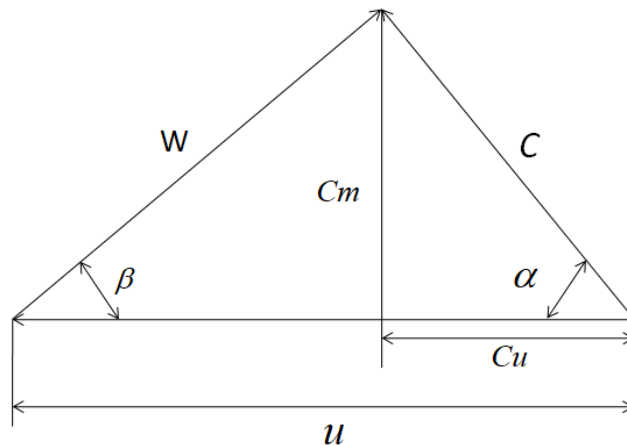


Figure 1.8 Velocity triangles with usual notations.

Head, discharge and speed for the pump are given for designing the impeller profile. For designing the impeller, one-dimensional calculations are done for estimating the velocity triangles at the inlet and the outlet. Figure 1.8 shows the velocity triangle. The velocities and blade parameters are represented by different symbols given below. From the symbols below, the blade angle of the shroud at the blade leading edge will be represented by β_{lo} and at the blade velocity by u_1 .

u	Blade velocity
C	Absolute Velocity of fluid
W	Relative velocity of fluid in blade passage
α	Angle between C and u
β	Blade angle measured between W and u
δ	Blade thickness
t	Blade to blade distance in circumferential direction
C_m	Flow component of absolute velocity
C_u	Tangential component of absolute velocity

1.4.3 Velocity slip at the blade outlet

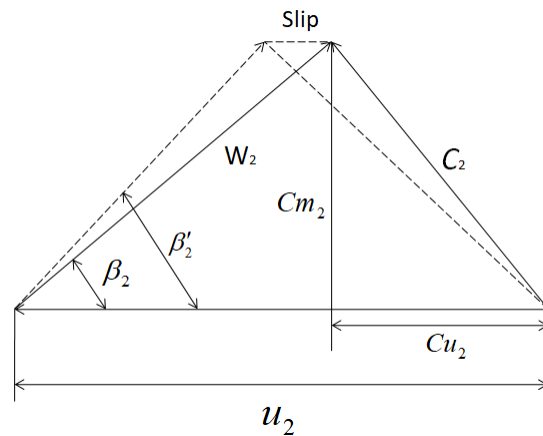


Figure 1.9 Velocity slip at the blade outlet

The angle at which the fluid leaves the impeller may not be the same as the outlet blade angle. This is because the leading side of the blade has higher pressure than the trailing side. The velocity at the leading side thus is lesser than the velocity at the trailing side, which results in slip. Slip changes the velocity triangle at the outlet, as shown in Figure 1.9.

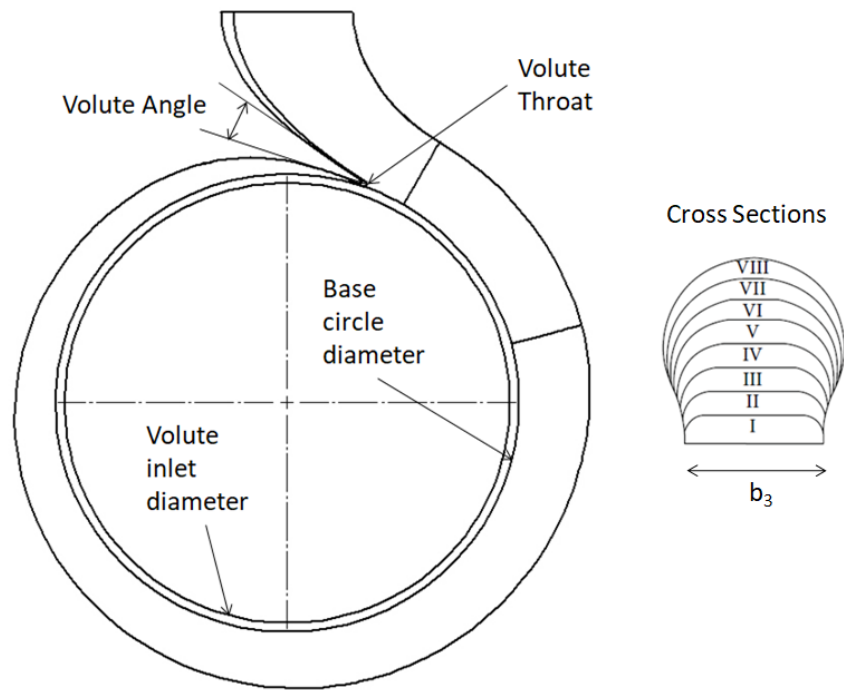


Figure 1.10 Basic volute geometry and different cross-sections

1.5 Volute Casing

The volute casing geometry is specified by the volute angle and different cross-sectional areas taken at 45° offset from the volute throat area. Figure 1.10 shows basic volute geometry and different cross-sections taken from throat to volute outlet (Number 'I' represents throat area). The cross-sectional area can be trapezoidal, circular or elliptic based on the requirement of the designer.

1.5.1 Nomenclature used for volute geometry

α_v : Volute angle

D_v : Volute inlet diameter. Can be same as impeller exit diameter D_2

D_3 : Base circle diameter

b_3 : Volute inlet width

1.6 Acoustics: Theory

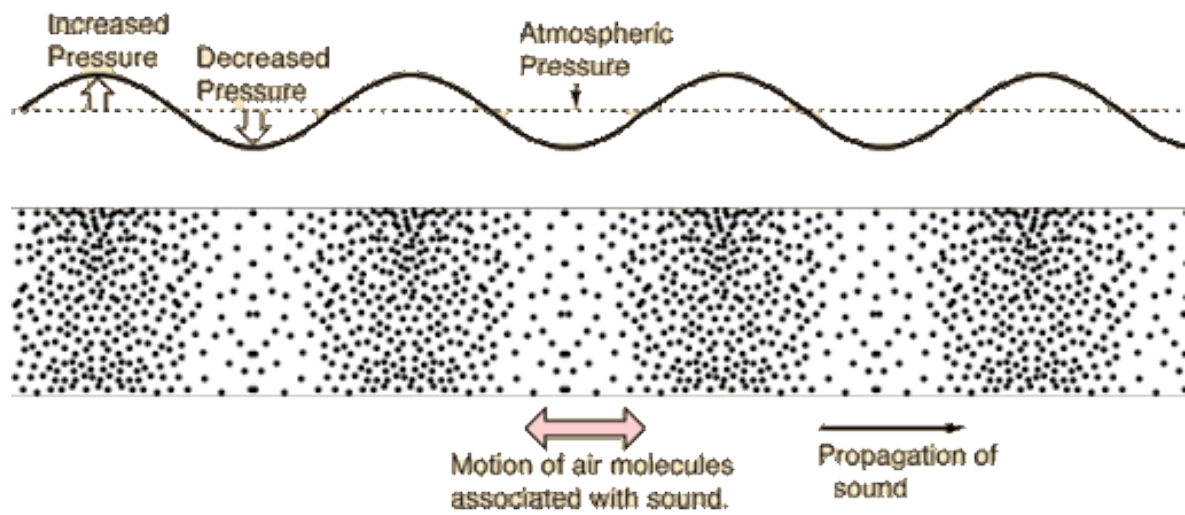


Figure 1.11 Propagation of sound through medium by compression and rarefaction.

1.6.1 Basic Definitions

1.6.1.1 Sound speed

Sound propagates through medium by compression and rarefaction of the fluid particles moving in a wave as shown in Figure 1.11. The sound speed is calculated by assuming adiabatic medium and can be given by Eq.1.11.

$$C = \sqrt{\frac{\gamma RT}{M}} \quad (1.11)$$

1.6.1.2 Wavelength and Wavenumber

Wavelength is the distance between the identical points of the cycle and it is denoted by ‘ λ ’. Wavenumber is the total number of cycles present in unit distance and it is denoted by ‘ κ ’.

1.6.1.3 Vibration speed

Vibration speed is the speed with which particles vibrate about the equilibrium position and it is denoted by symbol ‘ U ’.

1.6.1.4 Sound Pressure Level

The movement of the object or fluid causes disturbance which propagates in the compressible medium such as air. The sensitivity of the human hearing is over the large range and thus the sound pressure level (SPL) is expressed in terms of the ratio of sound pressure to the reference pressure on logarithmic scale.

$$SPL = 20 \log_{10} \left(\frac{P}{P_{ref}} \right) \cdot dB \quad (1.12)$$

The SPL can be given by the Eq.1.12 and it is measured in decibel (dB). The reference pressure P_{ref} is usually taken as $20\mu Pa$ which is the threshold sound pressure that human ears can detect.

1.6.1.5 Sound Power and Sound Intensity

Sound power is defined by the product of pressure force and the velocity of the moving wave. The formula for sound power is given below

$$Power = Force \cdot Velocity = F \cdot u = P \cdot A \cdot u$$

1.6.1.6 Sound Intensity

The net power passing through the unit area is called sound intensity. The formula for sound intensity is given below

$$Intensity = \frac{Power}{Area}$$

1.6.2 Types of sound measurement

1.6.2.1 Far-field

The measurement is said to be far-field if the pressure varies inversely with the radius in the region of measurement. At far-away distance from the source, the radius of the spherical wave is large enough to approximate it by the plane wave. In literature the distance is taken more than twice the wavelength.

1.6.2.2 Near-field measurement

In the near-field measurement there is complex relation between pressure and the distance from the source. Any measurement less than twice the wavelength distance is called near-field measurement.

1.6.3 Governing equations

1.6.3.1 Momentum Equation

The general momentum equation is given by Eq.1.13. The sound propagates in air by local vibration of air particles. The viscous effects are less dominant compared to the inertia and the pressure and thus are neglected from the momentum equation. The vibration velocity is very small compared to the wave propagation velocity in the medium thus the advective acceleration can also be neglected. The momentum equation (Eq.1.13) then reduces to Eq.1.14.

$$\rho \frac{Du}{Dt} = -\nabla p + \mu \nabla^2 u + \rho g \quad (1.13)$$

$$\frac{\partial p}{\partial x} = -\rho \frac{\partial u}{\partial t} \quad (1.14)$$

1.6.3.2 Equation of state

The wave of sound moves through the medium rapidly so that the process can be assumed to be adiabatic in nature. The governing equation for the adiabatic gas is given by Eq.1.15.

$$p \propto \rho^\gamma \quad (1.15)$$

1.6.3.3 Wave equation

Momentum and state equations can be combined together to give the general form of one dimensional wave equation given by Eq.1.16.

$$\frac{\partial^2 p}{\partial x^2} = \frac{1}{c^2} \frac{\partial^2 p}{\partial t^2} \quad (1.16)$$

1.6.4 Solution of the wave equation

Separation of variables can be used for Eq.1.16 as it is linear and homogeneous type of equation. The pressure can be expressed as $p(x,t) = p_1(x) \cdot p_2(t)$ and substituted back in Eq.1.16 to get separate equations of space and time given by Eq.1.17.

$$\frac{p_1''}{p_1} = \frac{\ddot{p}_2}{p_2} = -\kappa^2 \quad (1.17)$$

Equation is space	Equation is time
$p_1'' + \frac{\kappa^2}{c^2} p_1 = 0$	$\ddot{p}_2 + \kappa^2 p_2 = 0$
Guess $p_1(x) = P_1 \cdot e^{gx}$	Guess $p_2(t) = P_2 \cdot e^{ht}$
$p_1(x) = P_1 \cdot e^{\pm j \frac{\kappa x}{c}}$	$p_2(t) = P_2 \cdot e^{\pm j \kappa t}$

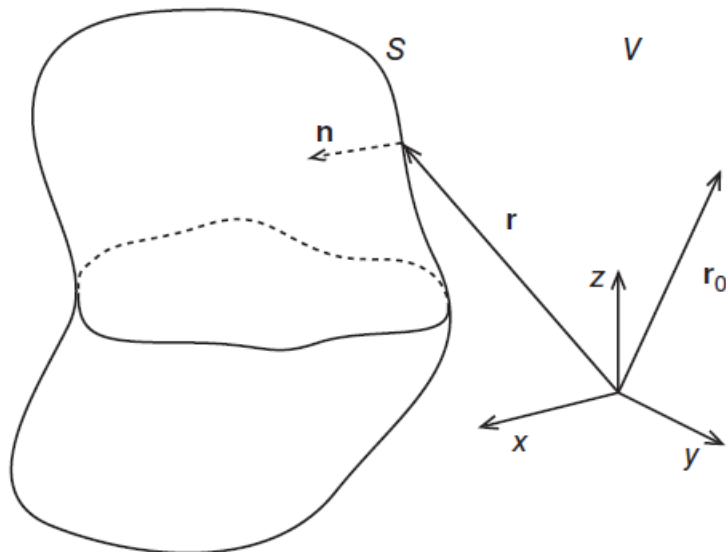


Figure 1.12 A vibrating body with arbitrary shape and surface area S in an infinite volume V with sound source at distance r_0

1.6.5 Kirchhoff- Helmholtz integral

When the wave equation is expressed in frequency domain, it is called as Helmholtz equation given by Eq.1.18. The Helmholtz equation (Eq. 1.18) is homogeneous and known as eigen value problem with multiple solutions. With the presence of vibrating body in acoustic field, a source pressure term has added on the RHS of the Helmholtz equation. Every vibrating part of the body acts as sound source in compressible fluid. The vibrating structure has different kind of modes which act as eigen values for the wave equation. The solution for the pressure field for a vibrating body with any arbitrary shape (Figure 1.12) can be obtained by using Kirchhoff-Helmholtz integral Eq.1.19 which solves inhomogeneous Helmholtz equation. The symbol G is known as Green's function and used to calculate the response of the system in acoustic field.

$$(\nabla^2 + \kappa^2)p = 0 \quad (1.18)$$

$$p(r_o) = - \int_S \left(j\omega \rho \mu_n G(r, r_o) + p(r) \frac{\partial G(r, r_o)}{\partial n} \right) dS \quad (1.19)$$

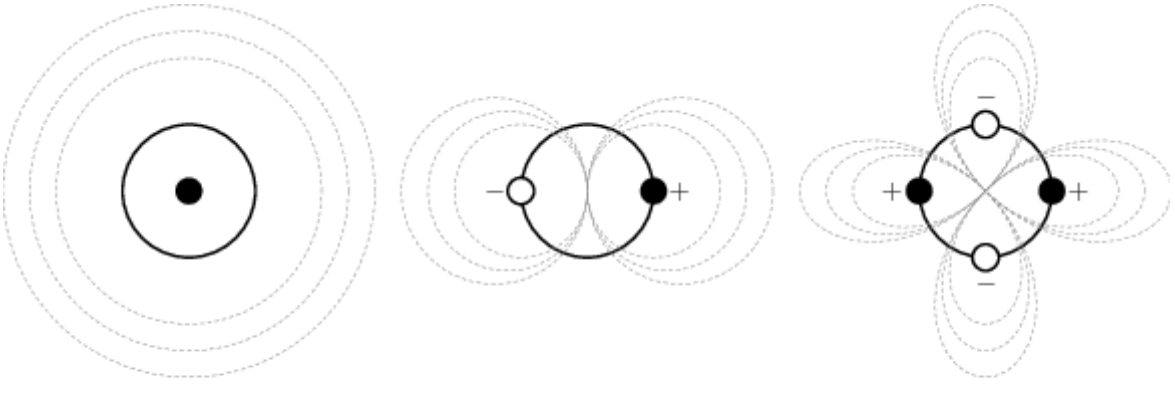
1.7 Types of noise sources

1.7.1 Introduction

The aerodynamic sources can occur because of the fluid moving over a boundary, pressure fluctuations or due to the turbulent flow. The noise sources are classified as monopole, dipole and quadrupole. Figure 1.13 shows the schematic of the different models of the noise sources.

1.7.2 Monopole

A monopole source propagates sound equally in all the directions. It can be imagined as the spherical sound source kept in enclosed space.



Monopole

Dipole

Quadrupole

Figure 1.13 Schematics of acoustic sources

1.7.2.1 Pressure field of monopole source

For a monopole source, variation of pressure is symmetric in spherical direction, and sound propagates only along the radial direction. Thus the variation of pressure in azimuthal and zenith direction is not considered for 3D wave equation. The wave equation in the spherical co-ordinates can be given by Eq. 1.20 which can be expressed differently by Eq.1.21 for mathematical manipulation. The radius term on the RHS of the Eq.1.21 is independent of time and thus can be taken inside the differentiation. The LHS of the Eq.1.21 can also be expressed as the product of pressure and radius inside the space differentiation and it can be given by Eq.1.22. The general solution of the Eq.1.22 for the monopole is given by the Eq.1.23. The constant P of pressure field in Eq.1.23 is evaluated by substituting the solution into the governing equation with appropriate boundary conditions.

$$\nabla^2 p = \frac{1}{r^2} \cdot \frac{\partial}{\partial r} \left[r^2 \frac{\partial p}{\partial r} \right] = \frac{1}{c^2} \cdot \frac{\partial^2 p}{\partial t^2} \quad (1.20)$$

$$\frac{1}{r} \cdot \frac{\partial}{\partial r} \left[r^2 \frac{\partial p}{\partial r} \right] = \frac{r}{c^2} \cdot \frac{\partial^2 p}{\partial t^2} \quad (1.21)$$

$$\frac{\partial^2 (pr)}{\partial r^2} = \frac{1}{c^2} \cdot \frac{\partial^2 (pr)}{\partial t^2} \quad (1.22)$$

$$p(r,t) = \frac{f(t - r/c)}{r} = \operatorname{Re} \left[\frac{P}{r} \cdot e^{j\omega(t - r/c)} \right] \quad (1.23)$$

1.7.2.2 Velocity potential function

Monopole source is an ideal source with no rotational field and thus velocity can be calculated by taking the gradient of velocity potential function ϕ . Since ϕ acts as the driving potential for velocity it has same form as the pressure solution. Velocity potential function ϕ can be given by Eq.1.24 and it is used for calculation of acoustic quantities like pressure and velocity (Eq.1.25).

$$\phi(r,t) = \frac{g(t - r/c)}{r} = \operatorname{Re} \left[\frac{A}{r} \cdot e^{j\omega(t - r/c)} \right] \quad (1.24)$$

$$u(r,t) = \frac{\partial \phi}{\partial r} = \operatorname{Re} \left[\frac{A}{r} \cdot e^{j\omega(t - r/c)} \cdot \left(\frac{-1}{r} - j \frac{\omega \cdot r}{c} \right) \right] \quad (1.25)$$

If we consider monopole source to be a sphere of radius ‘a’ having complex velocity given by Eq.1.25, then by combining Eq.1.25 and Eq.1.26 the value of constant A can be evaluated at radius ‘a’. U_a is the velocity of the pulsating surface and the wave number $K_o = \frac{\omega \cdot r}{c}$ is used in Eq.1.27.

$$u(a,t) = U_a \cdot e^{j\omega t} \quad (1.26)$$

$$A = - \left(\frac{U_a \cdot a^2}{1 + jK_o a} \right) \quad (1.27)$$

1.7.3 Volume velocity

The velocity of the pulsating surface can also be expressed in terms volume velocity. Volume velocity Q is the dot product of the surface velocity and the surface area of the pulsating body.

All the acoustic quantities like pressure, intensity, power, velocity at any distance can then be calculated from the volume velocity. From Eq.1.14 and Eq.1.28 we can get the relation between the pressure and velocity function (Eq.1.28).

$$\nabla p = -\rho \frac{\partial(\nabla \phi)}{\partial t} \text{ or } p = -\rho \frac{\partial \phi}{\partial t} \quad (1.28)$$

Table 1 Equations for acoustic quantities of monopole

Volume velocity	$Q = 4\pi a^2 U_a e^{j\omega t}$
Velocity potential function	$\phi = \operatorname{Re} \left[-\frac{Q}{4\pi \cdot r} \left(\frac{1}{1 + jk_o a} \right) \cdot e^{-j[k_o(r-a)]} \right]$
Pressure	$p = \operatorname{Re} \left[\frac{Q}{4\pi \cdot r} \left(\frac{j\omega\rho}{1 + jk_o a} \right) \cdot e^{-j[k_o(r-a)]} \right]$
Velocity	$u = \operatorname{Re} \left[\frac{Q}{4\pi \cdot r} \left(\frac{1 + jk_o r}{1 + jk_o a} \right) \cdot e^{-j[k_o(r-a)]} \right]$

1.7.4 Dipole

Two monopole sources placed in opposite direction make a dipole source. Membrane of the loudspeaker is the example of the dipole source. On one side, the compression wave is generated while on the other side the air is sucked by the membrane

1.7.4.1 Acoustic quantities for a dipole source

A dipole source is two monopole sources kept together, separated by some distance pulsating out of phase with each other. Figure 1.14 is the schematic of a dipole source for which the velocity potential ϕ can be calculated by summing the individual velocity potentials of the two monopole sources. The velocity potential can be given by Eq.1.29. The expressions for the quantities used in Eq.1.29 are given in Table 2.

$$\phi = -\frac{Q_1(t)}{4\pi r_1} e^{-jK_o r_1} - \frac{Q_2(t)}{4\pi r_2} e^{-jK_o r_2} \quad (1.29)$$

$$\phi(r, t) = -\frac{Q e^{j(\omega t - K_o r)}}{4\pi r} \left[e^{j(K_o d \cdot \cos(\theta + \pi/2))} + e^{-j(K_o d \cdot \cos(\theta + \pi/2))} \right] = -\frac{Q e^{j(\omega t - K_o r)}}{4\pi r} \sin(K_o d \cdot \cos \theta) \quad (1.30)$$

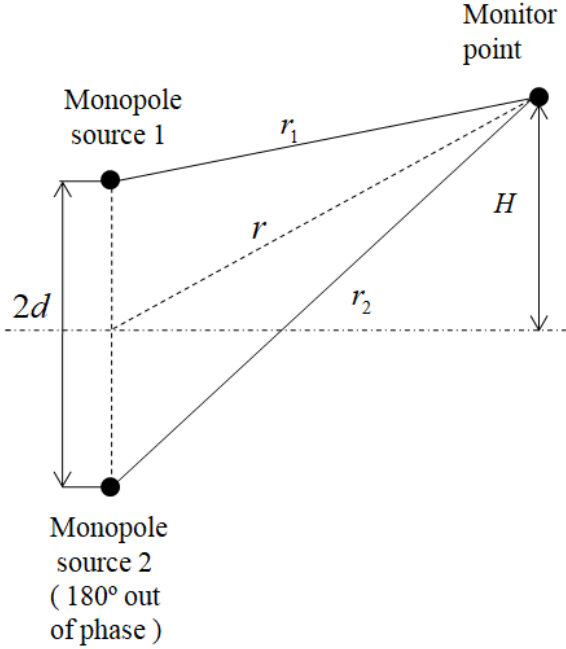


Figure 1.14 Schematic of dipole source reproduced from Manik[6]

Table 2 Expressions used for Eq.1.29

$Q_1(t)$	$Q \cdot e^{j(\omega t + \pi/2)}$	
$Q_2(t)$	$Q \cdot e^{j(\omega t - \pi/2)}$	
r_1	$r - d \cdot \cos \theta$	For $r \gg d$
r_2	$r + d \cdot \cos \theta$	

Table 3 Equations for acoustic quantities of a dipole source

Velocity potential function	$\phi(r, t) = \text{Re} \left[-\frac{Q e^{j(\omega t - K_o r)}}{4\pi r} \cdot (K_o d \cdot \cos \theta) \right]$
Pressure	$p = \text{Re} \left[-\frac{j\rho\omega Q e^{j(\omega t - K_o r)}}{2\pi r} \cdot (K_o d \cdot \cos \theta) \right]$
Velocity	$u = \text{Re} \left[-\frac{Q K_o d \cdot \cos \theta \cdot e^{j(\omega t - K_o r)}}{2\pi} \left(\frac{1 + j k_o r}{r^2} \right) \right]$

After substituting the values of Table 2 in Eq.1.29 we can write velocity potential as Eq.1.30. For $K_o d \ll 1$ we can write $\sin(K_o d \cdot \cos \theta) \approx K_o d \cdot \cos \theta$. By using formulae of Table 3, the pressure and velocity can be calculated at any distance ‘r’ from the center of a dipole.

1.7.5 Quadrupole

Quadrupole is formed when two dipole sources are kept opposite to each other. Clover-like pattern is formed by quadrupole.

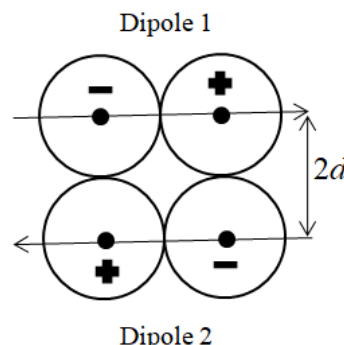


Figure 1.15 Schematic of a quadrupole source reproduced from Manik[6]

1.7.5.1 Acoustic quantities for a quadrupole source

Similar to dipole quadrupole is two dipole sources kept together, separated by some distance pulsating out of phase with each other. Figure 1.15 is the schematic of a quadrupole source for

which the velocity potential ϕ can be calculated by summing the individual velocity potentials of the two dipole sources.

1.8 Lighthill acoustic analogy

Pressure fluctuations generate a near-field noise which can be predicted with any commercial CFD software. The near-field noise gives basic estimation of the strength of the sound source. For acoustic design, far-field noise is important. Most of the CFD domain is fixed around the object creating the disturbance thus it is easy to predict the near-field noise. For the far-field noise prediction, the mesh has to be extended to the reception point, which might not be feasible in all the cases. Thus a simple approach of predicting the far-field noise is, to get the near-field noise from CFD code. The near-field noise is used as a source in a compressible gas medium through which the sound is propagating, and the wave equation is solved in that medium to get the far-field sound intensity. This approach is called as Lighthill acoustic analogy. This allows creation of much coarser mesh and saves the computation effort.

Chapter 2

Survey of Literature

2.1 Introduction

The canned motor pump generates more heat in the rotor and stator coils compared to the conventional motor because of the increased air gap. For keeping the rotor and stator temperature in the permissible limit, optimum coolant flow is required. The literature survey introduces the flow structure and heat transfer taking place in the rotor stator gap. The effect of various geometry and flow parameters on the heat and the flow characteristics is discussed in the literature survey. By understanding the mechanism of the flow and heat transfer in the air gap, optimum cooling arrangement can be designed.

The noise generation in the canned motor pump is reduced by the exclusion of the fan of the motor, and the coupling between the centrifugal pump and the induction motor. The hydrodynamic noise in the centrifugal pump can still be present if the impeller and the volute casing is not properly designed. The literature survey investigates the unsteady flow interactions in the pump so that the noise sources can be identified. By understanding the mechanism of noise generation by unsteady flow interactions, proper acoustic design can be done for noise and vibration reduction in the canned motor pump.

2.2 Flow structure in Stator-Rotor gap

2.2.1 Introduction

The flow over the rotor in a canned motor pump is maintained at a particular flow rate such that the heat is removed from the electrical components, and the temperature is kept within limits. The stator-rotor assembly can be simplified as two co-axial concentric cylinders with the inner cylinder rotating at constant angular velocity and fixed outer cylinder. Figure 2.1 shows the schematic diagram of a simplified Stator-Rotor assembly. The flow system consists of two concentric cylinders of length L with outer radius of inner cylinder labelled R_1 and the inner radius of the outer cylinder labelled R_2 . The fluid flows with an axial velocity V_a through the gap between the cylinders. This type of flow is called as Taylor-Couette-Poiseuille flow (TCPF). The flow structure of the Couette, Poiseuille and Taylor flow is studied individually to understand their combined effect in the rotor-stator gap.

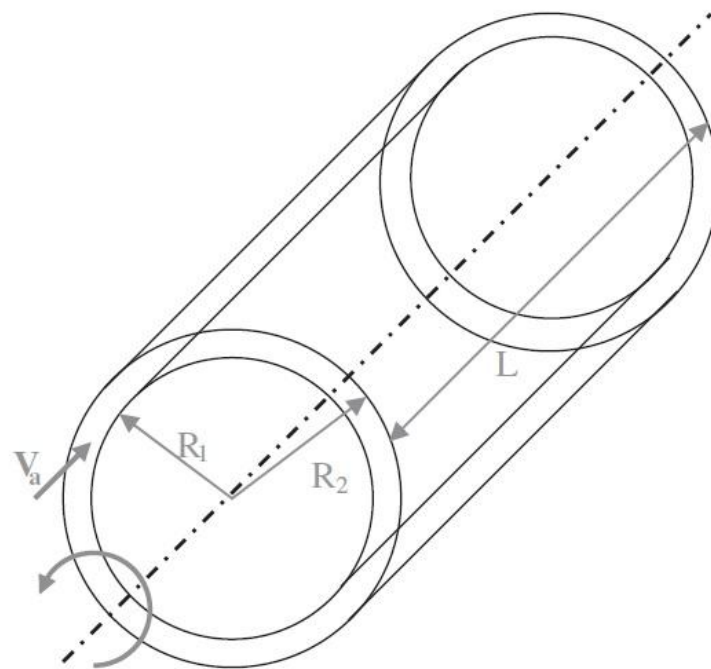


Figure 2.1 Schematic diagram of simplified Stator-Rotor assembly

2.2.2 Flow structure for Couette flow

The laminar Couette flow is explained in (Appendix E) and can be predicted by an analytic solution. It is difficult to get the analytic solution for the case of turbulent flow through the gap between the parallel plates. Thus either the experimental data or the direct numeric simulation data has to be referred in order to model the problem. Bech et al.[7] carried out a direct numerical simulation of the turbulent Couette flow at the Reynolds number of 1260. They recorded the transitional Reynolds number $Re = 360$ through experiment and DNS for the turbulent spots to survive. The Reynolds number defined by Eq.2.1 is based on half the plate velocity and half the plate gap.

$$Re = \frac{U_w h}{\nu} \quad (2.1)$$

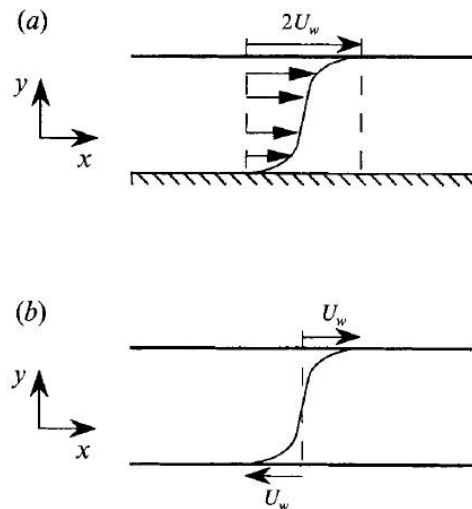


Figure 2.2 Mean velocity distribution in turbulent plane Couette flow a) One wall moving b) Walls moving in opposite direction Bech et al.[7]

The incompressible momentum equation was discretized by the second-order central difference scheme. Second-order Adams-Bashforth scheme was used for time discretization. The results were matched with the experimental results. The flow structure obtained by the simulation can be seen in Figure 2.2. Andersson and Pettersson[8] defined a modified wall function for the Launder and Shima RSM model for Bech et al.[7] geometry and found the exact match with the experimental data.

2.2.3 Flow structure for Taylor-Couette flow

2.2.3.1 Introduction

The Taylor–Couette flow consists of a viscous fluid confined in the gap between the two rotating cylinders. The presence of instability introduces vortices in the flow if a certain rotational speed called critical speed is achieved. Figure 2.3 shows the Taylor vortices for two different rotation speeds higher than the critical speed ω_c . For the low rotational speed, the flow is purely in the azimuthal direction and looks like a series of torus rings packed in the annular gap (left side Figure 2.3). The flow is known as circular Couette flow. The increase in the rotational speed causes distortions in the torus rings. The distortions cause the periodic warping of the toroidal rings (right side Figure 2.3). At higher rotational speed, the periodic warping of the toroidal rings increase. This causes bigger rings to split into the smaller rings and the flow gradually becomes turbulent.

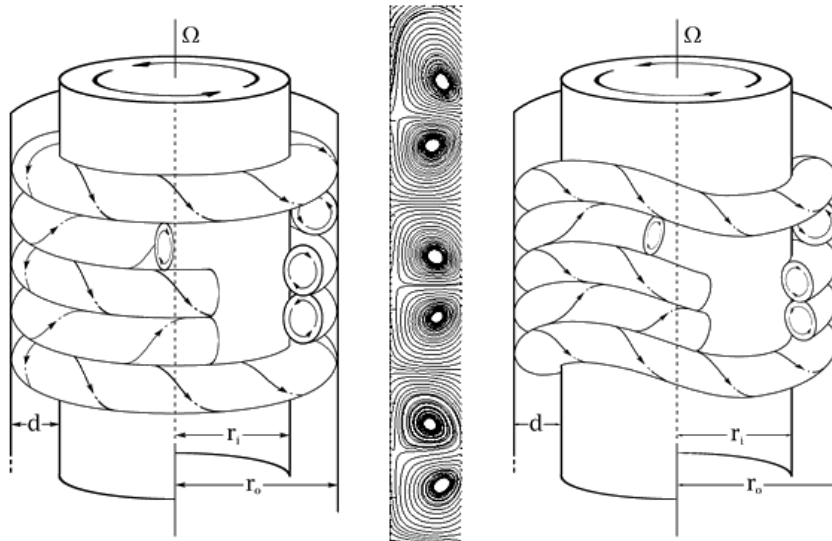


Figure 2.3 Schematic of Taylor-Couette flow Fénot et al.[9]

2.2.3.2 Geometry parameters

R_1	:	Outer radius of the stator
R_2	:	Inner radius of the rotor
$e = R_2 - R_1$:	Air gap between the rotor and the stator

$$\eta = \frac{R_1}{R_2} \quad : \quad \text{Radius ratio}$$

$$L \quad : \quad \text{Length of rotor and stator}$$

2.2.3.3 Critical Taylor number

Taylor[10] showed that when the angular velocity of the inner cylinder is increased above the critical rotation speed ω_c , Couette flow becomes unstable and instabilities structured in the form of torus ring emerge which are known as Taylor vortices. The onset of the instability can be predicted by the Taylor number. The Taylor number is the non-dimensional number which signifies the importance centrifugal force to the viscous force. Taylor number Ta can be defined by the Eq.2.2. Some of the authors use the square root of the Taylor number Ta^* for determining the flow characteristics.

$$Ta = \frac{\Omega^2 R_1 (R_2 - R_1)^3}{\nu^2} \quad (2.2)$$

Davey[11] solved the mathematical problem of Taylor-Couette flow by numerical method and reported the critical Taylor number of 1700 for a narrow annular gap. Stator-rotor gap is called narrow when the aspect ratio η approaches to unity. The aspect ratio is defined by the ratio of the radii of inner to outer cylinder of the annulus. The critical Taylor number of ~1700 is consistent throughout all the literature surveyed and can be used as a benchmark for predicting the onset of the Taylor instability.

2.2.3.4 Critical Taylor number for narrow gap

The critical Taylor number is ~1700 when the rotor-stator gap is very narrow. Fénot et al.[9] plotted the variation of the critical Taylor number with the radius ratio η . For the narrow gap, it can be observed from Figure 2.4 that the critical Taylor number remains constant. Yamada[12] varied the inner cylinder radius for the fixed outer cylinder radius and reported the critical Taylor number. From the results of Yamada[12], it was observed that for the ~600% rise in the gap, Taylor number changed only by 14%. Thus one can neglect the effect of cylinder gap thickness on critical Taylor number variation for narrow gaps.

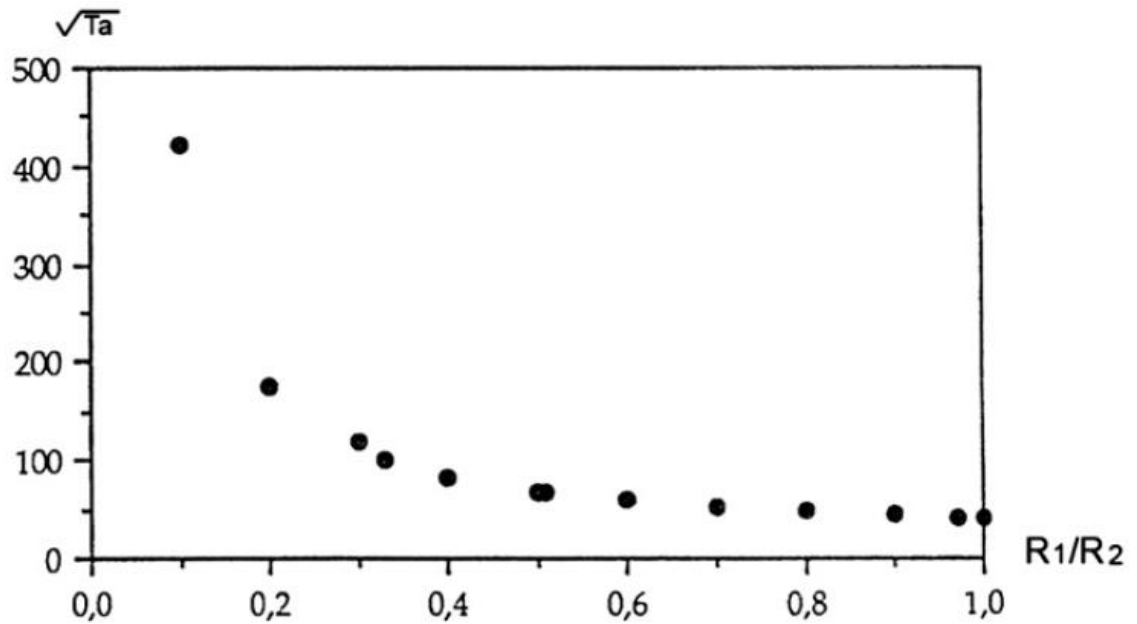


Figure 2.4 Influence of annular gap thickness on the transition to Taylor instability
Fénöt et al.[9]

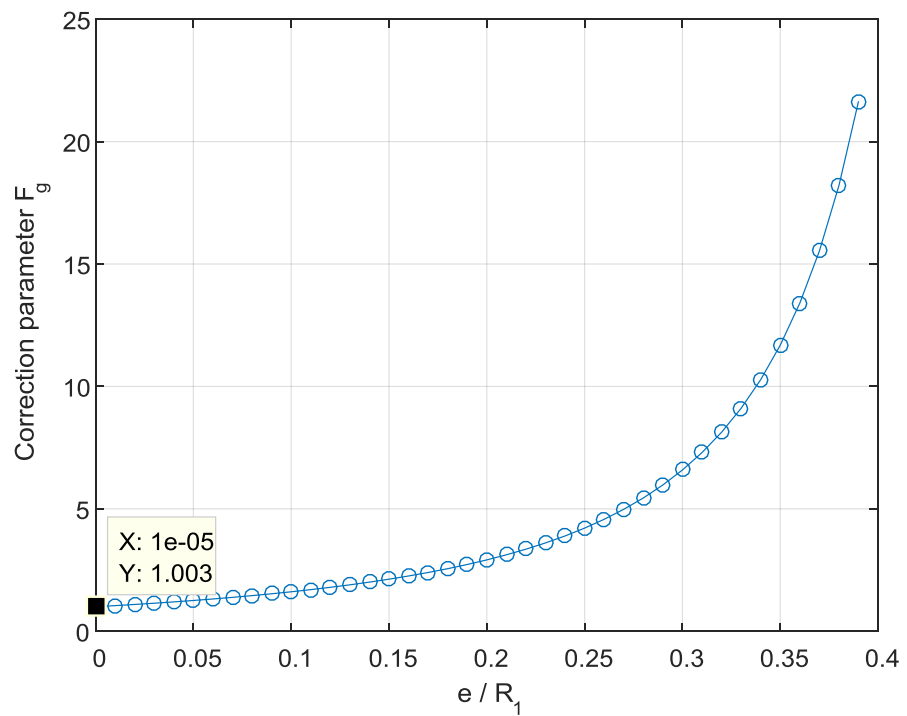


Figure 2.5 Gardiner and Sabersky[13] parameter for different gap thickness

2.2.3.5 Critical Taylor number for wide gap

The experiments are carried out with wider gap as the narrow gap poses difficulties for the flow visualization. The critical Taylor number value is affected by the radius of the rotor and stator as well as the radius ratio η if the gap between the stator and the rotor is wide enough. This effect can be seen in the Figure 2.4 for radius ratio η less than 0.4. The Taylor number definition is thus modified by multiplying the Eq.2.2 by the geometric parameter F_g . Gardiner and Sabersky[13] and Becker and Kaye[14] use an empirical relation given in Eq.2.3 for defining the geometric parameter F_g , which is plotted in Figure 2.5. It can be seen from Figure 2.5 that the multiplication factor approaches to one as the gap is reduced. The formula takes care of the variation of the gap and can be used for predicting the critical Taylor number for both narrow and wide gap.

$$F_g = \frac{1697}{\pi^4} \cdot \left(1 - \frac{e}{2R_1}\right) \left(1 + \frac{e}{R_1}\right) \cdot \left\{ 0.0571 \left[1 - 0.652 \left(\frac{e/R_1}{1-e/2R_1}\right)\right] + 0.00056 \left[1 - 0.652 \left(\frac{e/R_1}{1-e/2R_1}\right)\right]^{-1} \right\} \quad (2.3)$$

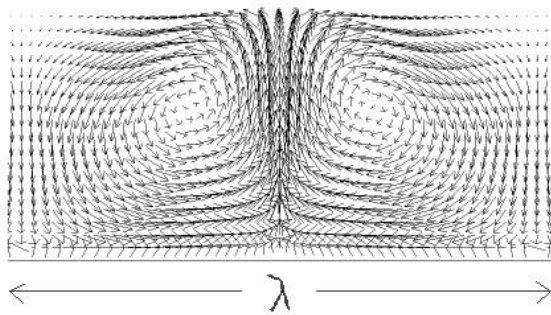


Figure 2.6 Axial wavelength for Taylor vortices

2.2.3.6 Prediction of size and number of vortices

Davey[11] with the help of linear instability solution proposed by Chandrasekhar[15] solved the non-dimensional form of the Navier-Stokes equation to get a characteristic differential equation in radial coordinates. The eigen values of the equation λ give the wavelength of the lobes described in Figure 2.6. The number of pair of lobes a can be determined by Eq.2.4.

$$a = \frac{2\pi e}{\lambda} \quad (2.4)$$

2.2.4 Flow structure in Taylor-Couette-Poiseuille Flow

Taylor-Couette-Poiseuille flow (TCPF) has axial flow superimposed with the Taylor-Couette flow and has two flow mechanisms, one which is driven by centrifugal effect induced by the rotor and the other which is affected by the axial velocity of the flow. Similar to the Taylor-Couette flow, TCPF also has transition from laminar to turbulent region as the rotational speed is increase.

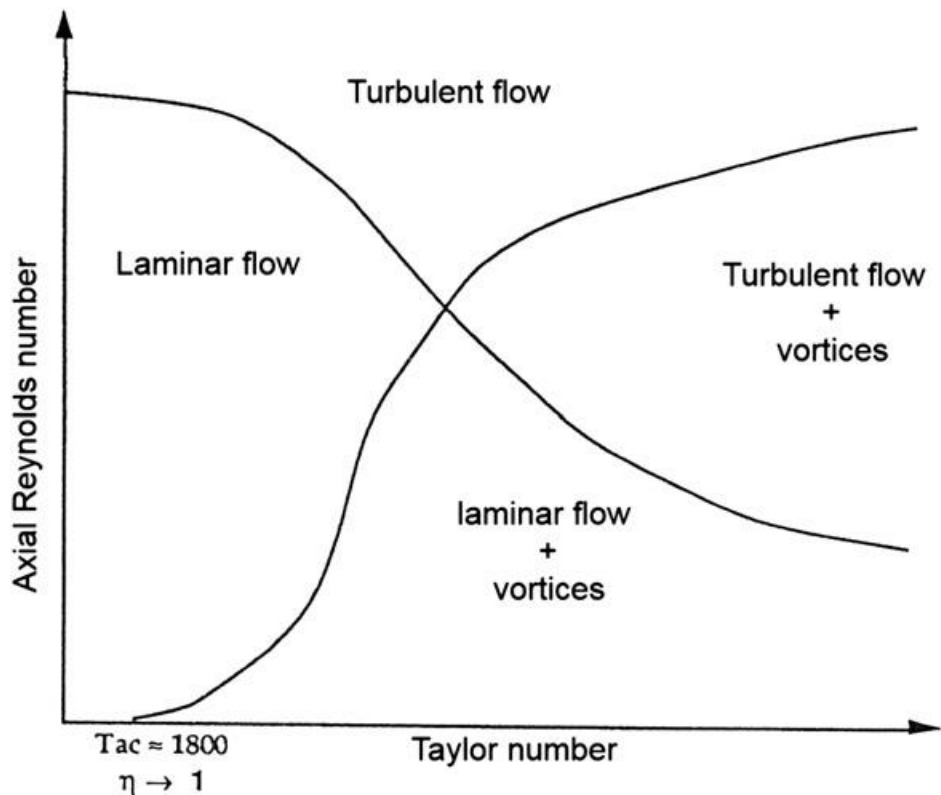


Figure 2.7 Flow regimes for Taylor-Couette-Poiseuille Flow Fénot et al.[9]

2.2.4.1 Effect of axial Reynolds number

Kaye and Elgar (Paper not available Ref. Fénot et al.[9]) described four different types of flow regimes plotted in Figure 2.7 for different cases of axial Reynolds number and Taylor number. They have performed the experiment for narrow cylindrical gaps to determine the

influence of axial Reynolds number on the flow transition and critical Taylor number. With an increase in axial Reynolds number, the critical value of Taylor number at which instability occurs increases. Abassi et al.[16] characterized the TCPF qualitatively by using PIV contour for vertical concentric cylinders. For $\eta = 0.85$, the experiment was performed in two ways. The first way called direct protocol includes the rotation of cylinder followed by the introduction of the axial flow. The second way called indirect protocol includes axial flow followed by the rotation of the cylinder. For the direct protocol, the Taylor number value $Ta^* = 100$ was kept constant and the axial Reynolds number is chosen such that the flow remains laminar and the Taylor vortices are present. They observed that for the case of a direct protocol with the low Reynolds number, the Taylor vortices move upwards with the axial flow and maintain the toroid shape. For higher Reynolds number $Re_a = 34$ the toroid starts breaking and the Taylor instability is delayed. Abassi et al.[16] observed the complete breaking of the helix for $Re_a = 120$ and the flow was dominated by axial component with only traces of Taylor instabilities. For the indirect protocol Abassi et al.[16] fixed Reynolds number to $Re_a = 34$ and varied the Taylor number. Abassi et al.[16] observed that the axial flow effect dominates the flow even after the estimated critical Taylor number is reached and the Taylor vortices are not formed. This means that the transition of flow from laminar to laminar flow with vortices will occur at higher critical Taylor number when Reynolds number is increased. This observation is consistent with Figure 2.7.

2.3 Heat transfer characteristics in Rotor-Stator gap

The pump is driven by an electric motor which has copper windings in stator and rotor. When an electric current is passed through windings, due to losses, heat is generated in the windings. This heat has to be convected out of the system, and thus an effective cooling system is required. The gap between the stator and the rotor is very small compared to the diameter of the components. Taylor instability affects the heat transfer characteristics in the stator-rotor gap. The effect of Taylor instability on Nusselt number is studied in the present study.

2.3.1 Basic definitions

2.3.1.1 Nusselt number

The definition of Nusselt number changes from one author to other but the widely used definition is given by Eq.2.5.

$$Nu = \frac{h \cdot D_h}{k} \quad (2.5)$$

2.3.1.2 Reynolds analogy

The simple way of measuring the convective heat transfer coefficient on the surface is to relate the heat transfer and momentum transfer by Reynolds analogy given by Eq.2.6. The Nusselt number variation is observed by using the friction factor obtained from the experiment.

$$\frac{f}{2} = \frac{Nu|_{Dh}}{\text{Pr} \cdot \text{Re}|_{Dh}} \quad (2.6)$$

2.3.2 Heat transfer in Taylor-Couette flow

2.3.2.1 Effect of Taylor number

Fénot et al.[9] has reviewed and compared the average value of the Nusselt number reported by different authors and plotted a graph shown in Figure 2.8. For a given fluid, the heat transfer coefficient scales with Taylor number and correlation of the form $Nu \propto Ta^\alpha$ can be fitted for the given experimental data. Becker and Kaye[14] performed an experiment for Taylor number range of 0 to 3.3×10^5 and axial Reynolds number up to 12000 for the temperature difference of 0°C to 17°C from inner to the outer cylinder. They found that the Nusselt number increases when the flow transitions from laminar to laminar flow with vortices. The increase in Nusselt number for turbulent flow with vortices was also reported.

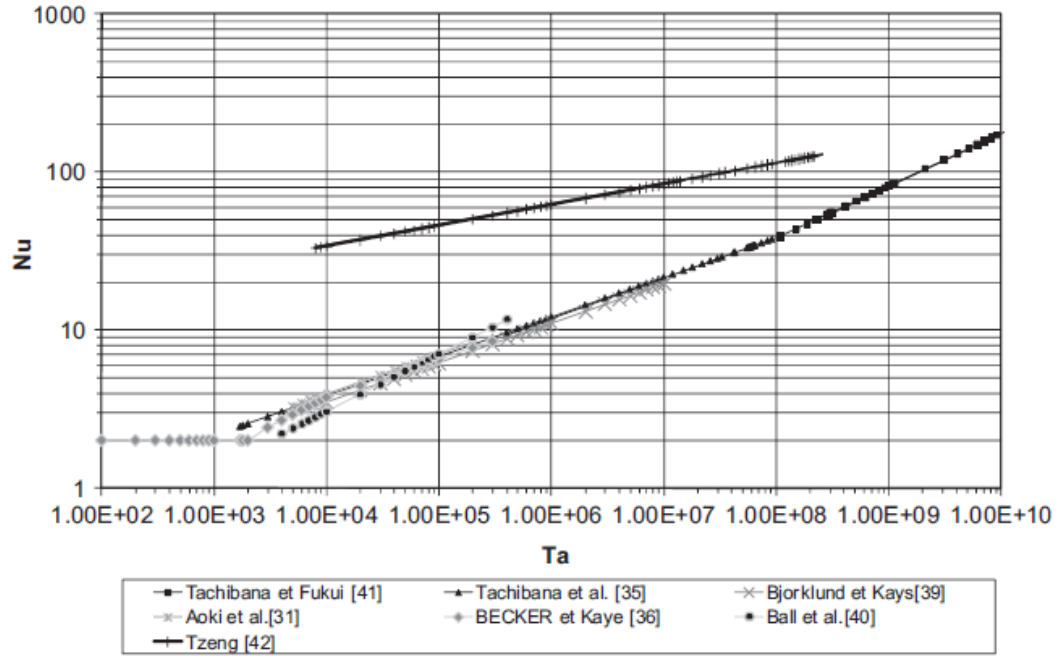


Figure 2.8 Comparison of different values of average Nusselt numbers reported by authors Fénöt et al.[9]

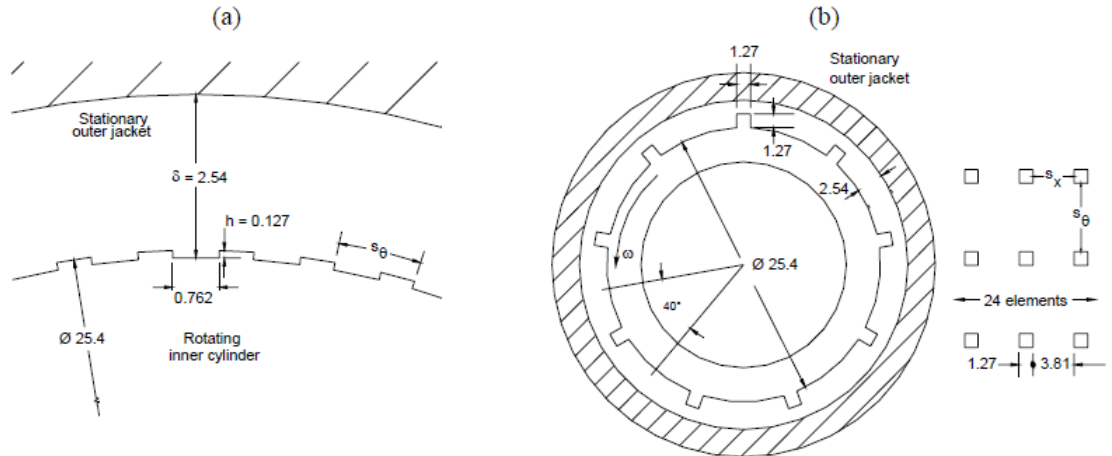


Figure 2.9 Schematic a) Two-dimensional rib roughness b) Three-dimensional protrusion Gilchrist et al.[17]

Jakoby et al.[18] performed an experiment for the Taylor number up to 10^9 and axial Reynolds number range 4000 to 30000. The heat transfer for the turbulent flow with vortices was affected only by the Taylor number. Gilchrist et al.[17] have performed an experiment for Taylor number range of 10^6 to 5×10^7 and axial Reynolds number of 900 to 2100 for the

rotating inner cylinder with water as a working fluid. Experiments were performed for three different geometry types A. Smooth surface B. Inner cylinder with surface protrusion C. Inner cylinder with slots. The geometry details are given in Figure 2.9. The test cylinder is enclosed in the acrylic water jacket, and the hot water is pumped through the annular gap. The inner cylinder is cooled by passing cold water through the inside of the cylinder. The cold water flow was kept constant, and the hot water flow was varied for different values of axial Reynolds numbers. The temperature along the axial direction was measured using T-type thermocouples. The aluminium cylinder of thickness 3.175 mm was used for a rotating cylinder.

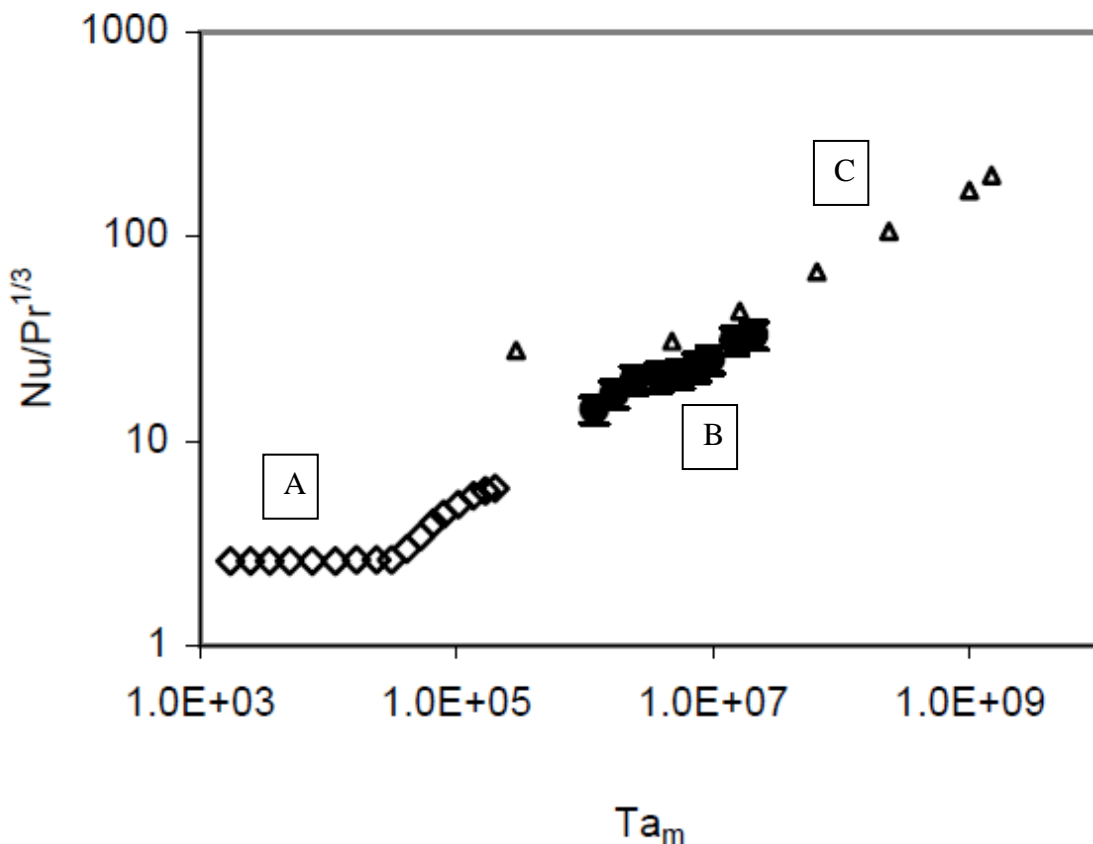


Figure 2.10 Change in Nusselt number with modified Taylor number for the paper A) Becker and Kaye[14] Re = 2015 B) Gilchrist et al.[17] Re = 2080 C) Jakoby et al.[18] Re = 4000

Comparison for Nusselt number variation with modified Taylor number is made in Figure 2.10 for the reviewed papers. The Nusselt number is divided by Prandtl number to normalize the effect of different properties of the coolant fluids on the heat transfer in the annular gap. Up to the critical Taylor number value of the Nusselt number can be predicted by solving the

energy equation for the laminar flow through the concentric gap. After the occurrence of the vortices in the flow, the heat transfer in the gap increases marginally as the Taylor number is increased. For Taylor number higher than the critical value for a given Reynolds's number, as long as the flow remains in laminar regime with vortices, Nusselt number can be predicted approximately by the co-relation of Eq.2.7 proposed by Gilchrist et al.[17].

$$Nu / Pr^{1/3} = 0.65 \cdot Ta_m^{0.226} \quad (2.7)$$

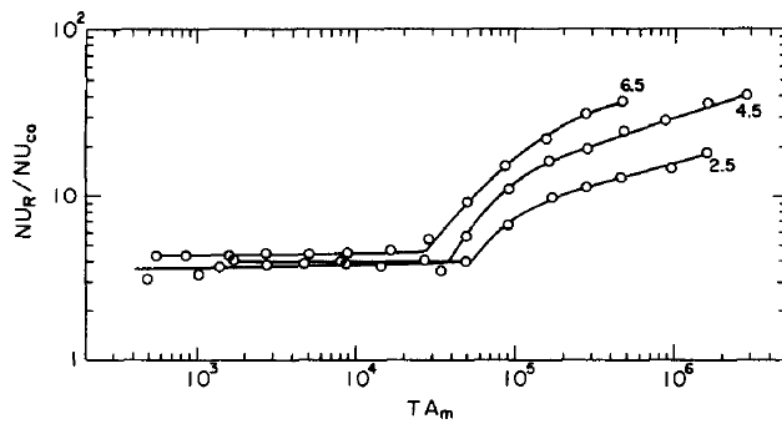


Figure 2.11 Effect of fluid properties on heat transfer in the annular gap. Gardiner and Sabersky[13]

2.3.2.2 Effect Prandtl number

Gardiner and Sabersky[13] studied the effect of fluid properties on the heat transfer characteristics in an annular gap. Figure 2.11 shows the variation of a dimensionless number for different values of the Taylor number. The dimensionless number is the ratio of the Nusselt number with rotation to the Nusselt number without rotation for the annular cylinders. The experiment was performed for different values of Prandtl numbers (2.5 – 6.5), and it can be concluded that the Nusselt number increases with the Prandtl number.

2.3.3 Heat transfer in Taylor-Couette-Poiseuille flow

2.3.3.1 Effect of gap thickness

Yamada[12] measured the Fanning friction factor f (λ in the Figure) for the various combinations of axial and rotational flows. The experiment was performed with horizontally placed co-axial cylinders which are driven by a motor with a maximum motor shaft speed of 2400 rpm. A step-up pulley is used to increase the rotational speed of the inner cylinder to 5000 rpm. The test was performed for six different sizes of the inner cylinder with constant outer cylinder radius with the clearance range of 0.431-3.315 mm.

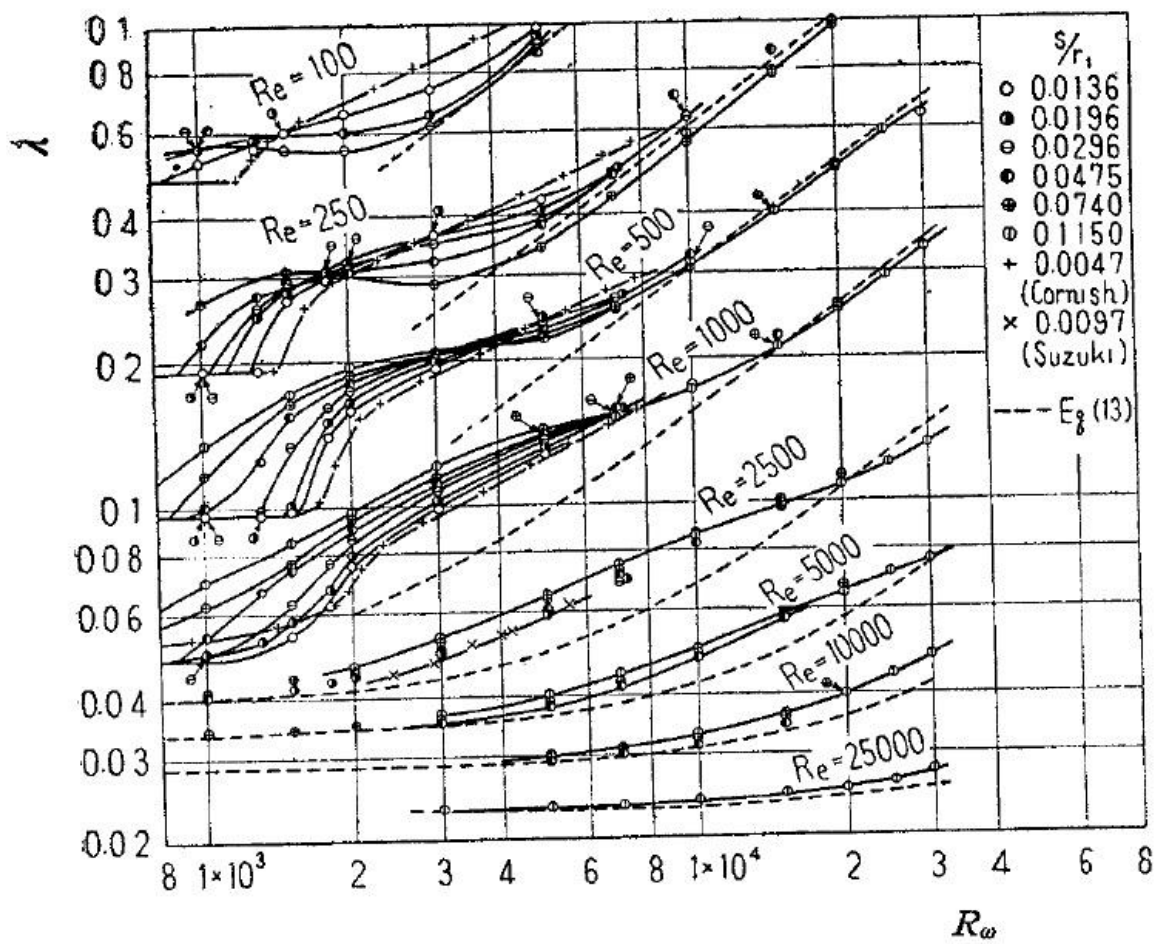


Figure 2.12 Variation of fanning friction factor $f = \lambda$ with rotating Reynolds number for different values of $e/R_1 = s/R_1$ Yamada[12]

Figure 2.12 shows the variation of fanning friction factor f ($\sim\lambda$) with the rotational Reynolds number R_ω given by Eq.2.8. The rotational Reynolds number can be interpreted as the square

root of Taylor number for constant e/R_1 . The effect of gap thickness is also plotted in Figure 2.12. All the plots have a Taylor number greater than the critical Taylor number. It can be observed that the measured friction factor is more for the narrow gap when the flow was laminar. If Reynolds analogy is applicable for the flow, the heat transfer will increase from the heated rotor to the surrounding fluid. For the case of the turbulent flow, the cylinder gap has no effect on the friction coefficient. The dotted lines indicate the estimated value of friction factor by the empirical relation derived by Yamada[12].

$$Re_\omega = \frac{\omega R_1 e}{\nu} \quad Ta^* = Re_\omega \cdot \left(\frac{e}{R_1} \right)^{\frac{1}{2}} \quad (2.8)$$

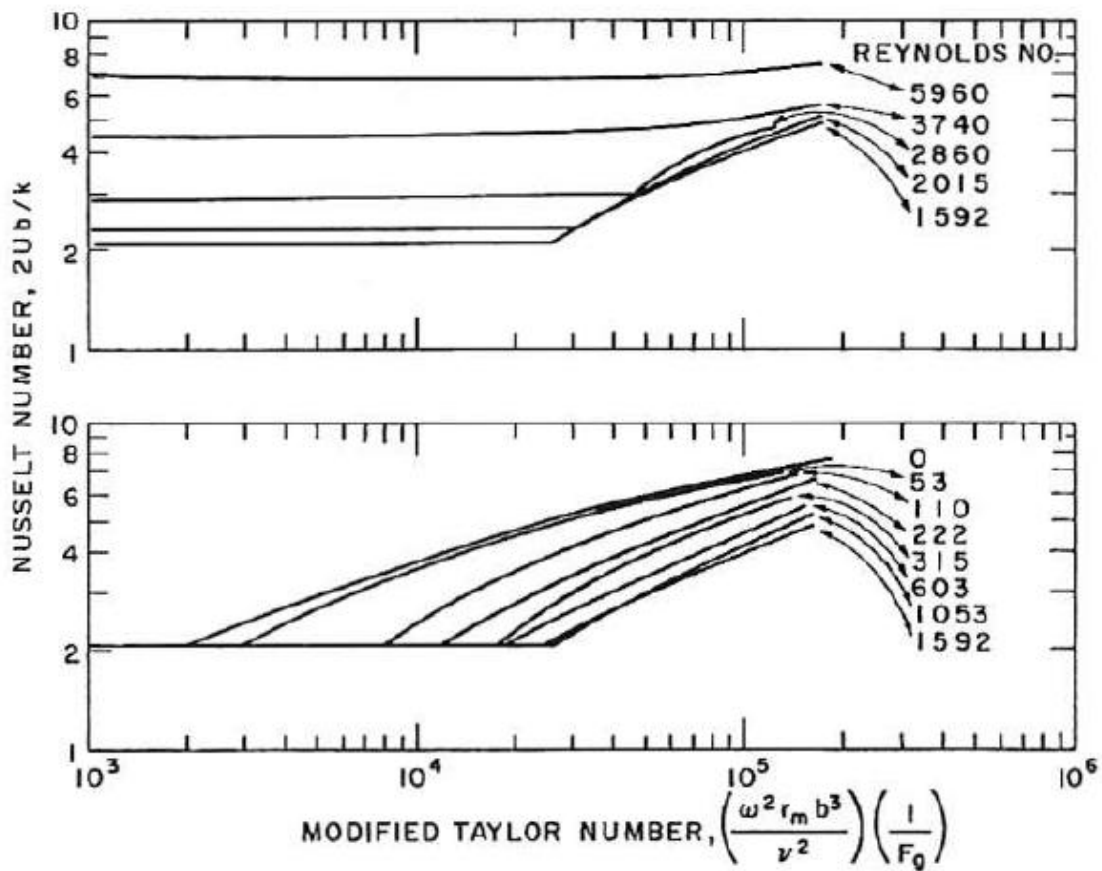


Figure 2.13 Composite of data for Nusselt number for combined rotation and axial flow Becker and Kaye[14]

2.3.3.2 Effect of axial Reynolds number

Becker and Kaye[14] have performed the experiment for the range of Reynolds number and plotted the variation of Nusselt number for different rotational speeds. The presence of axial flow tends to delay the occurrence of the Taylor instability, and it can be observed in Figure 2.13. This behaviour can also be seen in the friction factor variation reported by Yamada[12](Figure 2.12).

2.3.3.3 Effect of can material

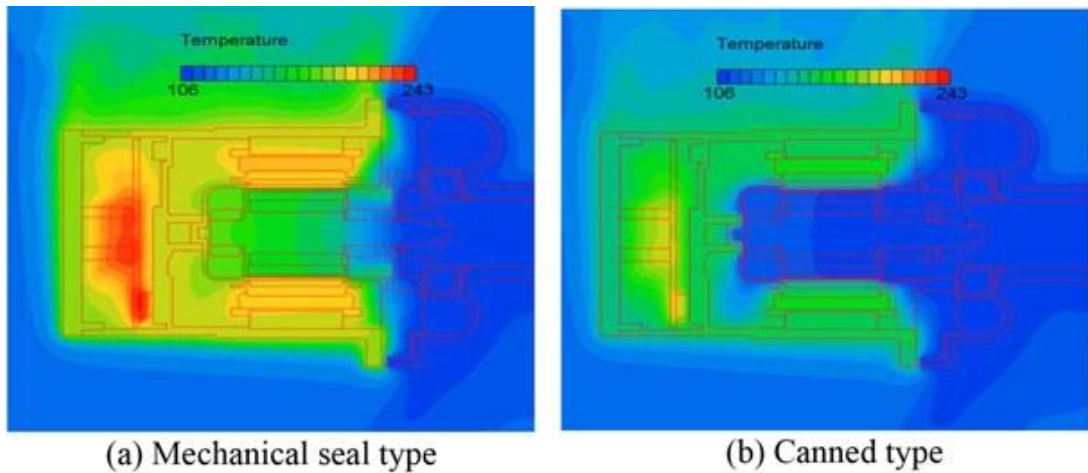


Figure 2.14 Temperature contours for mechanical seal type and canned type pumps Lim et al.[19]

Lim et al.[19] analyzed the canned electric water pump used for cooling the internal combustion engine of automobiles. Comparison between the mechanical seal type pump and the canned pump made with CFD software for various components is shown in Figure 2.14. The turbulent simulation was done by Lim et al.[19] with modified Kato-Launder $k - \varepsilon$ model to overcome the limitations of the model near the stagnation point. The maximum flow rate of the pump is 120 L/min. Pump rotates at 6000 rpm, and the fluid temperature is 106°C. An experiment was also performed to validate the numerical results. An increase in thermal performance of the cooling arrangement with an increase in thermal conductivity of the can material was reported.

2.4 Effect of TCPF on the pressure drop

Nouri-Borujerdi and Nakhchi[20] performed an experiment for the axial flow through rotors-stator gap. The stationary cylinder was grooved with ten grooves ($N_g = 10$) for enhancing the heat transfer in the annular gap. Figure 2.15(A) shows the variation of the pressure drop with axial Reynolds number (R_{eff}) when both cylinders are stationary. The pressure drop increased as the axial Reynolds number is increased which also increases the power requirement to maintain the same flow. The presence of the grooves on the stator also contributed to the pressure drop along the length of the gap.

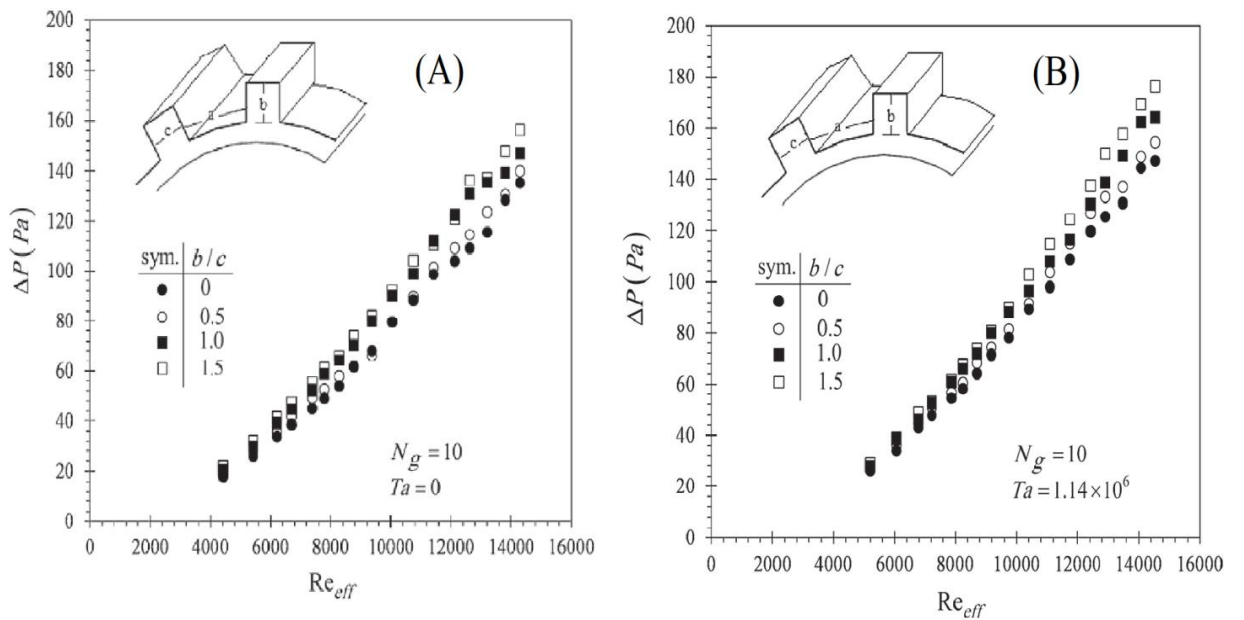


Figure 2.15 Pressure drop along the length of the rotor for the annular gap with and without rotation. Nouri-Borujerdi and Nakhchi[20]

The experiment was performed for the rotating cylinder for the Taylor number in the range $0 < Ta < 2.4 \times 10^6$. Figure 2.15(B) shows the variation of the pressure drop with axial Reynolds number (R_{eff}) when the inner cylinder is rotating. The slope of the pressure drop variation is more in the (B) than in (A). From the results of Nouri-Borujerdi and Nakhchi[20] it can be concluded that the pressure drop increased with the increase in rotational speed of the rotor.

2.5 Centrifugal Pump

2.5.1 Introduction

The presence of Taylor instability enhances the heat transfer and increases the power required for pumping the coolant through the annular gap. The increased power demand can be met with small external coolant pump or the secondary impeller on the motor shaft. The schematic diagram of canned motor pump with the secondary impeller is shown in Figure 2.16. The experimental data for the secondary impeller of the canned motor pump is not widely available. The conventional design of the centrifugal pump can act as a reference for designing the secondary impeller. Different impeller design approaches are studied in the present work for estimating the dimensions of the secondary impeller. The literature for noise generation and flow prediction in centrifugal impeller is also surveyed so that the optimum acoustic and hydraulic design is achieved.

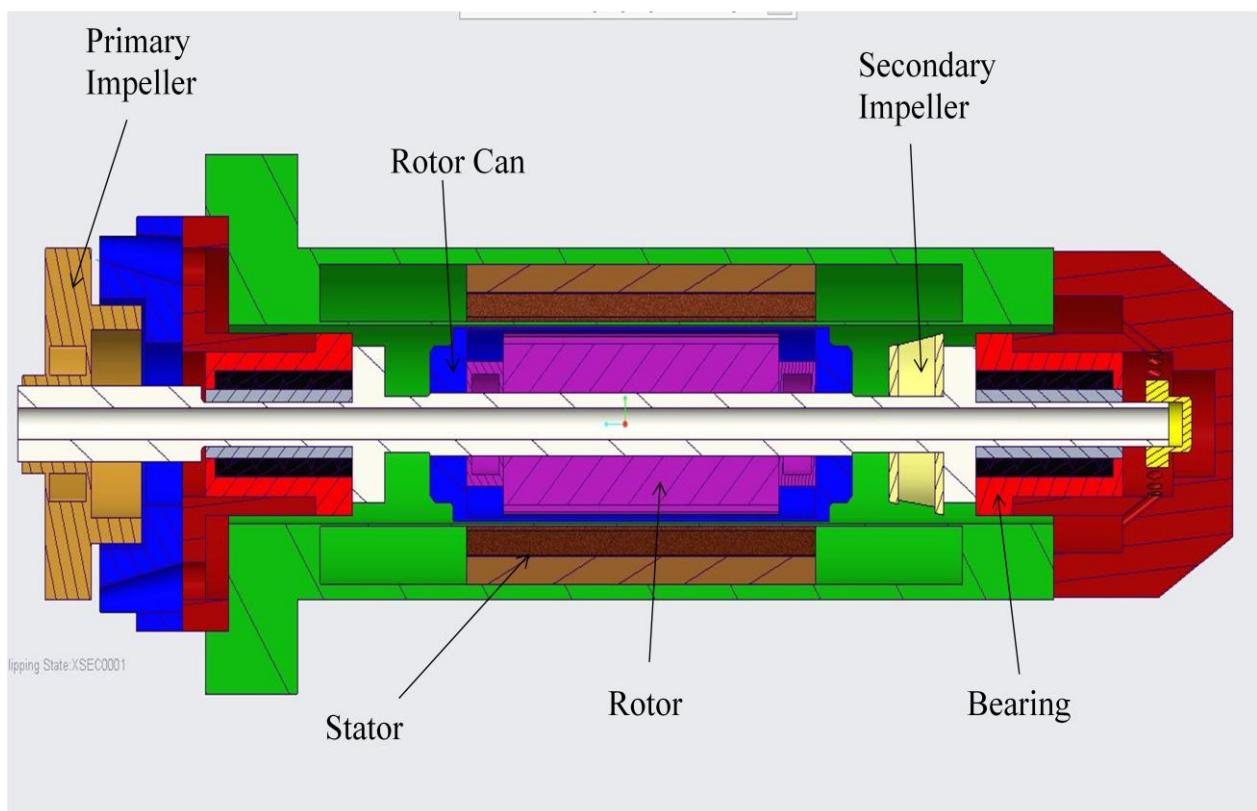


Figure 2.16 Canned motor pump with a secondary impeller cooling arrangement designed in SOLIDWORKS

2.5.2 1D Preliminary Impeller design

2.5.2.1 Introduction

The main dimensions of the impeller have to be determined for making the impeller in CAD software. One dimensional mean-line design approach is adopted as it helps for the initial design of the impeller, volute and the diffuser. Head, discharge and the rotational speed at the best efficiency point should be known for the initial calculations. Ideal streamline flow assumption where no circulation is present is used, and all the secondary flow and uneven velocity distributions are ignored in the mean-line design approach.

2.5.2.2 Hydraulic Design Methods

Different approaches have been developed for designing the centrifugal pump for a specific application. One such approach is modelling the pump based on the existing pump data. By performing the dimensional analysis, the geometric and fluid dynamic similarity is obtained between the pumps. Karassik et al.[21] handbook and Osterwalder[22] listed the modelling laws which can be used as a guide for the pump design by scaling approach. The scaled pump can also be modified to get the desired pump characteristics. Inlet geometry, blade angles, collector throat area are usually modified for better results of the scaled model. Various empirical relations are used in the absence of the available pump data. Empirical relations are obtained from experimental tests on the pump and can be used for a rough estimate of the pump geometry. Gongwer[23] has given the empirical co-relation for predicting the NPSH_r of the pump. Gülich[5] and Srinivasan[24] can be referred for various geometry and flow prediction formulae. Stepanoff[25] has given the charts of velocity and geometry variation with the specific speed. Worster[26] studied the effect of volute and impeller geometry on the performance of the pump and proposed the free vortex method for pump design. All of the mentioned methods can be combined and used for the optimum design.

2.5.3 Blade shaping

The one dimensional design values are used for generating the section of the blade in different planes. Blade shaping is an iterative process. Different geometry factors like blade angle, thickness, curvature of the blade; and different flow parameters like boundary layer,

circulation, blade loading etc have to be considered for optimum performance of the pump. Gülich[5] and Stepanoff[25] have given Kaplan's method of error triangles for shaping the blades. New computer codes make use of Bezier curves for blade generation. Casey[27] and Wang and Huang[28] have described the method of Meridional passage generation with Bezier curves. The same method is used in commercial code Vista CPD (Ansys®[29]) and BladeGen (Ansys®[30]) for blade generation. Srinivasan[24] has given an empirical approach which considers blade thickness for the vane development. All of the methods are discussed in detail in a later chapter.

2.5.4 Volute Design

Cho et al.[31] have given the empirical approach for the design of the different sections of the volute casing. The procedure is discussed in detail in a later chapter. The design method assumes constant flow velocity in the volute section. Stepanoff[25] has given the graph for different volute constants such as volute angle, base circle diameter etc. in a graph for simplifying the design steps. The volute can also be designed by constant angular momentum method, which is described in Gülich[5].

2.6 Performance prediction

For reducing the design iterations, some empirical and theoretical methods are used for predicting the H-Q characteristics of the pump. Win[32] has given the slip and loss method for pump characteristics prediction. Different head and friction loss co-relations can be referred from Gülich[5] for accurate prediction of the H-Q curve and efficiency. Pump characteristics can also be predicted by a theoretical method called Throughflow analysis. Wu[33] has given the detailed theory and the governing equations for solving the 2D flow in the Meridional passage. Casey and Robinson[34] used the Throughflow method for predicting the flow velocity and the pressure distribution for the centrifugal compressor with radial blades. The code by Casey and Robinson[34] is used in Vista TF (Ansys®[35]) for estimating the flow structure and head developed in the Meridional plane of the pump. Throughflow method saves a lot of time as it takes only a few seconds to give the converged results. Thus before going to full 3D analysis with FLUENT (Ansys®[36]) or CFX (Ansys®[37]), it is best to run Throughflow analysis first to predict the pump characteristics.

2.6.1 Throughflow method

2.6.1.1 Introduction

Throughflow method is used for predicting the flow structure and pressure distribution in the turbo-machinery. It is an iterative method and converges faster than the full 3D analysis of the impeller. The method is only applicable to the axis-symmetric geometry. The accuracy of the prediction is dependent on the loss co-relations used for calculation.

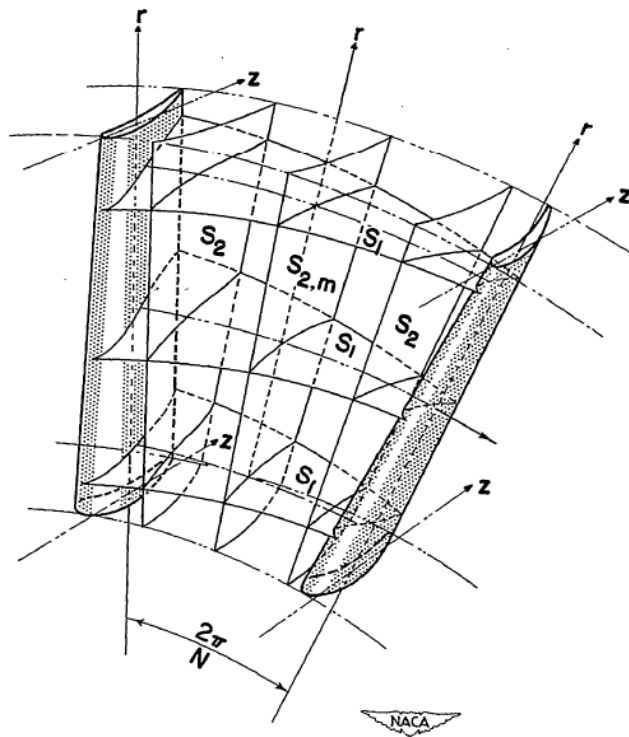


Figure 2.17 S1 and S2 surfaces in blade row Wu[33]

2.6.1.2 Nomenclature

Two surfaces S_1 and S_2 are defined in Figure 2.17. The surface S_2 represents Meridional section, and S_1 represents a circumferential plane in the radial impeller blade. If the blade does not have curvature, solving continuity, momentum and energy equations on S_2 surface is sufficient to predict the flow characteristics. The detailed derivation of governing equations is given in Wu[33] and Novak[38]. The equations can be referred from Novak[38].

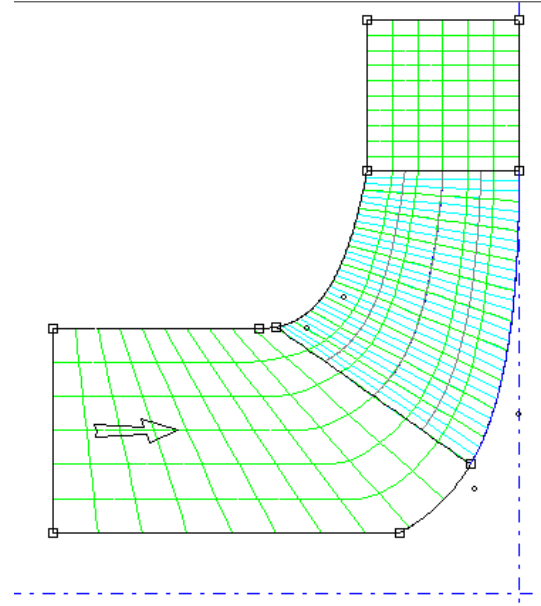


Figure 2.18 Computational grid used for Throughflow calculations Ansys®[35]

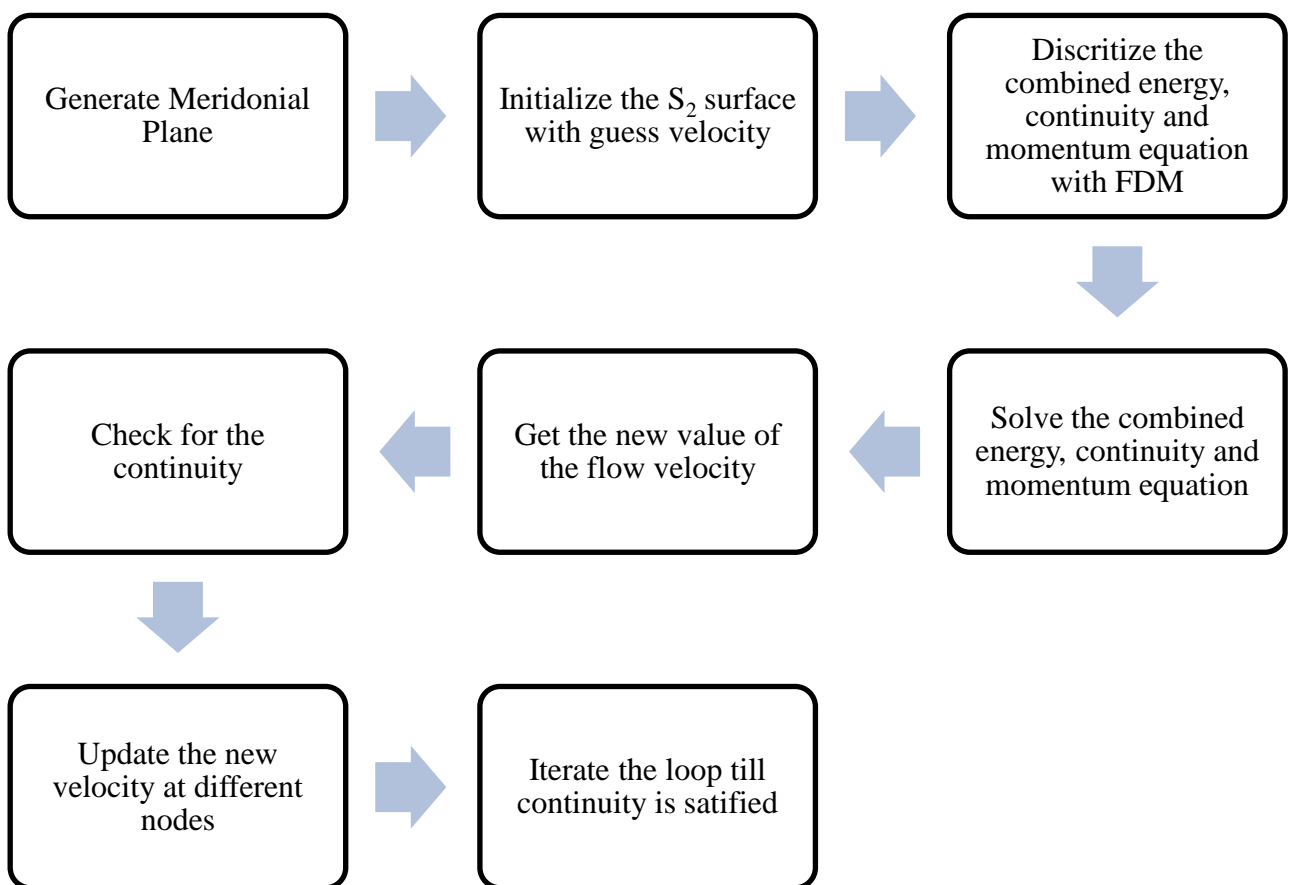


Figure 2.19 Throughflow calculation algorithm

2.6.1.3 Algorithm

A Meridional surface has to be created for solving the governing equations. For initial iteration, the surface is divided into equal streamlines, and flow velocity is assumed at every node in the grid. The grid used for the calculation can be referred from Figure 2.18. The algorithm for Throughflow method is given in Figure 2.19. The algorithm is used in Ansys Vista TF for the pressure and flow predictions.

2.6.2 Slip and loss analysis

Win[32] used correlations for different head losses listed in Table 4. If the impeller geometry is known, pump characteristics can be approximately estimated by Eq.2.9. The hydraulic efficiency can also be obtained by taking the ratio of the predicted head and the theoretical head. The accuracy of the prediction is dependent on the head loss co-relations. A good amount of empirical data is given in Gülich[5] or Karassik et al.[21] for different types of pumps.

$$H_{predicted} = H_{slip} - (h_s + h_1 + h_2 + h_3) \quad (2.9)$$

Table 4 Head losses described in Win[32] paper

Head	Nomenclature	Formula
H_{th}	Theoretical / Euler's head	$\frac{u_2 \cdot C_{u2}}{g}$
H_{slip}	Slip head σ is slip coefficient derived from empirical results.	$\frac{u_2 \cdot (u_2 \sigma - C_{m2} \cot \beta_2)}{g}$
h_s	Shock losses	$h_s \propto (Q - Q_{design})^2$
h_1	Impeller and volute friction losses	Refer Gülich[5] or Karassik et al.[21] for empirical relations.
h_2	Disk friction losses	Refer Gülich[5] or Karassik et al.[21] for

		empirical relations.
h_3	Recirculation losses	Refer Gülich[5] or Karassik et al.[21] for empirical relations.

2.7 Steady state pump simulation

Steady state pump simulation can be done using the mixing plane or frozen rotor approach. CFX provides both the approaches for steady state simulation. Gülich[5] has given the experimental results of the pump in the book. The data is used by Kaewnai et al.[39] for predicting and optimising the performance of the impeller with CFX. They simulated the flow within the impeller geometry using different turbulence models like $k - \varepsilon$, $k - \omega$, RNG for nine different grid sizes. (Ref. Figure 2.20). The choice of model made no significant difference in the predicted value for the steady state simulation if the flow is not separating. $k - \varepsilon$ model is widely used for most of the impeller simulations if the flow is not separating (Ref. Kaewnai et al.[39], Nataraj and Ragoth Singh[40]). For flow rates less than the design flow rates, $k - \varepsilon$ model does not perform well. Thus the model like $SST - k - \omega$ is used for separating flow.

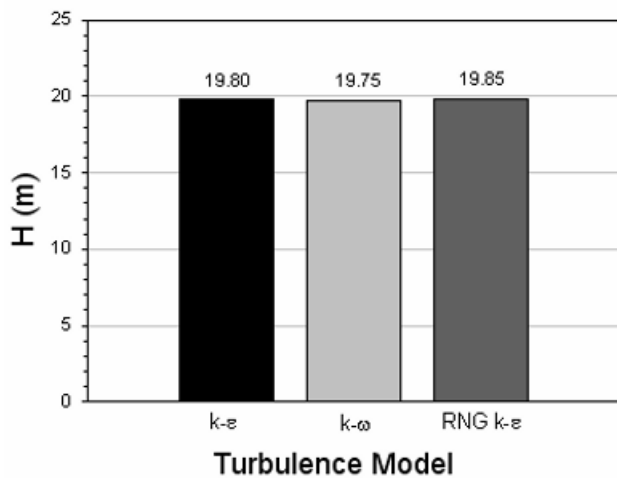


Figure 2.20 Pump impeller simulation for different turbulence models simulated by Kaewnai et al.[39]

Kim et al.[41] performed a CFD simulation for the pump geometry using the SST turbulence model. Optimization technique called response surface method (RSM) was used by Kim et al.[41] for improving the performance of the pump. Blade inlet and outlet angles were used as

control variables for optimization. An improvement in the pump characteristics was observed as shown in Figure 2.21. RSM technique also is used by Nataraj and Ragoth Singh[40] for optimization of head and power by varying the impeller eye diameter, vane exit angle, and width of the impeller blade at the exit.

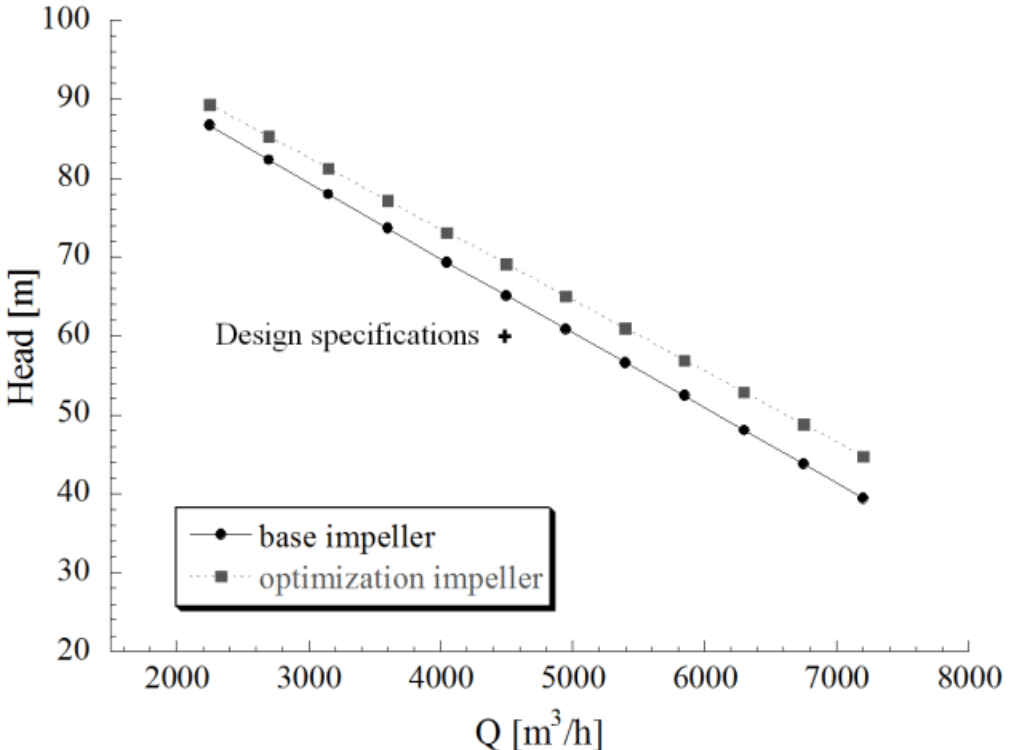


Figure 2.21 Comparison between regular and optimized impeller Kim et al.[41]

Páscoa et al.[42] using CFD investigated the effect of running the pump as a turbine for understanding the flow structure. Tan et al.[43] has studied the impact of variation of outlet blade angle, blade thickness and the number of vanes on the performance of the pump. Outlet angle variation has a significant effect on the pump characteristics. The variation of the head for different outlet angle values is shown in Figure 2.22. The pump performance is optimum for outlet blade angle between $10\text{--}25^\circ$. This observation is also given in Gülich[5] and Stepanoff[25]. Although 6° outlet angle shows the highest head, lower outlet angle values can cause recirculation at the impeller exit causing severe shock and vibrations.

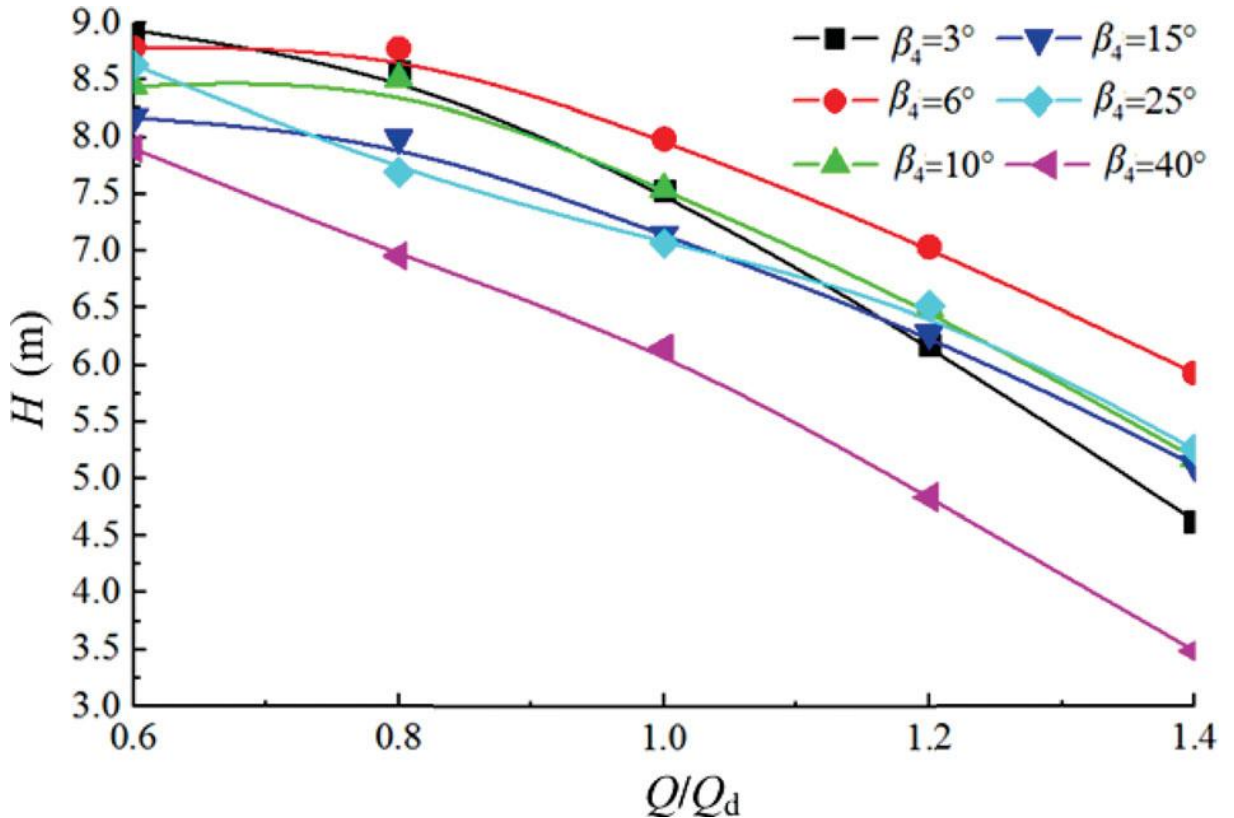
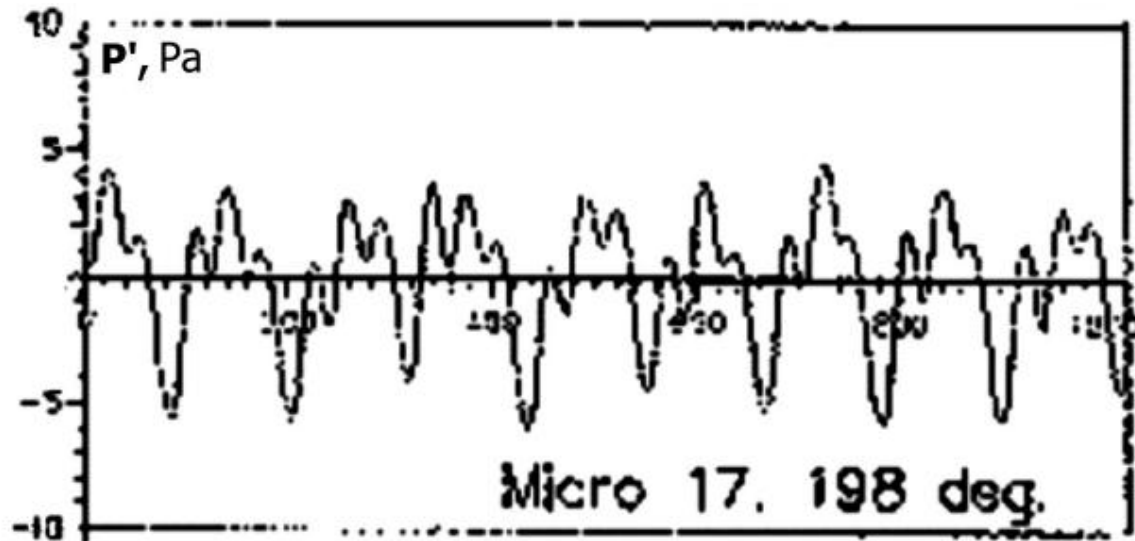


Figure 2.22 Effect of outlet blade angle on pump performance Tan et al.[43]

2.8 Unsteady state pump simulation and noise

Once the steady state behaviour is known, the data can be used as an initial condition for the unsteady case. Unsteady simulations are useful for understanding pressure pulsations in the volute and impeller. The pulsations act as a noise and vibration source, which can be undesirable in some applications. Dürer and Wurm[44] discussed different noise generating sources like turbulent flow, rotor imbalance, circulation, and hydraulic thrust on the impeller blades and volute casing. Reduction of the noise source is part of the design of the pump. Unsteady pressure pulsations can be captured using experimental data or CFD simulations. Timouchev and Tourret[45] measured the pressure pulsations for the centrifugal air pump with rotation speed of 1400 rpm and flow rate of $0.0139 \text{ m}^3 / \text{s}$. The numerical analysis was done for investigating the influence of flow rate, rotation speed and the radial gap on the pressure pulsations at the impeller exit and the volute throat. The pressure pulsation data measured at volute throat is given in Figure 2.23.



between the monitor points. (Ref. Figure 2.25). C_p is the ratio of pressure fluctuations with outlet kinetic energy. The average pressure in the impeller for the suction side(1SM, 2SM) is less than the pressure side (1PM, 2PM) for all the flow rates. Pressure fluctuations were less at the design point compared to off-design flow rate and are shown in Figure 2.25.

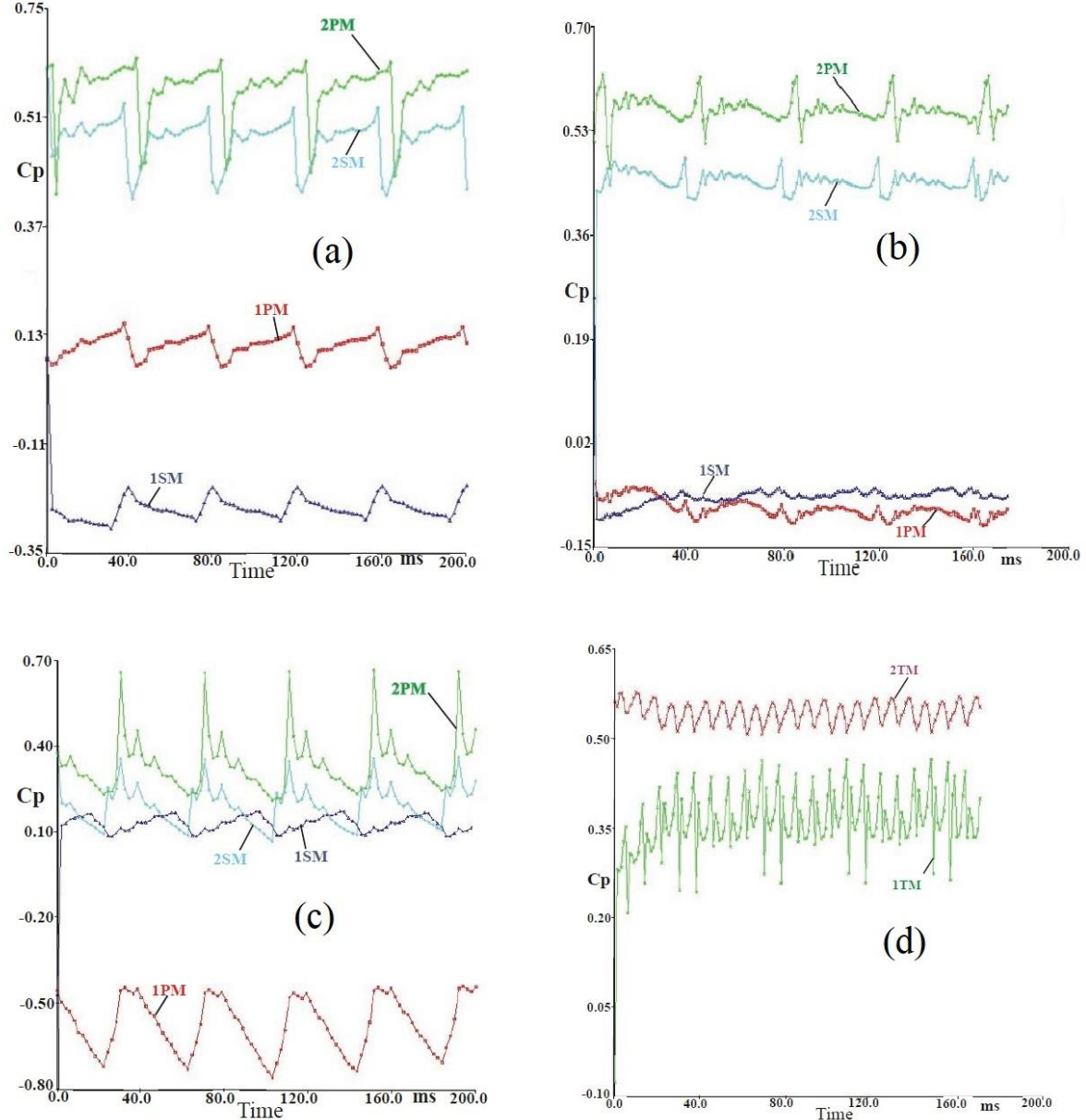


Figure 2.25 Pressure fluctuations for a) $Q < Q_d$ b) $Q = Q_d$ c) $Q > Q_d$ d) Volute throat Majidi[46]

Si et al.[47] simulated the unsteady fluctuations and compared them with the experimental results. SST-SAS- $\kappa-\omega$ model was used for simulation. The model uses a hybrid method which solves LES mesh in near boundary region and RANS equations in rest of the domain.

The pressure fluctuations were minimum at the design flow rate and are shown in Figure 2.26. A similar trend of pressure fluctuations was also observed by Lu et al.[48], Chen et al.[49], Wu et al.[50], and J. Yang et al.[51].

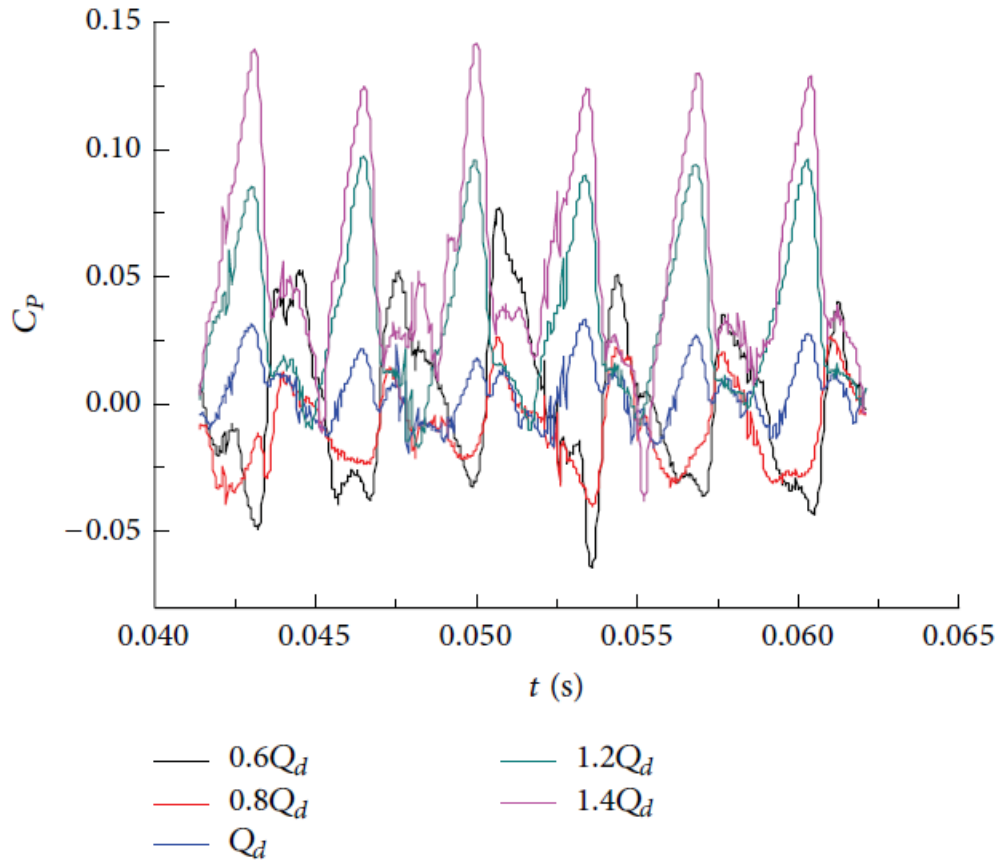


Figure 2.26 Pressure fluctuations at volute throat for different flow rates Si et al.[47]

Si et al.[47] set eight monitor points at different mesh locations of the volute surface. Monitor points on the volute casing can be referred from Figure 2.27. It was shown that the pressure fluctuations are maximum at blade pass frequency (BPF = 290 Hz) from simulation and experiment data. The FFT data showing peaks at BPF for different monitor points can be seen in Figure 2.28. Cao et al.[52] investigated the effect of pump casing clearance on the pressure fluctuations and observed that for small clearance, pressure fluctuation amplitude is higher. Guo et al.[53] performed an experimental study for understanding the noise generation in the pump. They have found that the noise level increases with increase in rotational speed of the pump (Figure 2.30). The sound pressure level was dipolar and the noise level was more in the volute tongue direction compared to the other directions. Chen et al.[49] carried out both the structural and acoustic simulation and confirmed the presence of dipolar noise. The dipolar sound pressure level pattern can be seen in Figure 2.29.

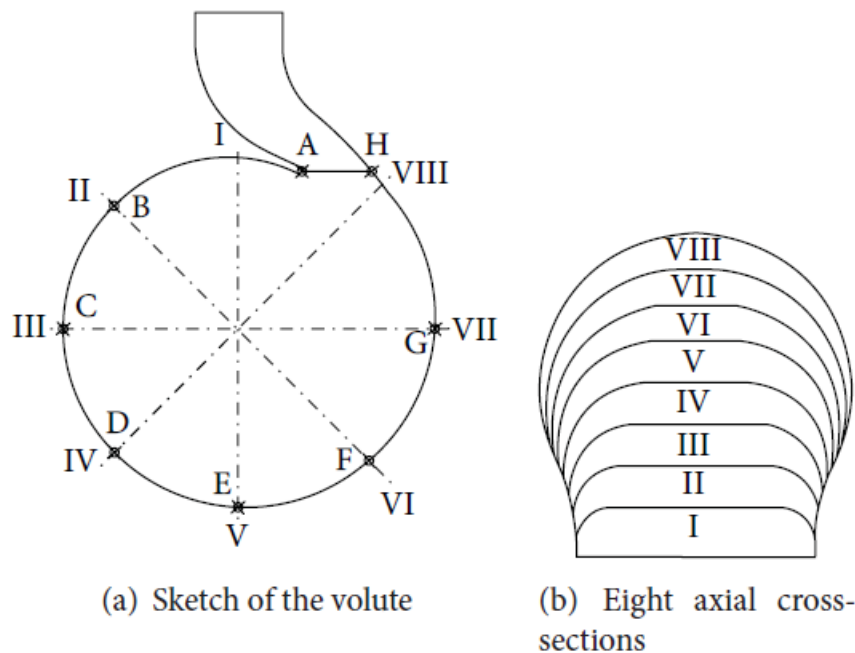


Figure 2.27 Monitor points used for recording the pressure fluctuation data by Si et al.[47]

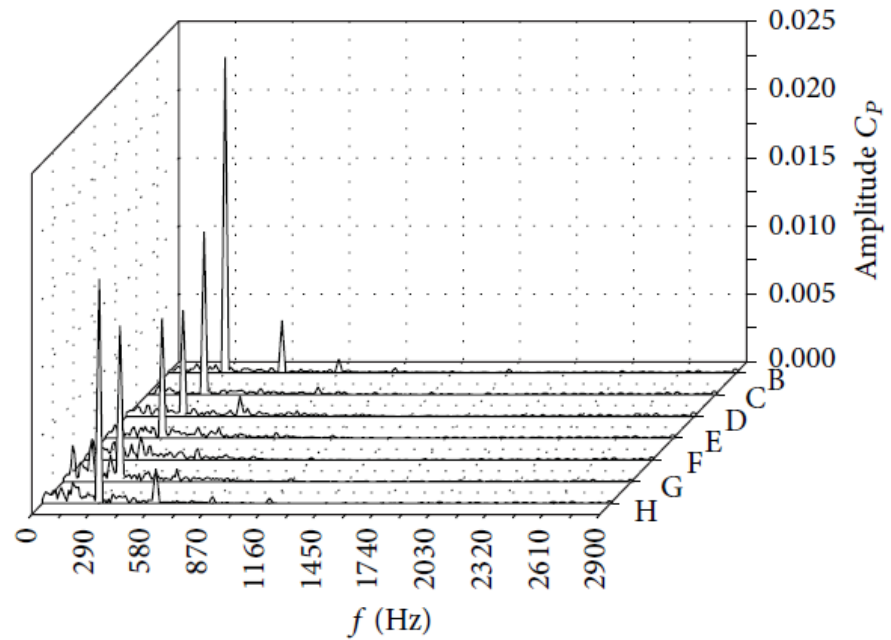


Figure 2.28 Pressure coefficient fluctuation in the frequency domain Si et al.[47]

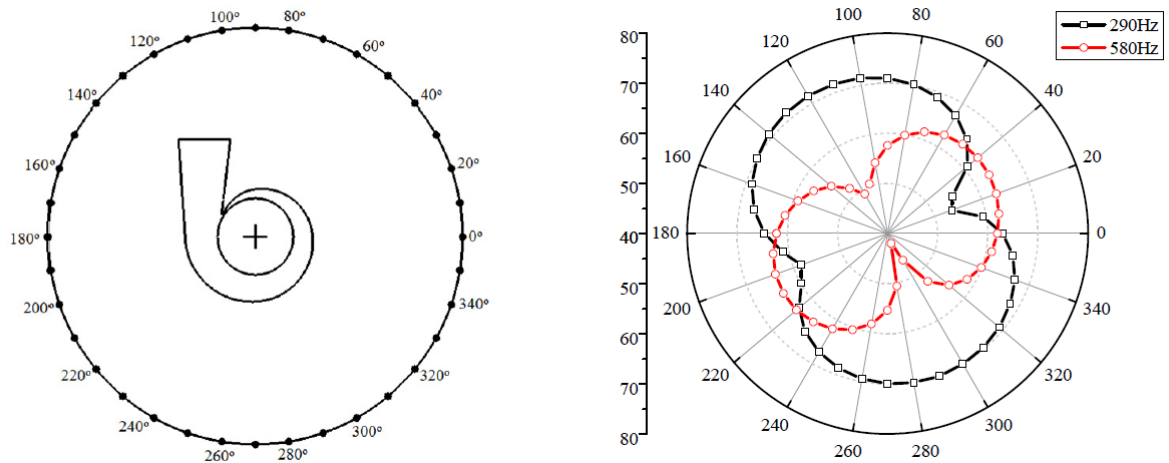


Figure 2.29 Sound Pressure Level distribution for the pump Chen et al.[49]

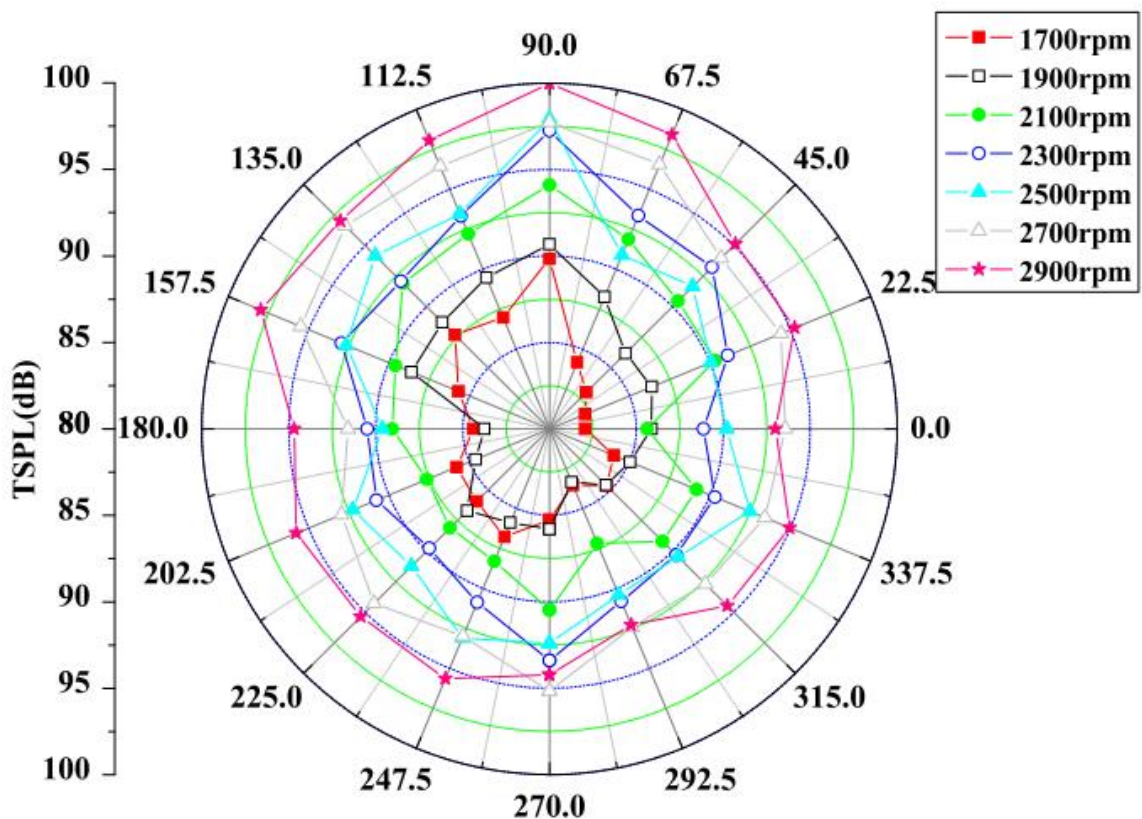


Figure 2.30 Sound Pressure Level variation from the pump for different rotational speed Guo et al.[53]

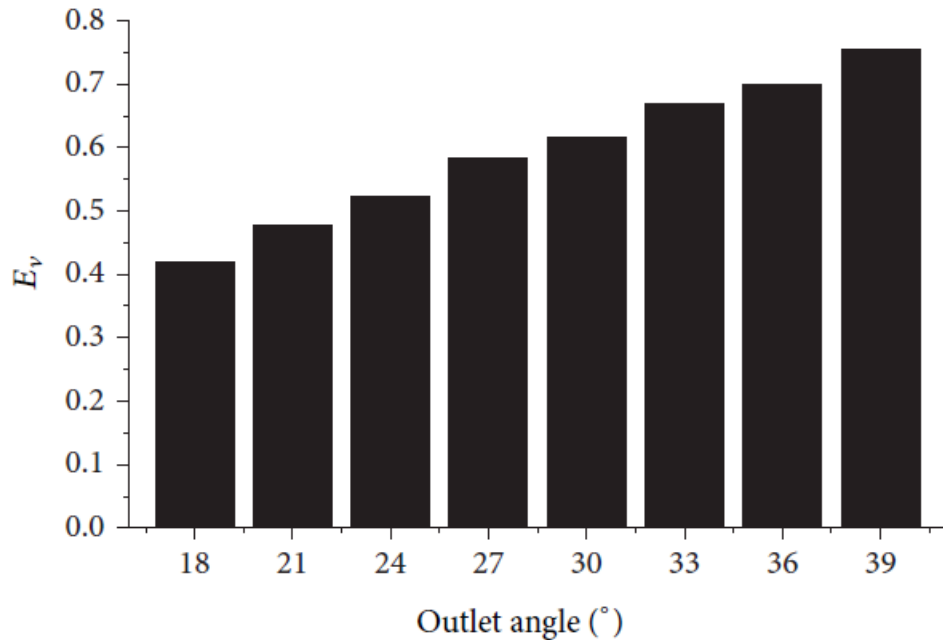


Figure 2.31 Sound fluctuation power variation with outlet blade angle A. Yang et al.[54]

A. Yang et al.[54] studied the effect of blade outlet angle on the noise generation form the pump. They reported an increase of 8.6 dB in sound pressure level when the outlet blade angle changes from 18° to 39° . Reduction in the pump efficiency with increase in outlet blade was observed. The variation of the sound fluctuation power E_v with outlet blade angle is given in Figure 2.31. The sound fluctuation power is defined by the ratio of fluctuating pressure amplitude to the square of the frequency. From Figure 2.31 it concluded that the pressure fluctuations increase with increase in outlet blade angle. Yu-qin and Ze-wen[55] studied the effect of blade number on pressure fluctuations. They found that for six number of blades, noise generation was minimum. The data from the study can be used for hydraulic optimization to get the low noise pump design.

2.9 Objective and Present work

A canned motor pump generates relatively lesser noise compared to conventional pump because of the exclusion of the mechanical couplings. From the literature survey, it can be concluded that the unsteady interactions of the flow with the casing also act as a source for the noise generation. If the flow behaviour is known it becomes helpful for the designer to make the changes in pump components. The dissertation is focussed on understanding and predicting the noise generation mechanism and unsteady interactions in different components of a canned motor pump. The various geometry parameters like rotor diameter, length, surface roughness and the flow parameters like Reynolds number, Taylor number were investigated to understand their impact on flow physics and the heat transfer characteristics in the rotor-stator gap. The unsteady behaviour of the flow in the volute casing and the impeller of the pump was studied through simulation.

A simplified model of the rotor-stator assembly is simulated in Ansys Fluent for comparing the reported Nusselt number and Taylor number values. The empirical design of the induction motor is discussed to get a rough estimate of the actual dimensions of the motor. The motor can be cooled by using the high temperature working fluid at the pump exit and routing it back into the motor casing. Alternately the cooling water is pumped by an by using a secondary impeller mounted on the same shaft as the rotor. The schematic diagram of the cooling arrangement with secondary impeller is shown in Figure 2.16. The choice of the cooling arrangement is dependent on the application, required flow rate, the temperature of the working fluid and the properties of the working fluid.

The present study focuses on the design of the secondary impeller for delivering the optimum flow rate for keeping the temperature of the windings within the permissible limit. The design and the experiment data for the secondary pump were not available. Thus a method for designing the centrifugal pump components was studied. Present work discusses the mean-line design of the impeller along with the study and comparison of characteristic curves for the designed pump with the real-world pump. Basic design approach of the volute casing was also provided so that both the impeller and the volute can be designed if the previous data is not known. Different flow and pressure head prediction algorithms for centrifugal pump are developed and discussed in detail.

Chapter 3

Design of Components of Canned Motor Pump

3.1 Design of basic dimensions of the impeller

3.1.1 Efficiencies

The desired flow rate, head, rotational speed, and the efficiency data are assumed to be given parameters without the existing pump data. Some co-relations provided by Gülich[5] are discussed.

3.1.1.1 Hydraulic efficiency

The empirical correlation given by Eq.3.1 is used for calculating η_h from specific speed and flow rate. The correlation is valid for the radial pumps with flow rate $Q \geq 0.005 m^3 / s$. Reference flow rate $Q_{ref} = 1 m^3 / s$ is used for determining the hydraulic efficiency and N_s is the specific speed.

$$\eta_h = 1 - 0.055 \left(\frac{Q_{ref}}{Q} \right)^m - 0.2 \left\{ 0.26 - \log \left(\frac{N_s}{25} \right) \right\}^2 \left(\frac{Q_{ref}}{Q} \right)^{0.05} \quad (3.1)$$

$$m = 0.08 \cdot a \cdot \left(\frac{Q_{ref}}{Q} \right)^{0.08} \left(\frac{45}{N_s} \right)^{0.06}$$

$$Q \leq 1 m^3/s; \quad a = 1$$

$$Q \geq 1 m^3/s; \quad a = 0.5$$

The efficiency equation suggested by Eq.3.1 is a fit obtained by using a large set of values of actual pumps. The deviation of magnitude $\Delta\eta = \pm 0.2 \cdot (1 - \eta_h)$ from mean data is expected if the correlation is used. The variation of the hydraulic efficiency with the specific speed at different flow rate is calculated from Eq.3.1 are plotted in Figure 3.1.

3.1.1.2 Overall efficiency

Overall efficiency η_o can be calculated from specific speed and flow rate with the empirical correlation given by Eq.3.2. The correlation is valid for the radial pumps with flow rate $Q \geq 0.005 m^3/s$. Reference flow rate $Q_{ref} = 1 m^3/s$ is used for determining the hydraulic efficiency. N_s is calculated in rotations per second in Eq.3.2. Overall efficiency is product of all the efficiencies. Thus power required for the pump can be calculated.

$$\eta_o = 1 - 0.095 \left(\frac{Q_{ref}}{Q} \right)^m - 0.3 \left\{ 0.35 - \log \left(\frac{N_s}{25} \right) \right\}^2 \left(\frac{Q_{ref}}{Q} \right)^{0.05} \quad (3.2)$$

$$m = 0.08 \cdot a \cdot \left(\frac{Q_{ref}}{Q} \right)^{0.08} \left(\frac{45}{N_s} \right)^{0.06}$$

$$Q \leq 1 m^3/s; \quad a = 1$$

$$Q \geq 1 m^3/s; \quad a = 0.5$$

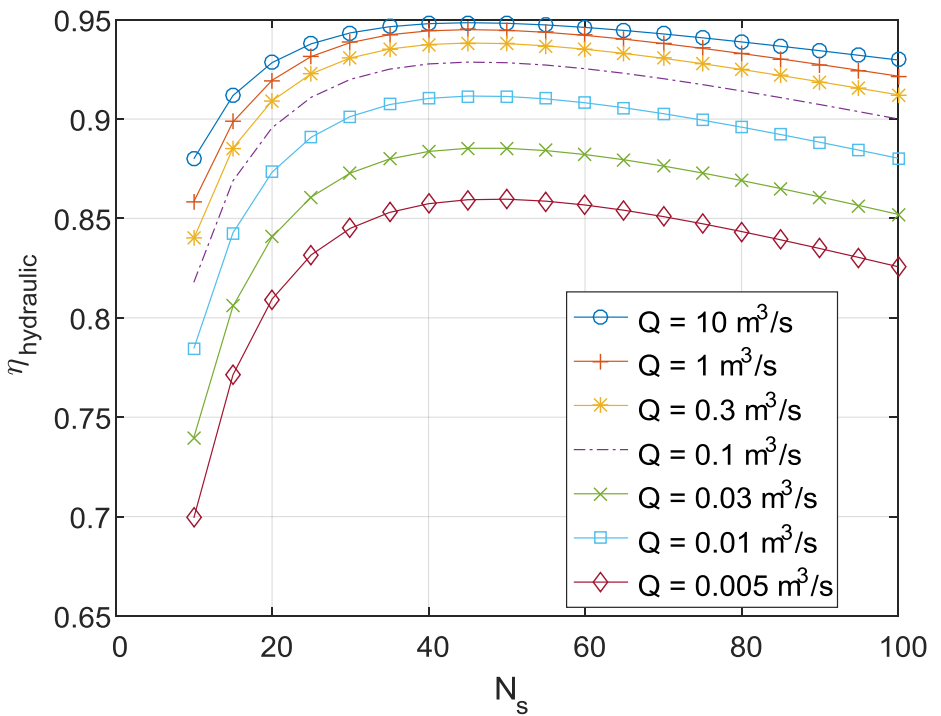


Figure 3.1 Hydraulic efficiency variation with specific speed for a single stage, single entry radial pump at different flow rates

3.1.1.3 Volumetric Efficiency

Gülich[5] proposed the empirical formula given by Eq.3.3 for calculation of the leakage through the annular seal. The approximation of the volumetric efficiency can be done by using Eq.3.3 and Eq.3.4 for the given pump.

$$\eta_v = \frac{1}{1 + \frac{Q_{seal}}{Q} + \frac{Q_{balance}}{Q} + \frac{Q_{bearing}}{Q}} \quad (3.3)$$

N_s	a	m	With balance Holes: $\Pi = 2$
< 27	4.1	1.6	
> 27	0.5	0.6	Else: $\Pi = 1$

3.1.2 Impeller suction diameter

Inlet diameter D_{le} (Ref. Figure 1.7) of the impeller is selected in such a way that the NPSH requirement is fulfilled. Gongwer[23] proposed a co-relation (Ref. Eq.3.5) giving the variation of NPSHr with the flow and tangent velocity at the inlet of the impeller. From the definition of the flow and tangential velocities, it can be said that NPSHr is dependent on the suction diameter (Ref. Eq.3.6). For optimum NPSHr, Eq.3.6 can be differentiated to get the optimum suction diameter for the impeller. The expression for the optimum suction diameter is given by Eq.3.8.

$$NPSHr = 1.8 \cdot \frac{C_{ml}^2}{2g} + 0.23 \cdot \frac{u_{1s}^2}{2g} \quad (3.5)$$

$$NPSHr = \frac{1.8}{2g} \cdot \left(\frac{4Q}{\pi D_{le}^2} \right)^2 + \frac{0.23}{2g} \left(\frac{\pi N D_{le}}{60} \right)^2 \quad (3.6)$$

$$\frac{d(NPSHr)}{d(D_{le})} = \left(\frac{1.8}{2g} \cdot \frac{16Q^2}{\pi^2} \right) \cdot \left(-\frac{4}{D_{le}^5} \right) + \left(\frac{0.23}{2g} \right) \cdot \left(\frac{\pi N}{60} \right)^2 \cdot (2D_{le}) = 0 \quad (3.7)$$

$$D_{le} = 5.14 \cdot \sqrt[3]{\frac{Q}{N}} \quad (3.8)$$

3.1.3 Shaft and hub diameter

The shaft is likely to fail when torsional stress exceeds a critical value. The shaft diameter is calculated from Eq.3.9 if the material of the shaft is known. The calculated dimension of the shaft is increased by some amount by considering fatigue and bending stress along with the bearing clearance. Hub diameter D_h (Ref. Figure 1.7) is obtained by multiplying shaft diameter with a multiplication factor in range of 1.1 to 1.5.

$$D_s = \sqrt[3]{\frac{16 \cdot Torque}{\pi \cdot Stress}} \quad (3.9)$$

3.1.4 Impeller inlet diameter

The inlet diameter of the blade D_1 at the outer streamline (Ref. Figure 1.6) is chosen based on cavitation characteristics at the inlet of the pump. Gülich[5] has given three cases which are used for estimating the inlet diameter. The design is an iterative process, and hence with an initial estimate, all the design quantities such as velocity, geometry parameters are calculated. In the present work, design for a selected suction specific speed N_{ss}^{**} , which is given by Eq.3.10 is studied. Suction speed defines the quality of suction impeller for the given NPSH at the best efficiency point. Suction speed is some function of the parameter K_h which is the ratio of the diameters of the hub and the impeller blade inlet. The value of K_h has to be guessed for the initial iteration. Suction specific speed is assumed from the recommended values of suction specific speed for different applications.

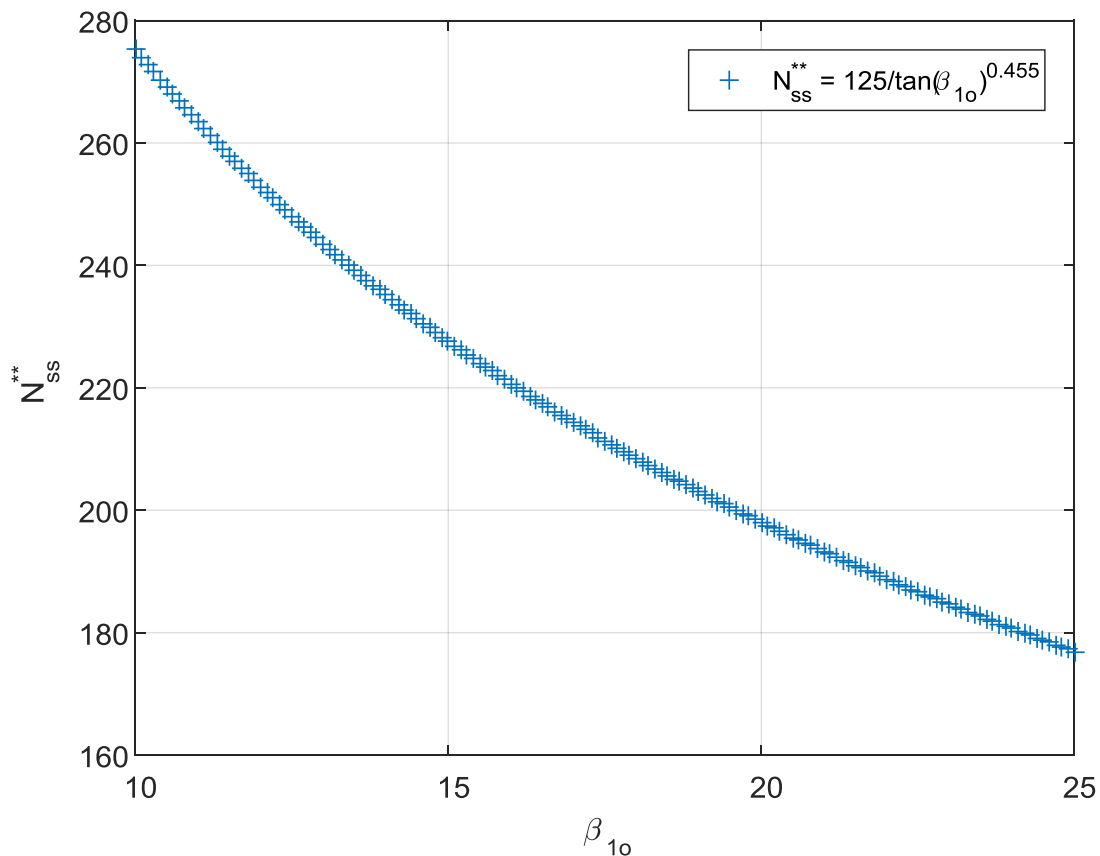


Figure 3.2 Normalized suction specific speed as a function of flow angle the outer streamline of the impeller reproduced from Gülich[5]

$$N_{ss} = \frac{N\sqrt{Q}}{(NPSH)^{3/4}} \quad (3.10)$$

$$N_{ss}^{**} = \frac{N_{ss}}{\sqrt{K_h}} \left(\frac{27}{N_s} \right)^{0.19} \quad (3.11)$$

Once the suction specific speed is known, a relation between normalized suction speed N_{ss}^{**} and the flow coefficient φ is used to get a rough estimate of the inlet blade angle. From Figure 3.2, the flow angle β_{lo} required to avoid cavitation at the inlet is determined. Once the flow angle is known, the initial guess for the inlet impeller diameter is made with an empirical relation of Eq.3.12.

$$D_1 = 2.9 \cdot \sqrt[3]{\frac{Q}{NK_h \tan(\beta_1)} \left(1 + \frac{\tan(\beta_1)}{\tan(\alpha_1)} \right)} \quad (3.12)$$

3.1.5 Inlet Velocity Triangle

If the volumetric efficiency η_v is known, the flow rate Q can be used to calculate the theoretical flow rate Q_{th} . Formulae used for calculation of the impeller inlet velocity triangle are listed in Table 5. Suction pipe diameter D_{le} is calculated from Eq.3.8 for the calculation of velocity C_0 at the eye of the impeller. With an assumption of no losses in the bend section from the eye to the inlet of the blade, the flow velocity C_{m0} is taken to be equal to C_0 . Once all the geometry parameters at the inlet are known, the velocity triangle can be generated from the formulae listed in Table 5.

3.1.5.1 Normal entry

The direction of the flow in the suction pipe before entering the impeller blade is normal to the cross-section of the pipe. The blade is designed in such a way that the flow remains normal to the blade inlet cross-section ($\alpha_1 = 90^\circ$)

3.1.5.2 Effect of blockage due to the finite blade thickness

At the inlet of the blade, due to finite vane thickness the area is blocked. The total length of the area blocked at the inlet is a function of a number of blades Z , blade thickness δ_1 and the blade angle β_1 . A simplified geometry triangle at the blade inlet is sketched in Figure 3.3. The total length blocked by the Z number of blades at the inlet is given by formula $Z \cdot S_1$.

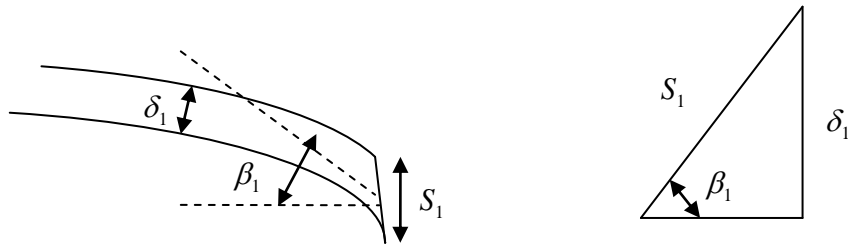


Figure 3.3 Simplified geometry triangle at the blade inlet

Due to the blockage, the flow velocity C_{m0} increases to C_{m1} and the inlet angle β_{10} changes to β_1 . The flow velocity can C_{m1} be calculated by multiplying blockage factor K_1 to the C_{m0} . Mathematical expression for K_1 is derived by using the continuity equation between point 0 and 1.

$$C_{m1} = \left(\frac{\pi D_1}{\pi D_1 - ZS_1} \right) \cdot C_{m0} = C_{m0} \cdot K_1 \quad (3.13)$$

$$K_1 = \left(\frac{\pi D_1}{\pi D_1 - ZS_1} \right) = \frac{1}{1 - \frac{ZS_1}{\pi D_1}} = \frac{1}{1 - \frac{Z\delta_1}{\pi D_1 \sin(\beta_1)}} \quad (3.14)$$

For initial calculation, the blockage factor is assumed to be an arbitrary number. The code is iterated to by changing β_1 get the converged value of the blockage factor. For the converged value of K_1 , the inlet blade angle β_1 is calculated. Inlet blade angle β_1 can also be calculated empirically from β_0 , which is blade angle when the blockage is not considered. For the calculation, the incidence angle I is be assumed between 3° to 10° for best performance in

cavitation and added to β_0 to get the inlet blade angle β_1 . Gülich[5] suggested angle exaggeration method given by Eq.3.15 to avoid assuming incidence angle ‘ I ’.

$$\begin{aligned}\beta_1 &= \tan^{-1}(k \cdot \beta_0) \\ k &\sim 1.1 - 1.4\end{aligned}\quad (3.15)$$

Table 5 Inlet Velocity Triangle calculations

Velocity Triangle at Impeller inlet	Equations
Theoretical discharge	$Q_{th} = \frac{Q}{\eta_v}$
Axial velocity at the impeller eye	$C_0 = \frac{4Q_{th}}{\pi D_{le}^2}$
Blade speed	$u_1 = \frac{\pi \cdot D_1 \cdot N}{60}$
Circumferential component of absolute velocity	$C_{u1} = \frac{C_{m1}}{\tan(\alpha_1)}$
Relative velocity	$W_1 = \sqrt{C_{m1}^2 + (u_1 - C_{u1})^2}$
Inlet breadth	$B_1 = \frac{Q_{th}}{\pi D_1 C_{m0}}$
Flow angle without considering the blockage	$\beta_{10} = \arctan\left(\frac{C_{m1}}{u_1 - C_{u1}}\right)$
Total length blocked by blade at the inlet	$S_1 = \frac{Z\delta_1}{\sin(\beta_1)}$
Inlet blockage multiplication factor	$K_1 = \left\{1 - \frac{z\delta_1}{\pi D_1 \sin(\beta_1)}\right\}^{-1}$
Incidence angle	I
Blade angle with incidence	$\beta_1 = \beta_0 + I$

3.1.6 Impeller outlet dimensions

The manometric head H_m is calculated from the known value of hydraulic efficiency η_h and the static head H . Formulae used for calculation of the impeller outlet velocity triangle are listed in Table 6.

3.1.6.1 Outlet diameter

The outlet diameter D_2 is selected based on the pressure coefficient ψ given by Eq.3.16 given below. The pressure coefficient can be selected by empirical relation given by Eq.3.17. (Ref. Gülich[5]). From Eq.3.16,3.17 and Table 6 the outlet diameter can be calculated.

$$\psi = \frac{2gH}{u_2^2} \quad (3.16)$$

$$\psi = 1.25 \cdot \exp(-0.3 \cdot N_s / 100) \quad (3.17)$$

3.1.6.2 Outlet blade angle selection

The manometric head H_m generated by the pump for the axial entry is given by the Eq.3.19. A dimensionless parameter \bar{C}_{u2} which is defined in Table 6 is used for estimation of the outlet blade diameter. It can be seen from Figure 3.4 that the manometric head H_m changes with \bar{C}_{u2} . From Eq.3.20 it can be said that \bar{C}_{u2} is a function of the outlet blade angle β_2 . The change in blade angle β_2 thus affects the manometric head developed by the pump. The manometric head is comprised of the dynamic head H_{dy} and pressure head H_p which are given by Eq.3.21 and Eq.3.22 respectively. For simplicity, all the head values are converted into dimensionless quantities represented by Eq.3.23 -3.25. The variation of dimensionless head coefficients with \bar{C}_{u2} is shown in Figure 3.4. For radial blades $\beta_2 = 90^\circ$ and $\bar{C}_{u2} = 1$

Based on the choice of the blade, which can be backward, radial or forward, \bar{C}_{u2} is taken from Figure 3.4 for the initial calculations of the outlet blade angle. Another way of obtaining outlet blade angle is by assuming stability factor defined by Eq.3.18. By assuming the stability

factor greater than or equal to one (Ref. Gülich[5]), outlet tangential velocity C_{u2} and velocity triangle can be estimated. Stability factor ensures that the pump has stable head – flow characteristics.

$$K_{stab} = \frac{u_2 - u_1}{C_{u2}} \quad (3.18)$$

$$H_m = \frac{C_{u2} \cdot u_2}{g} = \frac{\bar{C}_{u2} \cdot u_2^2}{g} \quad (3.19)$$

$$\bar{C}_{u2} = \frac{1}{u_2} \cdot \left(u_2 - \frac{C_{m2}}{\tan(\beta_2)} \right) \quad (3.20)$$

$$H_{dy} = \frac{C_{u2}^2}{2g} \quad (3.21)$$

$$H_p = H_m - H_{dy} \quad (3.22)$$

$$\bar{H}_m = \frac{H_m}{\left(\frac{u_2^2}{2g} \right)} = \frac{C_{u2} \cdot u_2}{\left(\frac{u_2^2}{2} \right)} = \frac{\bar{C}_{u2} \cdot u_2^2}{\left(\frac{u_2^2}{2} \right)} = 2 \cdot \bar{C}_{u2} \quad (3.23)$$

$$\bar{H}_{dy} = \frac{H_{dy}}{\left(\frac{u_2^2}{2g} \right)} = \frac{C_{u2}^2}{u_2^2} = \bar{C}_{u2}^2 \quad (3.24)$$

$$\bar{H}_p = \bar{H}_m - \bar{H}_{dy} = \bar{C}_{u2} \cdot (2 - \bar{C}_{u2}) \quad (3.25)$$

3.1.6.3 Blade outlet width

Blade outlet width and the outlet angle should be selected such that the stable H-Q characteristics are obtained. They cannot be selected independently, and thus the empirical

relation is proposed by Gülich[5]. The relative outlet width B_2^* proposed by Gülich[5] is the ratio of the outlet width to the outlet diameter. It is given by the Eq.3.26.

$$B_2^* = 0.017 + 0.262 \cdot \left(\frac{N_s}{100} \right) - 0.08 \cdot \left(\frac{N_s}{100} \right)^2 + 0.0093 \cdot \left(\frac{N_s}{100} \right)^3 \quad (3.26)$$

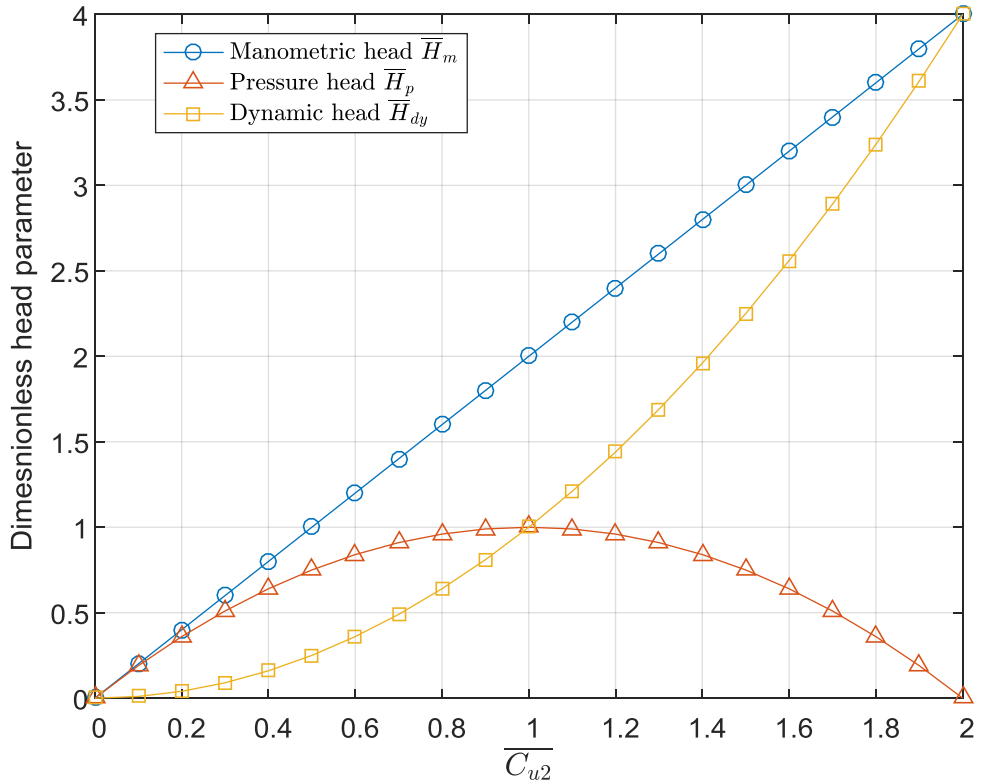


Figure 3.4 Variation of dimensionless head developed by the pump with dimensionless velocity parameter

3.1.7 Slip factor

There are various models given in Srinivasan[24] and Gülich[5] which are used to predict the value of the slip factor ‘p’. The head developed by the pump H_m is multiplied by the slip factor to get the total head H_∞ . Since the slip factor ‘p’ is dependent on the outlet blade angle β_2 , an iterative procedure has to be followed till the total head H_∞ matches with the design head. (Ref. A.5)

3.1.8 Outlet Velocity Triangle

3.1.8.1 Relative velocity ratio

In an ideal case, the fluid glides over the blade without any friction. For simplicity it can be assumed that the relative velocity W is constant over the blade profile. For initial calculation, the relative velocity ratio W_1/W_2 is assumed to be between 1-1.15.

Table 6 Outlet Velocity Triangle calculation

Velocity Triangle at Impeller outlet	Equations
Manometric head	$H_m = \frac{H}{\eta_h}$
Non-dimension parameter	$\bar{C}_{u2} = \frac{C_{u2}}{u_2}$
Blade speed	$u_2 = \frac{\pi \cdot D_2 \cdot N}{60}$
Circumferential component of absolute velocity	$C_{u2} = \bar{C}_{u2} \cdot u_2$
Relative velocity ratio	$\frac{W_1}{W_2}$
Flow velocity at trailing edge	$C_{m2} = W_2 \cdot \sin(\beta_2)$
Outlet breadth	$B_2 = \frac{Q_{th}}{\pi D_2 C_{m2}}$
Outlet blockage multiplication factor	$K_2 = \left\{ 1 - \frac{z\delta_2}{\pi D_2 \sin(\beta_2)} \right\}^{-1}$
Head with slip	$H_\infty = (1 + p) \cdot H_m$
Outlet blade velocity with slip effect	$u_2 = \frac{C_{m2}}{2 \tan(\beta_2)} + \sqrt{\left(\frac{C_{m2}}{2 \tan(\beta_2)} \right)^2 + g H_\infty}$

3.1.9 Commercial software

Ansys has a module named Vista CPD which gives meanline design for the pump if the design inputs like head, discharge and rotational speed are known. The Vista CPD values and the values generated by our MATLAB code (Ref. Chapter 5) are compared and very less deviation is found for all the cases tested on both the codes.

3.2 Shaping of the blades

3.2.1 Meridional section basic dimensions

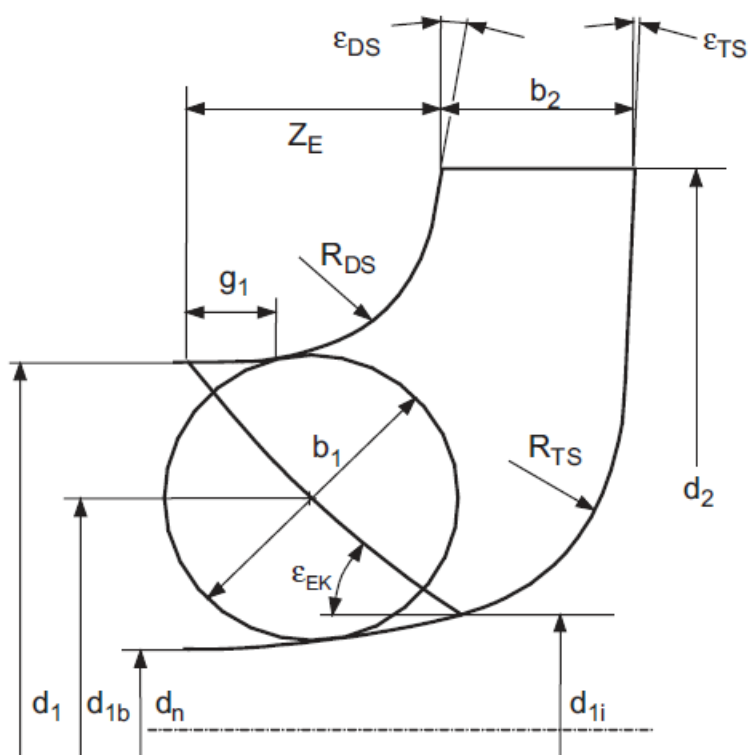


Figure 3.5 Design parameters for Meridional section taken from Gülich[5]

The meanline design gives the basic dimensions at the inlet and the outlet along with the velocity triangle. The axial distance for forming the Meridional passage is still unknown. For this purpose, either scaling with known impeller or empirical relations can be used. Gülich[5]

has given empirical relations which help in forming the Meridional section. The design parameters can be referred from Figure 3.5. Some of the parameters given in Eq.3.27 are used for tracing the outer streamline of the Meridional section.

$$Z_E = a \cdot \frac{d_1 - d_n}{2} \cdot (N_s)^x$$

$$a = 0.75$$

$$x = -0.05$$

$$R_{Ds} = (0.6 \sim 0.8)b_1$$
(3.27)

A small gap $g_1 = (0.2 \sim 0.3)b_1$ is provided for smooth transition of the flow from axial to radial direction. Angles ε_{DS} and ε_{TS} at the outer diameter of the impeller are chosen if outlet triangle needs some manipulation to avoid flow separation. The recommended value for high specific speed impeller is $15 - 20^\circ$. The inlet blade draft angle ε_{EK} is taken to be $30 - 40^\circ$ for optimum performances as per Gülich[5].

3.2.2 Meridional section shaping

3.2.2.1 Kaplan method of error triangles

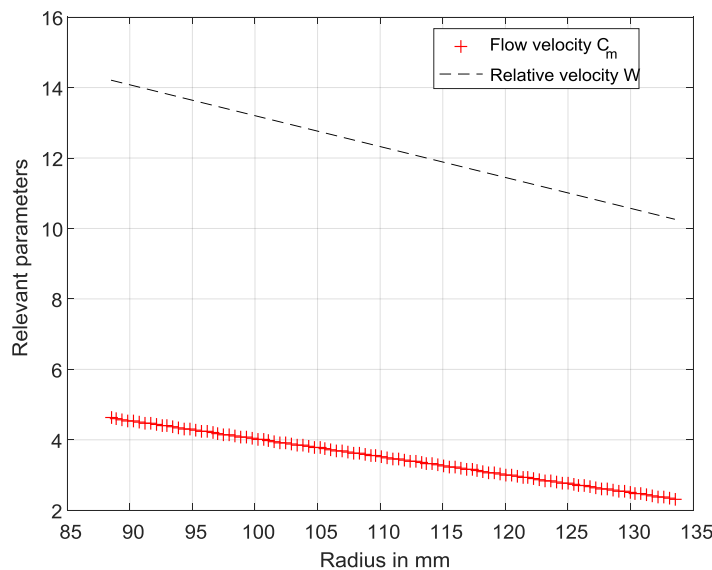


Figure 3.6 Flow velocity and relative velocity variation from inlet to outlet of the impeller blade

Once the geometry and flow profiles are fixed, the profile of the blade in the Meridional section can be generated. The velocity triangle values and the blade width change from inlet to outlet. For estimating the change in geometry from inlet to outlet, the change of flow velocity and relative velocity from inlet to outlet can be chosen from a random function varying from inlet to outlet. The variation of the function can be linear, parabolic or can be of any order. Figure 3.6 gives a variation C_m and W with a radius for linear profile assumption. For a simple linear profile assumption, C_m and W at all the locations on Meridional plane can be calculated by Eq.3.28 and 3.29.

$$C_m^{i+1} = C_m^i + \frac{dC_m}{dR} \cdot (R^{i+1} - R^i) = C_m^i + \frac{C_{m2} - C_{m1}}{R_2 - R_1} \cdot (R^{i+1} - R^i) \quad (3.28)$$

$$W^{i+1} = W^i + \frac{dW}{dR} \cdot (R^{i+1} - R^i) = W^i + \frac{W_2 - W_1}{R_2 - R_1} \cdot (R^{i+1} - R^i) \quad (3.29)$$

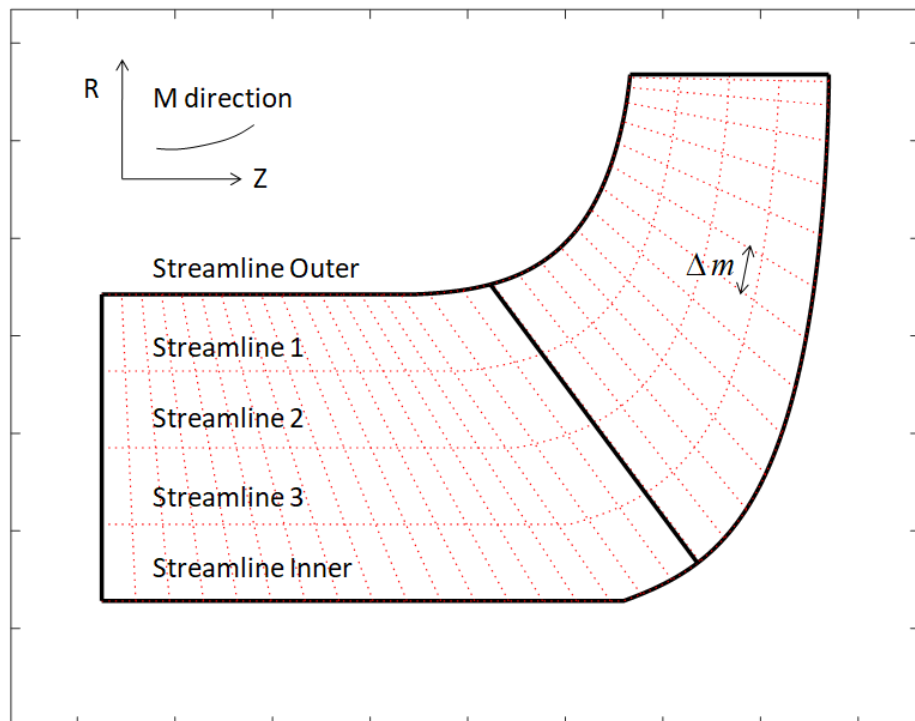


Figure 3.7 Basic definition for Kaplan error triangle in Meridional section

Once the value of flow velocity at each section is known, the width of the blade at different radii can be calculated from the continuity equation. The thickness of the blade for the initial

calculation is assumed to be constant. The radii are chosen in such a way that the Meridional section is divided in small distances of the length Δm as shown in Figure 3.7. The choice of Δm is random.

3.2.2.2 Bezier curve method

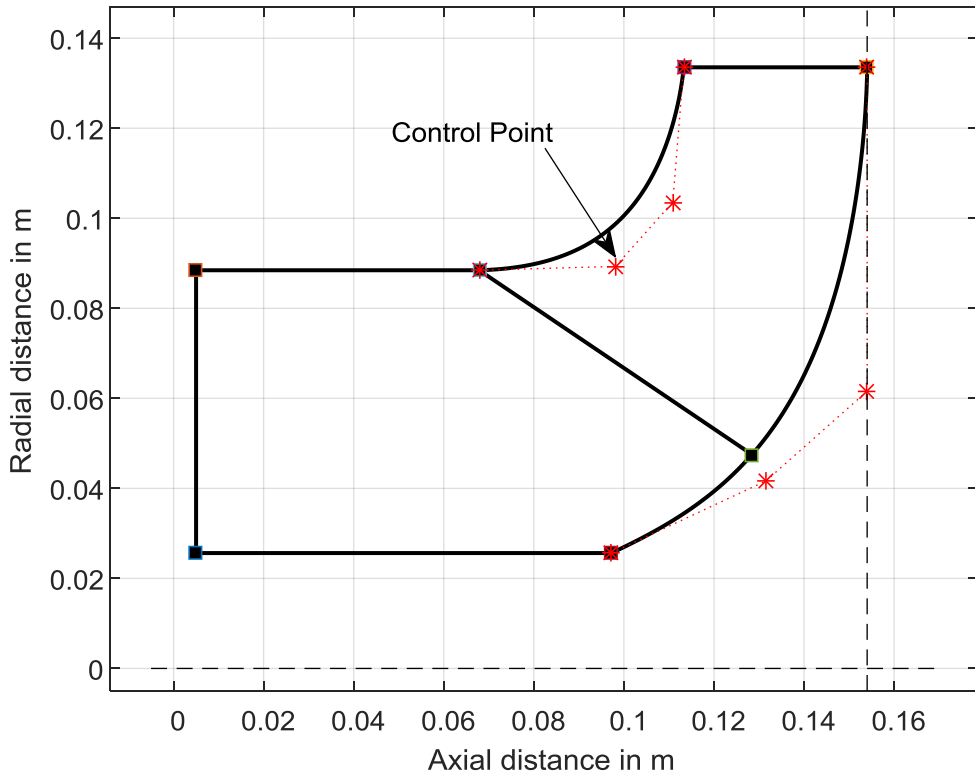


Figure 3.8 Meridional section generated by Bezier curve

In the Bezier curve (Ref. Appendix C) method, control points are decided by the designer for smooth generation of the blade profile. This method is easier compared to that of Kaplan triangle because it is easy to manipulate the shape of the curve just by changing the control points of Figure 3.8. A graphic user interface (GUI) is required for changing the control points. We have written a MATLAB code (Ref.H.2) which takes input of control points from the user to generate the Meridional section. The third order Bezier curve is generated by using the methodology suggested in Casey[27].

3.2.3 Blade shape in front view

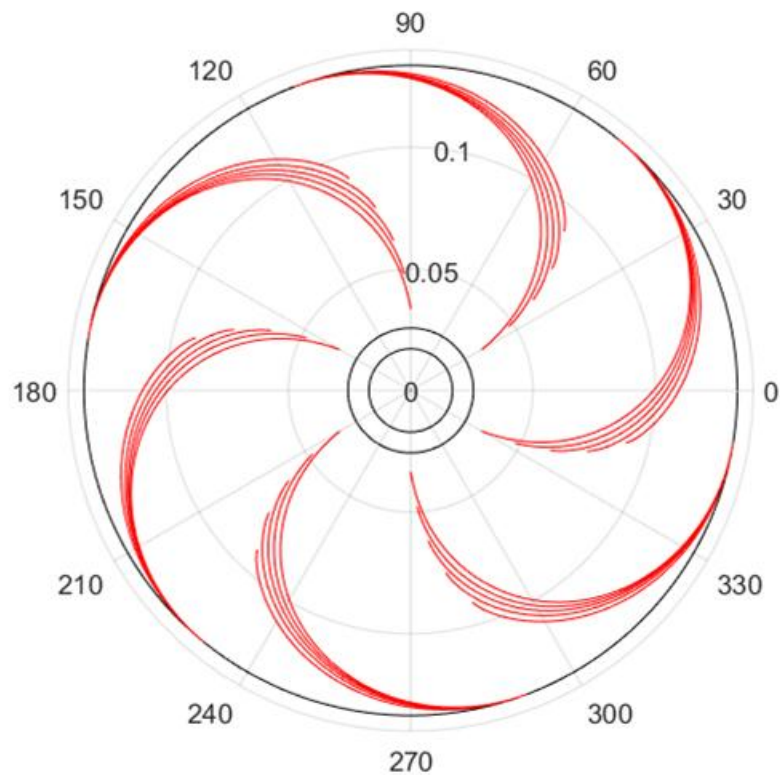


Figure 3.9 Six blade impeller viewed in Front view

3.2.3.1 Kaplan method of error triangle

Once the Meridional section is designed, the front view of the blade can be traced using the meanline distance and the blade angle variation. The distance Δu along the circumferential direction is given by Eq.3.30. The variation for the blade angle at every grid point has to be assumed. For this purpose variation of β similar to Figure 3.6 has to be assumed. Once the circumferential distance is evaluated, the grid points are plotted to get the complete blade profile in the front view. This method is very approximate and depends on the number of grid points. The effect of the blade thickness is not considered while generating the curve.

$$\Delta u_j = \frac{\Delta m_j}{\tan \beta_j} \quad (3.30)$$

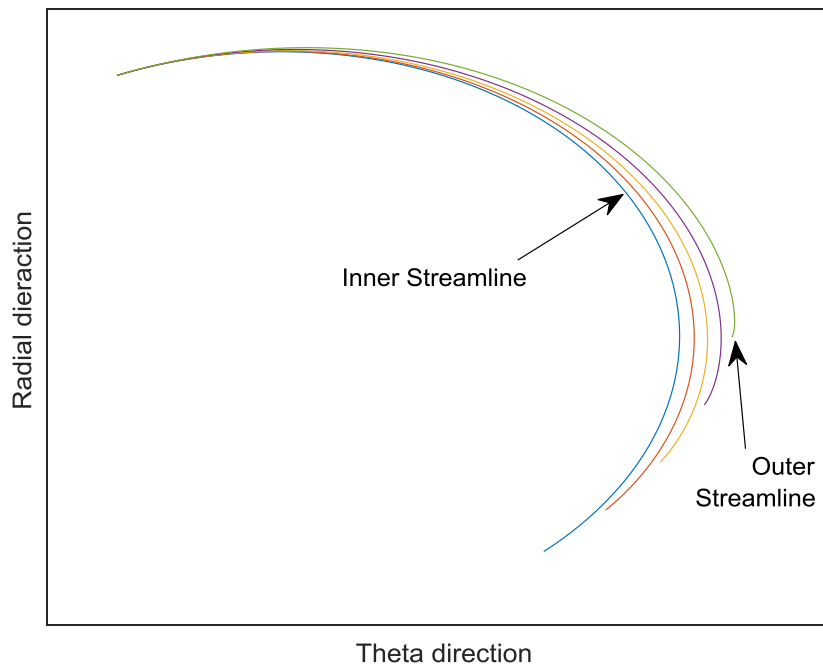


Figure 3.10 Blade profile generated by Kaplan error triangle method with 5 streamlines and 201 points viewed in front view

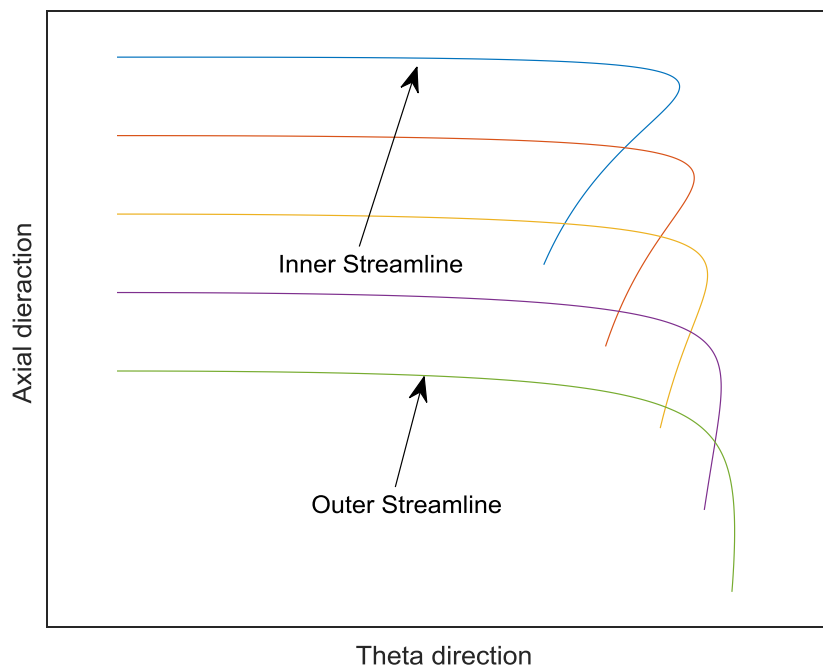


Figure 3.11 Blade profile generated by Kaplan error triangle method with 5 streamlines and 201 points viewed in top view

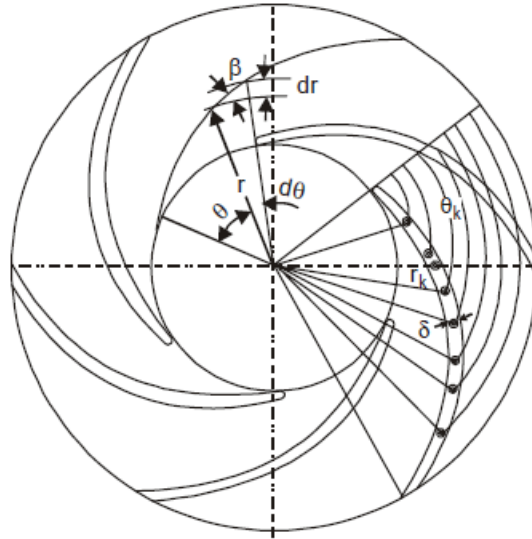


Figure 3.12 Vane development by point by point method Srinivasan[24]

3.2.3.2 Single curvature blade development by point by point method considering blade thickness effect

Point by point method specified by Srinivasan[24] is used for generating the airfoil when blade thickness variation is to be included in the design. The radius r and the angular position θ from a fixed reference axis are specified to get the profile of the airfoil. From Figure 3.12, a differential equation Eq.3.31 which relates angular position θ , radial location r and the blade angle β can be written which can be integrated from inlet to outlet radius for generating smooth airfoil.

$$d\theta = \frac{dr}{r \cdot \tan(\beta)} \quad (3.31)$$

Eq. 3.31 is converted into numerical integration by using the conversions of Eq.3.32 and Eq.3.33. The blade thickness is added to streamline to get the complete profile of the blade. Thus the mathematical formulation for the blade angle β is altered to Eq.3.35. The value of step size dr is chosen arbitrarily. Figure 3.13 is the streamline of the airfoil obtained from the code. The thickness is assumed to be varying as 5 mm for first 30%, 10 mm in the middle, and 5 mm in the end portion of the blade. Code is written in MATLAB to get the one dimensional design and the vane development curve. The code is given in H.4.

$$G(r) = \frac{1}{r \cdot \tan(\beta)} \quad (3.32)$$

$$\theta^{i+1} = \theta^i + \left(\frac{G^{i+1} - G^i}{2} \right) \cdot (R^{i+1} - R^i) \quad (3.33)$$

$$t = \frac{\pi D}{z} \quad (3.34)$$

$$\sin(\beta) = \left(\frac{C_m}{W} + \frac{\delta}{t} \right) \quad (3.35)$$

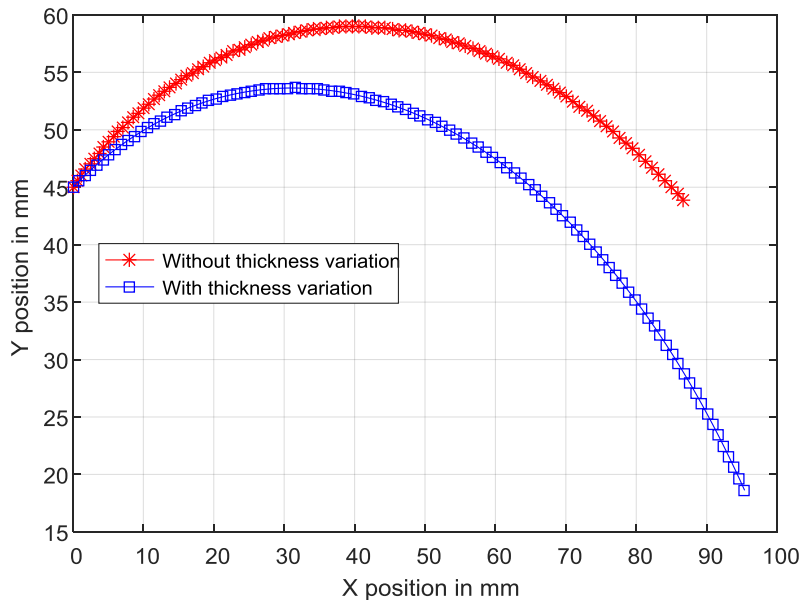


Figure 3.13 Airfoil generated by point by point method for static head $H = 13.8$ m and discharge $Q = 16$ lps with 101 points used for numerical integration.

3.2.4 Commercial software

Ansys has a module named BladeGen which takes the input from Vista CPD or the user input, to generate the Meridional passages. The software is user friendly. MATLAB code (H.2, H.3, and H.4) is written to understand how the software works so that it would not be used as a

black box. BladeGen also gives final view of the 3D CAD model shown in Figure 3.14 for better visualization.



Figure 3.14 3D CAD profile of Impeller generated by Ansys BladeGen

3.3 Design of basic dimensions of the volute

3.3.1 Throat diameter

The clearance between the impeller outer diameter and the volute throat affects the pressure pulsations at the throat. Gülich[5] has given an empirical relation given by Eq.3.36 for calculating the minimum cutwater diameter D_3 so that the pressure pulsations can be reduced. If specific speed N_s in RPM, head H and density ρ is known, the minimum throat diameter can be calculated. Water is used as reference fluid for ρ_{ref} calculation.

$$\frac{D_3}{D_2} \geq 1.03 + 0.1 \cdot \frac{N_s}{40} + 0.07 \cdot \frac{\rho}{\rho_{ref}} \cdot \frac{H}{1000} \quad (3.36)$$

3.3.2 Volute inlet width

Volute inlet thickness b_3 affects the secondary flow in the volute. Wider volute can have flow circulation at the extreme ends. Thus the ratio b_3 / b_2 (Width of volute inlet to impeller outlet) is chosen to be 1.05 to 1.25 (Ref. Gülich[5]).

3.3.3 Volute wall thickness

Volute wall is chosen by suction pipe diameter table given by Cho et al.[31]. The method is empirical and structural analysis should be carried out before finalizing the dimensions.

Table 7 Suction pipe diameter versus volute wall thickness

Suction pipe diameter (mm)	40~50	100~250	300	400	500
Minimum thickness (mm)	5	6	8	10	12

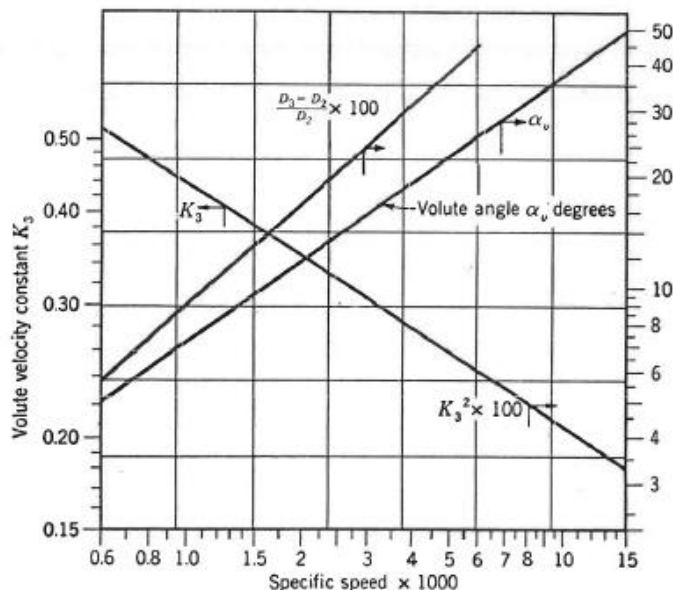


Figure 3.15 Volute constant data taken from Stepanoff[25]

3.3.4 Volute throat angle

Volute throat angle is chosen in such a way that the impeller outlet velocity angle α_2 and the cutwater angle α_v match with each other. Stepanoff[25] has given the variation of the volute constants with specific speed. The Figure 3.15 can be used for calculating volute throat angle. Sample calculations can be referred from Appendix B.

3.4 Shaping of the volute

3.4.1 Volute cross section shaping

Volute can be designed by assuming constant angular momentum or constant velocity in the volute section. Generalized method cannot be designed for a constant angular momentum approach and cross-section is designed in iterative process. Constant velocity method is relatively simpler approach and area cross-sections (Ref. Figure 3.16) can be generated easily with some empirical formulae.

3.4.2 Average flow velocity in casing

Average flow velocity is calculated by Eq.3.37. The multiplication factor K_3 is calculated from the Figure 3.15 from Stepanoff[25] data.

$$C_{av} = K_3 \sqrt{2gH} \quad (3.37)$$

3.4.3 Area variation at different cross sections

Volute is generally divided into finite number of sections with increasing area from the throat to the diffuser. The area of the last section is calculated from the Eq.3.38. Once A_v is calculated area at any cross-section ‘ i ’ out of ‘ N ’ sections can be calculated by Eq.3.39.

$$A_v = \frac{Q}{C_{av}} \quad (3.38)$$

$$A_{vi} = A_v \cdot \frac{i}{N} \quad (3.39)$$

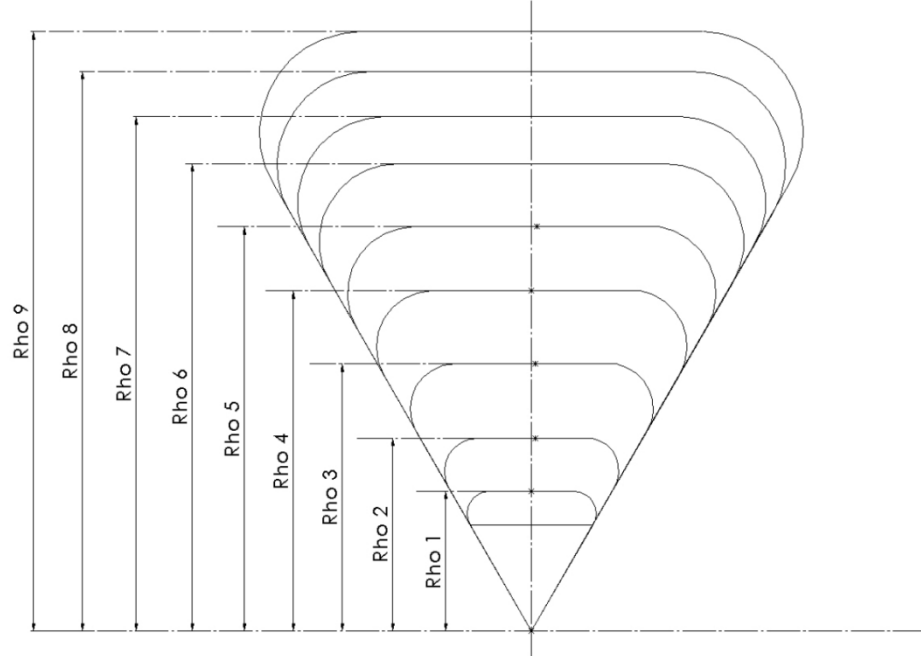


Figure 3.16 Relative distance from volute throat (Figure not to scale)

3.4.4 Relative distance from cutwater

The relative distance ρ_v (Ref. Figure 3.16) from the volute throat can be predicted using empirical formula of Eq.3.40 provided by Cho et al.[31]. The distance can be used for generating the elliptical, rectangular or trapezoidal cross-sections of the volute. MATLAB code (Ref.B.2) is written for the calculations.

$$\rho_{vi} = \sqrt{\frac{A_{vi} + 0.604 \cdot b_3^2}{0.367}} \quad (3.40)$$

3.5 Empirical design of an Induction motor

3.5.1 Introduction

The purpose of studying the design of the induction motor is to get a rough estimate of the dimensions of the stator and rotor. For calculating the dimensions of the stator, various parameters like specific magnetic loading B_{av} , specific electric loading q , full load efficiency η , full load power factor $\cos(\varphi)$ and winding factor K_w are needed. Since designing the induction motor is not in the scope of the current study, empirical data is referred from electric machine design handbook Boldea and Nasar[56]. Only the definition of relevant parameters required for designing is given.

3.5.2 Dimensions of the Stator

The desired output Q in Watt for the motor is calculated by the empirical formula given by Eq.3.41 and 3.42. The term n_s in Eq.3.41 is synchronous speed calculated from specific speed in the units as a number of rotations per second. The output equation gives the relation between $D_2^2 L$ and the output of the machine. D_2 is the inner diameter of the stator and L is the length of the stator. To get the value of D_2 and L , a relation has to be assumed. If the number of poles P is known, the diameter and length relation can be calculated from Eq.3.43.

$$Q = C_O n_s D_2^2 L \quad (3.41)$$

$$C_O = 11 \cdot B_{av} q K_w \eta \cos(\varphi) \quad (3.42)$$

$$D_2 = 0.135 P \sqrt{L} \quad (3.43)$$

3.5.3 Dimensions of the rotor

Magnetizing current and power factor are important parameters in deciding the performance of the induction motor. Considering these parameters, the air gap is chosen, and the value is

kept as minimum as possible. The empirical relation for calculating air gap l_g in mm is given by Eq.3.44. The diameter D_1 of the rotor is then calculated by the Eq.3.45.

$$l_g = 0.2 + 2\sqrt{D_2}L \quad (3.44)$$

$$D_1 = D_2 - 2 \cdot l_g \quad (3.45)$$

Table 8 Design dimensions for 30kW ac induction motor from the empirical relations

Input Parameters		Output Parameters	
Parameter	Value	Parameter	Value
Power Q in W	30000	Co	99218.3
Frequency F in Hz	50	Synchronous speed Ns in rps	50
Number of Poles P	4	$D_2^2 \cdot L$	0.1449
Specific Magnetic Loading B_{av} in Tesla	0.48	D_2 / \sqrt{L}	0.27
Specific Electric Loading q in A/m^2	26000	Stator diameter D_2 in m	0.144062581
Full load efficiency	0.88	Length of stator L in m	0.288
Full load power factor $\cos(\phi)$	0.86	Air gap length l_g in mm	0.55
Winding Factor K_w	0.955	Rotor diameter D_1 in m	0.144901124

The calculations for 30kW ac induction motor are given in Table 8 for reference. The calculation is done to get the idea of typical dimensions of rotor and stator used in an induction motor. The air gap separation is an essential parameter in deciding the overall efficiency of the motor. Higher air gap results in reduced efficiency and increased losses (Ref. Sawhney[3]).

Chapter 4

Numerical Simulation

4.1 Flow structure in Stator-Rotor gap

4.1.1 Turbulent Couette flow

Finite volume method is used for solving the turbulent plane Couette flow problem. Water is used as a working fluid. The simulation was carried out for the geometry defined in Table 9. The comparison between the numerical and analytic solution is shown in Figure 4.1. All the models give qualitative agreement with DNS with maximum 25% difference in the predicted value. The $\kappa - \omega - SST$ model is used for TCPF gap due to relatively less error.

Table 9 Simulated domain from Bech et al.[7]

Height of channel	20 mm
Length of channel	360 mm
Reynolds number	1260
Upper plate velocity	0.253 mm/s

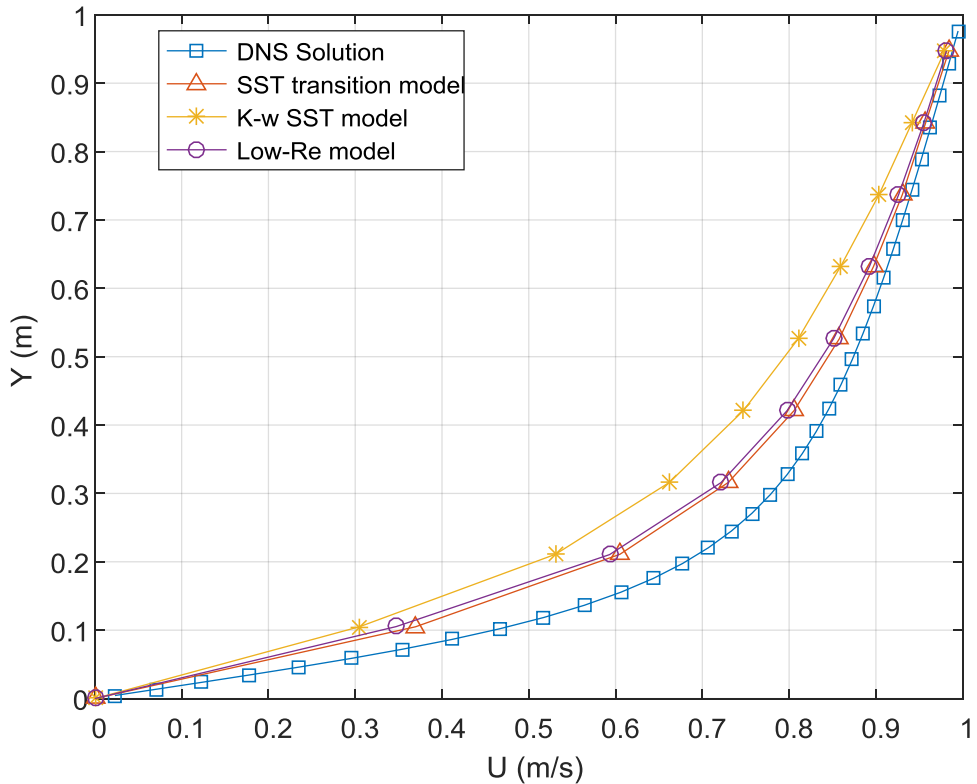


Figure 4.1 Comparison of DNS model of Bech et al.[7]and Numerical simulation models for turbulent flow.

4.1.1.1 Grid independence study

The grid independence study was done for the mesh sizes given in Table 10. The solution is independent above the 21000 elements. The results are plotted in Figure 4.2.

Table 10 Grid details for Turbulent Couette flow

Type of grid	Number of divisions along the length	Number of divisions along the gap
Finest	720	100
Fine	420	50
Coarse	360	20

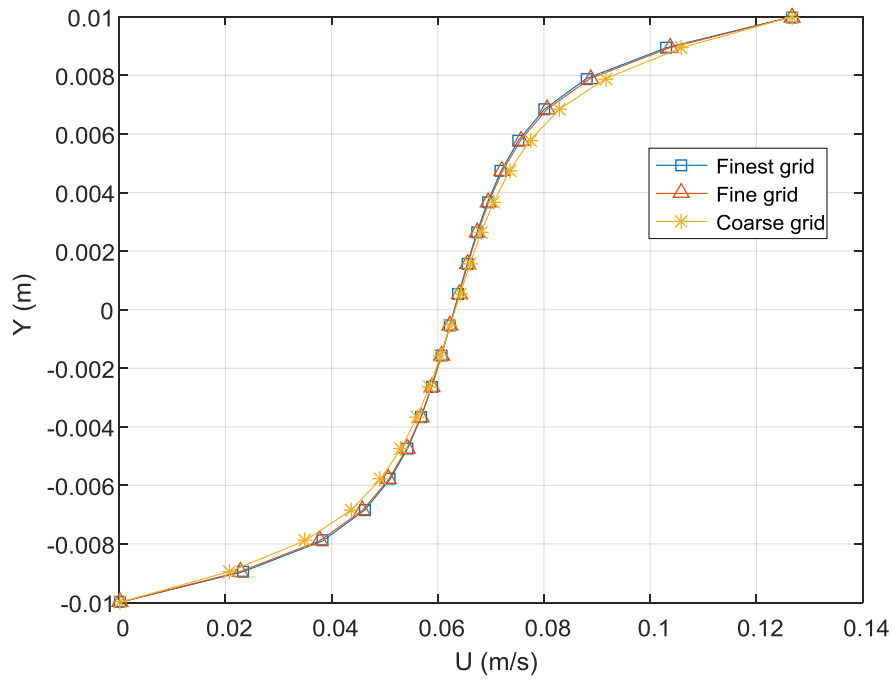


Figure 4.2 Grid independence study for the turbulent flow through parallel plates for Bech et al.[7] geometry

4.1.2 Taylor-Couette flow

The simulation was carried out for co-axial cylinders to get the toroidal flow structure described in the literature. The simulation is carried out for the geometry and flow parameters given in Table 11 for visualization of flow pattern. Comparison of velocity contours for Taylor number below and above the critical Taylor number is given Figure 4.3 B and C.

Table 11 Numerical simulation for Taylor-Couette flow

Geometry Details		Relevant Parameters	
R1	0.5 m	Fluid	Water
R2	1 m	Density	998.2
L	4 m	Cp	4182
Mesh Details		K	0.6
Edge	Number of divisions	μ	0.001003
Circumference	40	ν	1.00481×10^{-6}
Cylinder Gap	25	Ta	500
Length	100	ω	8.987×10^{-5}

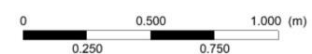
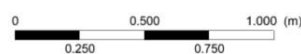
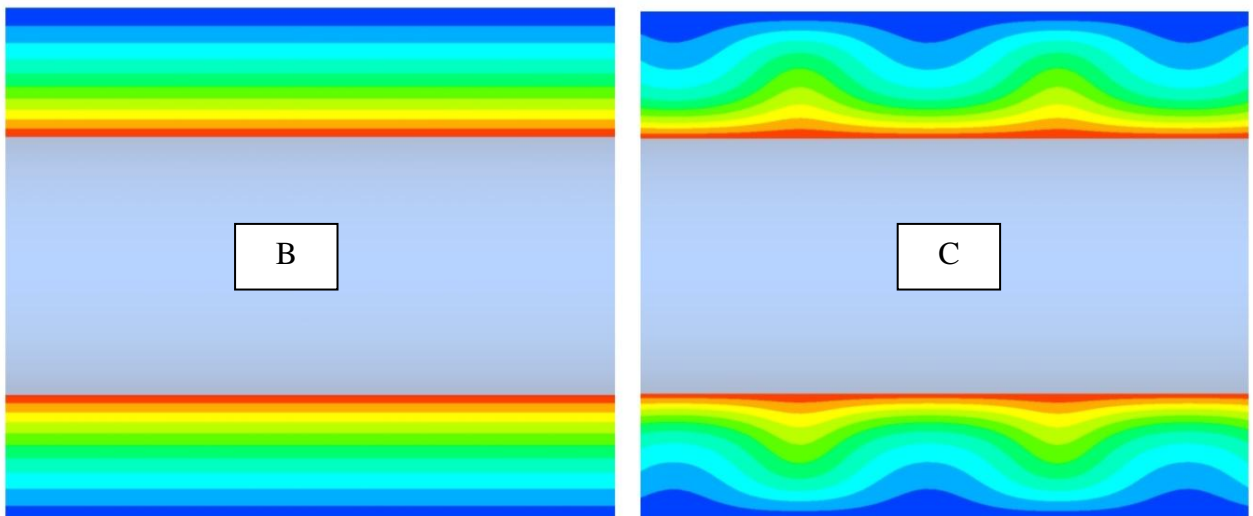
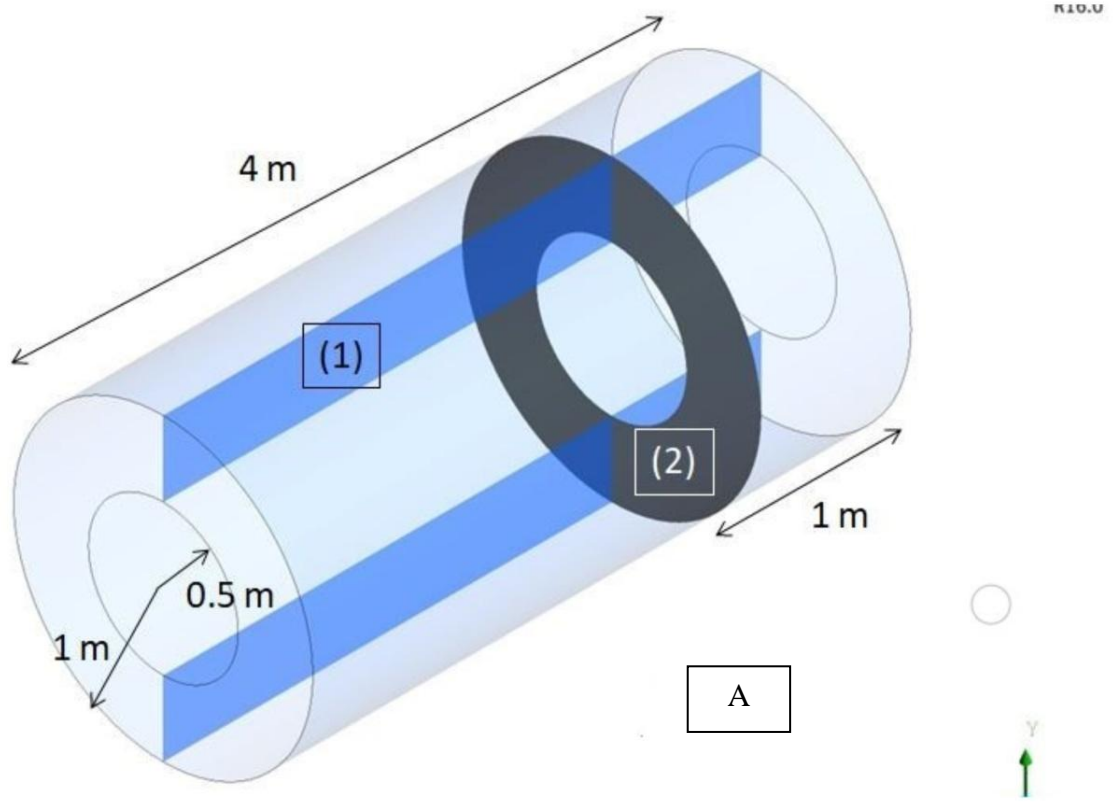


Figure 4.3 Numerical simulation results A) Geometry details B) Velocity contours for $T_a = 500$ C) Velocity contours for $T_a = 5000$.

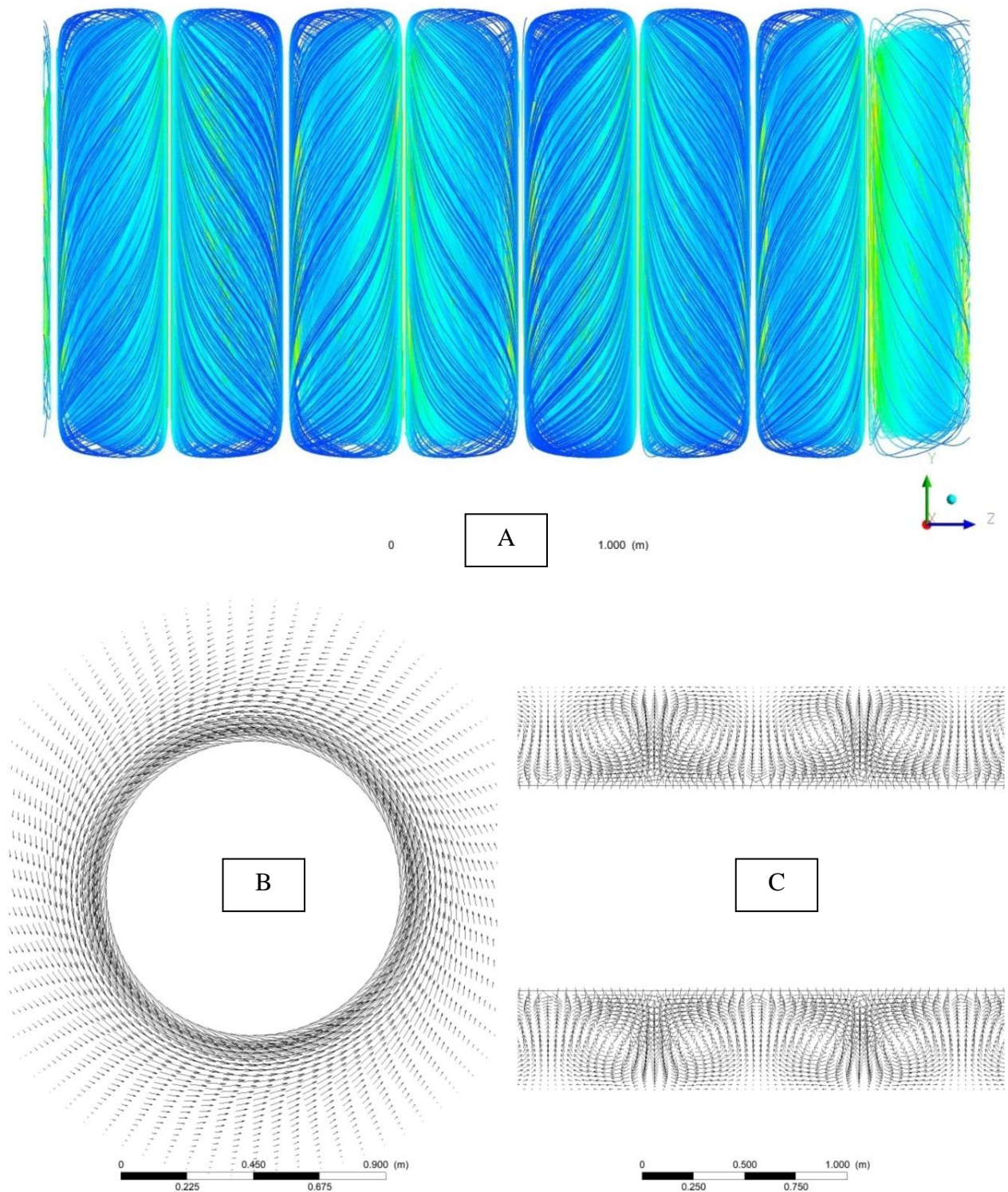


Figure 4.4 Numerical simulation results A) Velocity streamline plot B) Velocity vectors for $T_a = 5000$ for plane (1) of Figure 4.3.A C) Velocity vectors for $T_a = 5000$ for plane (2) of Figure 4.3.A

4.1.2.1 Data validation

Adebayo and Rona[57] measured the local velocities with PIV measurements. They have performed numerical simulation and validated the results with the PIV measurements. The geometry and mesh details are taken from the Adebayo and Rona[57] paper and can be referred from Table 12. Realizable $\kappa-\varepsilon$ model is used by Adebayo and Rona[57]. For numerical simulation, the same model as authors is used. Moving wall boundary condition is specified at the rotor boundary. Comparison of PIV data and numerical simulation data for radial and axial velocity is done and can be referred from Figure 4.5 and Figure 4.6. Grid independence study is not done as the mesh was referred from the paper.

Table 12 Numerical simulation for Adebayo and Rona[57] geometry

Geometry Details		Relevant Parameters	
R1	0.025 m	Fluid	Air
R2	0.057 m	Density	1.225
L	0.25 m	Cp	1005
Mesh Details		K	0.6
Edge	Number of divisions	μ	1.48×10^{-5}
Circumference	20	v	1.81×10^{-5}
Cylinder Gap	128	Ta	6.86×10^6
Length	500	ω	52.36 r/s

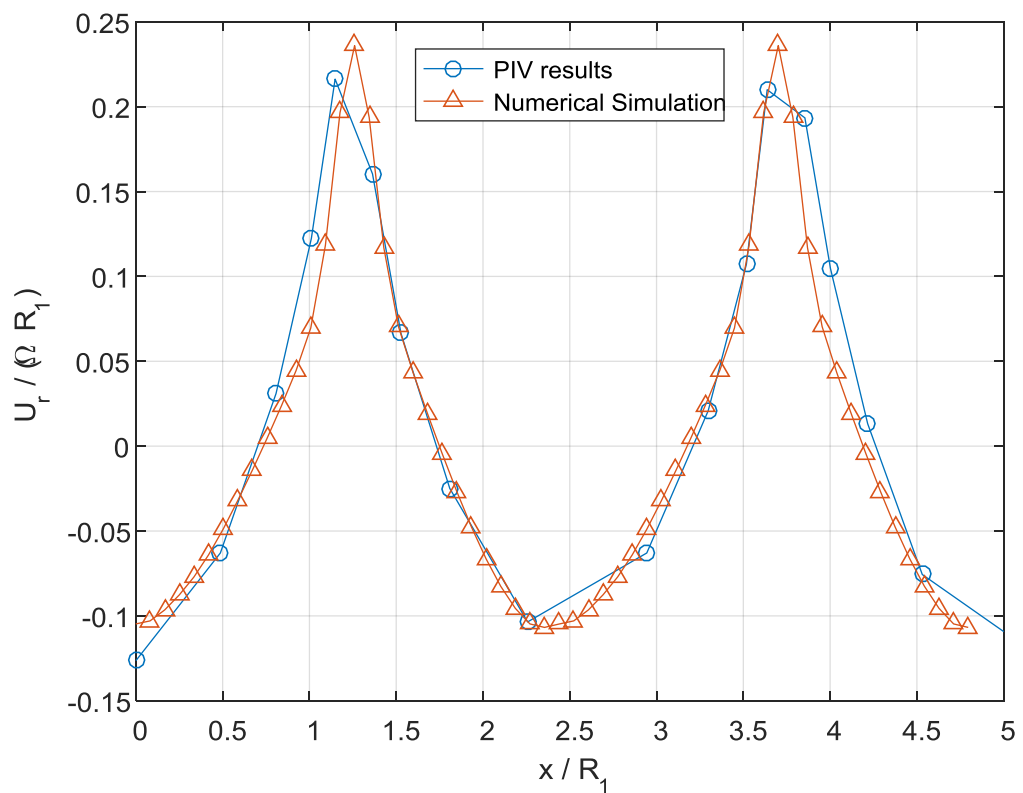


Figure 4.5 Radial velocity profile variation at $R = 0.041$ m with axial distance

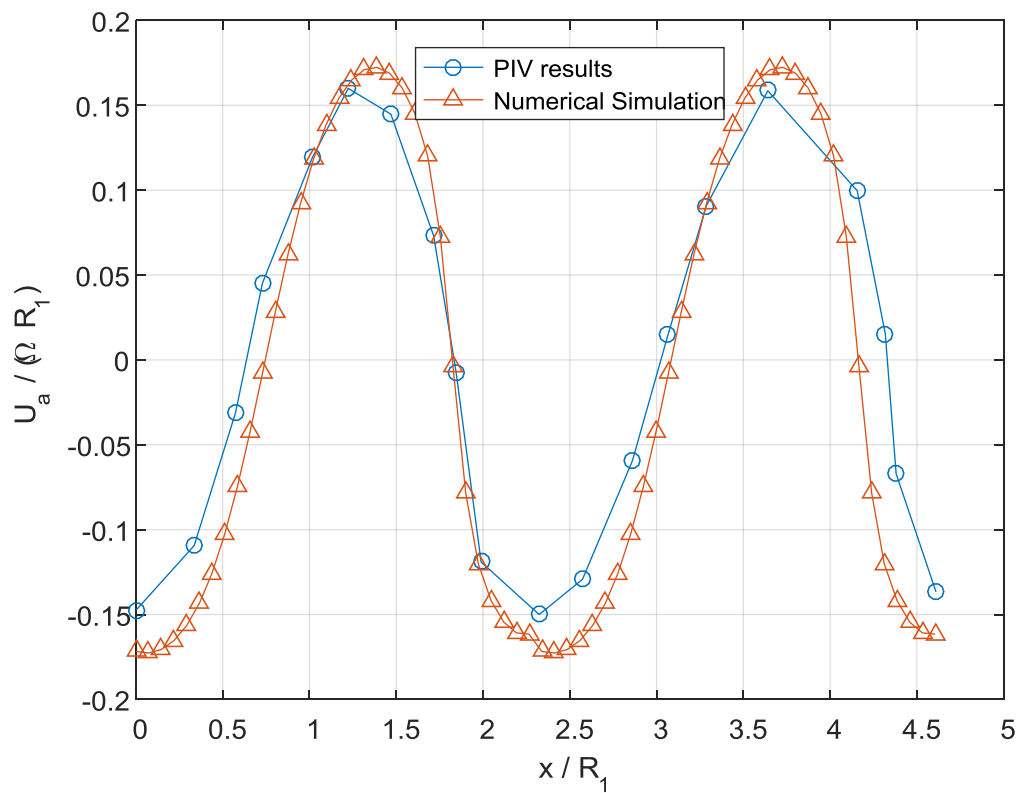
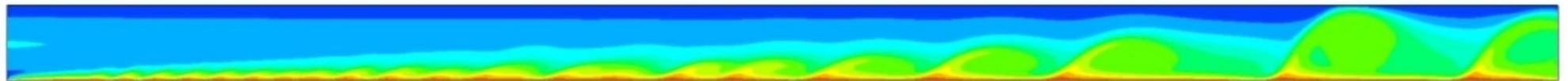


Figure 4.6 Axial velocity profile variation at $R = 0.029$ m with axial distance

A



B

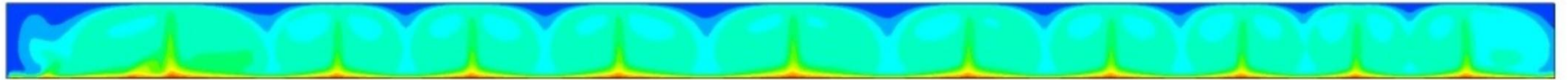


Figure 4.7 Velocity contours for unsteady simulation of Taylor-Couette-Poiseuille flow at the square root of $Ta^* = 1474$ and A) $Re = 500$ B) $Re = 28.8$ for the geometry of Kataoka et al.[58]

4.1.3 Taylor-Couette-Poiseuille flow

The unsteady simulation was carried out for co-axial cylinders to get the toroidal flow structure which moves in the axial direction as described in the literature. The simulation is carried out for the geometry and flow parameters given in Table 13, referred from Kataoka et al.[58]. The geometry is made with 1° sector of a circle, and periodic boundaries are defined to make an axis-symmetric cylinder. $\kappa - \omega - SST$ turbulence model was used with curvature correction for rotating flow. Comparison of velocity contours for the square root of Taylor number $Ta^* = 1474$ at axial Reynolds number $Re = 500$ and 28.8 is given Figure 4.7 A and B.

Table 13 Numerical simulation for Taylor-Couette-Poiseuille flow

Geometry Details		Relevant Parameters	
R1	29 mm	Fluid	Water
R2	47 mm	Density	998.2
L	380 mm	Cp	4182
Mesh Details		K	0.6
Edge	Number of divisions	μ	0.001003
Circumference	2	v	1.00481×10^{-6}
Cylinder Gap	54	Ta	1474
Length	76	ω	3.6

4.2 Heat transfer characteristics in Stator-Rotor gap

4.2.1 Taylor-Couette flow

Kataoka[59] performed an experiment for concentric cylinders with the inner rotating cylinder and measured the local Nusselt number on the inner surface of the stationary outer cylinder. The experiments are performed by the electrochemical technique, and the heat-mass transfer analogy is used to calculate the local heat transfer. The temperature of the rotor and stator is kept constant throughout the experiment. The authors compared the results of the experiment

with the values obtained from nonlinear instability theory for different values of rotational Reynolds number defined by Eq.4.1.

$$\text{Re}_\omega = \frac{R_l e \omega}{\nu} \quad (4.1)$$

4.2.1.1 Geometry and Flow details

Inner cylinder radius	29 mm
Outer cylinder radius	47 mm
Length of the cylinder	380 mm
Fluid	Electrolyte
Number of revolutions	13 ~ 200
Rotational Reynolds number	55.3 ~ 845
Schmidt number	$2.1 \times 10^4 \sim 4.31 \times 10^5$

The inner and outer radius of the simulation geometry is kept the same as the cylinder used in the experiment. The length of the cylinder is reduced to 76 mm, and the simulation is run for 10° sector of the cylinder to reduce the computational effort. Steady state laminar equations are solved. Three cases of Taylor number are simulated, and the result of Nusselt number variation is compared with the results of Kataoka[59]. The details of the simulation can be found in Table 15.

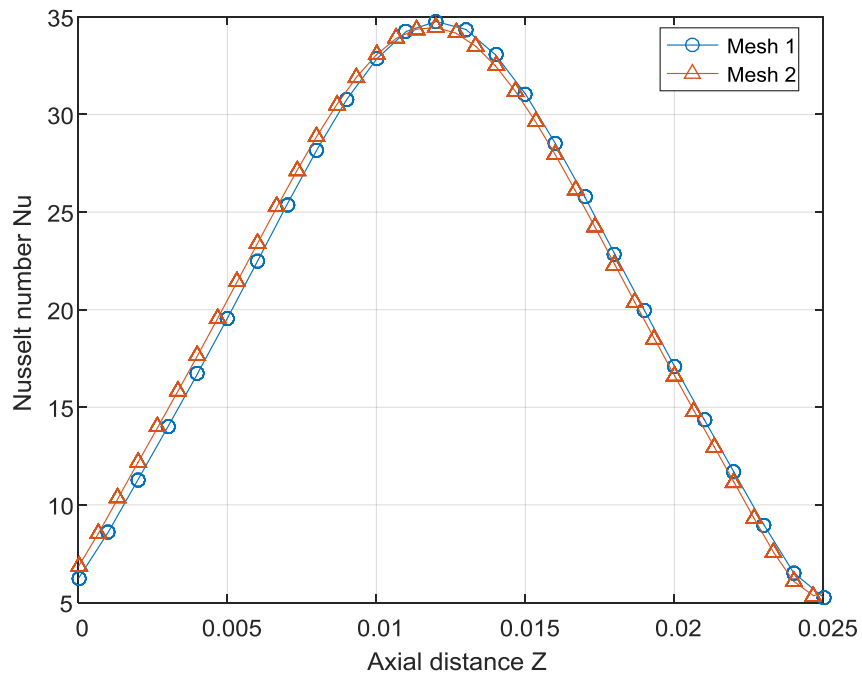


Figure 4.8 Grid independence study for Local Nusselt number variation along the length of the stator at $T_a \sim 24828$ using two different meshes.

4.2.1.2 Grid independence study

The grid independence study is done for two different meshes. The details of the mesh can be found in Table 14. The maximum difference in the result of Nusselt number variation is not significant (2.18%) and can be observed in Figure 4.8. Thus the simulation for all the cases was carried out using element sizes used for the first mesh.

Table 14 Mesh used for grid independence study

Geometry Details	Mesh 1	Mesh 2
Length of the cylinder	76 mm	76 mm
Angle of the sector	5°	5°
Circumference division	10	15
Number of divisions along gap	54	81
Number of divisions along length	26	39
Total number of elements	14040	47385

Table 15 Details of the cases simulated in Ansys Fluent

Parameters	Critical Taylor case	Case 1	Case 2	Case 3
Fluid	Water	Water	Water	Water
R1	29 mm	0.029 m	0.029 m	0.029 m
R2	47 mm	0.047 m	0.047 m	0.047 m
e	18 mm	0.018 m	0.018 m	0.018 m
η	0.617	0.617	0.617	0.617
L_exp	380 mm	0.38 m	0.38 m	0.38 m
L_simulation	76 mm	0.076 m	0.076 m	0.076 mm
Number of vortices	Minor Instability	None	4	4
Rotational Reynolds number R	69.93	50	200	400
Rotational velocity	0.1346 r/s	0.0962 r/s	0.3850 r/s	0.76997 r/s
Pr	7	7	7	7
g (m/s^2)	9.81	9.81	9.81	9.81
β	0.000214	0.000214	0.000214	0.000214
Taylor number	3035.3	1551.7	24827.6	99310.3
Grashoff Number	100	100	100	100
T1 (K)	350	350	350	350
T2 (K)	349.99175	349.99175	349.99175	349.99175

4.2.1.3 Effect of Prandtl number variation

Kataoka[59] reported that the results of the mass transfer experiment are best simulated using the liquid with $\text{Pr} \sim 1$. The current simulation is carried out with water as a working fluid. Figure 4.9 is plotted with a non-dimensional value of Nusselt number $\text{Nu} / \text{Pr}^{0.375}$ against non-dimensional axial distance Z / λ so that the Prandtl number effect on Nusselt number can be excluded. The parameter λ is the total length of the Taylor vortex pair and can be referred from Figure 2.6 for clarification. The index of Pr is taken from the Kataoka[59] paper and two different fluids were used for simulation. The ratio of Nu to Pr^n is constant indicating the choice of working fluid does not alter the variation of heat transfer along the axial direction.

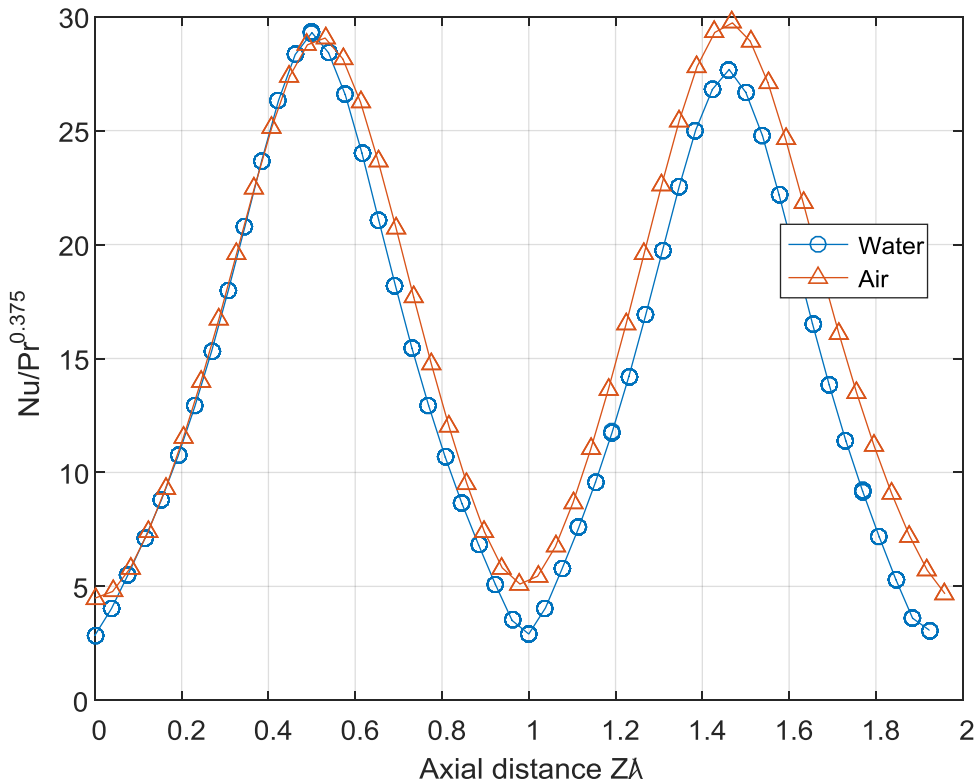


Figure 4.9 Nusselt number variation with axial direction for two different working fluids, Air and Water.

4.2.1.4 Validation of Numerical data

The flow simulation was done for solving $\kappa - \omega - SST$ model continuity, momentum and energy equation. Kedia et al.[60] carried direct numeric simulation of the geometry of Kataoka[59] paper and found the exact match with the experimental results. For the current

study, the simulation over-predicts the local Nusselt number for both laminar and turbulent model. The reason for over-prediction is not known. Figure 4.10 and Figure 4.11 can be referred for comparison of numerical data with experimental results. The comparison for the case of plane Couette flow and Taylor Couette flow is also made, and Figure 4.13 can be referred. It can be concluded from the data of Figure 4.13 and Figure 4.12 that the Taylor vortices enhance the mixing of the fluid and increase the heat transfer from the stator surface. It can be observed from Figure 4.13 that the heat transfer increases as the Taylor number increases.

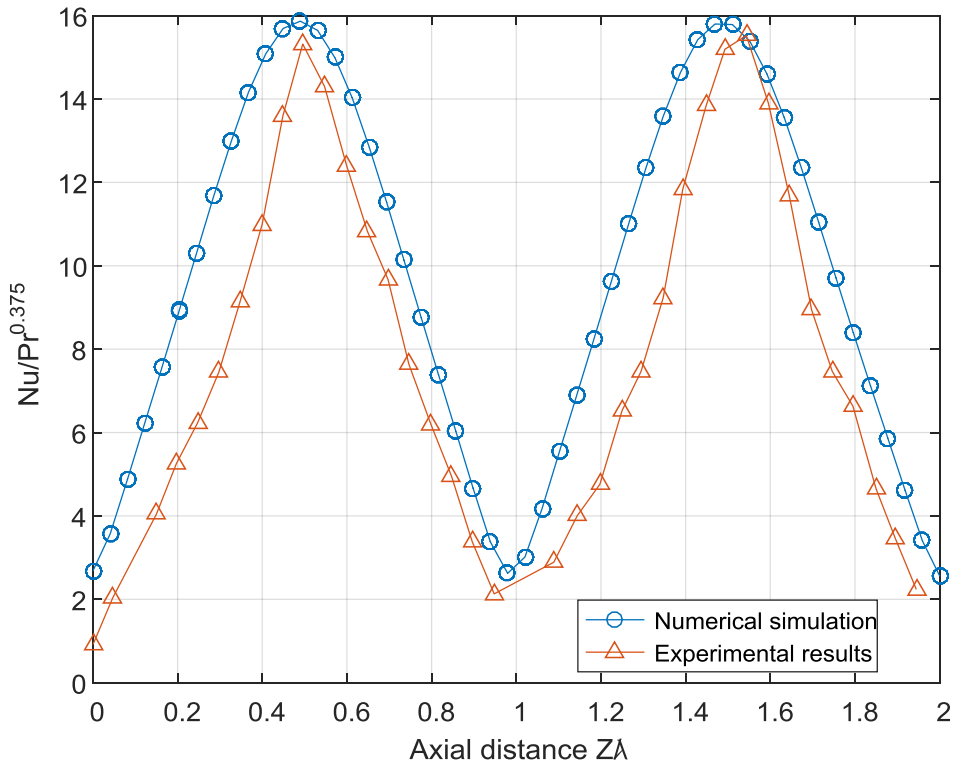


Figure 4.10 Nusselt number variation with axial direction for the $\text{Ta} \sim 24900$ compared with Kataoka[59]

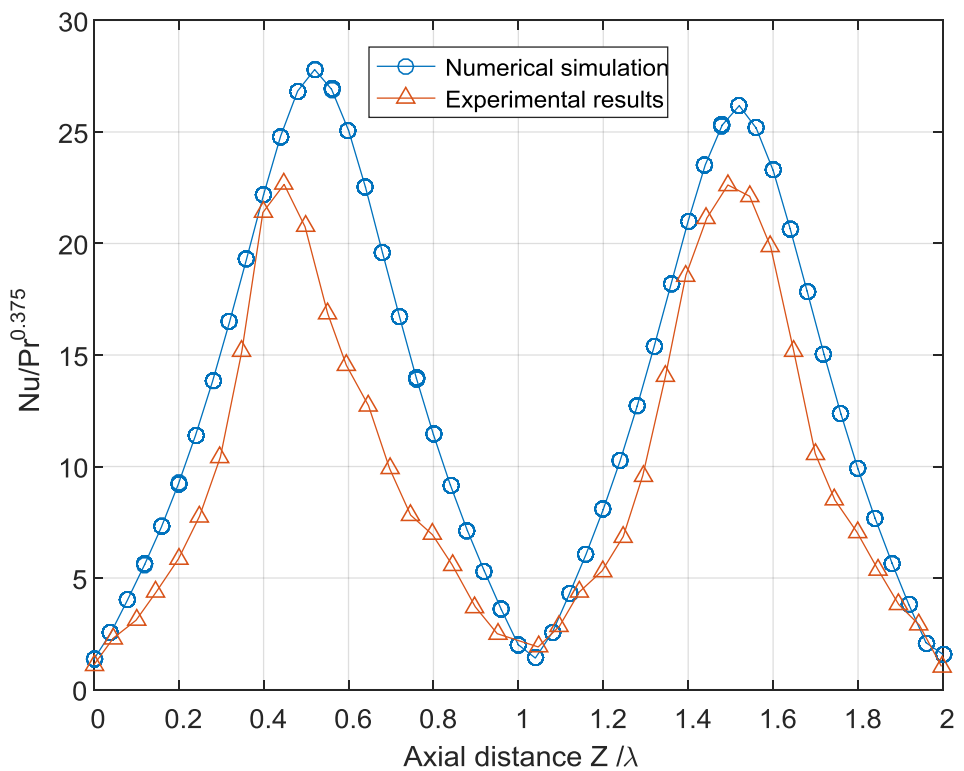


Figure 4.11 Nusselt number variation with axial direction for the $\text{Ta} \sim 99300$ compared with Kataoka[59]

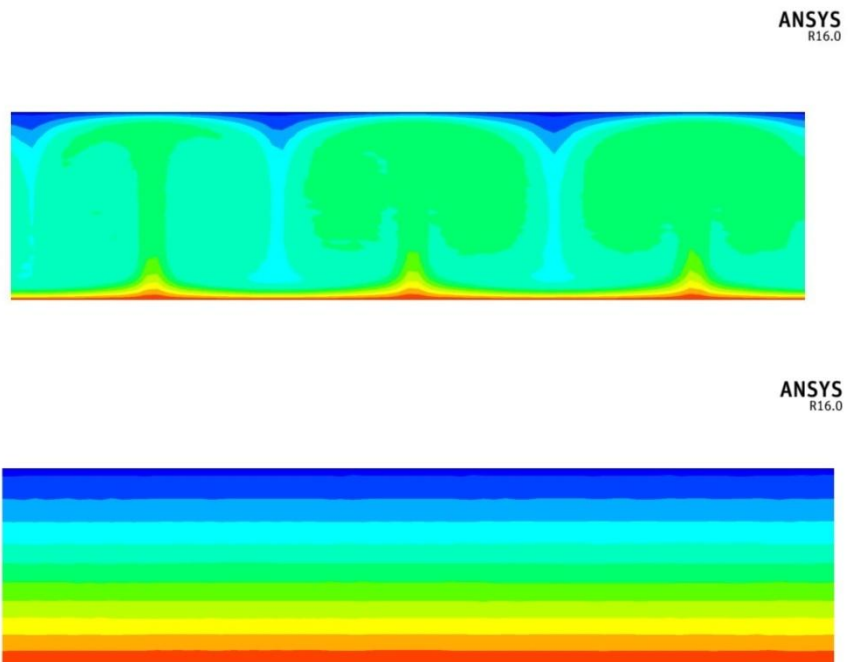


Figure 4.12 Temperature variation for the Taylor-Couette (Top) flow and the Couette flow (Bottom).

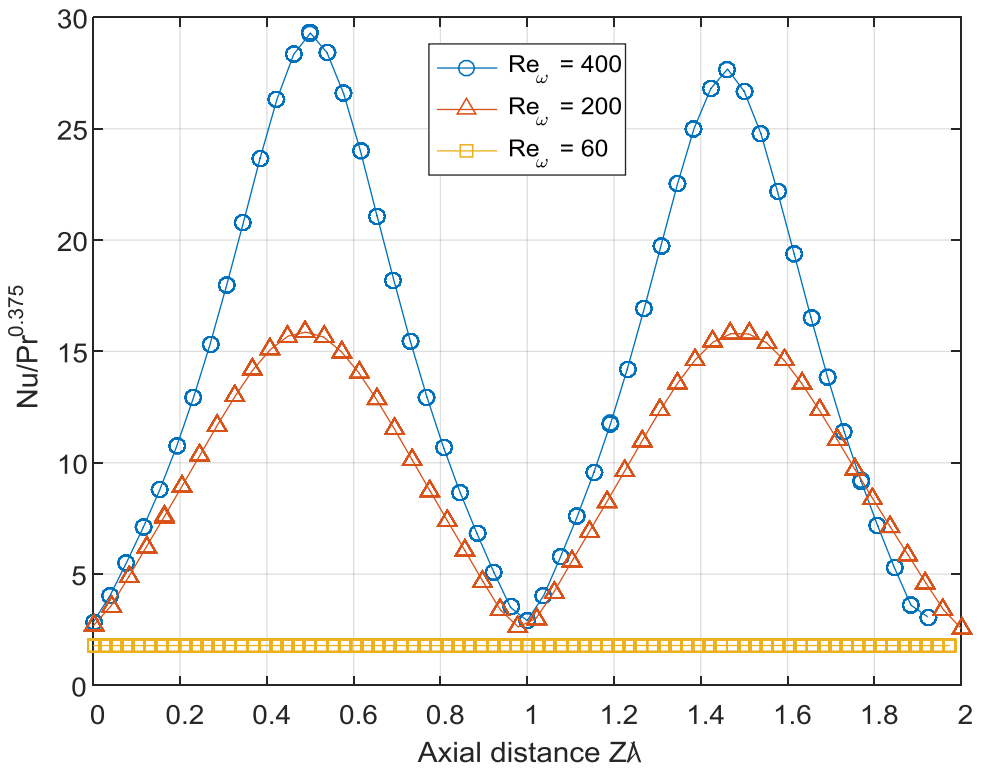


Figure 4.13 Comparison of Nusselt number variation for Couette flow for rotational Reynolds number $R = 60$ and Taylor-Couette flow $R = 200$ and 400 referred from Kataoka[59].

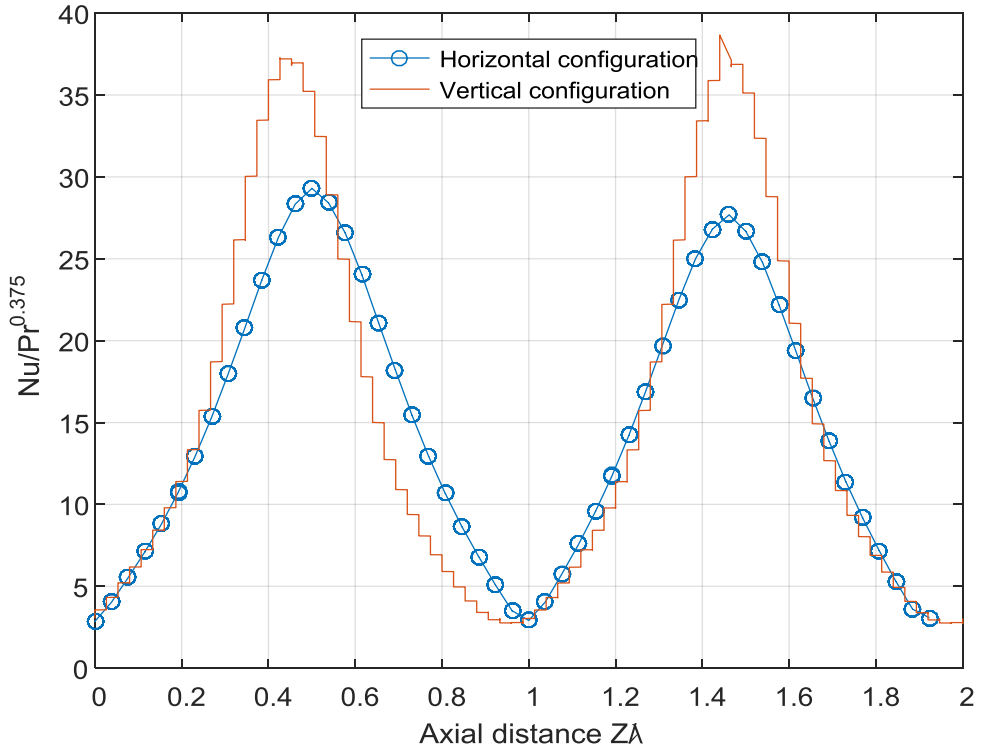


Figure 4.14 Nusselt variation for horizontal and vertical configuration of the rotor.

4.2.1.5 Effect of cylinder configuration

The heat transfer in Taylor-Couette flow is likely to be affected by natural convection along the cylinder surface. Thus the effect of geometry configuration was studied by simulating the verified geometry. It was observed that the vertical configuration gives more heat transfer compared to the horizontal configuration. The results are plotted in Figure 4.14.

4.2.2 Taylor-Couette-Poiseuille flow

4.2.2.1 Introduction

The canned motor pump has flow in both azimuthal and axial direction. The effect of axial flow on the heat transfer from the stator was studied in another experimental study by Kataoka et al.[58]. The author has given the variation of dimensionless Nusselt number for different values of Nusselt number. It was observed that the presence of axial flow delays the Taylor instability and thus reduces the overall heat transfer from the stator surface. Thus for designing canned motor, it is important to study the effect of axial flow on heat transfer. Taylor number in Figure 4.15 is the square root of the Taylor number.

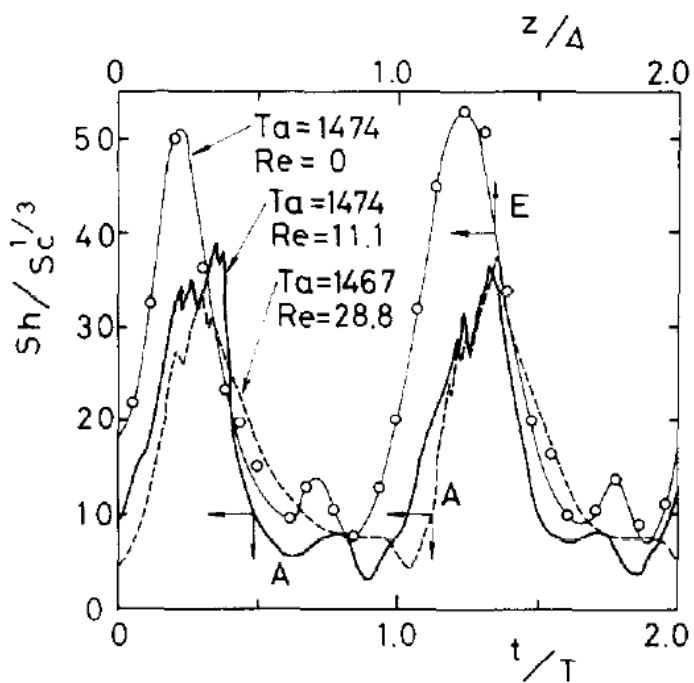


Figure 4.15 Variation of Mass/Heat transfer on the stator with Reynolds number
Kataoka et al.[58]

The grid was kept the same as Taylor-Couette flow case for simulating the axial flow case. Boundary conditions at the inlet are changed from translational periodic to the user defined function (UDF). Details of the UDF can be found in Appendix F. The fully developed velocity distribution of Figure 4.16 is applied as a boundary condition at the inlet. Outflow boundary condition is applied at the outlet of the geometry.

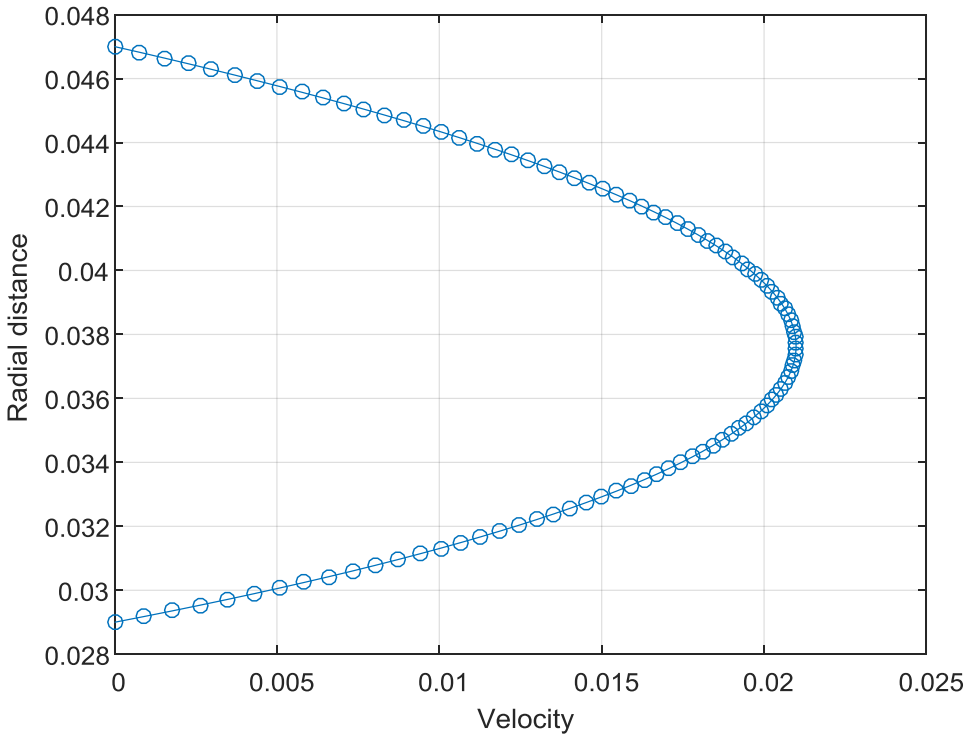


Figure 4.16 Fully developed velocity profile at the inlet of concentric cylinder for $Re = 500$ and geometry of Kataoka et al.[58]

4.2.2.2 Validation of results

The square root of Taylor number of 1474 (from Kataoka et al.[58]) was chosen for validation of the results so that the estimate of heat transfer in an actual canned pump can be made. It can be observed by comparing Figure 4.17 and Figure 4.15 that the simulation over-predicts the Nusselt number variation, but the trend of decline in Nusselt number is followed. It was also observed that the simulation for other cases of Taylor number gives the same over-prediction (Two times the reported value by Kataoka et al.[58]) for Reynolds number greater than 0. The deviation from experimental results for a simulated case of Reynolds number equal to 0 is not significant and can be observed from Figure 4.18 and Figure 4.19.

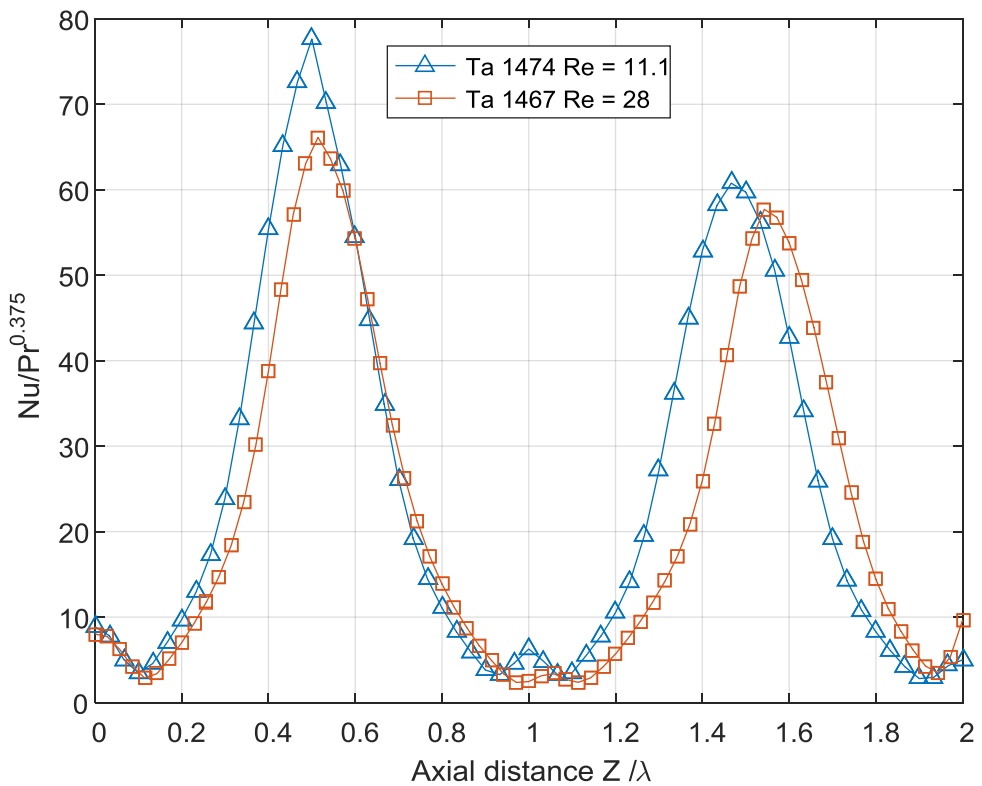


Figure 4.17 Simulation results for variation heat transfer for Kataoka et al.[58] geometry

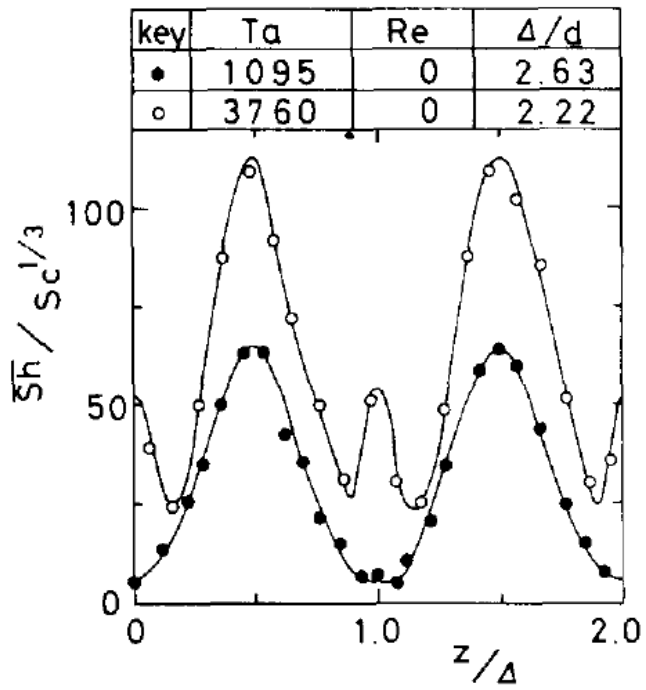


Figure 4.18 Local Nusselt number variation reported by Kataoka et al.[58]

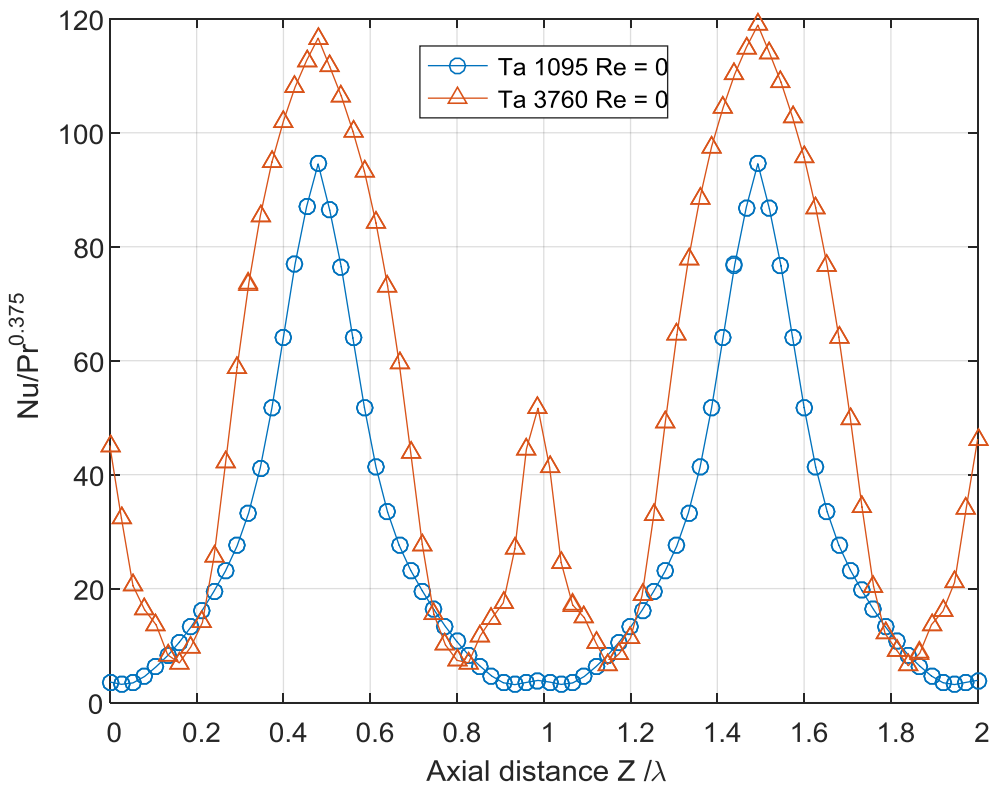


Figure 4.19 Simulation results for variation heat transfer for Kataoka et al.[58] geometry

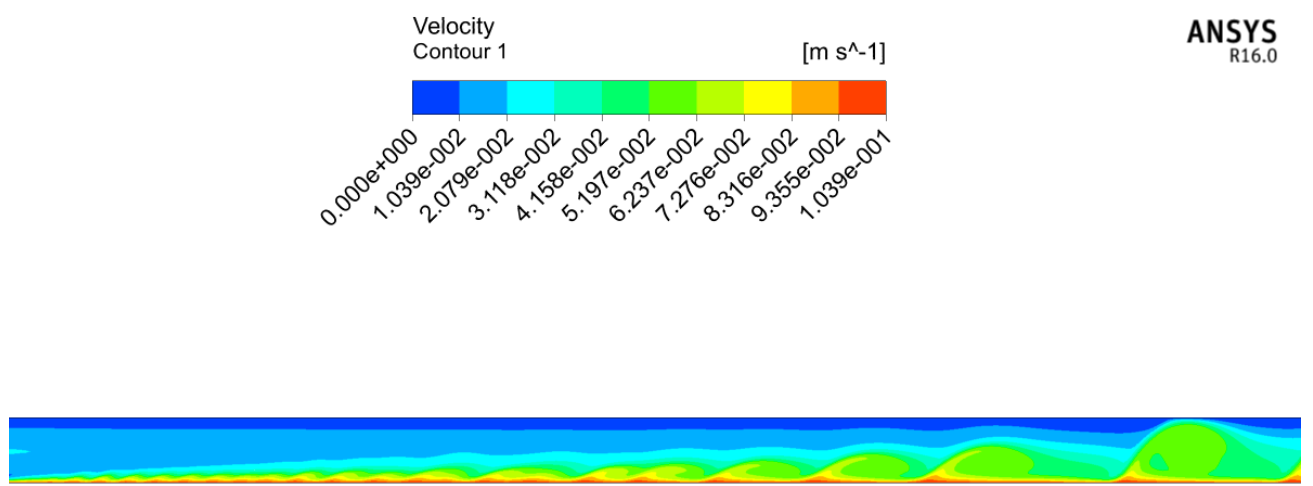


Figure 4.20 Velocity contours for unsteady simulation of Taylor-Couette-Poiseuille flow at square root of $\text{Ta} = 1474$ and $\text{Re} = 500$ for geometry of Kataoka et al.[58]

4.2.2.3 Unsteady flow calculation

With the introduction axial flow in Taylor-Couette flow, vortex pair tends to move with the flow in the axial direction. Thus it is difficult to get converged results by steady flow simulation. Thus unsteady flow simulation was carried out. The flow in Figure 4.20 is not fully developed in a radial direction. Unsteady simulation is carried out. We have done steady simulation and calculated the Nusselt number at the outlet where the flow is fully developed, both radially and axially. For every iteration, different Nusselt number value is obtained.

4.2.3 Minimum flow rate

NEMA specifies the letter grade given in Table 16 for the thermal insulation used in the electric motor. The letter grades are given for the motor with service factor equal to one. For the designed motor in Table 8, calculation for minimum flow rate was carried out by simple energy balance between inlet and outlet of the annular space. For the analytic calculation, rotor was kept stationary. The calculated values are given in the Table 16. For designed geometry, square root of Taylor number is calculated to be $Ta^* = 720$. Thus from the literature review and our simulations it can be concluded that the TCPF flow will help in reducing the rise in temperature at minimum flow rate. In some cases of canned motor pump, motor power is large and requires large flow rates. The flow rate is achieved by the secondary impeller for maintaining the required temperature.

Table 16 Letter grades for thermal insulation used in motor

Motor Insulation Temperature rating		Temperature rise	
Class	Maximum Temperature (°C)	Ambient (°C)	Allowable Temperature rise
A	105	40	60
B	130	40	80
F	155	40	105
H	180	40	125

Table 17 Temperature change from inlet to outlet on rotor for flow through annulus

Inlet Temperature (K)	Outlet Temperature (K)	Flow velocity (m/s)	Axial Reynolds number
300	405.3	0.2	170
300	384.22	0.25	210
300	370.18	0.3	250
300	360.16	0.35	295

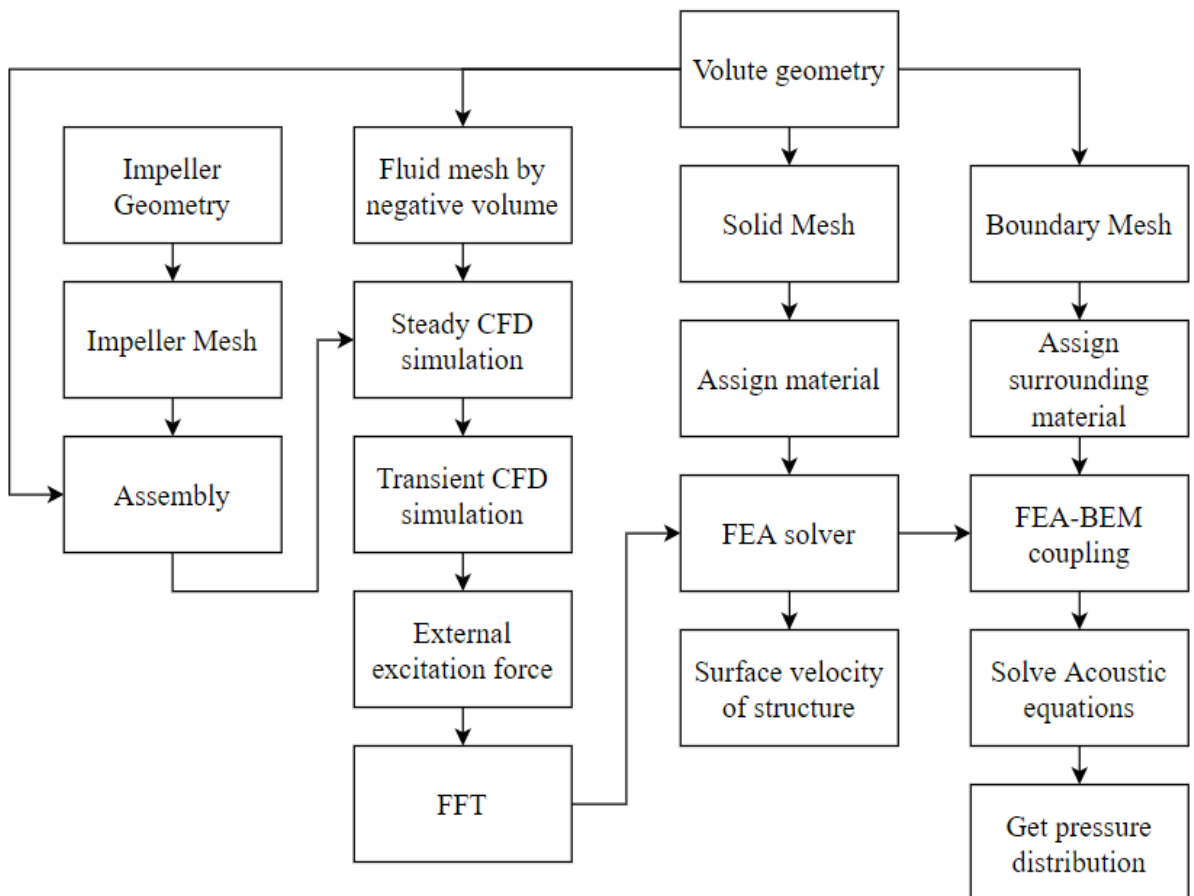


Figure 4.21 General process flow for centrifugal pump simulation

4.3 Centrifugal pump simulation work flow

Simulation of the centrifugal pump involves steady state simulation followed by transient analysis. Steady state simulation is done with frozen rotor approach discussed in a later section. Steady state solution acts as an initial condition for the transient simulation. The transient data generated by the CFD code for the fluid mesh is then transferred to the Ansys Mechanical solver for structural simulation with FEA mesh of the casing. To identify the frequency at which unsteady behaviour is maximum, FFT of the data has to be done. A generalized code is written for the FFT (Ref.H.7) of the pressure data. Ansys Mechanical solver solves the FEA mesh and gives surface deformation and vibration velocity. This data is then transferred to the shell like boundary mesh called BEM for solving the acoustic equations. General process flow is given in Figure 4.21 in terms of flow chart for better understanding.

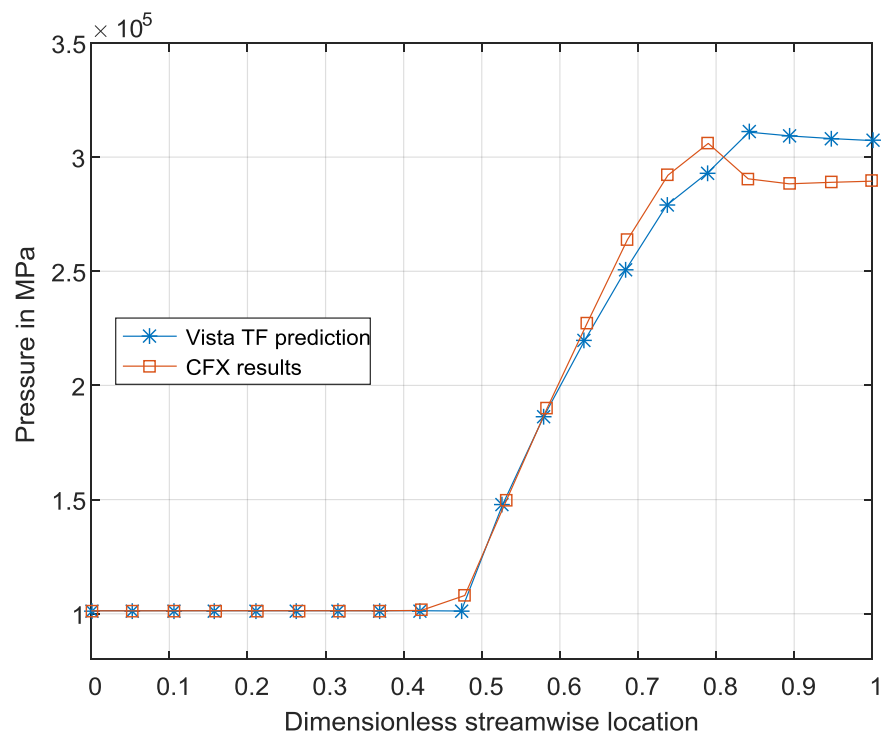


Figure 4.22 Average pressure comparison between Throughflow method and CFX results measured from inlet to outlet of Kaewnai et al.[39] impeller for design flow rate $Q = 528 \text{ m}^3/\text{hr}$.

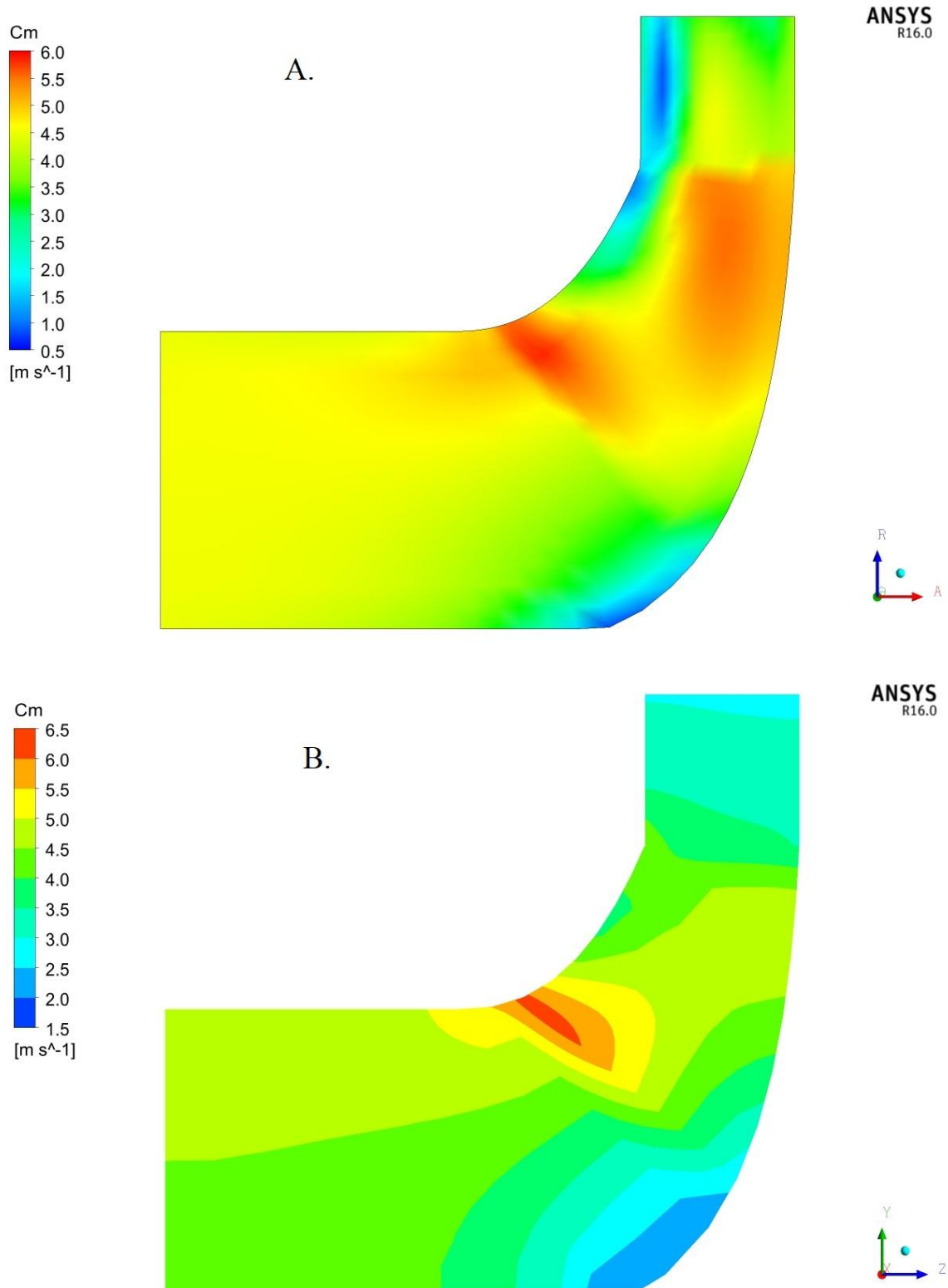


Figure 4.23 Contour plot of flow velocity calculated by Throughflow method with 3D solution A. CFX solution B. Throughflow solution at Meridional plane for Kaewnai et al.[39] impeller.

4.4 Performance prediction

4.4.1 Pump characteristics prediction by Throughflow method

Throughflow analysis was done with water as a working fluid. The total pressure of 1 atm at the inlet and the design mass flow rate at the outlet is given as boundary condition. The results of Throughflow analysis are compared with the full 3D simulation done with Ansys CFX. The impeller geometry is referred from Kaewnai et al.[39] (Table 19) and Kim et al.[41] (Table 18). The full 3D simulation is run for both for design and off-design cases. Results of design flow comparison for Kaewnai et al.[39] is given in Figure 4.23. It can be seen from Figure 4.23 that the average pressure estimated along the dimensionless streamline locations m (Ref. Figure 3.7) by the Throughflow method for the design (Ref. Figure 4.22) and off-design (Ref. Figure 4.24) case is also very close to the simulated pressure value.

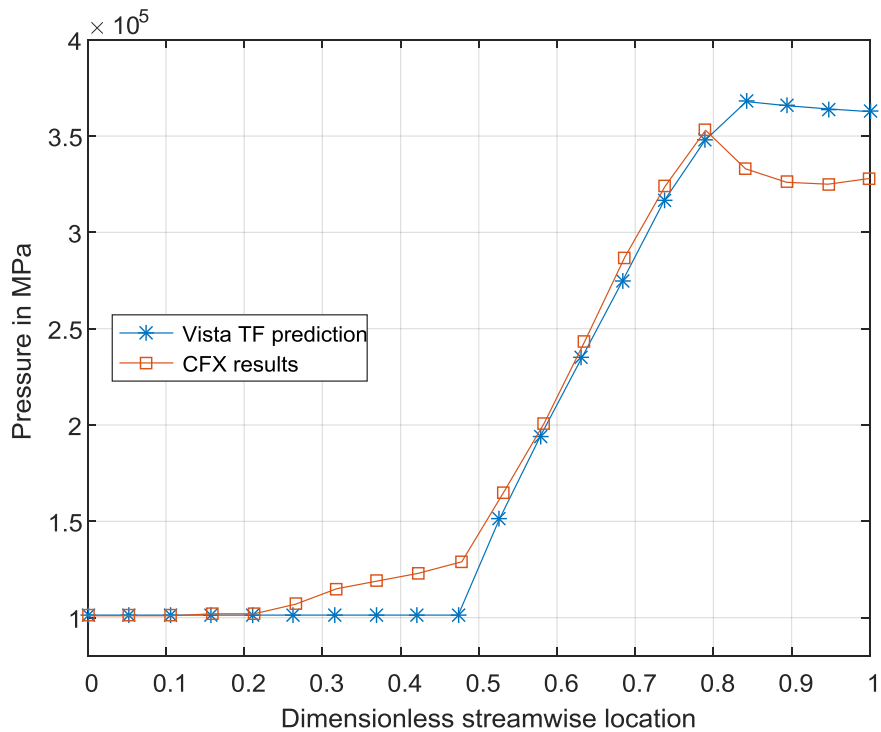


Figure 4.24 Average pressure comparison between Throughflow method and CFX results measured from inlet to outlet of Kaewnai et al.[39] impeller for design flow rate $Q = 360 \text{ m}^3/\text{hr}$.

4.4.2 Pump characteristics prediction by slip and loss analysis

Win[32] has given a method for predicting the head generated by the pump. MATLAB code (Ref.H.6) is written for slip and loss analysis. The slip co-relation used in the code is valid for specific speed less than 60, thus code can give erroneous results for higher specific speeds. The co-relations are given in Gülich[5] and Karassik et al.[21] and are used in our MATLAB code. Win[32] simulated the pump geometry with head of 35 m at the design flow rate of 468 m^3/hr and the rotational speed of 1470 rpm. Figure 4.25 and Figure 4.26 give the pump characteristics predicted by our code for Win[32] geometry and the maximum difference of 7.93% is observed. Since only head, discharge and flow rate were given, we have used our Impeller scratch code (Ref.H.1) for calculating the velocity triangles. Win[32] has not provided the empirical constants for some of the co-relations used in the paper. The data was interpolated from the head-loss graph given in the paper for finding the unknown empirical constants.

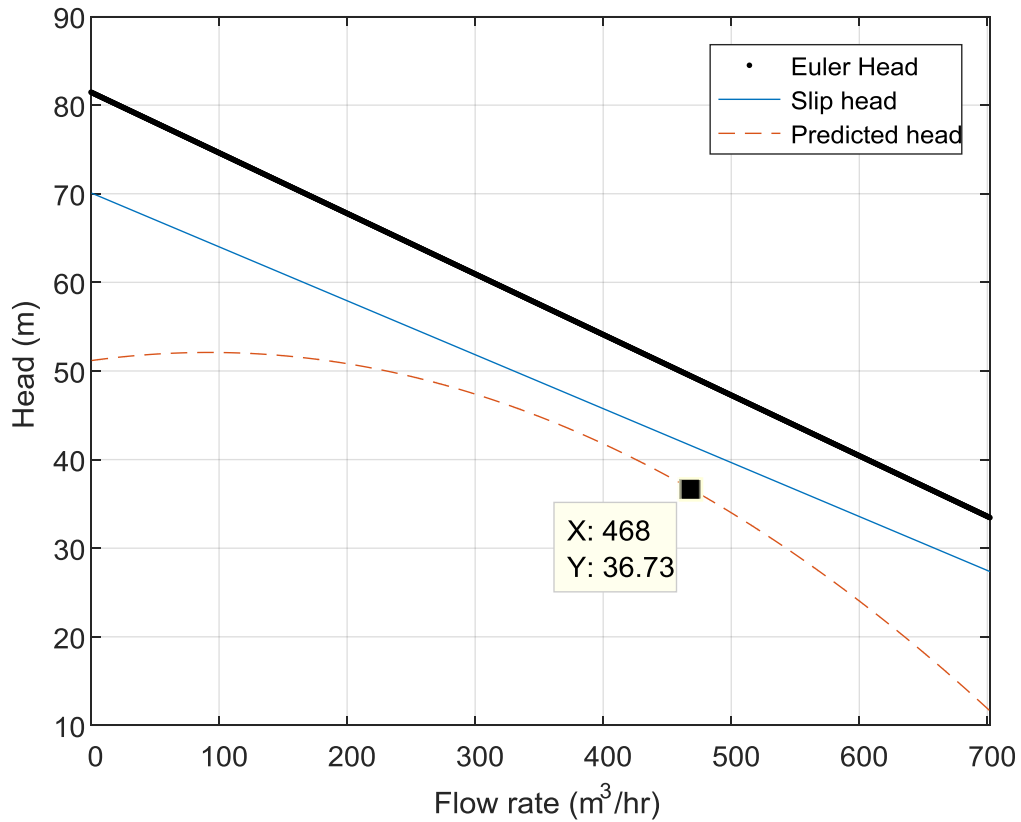


Figure 4.25 Head vs Discharge characteristics for Win[32] geometry

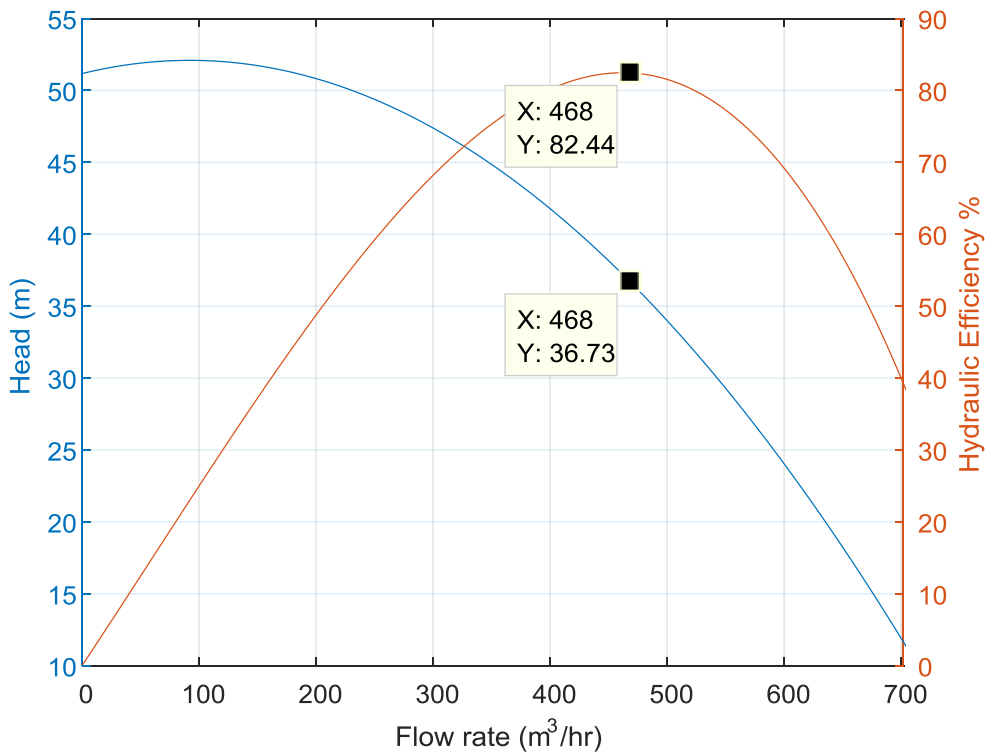


Figure 4.26 Head and Efficiency variation with flow rate for Win[32] geometry

The design head (35 m) is bit different than the predicted head (36.73 m) at the design flow rate (Ref. Figure 4.25). It should be noted from Figure 4.26 that the maximum efficiency is obtained at the point close to the design flow rate. Institution of Mechanical Engineers (Great Britain)[9] have given the characteristic curves and design specifications for the actual pump. The slip and loss analysis was done for the pump. The maximum deviation of 7.3% from the manufacturer's data is observed. The prediction error remained less than 8% for H-Q characteristics of Kaewnai et al.[39] and Kim et al.[41].

4.5 Impeller and volute pre-processing

4.5.1 General work flow

Although the in-house codes were written, it was convenient to use commercial codes of ANSYS for quick changes in the pump design. The general process flow with ANSYS is given in Figure 4.27.

4.5.2 Impeller and volute geometry

Impeller and Volute are generated using commercial code of ANSYS for most of the cases. For special type of volutes, SOLIDWORKS is used. Figure 4.28 and Figure 4.29 can be referred for visualizing the pump assembly.

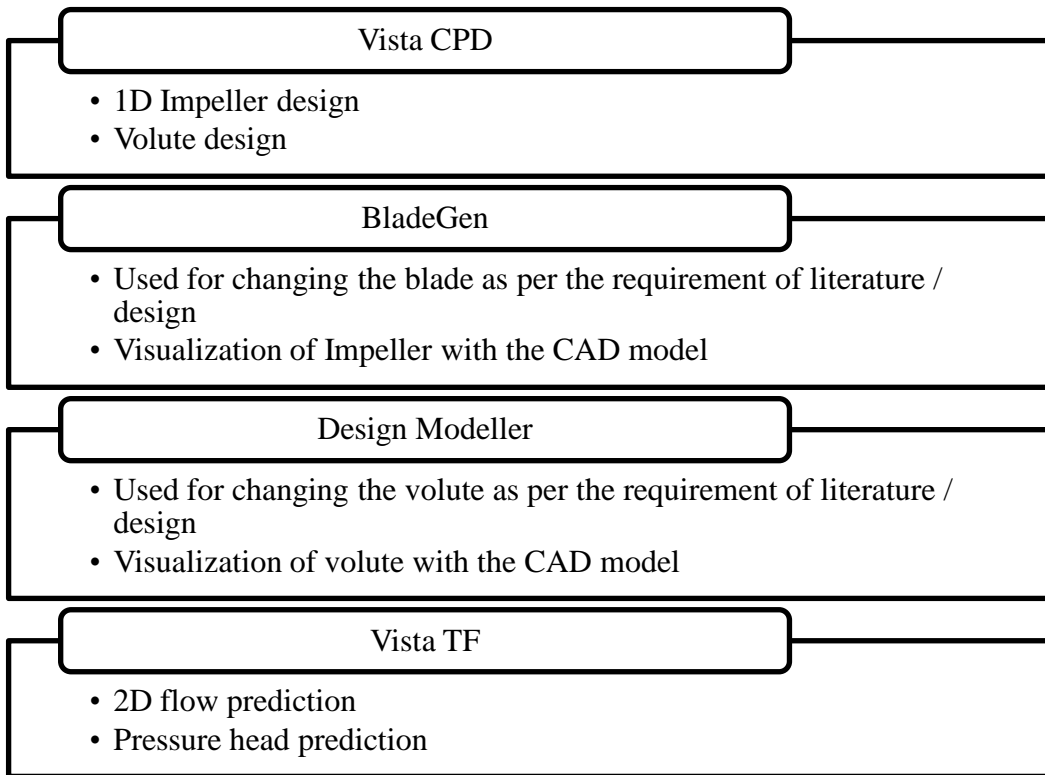


Figure 4.27 Flow chart for impeller and volute design with ANSYS

4.5.3 Impeller and volute CFD mesh

ANSYS mesh generator or ICEM can be used for the mesh generation. ANSYS has a module named TurboGrid which generates high quality hexahedral mesh for the impeller. Process of mesh generation is simple with TurboGrid. For all the impeller geometries, TurboGrid is used. The impeller mesh is shown in Figure 4.30. Tetrahedral meshing is used for volute of Figure 4.31.

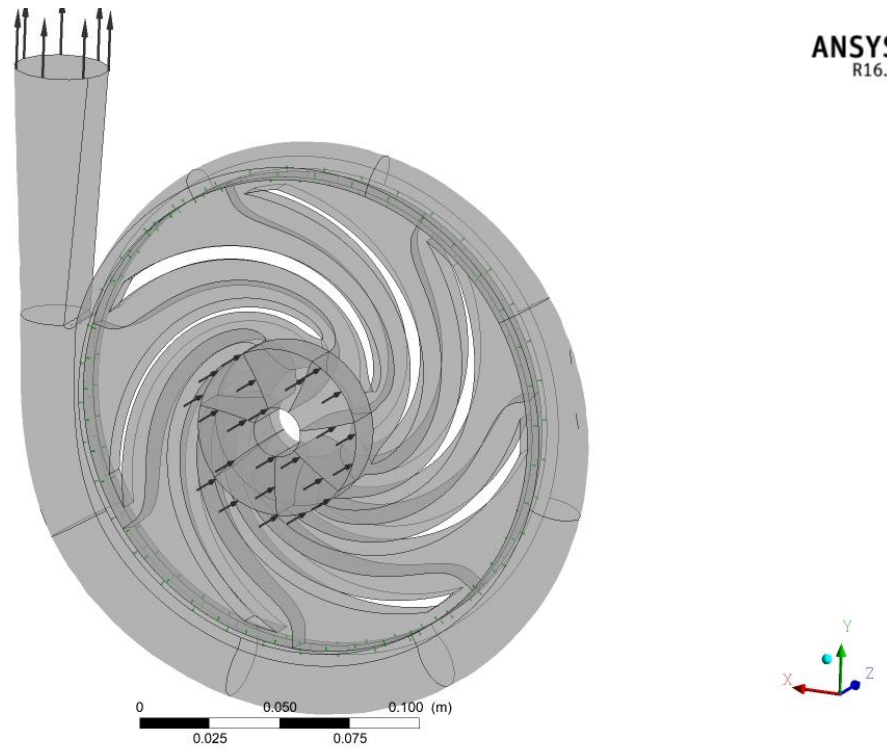


Figure 4.28 Assembly of impeller and volute generated by ANSYS

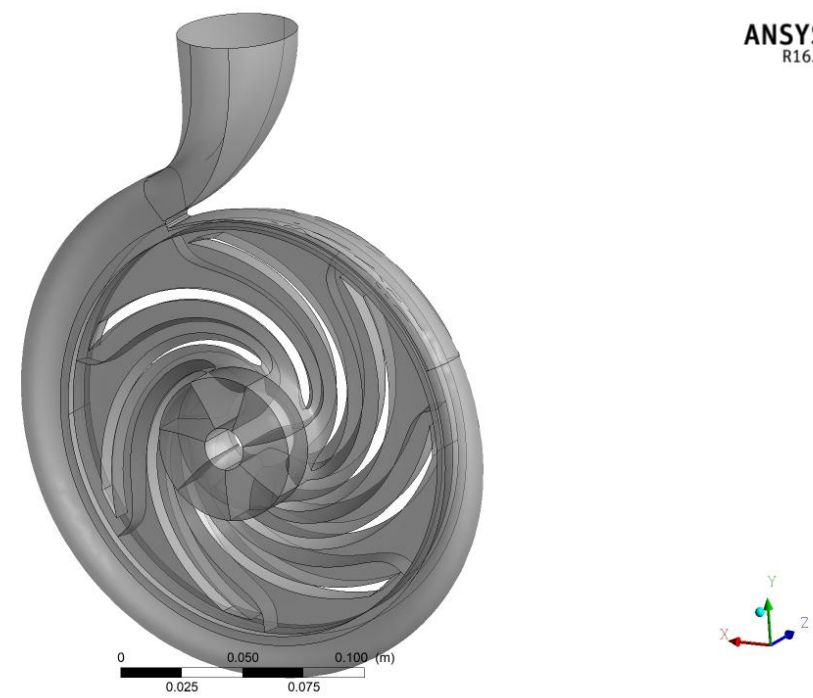


Figure 4.29 Assembly of impeller generated by ANSYS and volute generated by SOLIDWORKS for Si et al.[47] pump geometry

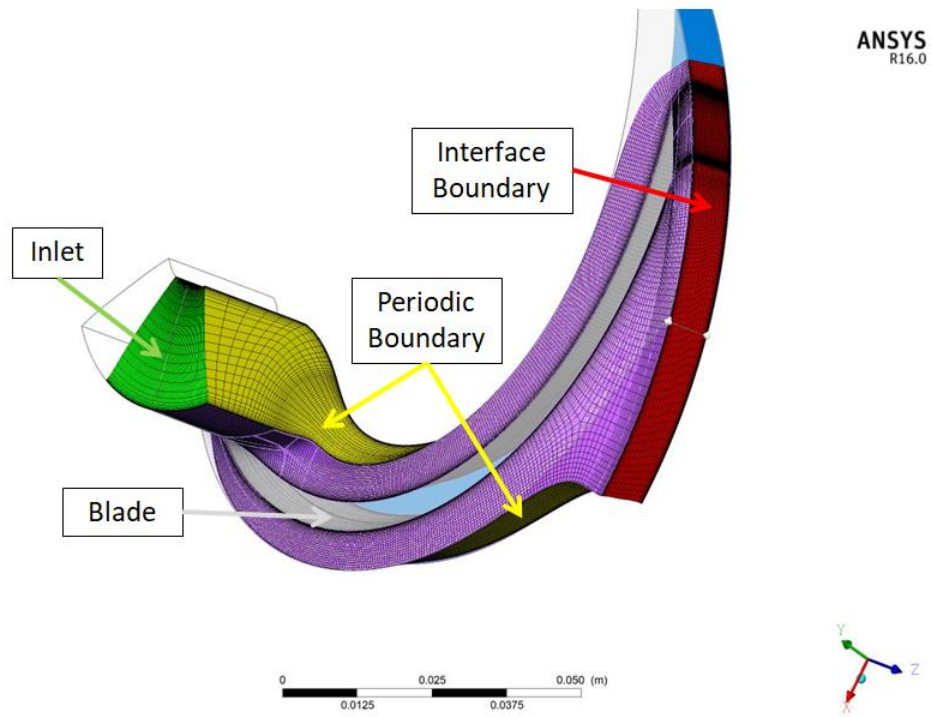


Figure 4.30 Impeller CFD mesh generated by TurboGrid for all the cases of the literature

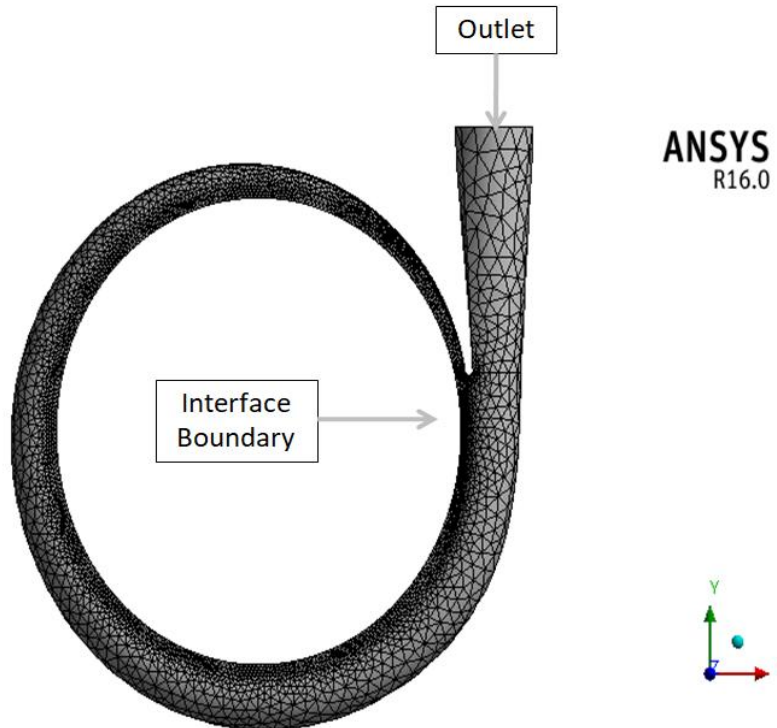


Figure 4.31 Volute CFD mesh generated by ANSYS

4.5.4 Impeller and Volute boundary conditions

The momentum equation is solved in an impeller considering the moving reference frame approach. The moving reference frame (MRF) solves the ordinary Navier-stokes equation with some additional terms like coriolis acceleration, rotational acceleration and vorticity terms. Ansys provides two methods namely mixing plane and frozen rotor for solving the MRF equations. The prediction accuracy of frozen rotor method is more than the mixing plane method. The frozen rotor approach is used for all the steady state simulation cases of the dissertation. The periodic boundary conditions for the impeller geometry are used for saving the computational effort for the steady state simulation. Ansys offers Fourier Transform method where only two blade passages are simulated and the results are interpolated for the rest of the geometry. This method is only effective if the number of blades is large as the phase correction requires the blades to complete some rotations for each time step. The computational effort is reduced by Fourier Transform method. For the unsteady simulation a full blade passage of the impeller is used instead of Fourier Transform. The impeller mesh is simulated with sliding mesh approach which solves the momentum equation by the actual movement of the impeller mesh. The volute mesh is solved with stationary frame of reference for all the simulations.

Velocity inlet and pressure outlet boundaries are used for the flow rate equal to and greater than the design flow rate. For the flow rate less than the design flow, flow reversal from outlet to inlet was observed. The reversal resulted in divergence of the results. This was corrected by using static pressure boundary at the inlet and specified mass flow rate at the outlet boundary. The interface boundary is specified at the interface between the outlet of the impeller and the inlet of the volute. Since only the portion of the impeller is simulated for steady simulation, the pitch at the interface was less than one. The pitch is the ratio of total azimuth angle of volute to impeller mesh at the interface. The azimuth angle of the impeller is calculated from number of blades Z and is given by $\theta_{\text{Impeller}} = 2\pi/Z$. For the volute the azimuth angle is $\theta_{\text{Volute}} = 2\pi$. The pitch has to be specified in Ansys as the default setting has pitch equal to one. The impeller outlet boundary may not always match with the volute inlet boundary. The mismatch is taken care by the GGI interface selection in Ansys. For the volute and impeller mesh, inflation at boundaries was provided. The sample calculation for y^+ is given in (Appendix C). The RMS value of the residues were kept below 10^{-4} (Ref. Ansys®[37]) for convergence.

4.6 Steady state simulation

4.6.1 Comparison with literature

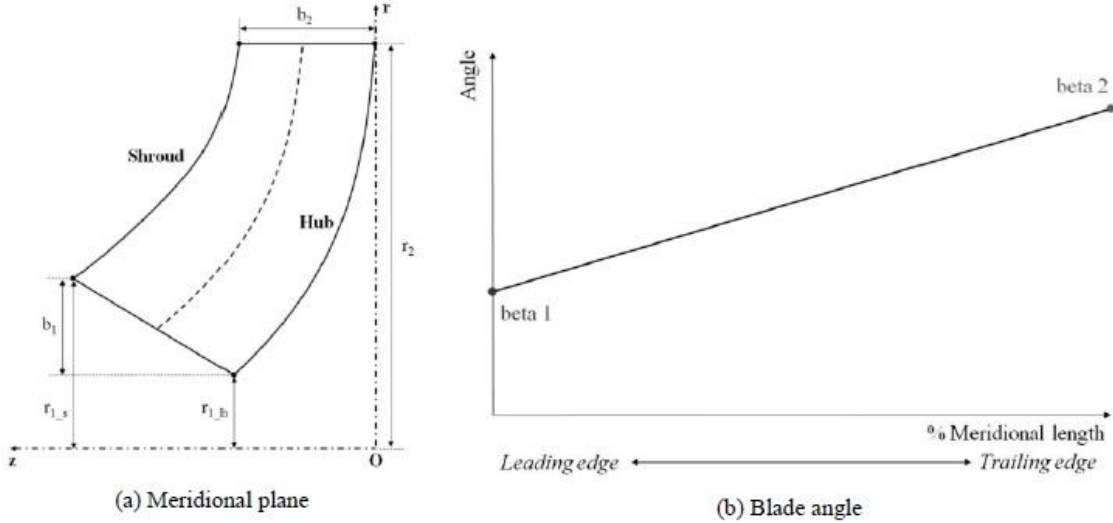


Figure 4.32 Blade geometry used by Kim et al.[41] for simulation.

Geometry parameters used by Kim et al.[41] are listed in Table 18. The Meridional passage detail was provided by Kim et al.[41] and can be referred from Figure 4.32. The solution is grid independent for the nodes greater than 0.2 Million. The y^+ value was taken ~ 5 for the mesh. SST $\kappa-\omega$ model is used for solving the turbulence. The comparison of pump characteristics of Kim et al.[41] and our simulation is shown in Figure 4.33.

Table 18 Design details given by Kim et al.[41]

Design Specifications	Value	Design Specifications	Value	Design Specifications	Value
Flow rate $Q(m^3/h)$	4500	r_2 (mm)	550	β_1	21°
Head (m)	60	r_{1h} (mm)	142	β_2	24°
Rotation speed (rpm)	600	r_{1s} (mm)	275	Number of blades	6
Efficiency	Maximum	b_1 (mm)	133	b_2 (mm)	100.

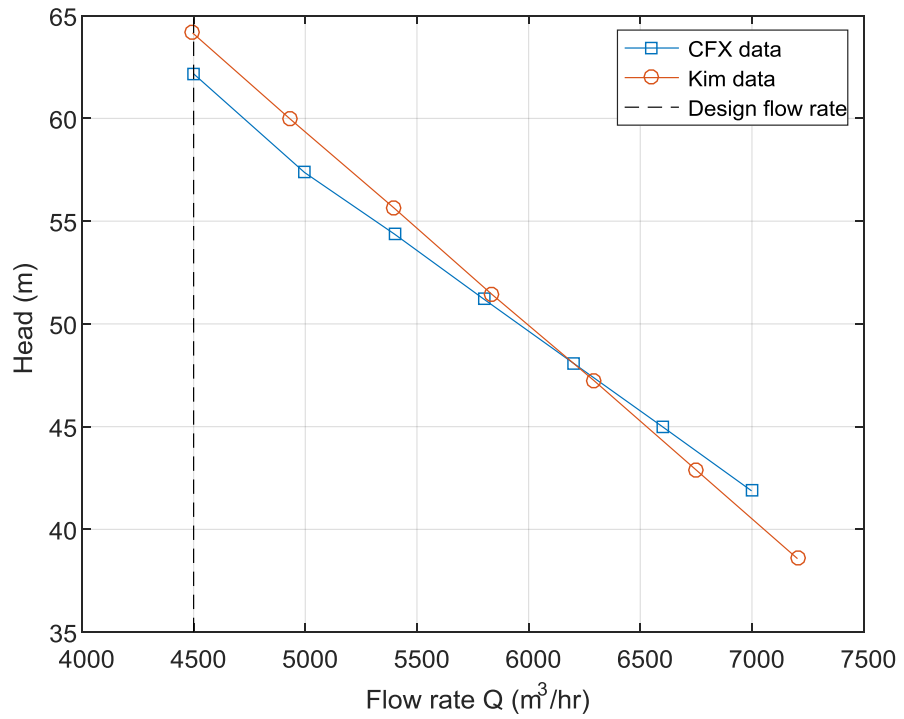


Figure 4.33 Head vs Discharge characteristics comparison for our simulation with the Kim et al.[41] pump.

Geometry parameters used by Kaewnai et al.[39] are listed in Table 19. The solution is grid independent for the nodes greater than 75 thousand. The y^+ value was taken ~ 15 for the mesh. $\kappa-\varepsilon$ model is used for modelling the turbulence. The comparison of pump characteristics of Kaewnai et al.[39] and our simulation is shown in Figure 4.34 and Figure 4.35.

Table 19 Design details given Kaewnai et al.[39]

Design Specifications	Value
Flow rate $Q(m^3/h)$	528
Head (m)	20
Rotation speed (rpm)	1450
Number of blades	7
Efficiency	Maximum
β_1	24.5

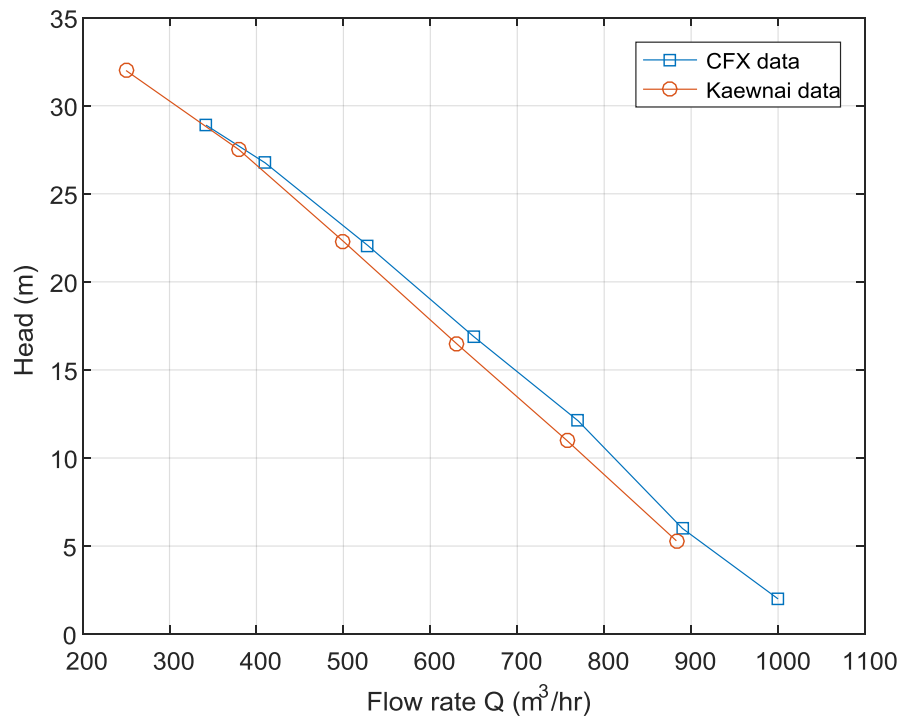


Figure 4.34 Head vs Discharge characteristics comparison for our simulation with the Kaewnai et al.[39] pump.

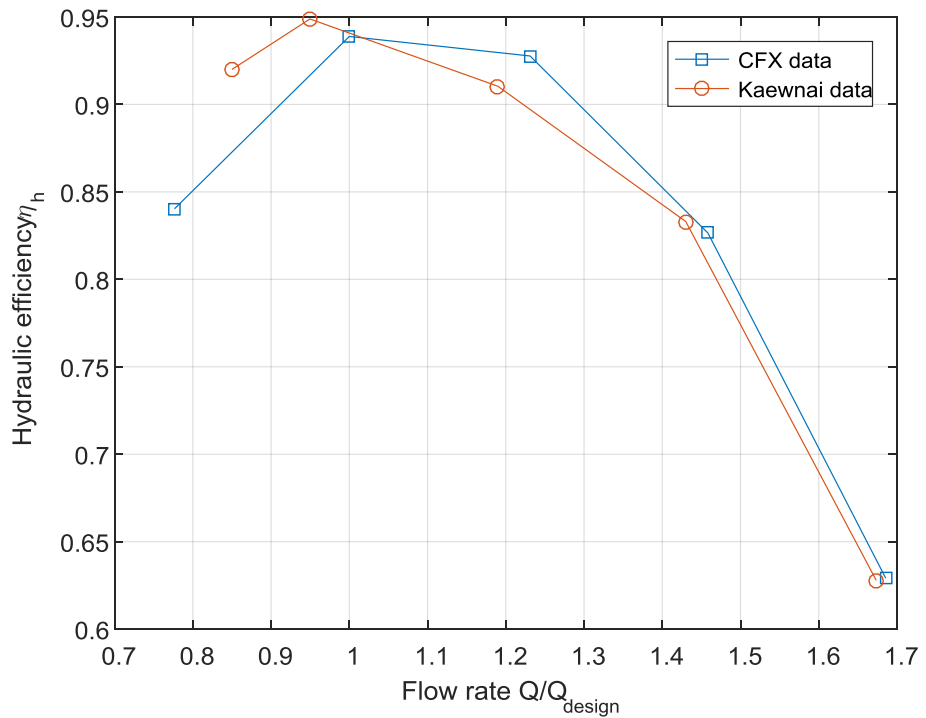


Figure 4.35 Hydraulic efficiency vs Discharge characteristics comparison for our simulation with the Kaewnai et al.[39] pump.

4.6.2 Comparison with real pump

The canned motor pump data provided by Hydrodyne Pumps is used for simulation. The input parameters for design and geometry parameters are given in Table 20. Based on the design details, the mean-line design for the impeller is done with a MATLAB code (Ref. H.1 and H.2). The general work flow from Figure 4.27 is followed.

Table 20 Pump data for the canned motor pump provided by Hydrodyne Pumps

Design Specifications	Value	Design Specifications	Value
Motor rating (kW)	60	Flow rate $Q(m^3 / h)$	150
Head (m)	80	Overall Efficiency %	55
Rotation speed (rpm)	2900	Impeller Dia. (mm)	255

4.6.2.1 Mesh details

Meshing is done by using the TurboGrid module provided by the Ansys. Inflation is provided near the blade boundaries such that the $y^+ \approx 1$. Total of ~ 184500 hexahedral mesh elements are created for the impeller. Volute meshing is done with tetrahedral mesh with ~ 120000 elements shown in Figure 4.31.

4.6.2.2 Simulation setup

The simulation is steady state simulation and SST $\kappa-\omega$ model used for modelling the turbulence. The simulation is run till the RMS value of the residues converges to 10^{-6} .

4.6.2.3 Boundary conditions

The static pressure of 1 atm is specified at the inlet of the impeller and the mass flow rate calculated from discharge, at the outlet of the volute. For saving the cost of meshing, the impeller is divided into 6 equal parts by using periodic boundary condition.

4.6.2.4 Results and discussion

The blade and the volute generated from the empirical relation are assembled in ANSYS. The comparison of the pump H-Q characteristics generated by the simulation and the real pump data is made in Figure 4.36. The deviation from the real pump data is found as the flow rate is reduced and the maximum value is 5.26%. This can be because of the difference in volute geometry, as volute details were not provided to us. The velocity contours of Figure 4.37 indicate that flow does not separate at the design flow rate which is expected from the pump. The efficiency given by the ansys does not consider disk friction on the front and back cavities of the impeller, leakage flow power loss through the front and rear seals, power loss due to recirculation flows returning back to the impeller, bearing windage power losses. (Ref. Turbo[62]). Due to this the power given by Ansys for efficiency calculation gives wrong estimate of hydraulic efficiency ($> 90\%$) for the simulated cases. This can also be observed from Kaewnai et al.[39] results in Figure 4.35. Thus the CFX should only be used for qualitative agreement of the efficiency with an actual pump data. The H-Q prediction is accurate as it only involves pressure in the formulation and thus it is used for comparison by Kaewnai et al.[39], Kim et al.[41], and in the current dissertation.

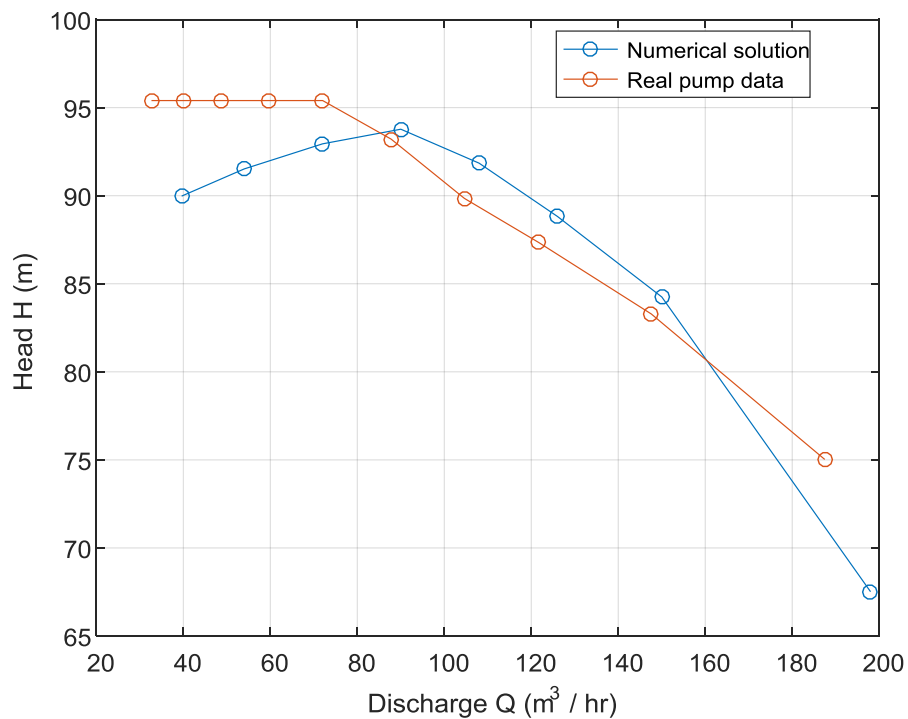


Figure 4.36 Head vs Discharge comparison for simulation and Hydrodyne Pump data

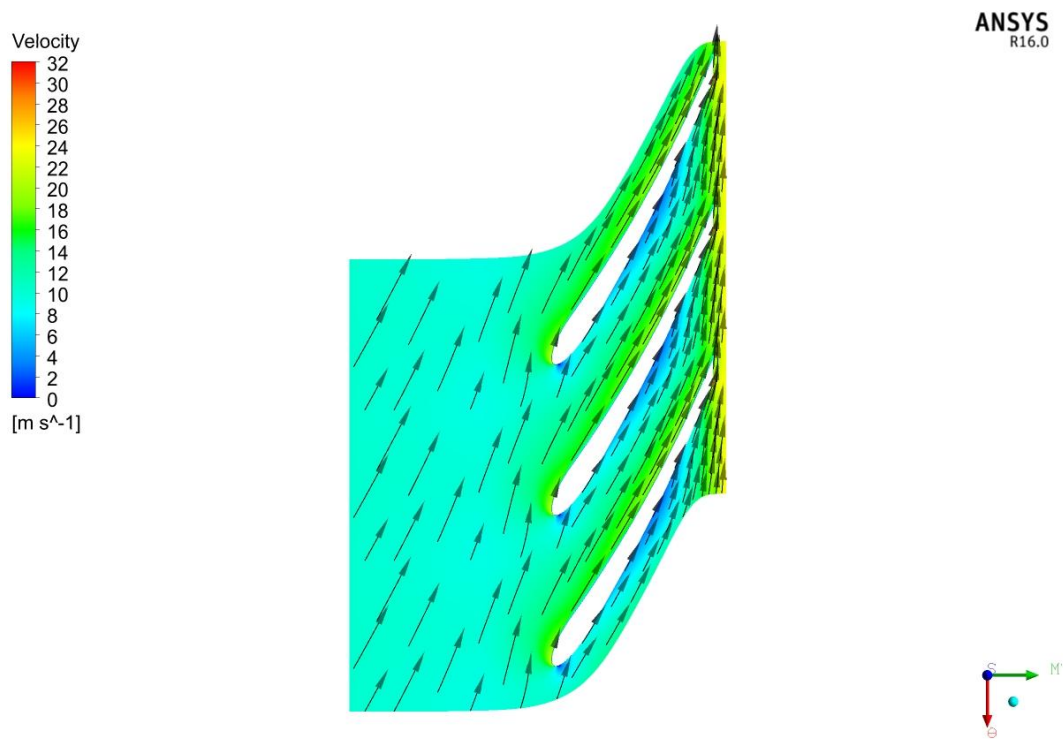


Figure 4.37 Velocity contours for the simulation of the Hydrodyne pump

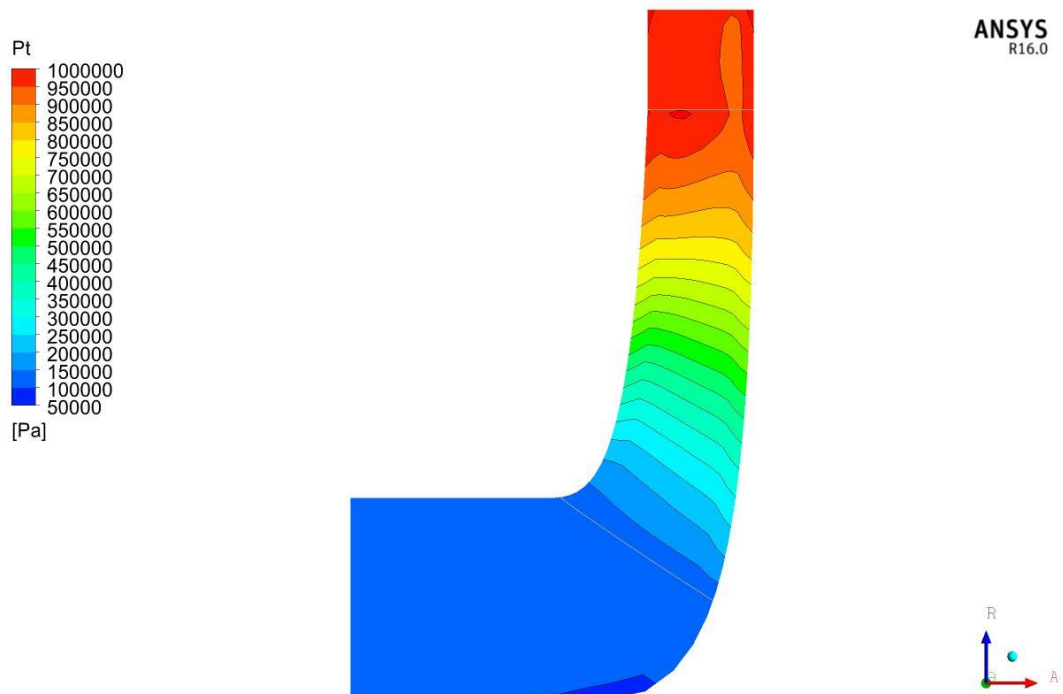


Figure 4.38 Pressure variation for the Meridional cross-section of the Hydrodyne pump

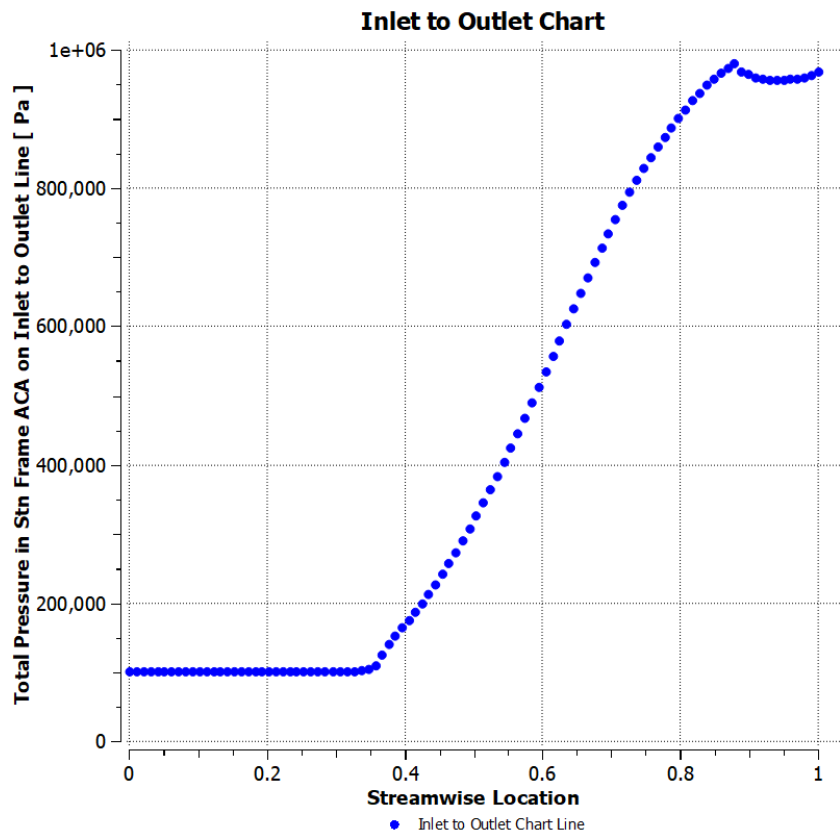


Figure 4.39 Pressure variation from inlet to outlet along the mean streamline in the Meridional view for the Hydrodyne pump. (Chart generated in Ansys)

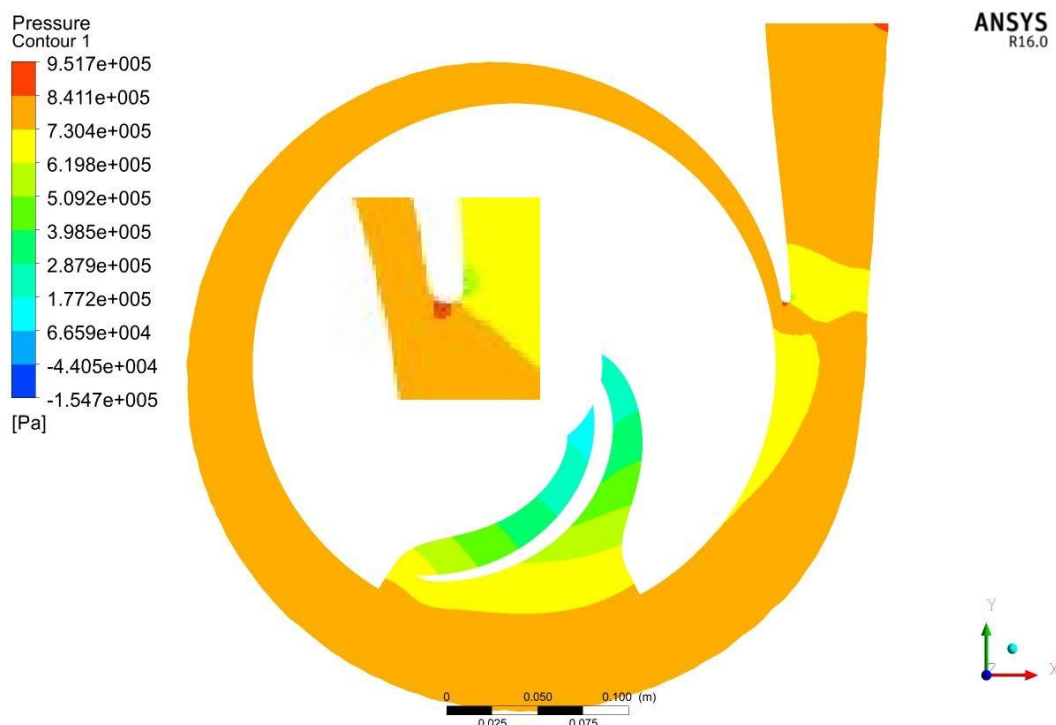


Figure 4.40 Pressure contours for the pump at the cut-section taken at the midplane.

Figure 4.38 shows the variation of the pressure in the Meridional section. The pressure transition is smooth and indicates no recirculation and unsteady behaviour in the Meridional plane. The plots given for the Hydrodyne pump are generated for the design flow rate and thus the steady flow is expected. Figure 4.39 is pressure variation from leading edge to volute inlet interface. It can be seen from the pressure contour of the Figure 4.40 that there is local pressure rise at the volute tongue and it is studied section 4.7. The pressure variation contours at the leading edge and trailing edge of the impeller are given in Figure 4.41 C and Figure 4.41 D. The uniform pressure contours at both the leading and trailing edge indicate that the flow is fully developed and had steady behaviour.

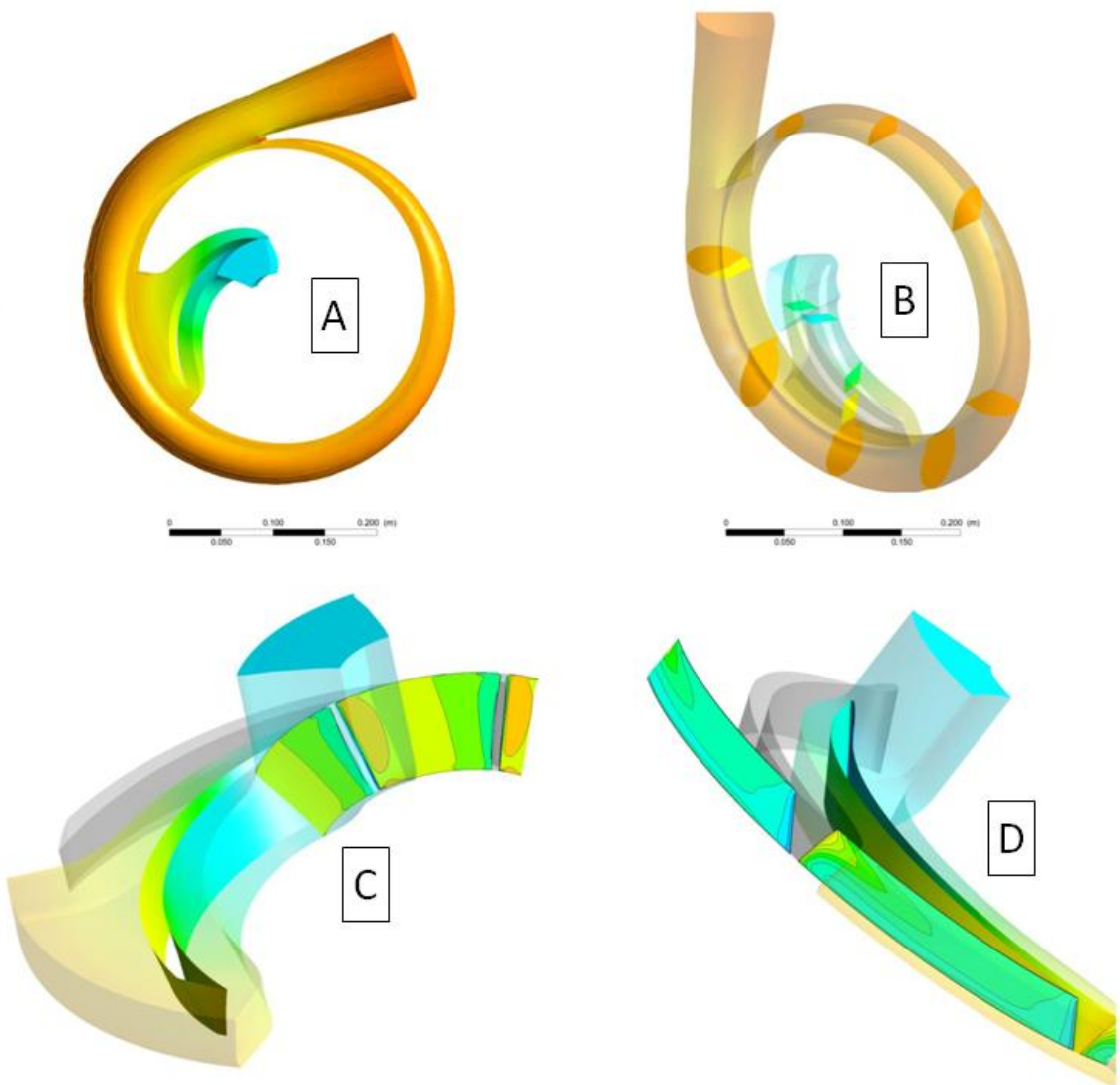


Figure 4.41 Hydrodyne pump pressure contours for A) Complete pump assembly B) At different sections C)At the blade leading edge D) Blade trailing edge.

4.7 Unsteady state simulation

4.7.1 Ansys setup for unsteady case

The unsteady case setup is very easy if the CFX is used for the pump simulation. For the sliding mesh approach moving domain has to be defined for the impeller domain. The counter-rotating domain with 2900 RPM was set for the impeller. The GGI interface is set for the impeller and volute connection. CFX provides hybrid initialization for the entire domain which can be used in the absence of initial data. For the current simulation steady state fully converged solution was used as an initial condition for unsteady setup. The CPU used had 32GB RAM and 8 cores, out of which 4 cores were used for parallel computing. The full unsteady simulation takes 14GB memory space with four cores for the coarse geometry mentioned below. For the LES mesh, 28 GB memory space is used. The one full rotation of the impeller creates the transient data of ~12 GB for coarse mesh and ~23 GB for LES mesh with CFX and thus requisite space should be kept in the hard disk during simulation. The simulation for the coarse mesh took 4 days and 20 hours for 9 complete rotations. The estimated time for LES simulation was 13 days. METIS partitioner which is used as default in ANSYS gives the memory allocation error. Thus Optimised RCB partitioner with memory allocation equal to 1.2 is used for first 100 iterations followed by METIS partitioner to avoid memory allocation errors. Any other choices for partitioning will give severe deviations from the solution and can result in segmentation errors.

4.7.2 Results and discussions

Geometry parameters used by Si et al.[47] are listed in Table 21. The geometry and the number of data points are used for current simulation. Monitor points used by Si et al.[47] are shown in Figure 2.27 Monitor points used for recording the pressure fluctuation data by Si et al.[47]. One fifth of the mesh used by the Si et al.[47] was used for the present simulation and initial calculations. SST- $\kappa-\omega$ model was used for simulation as SAS model used by Si et al.[47] requires fine mesh. $\kappa-\varepsilon$ model was giving erroneous results at some data points and thus was not used for the simulation. The pressure fluctuations are expressed in terms of coefficient of pressure C_p and the pulsation coefficient K_p for all the figures. C_p and K_p are given by Eq.4.2 and Eq.4.3 respectively.

$$C_p = \frac{p - p_{ref}}{0.5 \cdot \rho u_2^2} \quad (4.2)$$

$$K_p = \frac{\sqrt{(1/N) \sum_1^N (p_{node} - p_{mean})^2}}{p_{mean}} \quad (4.3)$$

The time step used for simulation is 5.7471×10^{-5} s which corresponds to 0.5° rotation of the impeller. The simulation was run for 6 complete rotations after which steady fluctuating data was obtained. The data was recorded for 3 more rotations of the impeller after 6 rotations were completed. The steady pressure fluctuation data for one complete rotation is given in Figure 4.42. The fluctuating data is then processed with FFT code (Ref. H.7) and converted in frequency domain from time domain. It can be observed from Figure 4.43 and Figure 4.46 that the maximum pressure is observed at blade pass frequency (BPF). Pulsation coefficients were compared with those reported by Si et al.[47] literature in Figure 4.44. Our simulation under-predicts the value, which can be because of the coarse mesh size used.

Table 21 Design details for the case simulated by Si et al.[47]

Design Specifications	Value
Flow rate $Q(m^3 / h)$	25
Head (m)	32
Rotation speed (rpm)	2900
Number of blades	6
Impeller diameter (mm)	165
Volute inlet diameter (mm)	176

Vorticity variation at different pump sections was also evaluated. Figure 4.45 shows contour of vorticity variation taken at mid-section of the pump. Vorticity contours are given for visualizing the recirculation regions in the pump near the blade and the volute exit. The recirculation was only dominant in the nozzle area near the wall and can be seen in Figure 4.45. The unsteady flow interactions with volute throat can be seen from Figure 4.47. The contours are plotted for every 15° rotation of the impeller.

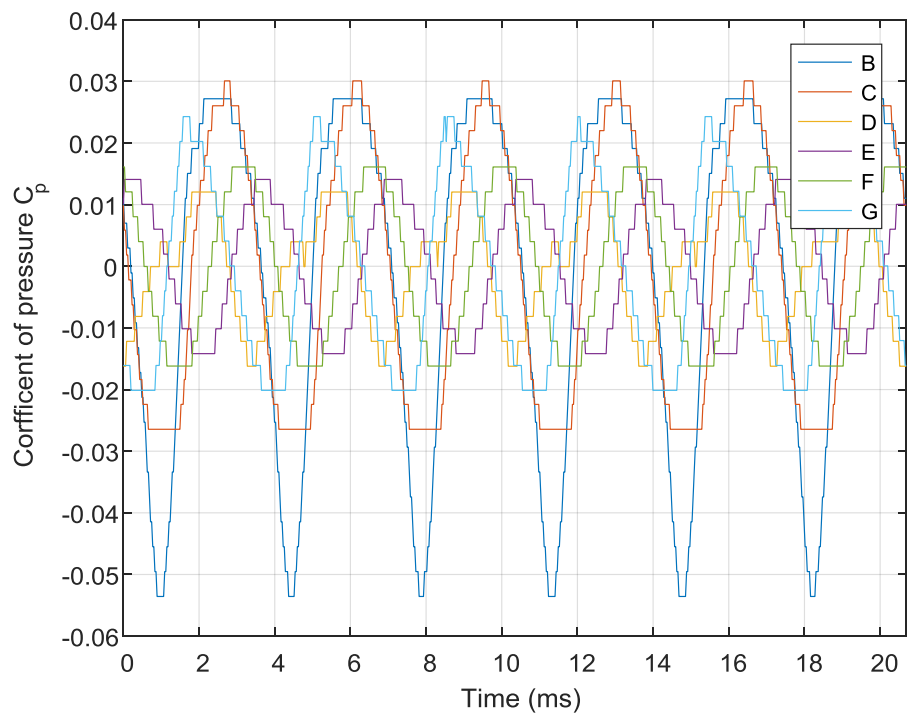


Figure 4.42 Pressure fluctuations for fully developed flow for one rotation of the impeller

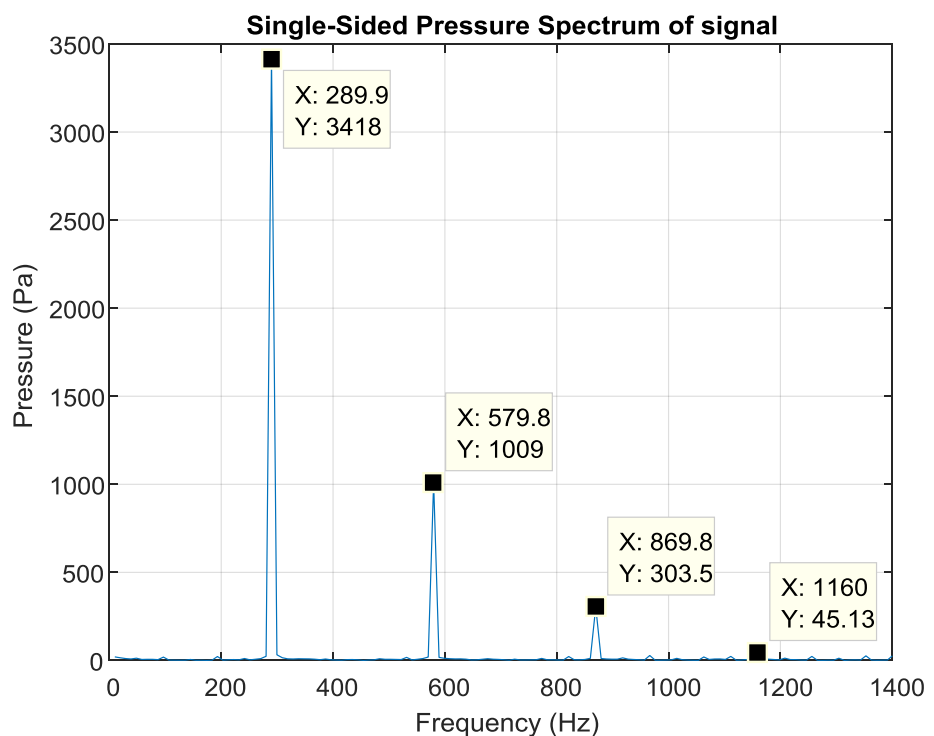


Figure 4.43 Pressure variation at throat point in frequency domain

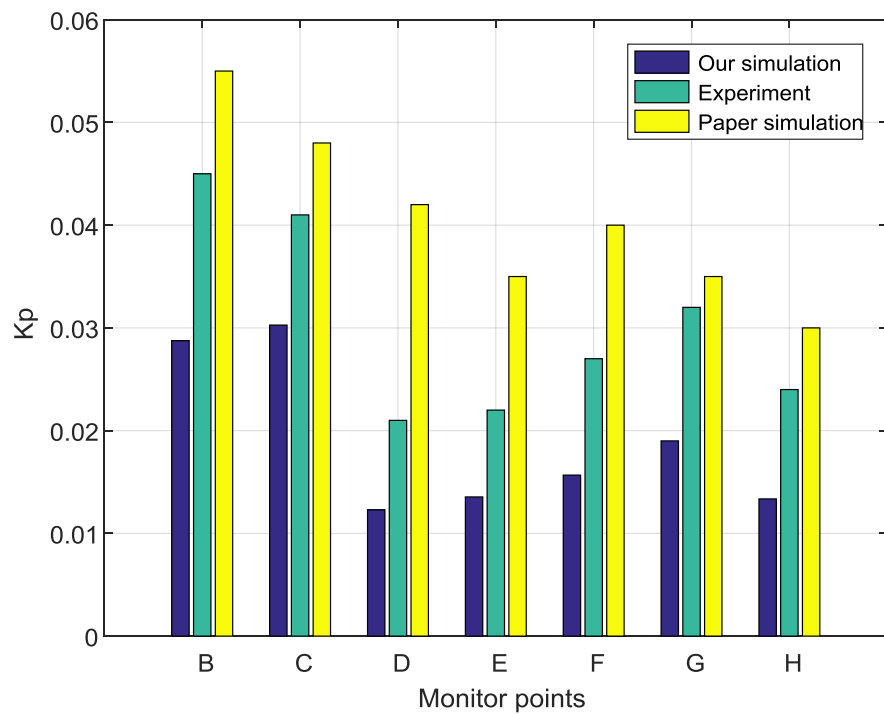


Figure 4.44 Coefficient of pulsation comparison with Si et al.[47] at different design points

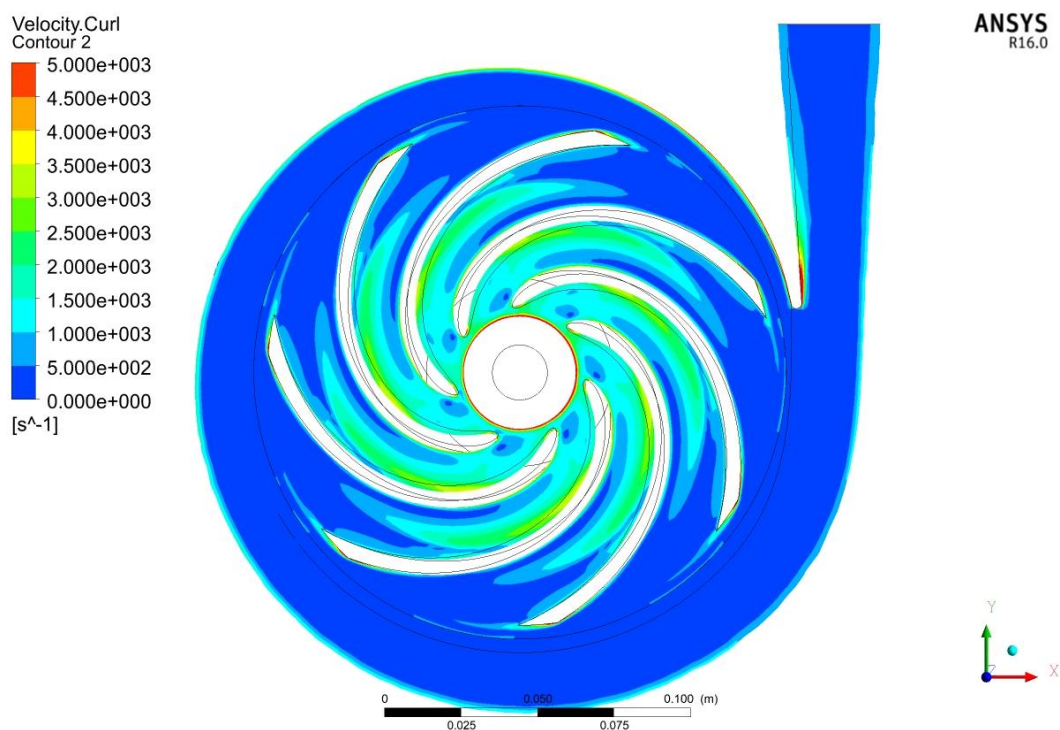


Figure 4.45 Vorticity variation for the simulated pump

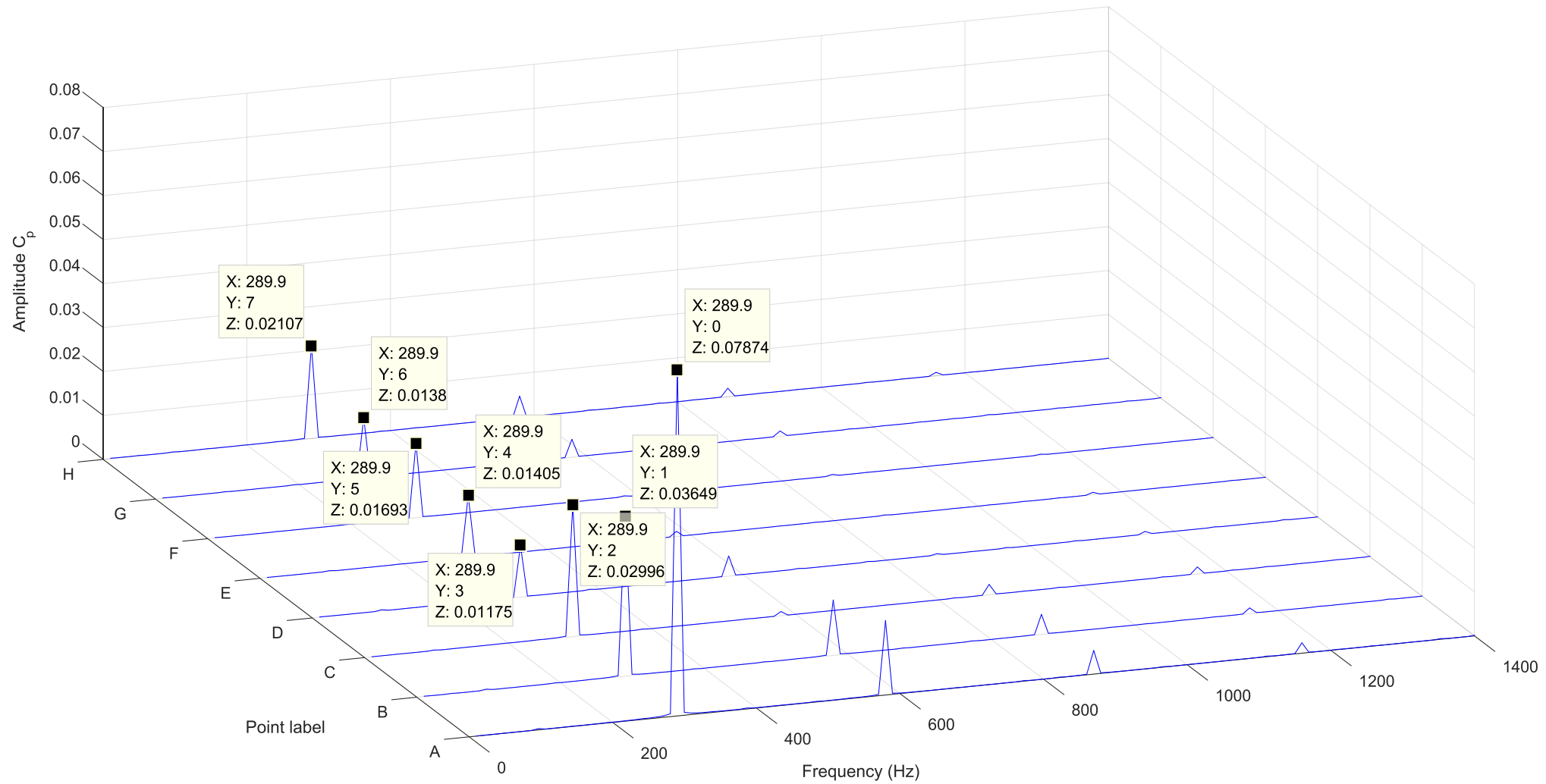


Figure 4.46 Pressure fluctuation at different monitor points plotted in frequency domain

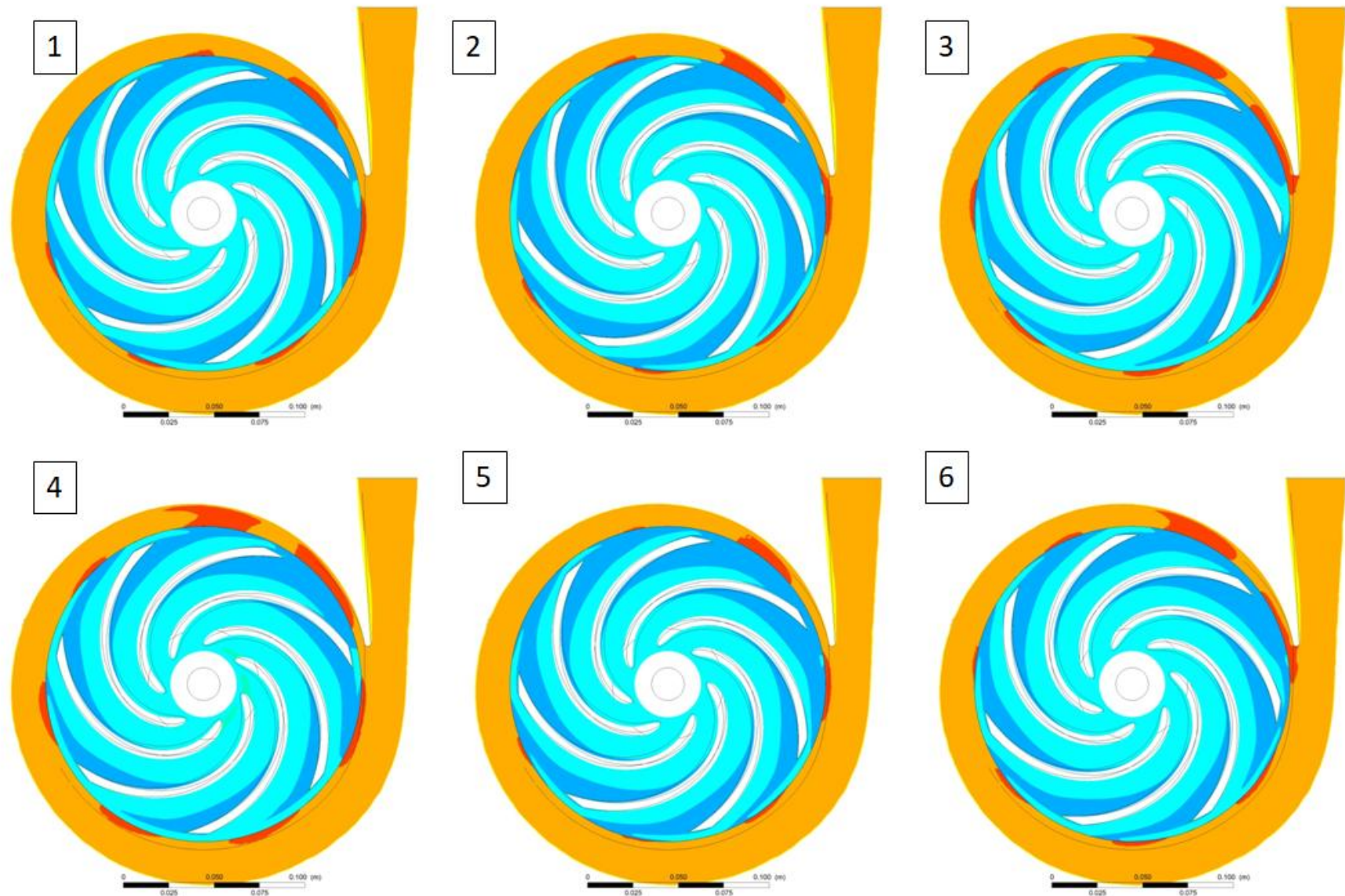


Figure 4.47 Pressure contours for different rotation angles of the impeller (Varying from 0 to 90° taken at 15° interval)

4.8 Acoustics simulations

Pressure distribution of the basic point sources was derived in the section 1.6. Some formulae for baffled piston and quadrapole sources were referred from Manik[6] and Howard[63]. COMSOL is used for simulation of acoustic mesh.

4.8.1 Basic sources

A MATLAB code (Ref. H.8) was referred (NIOT[64]) to confirm the pattern of far-field pressure distribution with theory. The generated pressure field can be seen in Figure 4.48.

4.8.2 Basic sound source simulation on COMSOL

Basic sources like monopole and dipole were compared in COMSOL with analytic solution. COMSOL provides analytic sources in frequency analysis of Acoustic module. As stated before, dipole is formed by two out of phase monopole sources of different intensity kept at some distance from each other. Acoustic simulation is done for a range of distance between two monopole sources shown in Figure 4.51. Far-field quantities are measured at a distance three times the wavelength of the sound ($\sim 1\text{m}$). A comparison of pressure and sound pressure level (SPL) is done with the analytical solution and the results are plotted in Figure 4.49 and Figure 4.50.

4.8.3 Multiple monopole sources

It was observed from simulation that the two monopole sources give dipole like structure. In centrifugal pump, dipole structure similar to Figure 4.48 is obtained. The only difference is one of the lobes of the dipole is bigger than that of the other. In order to reproduce such dipole pattern, four monopole sources are kept in a spherical domain as shown in Figure 4.52. The SPL radiation pattern can be seen in Figure 4.53

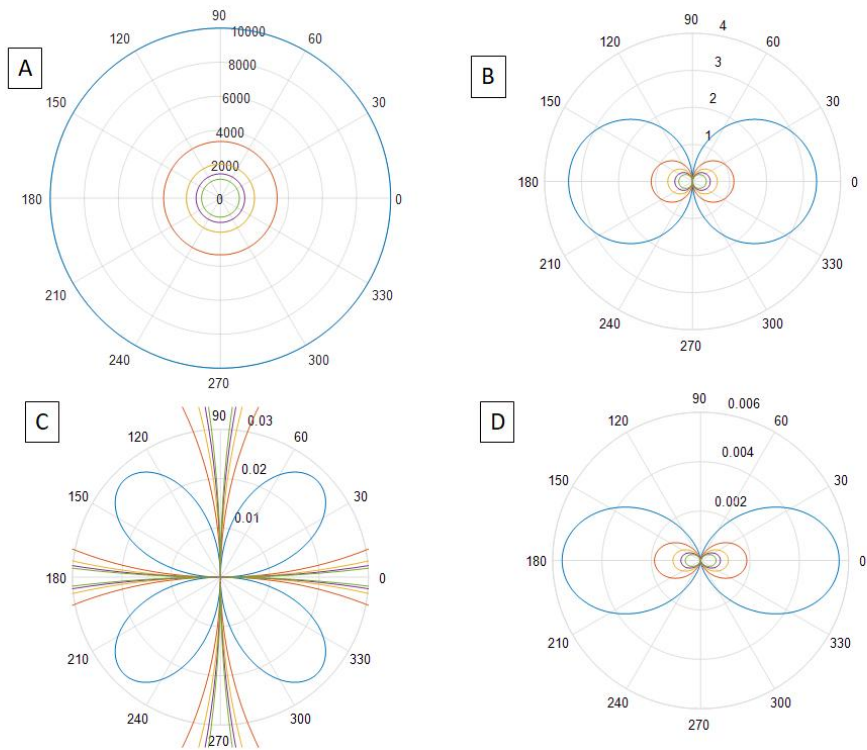


Figure 4.48 Far-field pressure distribution A. Monopole B. Dipole C. Quadrupole D. Linear Quadrupole

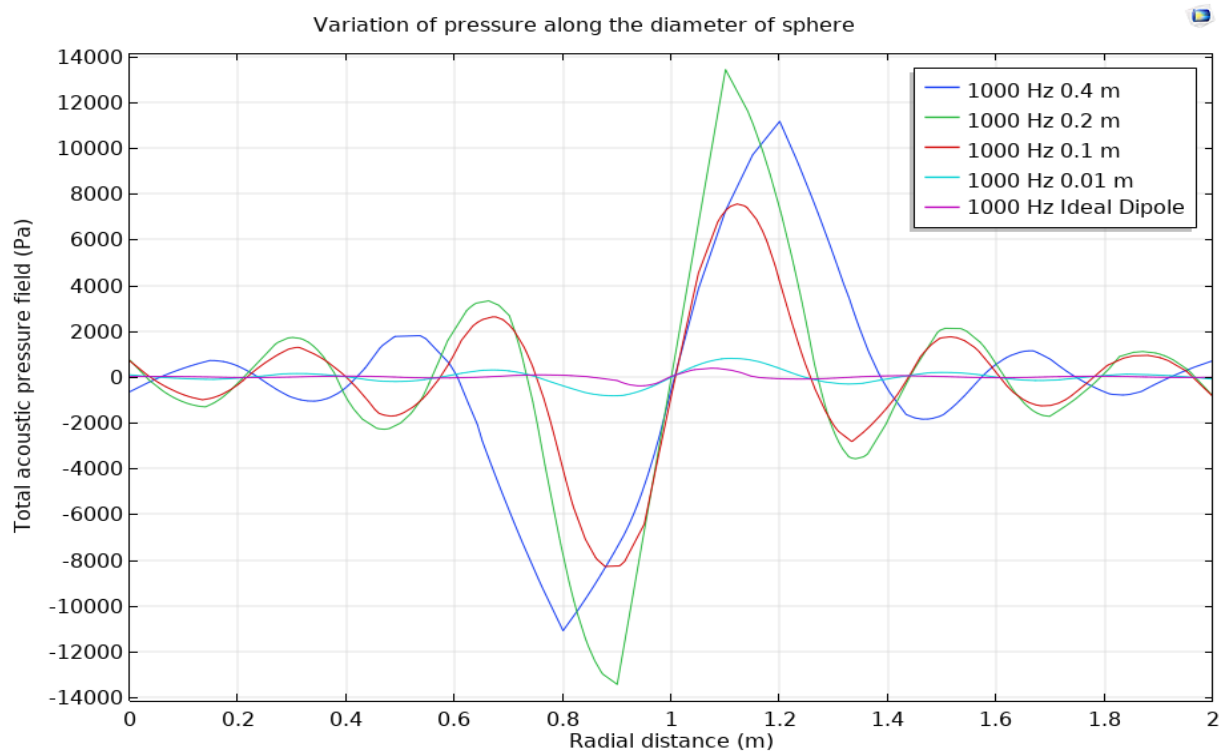


Figure 4.49 Comparison of far-field pressure on the sphere at a distance = 1m from the source

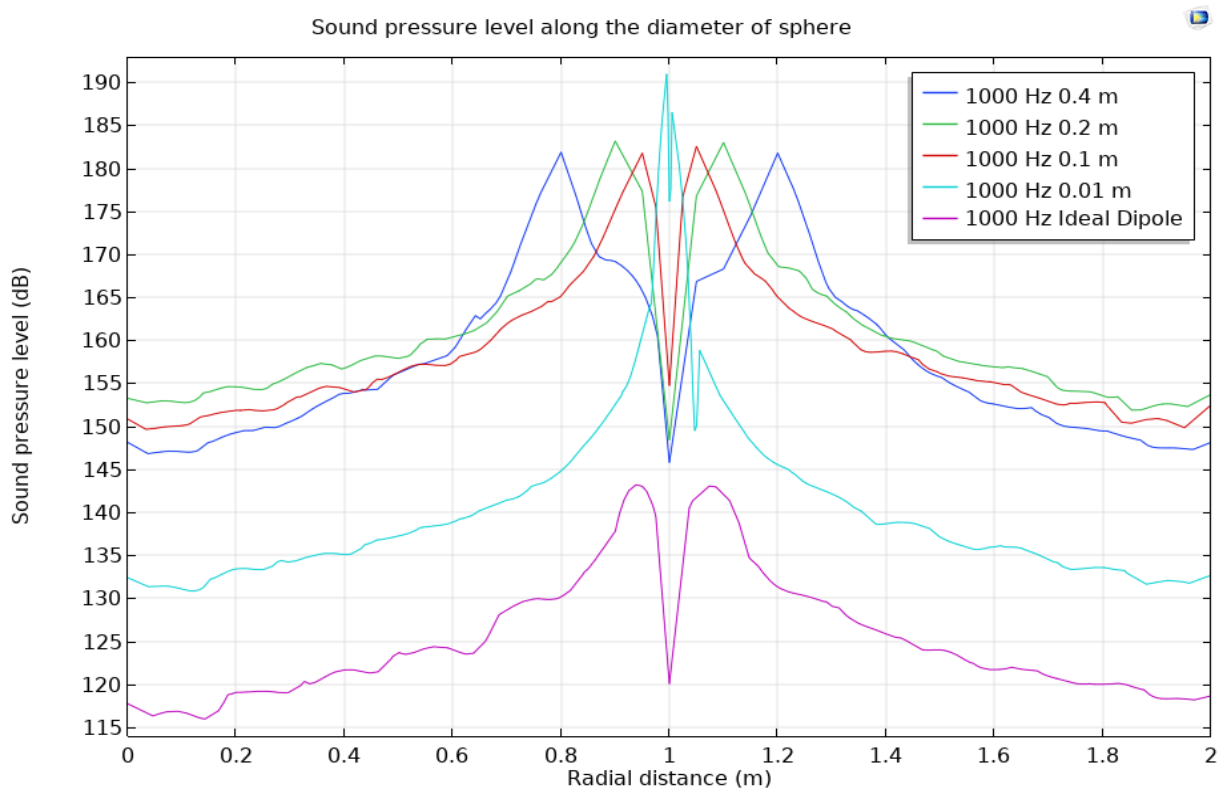


Figure 4.50 Comparison of far-field SPL on the sphere at a distance = 1m from the source

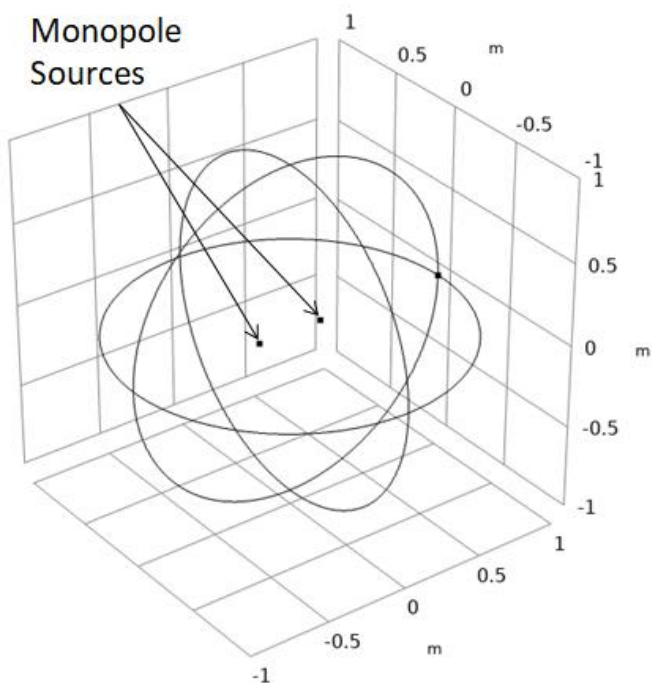


Figure 4.51 Geometry details for the dipole simulation in COMSOL

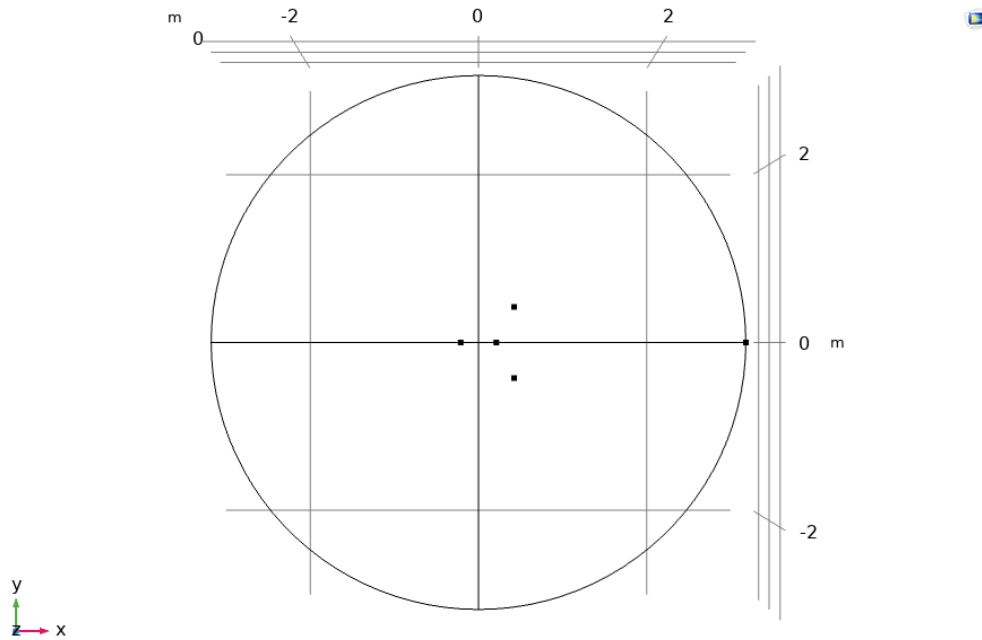


Figure 4.52 Multiple monopole sources simulated in COMSOL

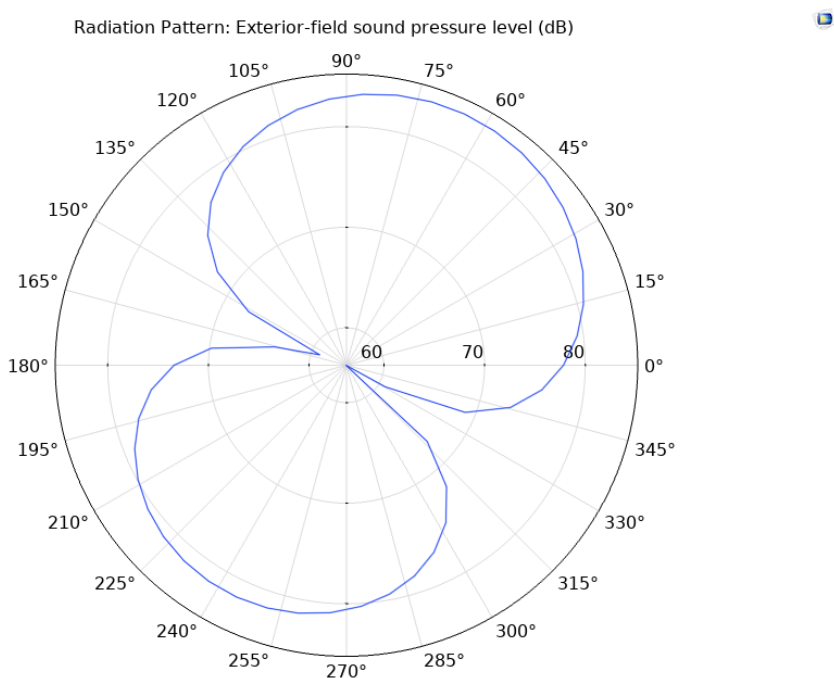


Figure 4.53 Sound pressure level radiation pattern for multiple monopole sources

4.8.4 Sound radiation by baffled piston

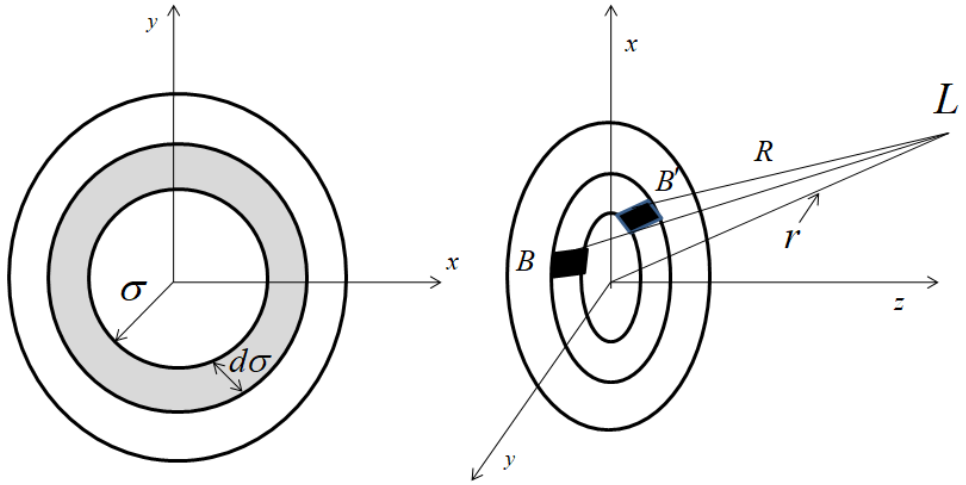


Figure 4.54 Schematic diagram for a baffled piston surface

A baffled surface is a surface which extends to the infinity and only the small portion of the surface is vibrating. The circular piston can be imagined as the series of the annular rings acting as sound sources (Ref. Figure 4.54). The solution for the pressure field can be obtained by integrating pressure solution for variable ring (Ref. Appendix F) with average radius σ and the ring thickness of $d\sigma$. The pressure field for the baffled piston at any location R can be given by Eq.4.5. The far-field solution of the annular ring is used to evaluate the far-field solution for the piston. The Eq.4.5 is integrated with variable radius σ to obtain the solution Eq.4.6.

$$R = \sqrt{r^2 + \sigma^2 - 2r\sigma \sin \theta \cos \psi} \quad (4.4)$$

$$p = \frac{jk\rho_o c_o u_o}{\pi} \cdot e^{j\omega t} \cdot \int_0^\pi d\psi \int_0^a \sigma \frac{e^{-jkR}}{R} d\sigma \quad (4.5)$$

$$p = \frac{jk a \rho_o c_o u_o}{r} \cdot e^{j(\omega t - kr)} \cdot \frac{J_1(ka \sin \theta)}{\sin \theta} \quad (4.6)$$

2D axis-symmetric geometry is made in COMSOL for the simulation. Velocity input $u_{piston} = u_0 e^{j\omega t}$ is given to the piston surface. Frequency analysis is done for different frequencies ranging from 10 to 16,000 Hz. Analytical solution for SPL and pressure is compared for the baffled piston. Details of the geometry can be seen in Figure 4.55.

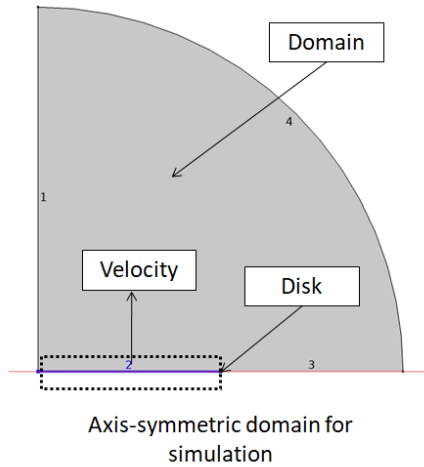


Figure 4.55 Baffled piston geometry created in COMSOL

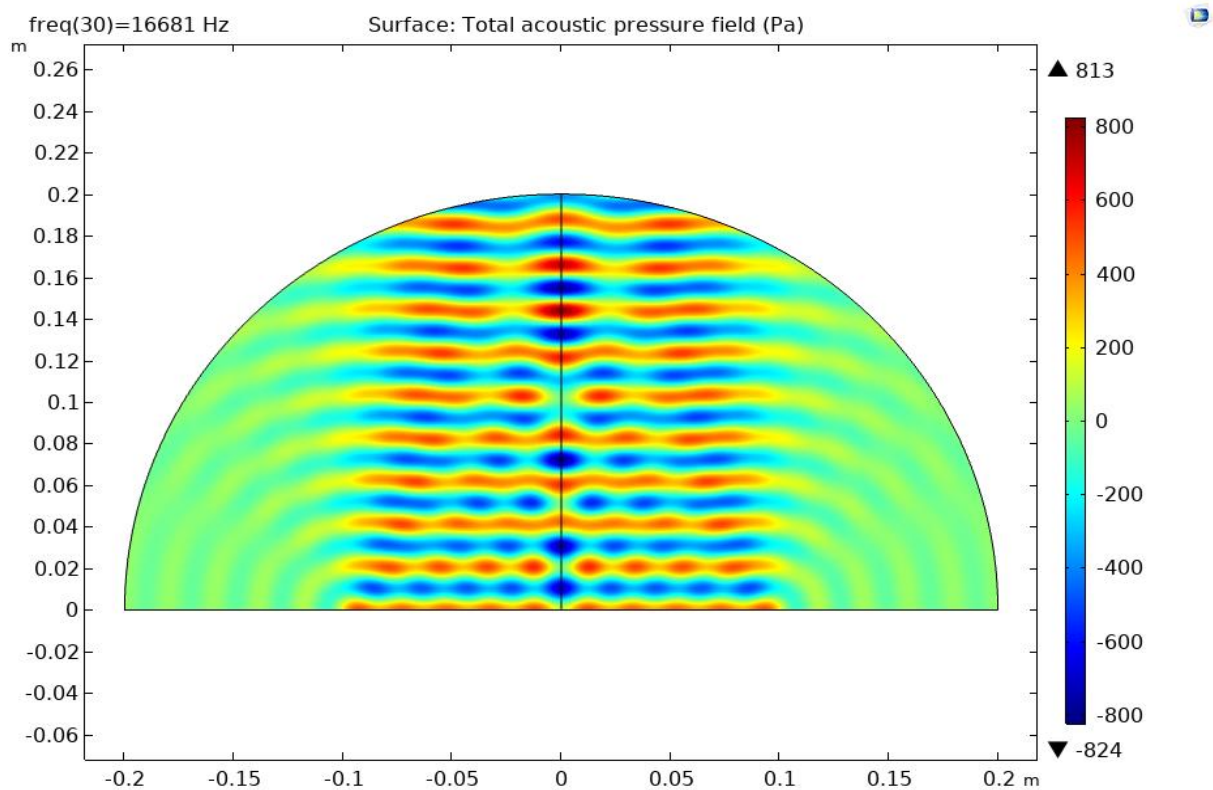


Figure 4.56 Acoustic pressure contours due to vibrating baffled piston

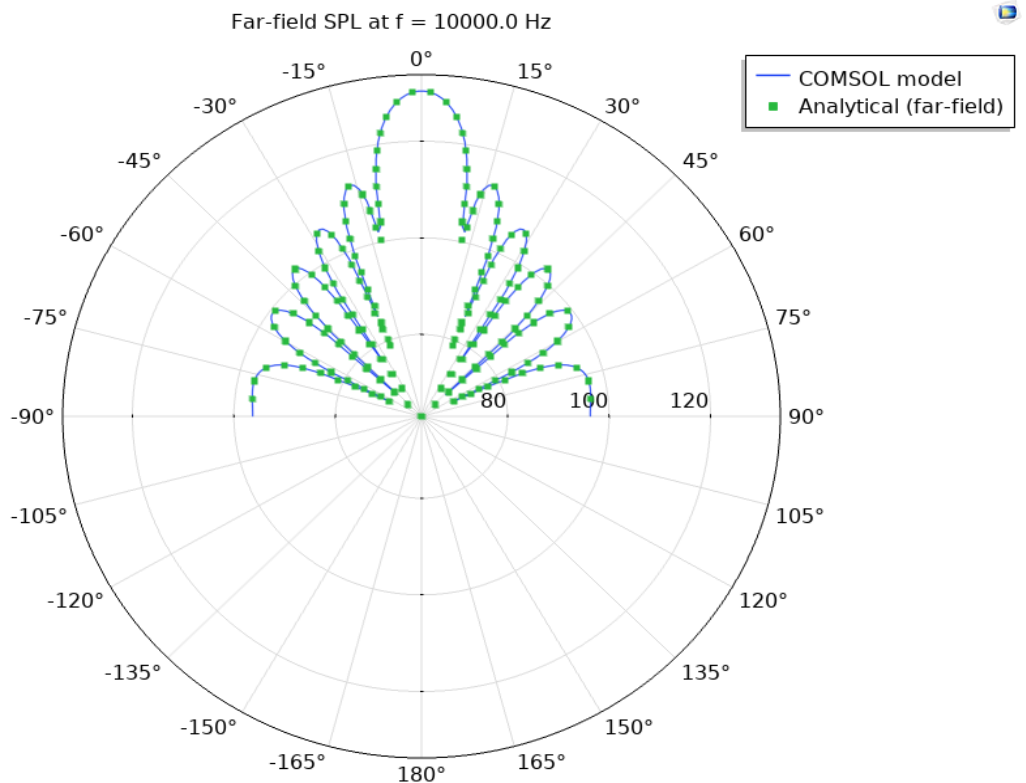


Figure 4.57 Sound pressure level comparison for COMSOL model with Analytic solution

Figure 4.56 shows the pressure variation by the baffled piston. The contraction and the rarefactions in air due to vibrating source can be visualized from the pressure contours. Figure 4.57 shows the directivity pattern of the sound pressure level measured at the distance three times the sound wavelength. The exercise was conducted to give the custom velocity distribution as boundary condition at the Baffle plate. The CSV file was used for the velocity input. The similar approach has to be followed for transferring deformation and surface velocity data from recorded on the structural mesh in ANSYS Harmonic analysis to the COMSOL Acoustics.

Chapter 5

Conclusion and Future scope

1. Owing to the unavailability of the computational resources due to pandemic (COVID 19), structural simulation and acoustic predictions for the centrifugal pump were not carried out in the current study. The flow simulation showed that, the pressure fluctuations are highest at volute throat point for the blade pass frequency (290 Hz for 6 blades at 1450 rpm). (See Figure 4.46) From the simulation of a simple piston, it can be concluded that the acoustic sound pressure level is maximum in the direction of the noise source (See Figure 4.57) which confirms the claims from literature review (Guo et al.[53]). It can be concluded that for proper design of the volute tongue and the impeller blades, unsteady flow behaviour has to be studied.

2. Different algorithms are written for the design of the impeller and the volute casing. It can be concluded that prediction methods like slip-loss analysis and Throughflow analysis can be used for initial optimization of the pump before running full scale 3D simulation as the predicted values give good estimation of the pump characteristics. (See Figure 4.22 and Figure 4.25) The effect of various parameters like NPSH, blade width,

blade angles on pump characteristics was reviewed and the optimized design is given in the dissertation. From comparison with the commercial code and the real-life pump, one can use the design method of the dissertation for generating the Impeller and volute design from if no known data is present.

3. If the power requirement for the pump is known or if it is calculated from head and discharge requirement of the application, the induction motor can be designed from the empirical approach presented in the dissertation. The design approach is used for predicting the size of the rotor and stator in actual canned motor pump. If the size is known, the minimum flow rate for annular gap can be estimated. It was observed from simulation that the presence of Taylor vortices enhanced the heat transfer in the annular gap. (See Figure 4.13) By knowing the flow structure in the annular gap, rotor surface can be indented with small spots for further enhancing the heat transfer.

4. It is known from the literature review that, the dipole variation for the noise is observed in the pump. It was observed from the simulation of the basic sound sources that the two monopoles give dipole variation with different SPL if the distance between the sources is varied. (See Figure 4.49) If the full acoustic simulation is carried out, different monopole sources can be kept at the volute tongue line to get the same effect as that of the simulation. The analysis will help for designing the optimum volute tongue profile for reducing the noise.

Appendix A

Design of Single Stage Centrifugal Pump Impeller

A.1 Design Specifications

Flow rate Q	: 16 litre per second
Head H	: 13.8 m
Rotation speed N	: 1800 rpm
Density of Liquid	: 1000

Assumptions :

- Seven blades are assumed for calculation.
- The leakage through balance hole is considered zero. Constant blade thickness is assumed.
- Flow is fully developed at the blade inlet
- Thickness of the blade is constant

A.2 Basic Calculations

Flow rate conversion Q	16 litre per second	$57.6 \text{ m}^3 / \text{hr}$ or $16 \times 10^{-3} \text{ m}^3 / \text{s}$ (m^3 / s is used for N_s)
Hydraulic Efficiency η_h	Ref. Eq.3.1	88.96 %
Volumetric Efficiency η_v	Ref. Eq.3.4	96.87 %
Overall Efficiency η_o	Ref. Eq.3.2	77.55 %
Theoretical Flow rate	$Q_{th} = \frac{Q}{\eta_v}$	16.52 litre per second
Specific speed N_s	$N_s = \frac{N \sqrt[3]{Q}}{H^{3/4}}$ $N : RPM$ $Q : \text{m}^3 / \text{s}$ $H : m$	32.31
Suction pipe diameter D_{1e}	$D_{1e} = 5.14 \cdot \sqrt[3]{\frac{Q}{N}}$ $N : RPM$ $Q : \text{m}^3 / \text{s}$	107.6 mm
Inlet blade diameter D_1	$D_1 = 1.005 D_{1e}$	107.7 mm
Shaft diameter	$D_s = \sqrt[3]{\frac{16 \cdot \text{Torque}}{\pi \cdot \text{Stress}}}$	17.24 mm
Hub diameter	$D_h = 1.5 \cdot D_s$	25.85 mm
Pressure coefficient ψ	$\psi = 1.25 \cdot \exp(-0.3 \cdot N_s / 100)$	1.0378
Inlet blade diameter D_2	$\frac{60}{\pi N} \cdot \sqrt{\frac{2gH}{\psi}}$	171.39 mm
Blade thickness δ	$\delta = 0.03 \cdot D_2$	5.14 mm

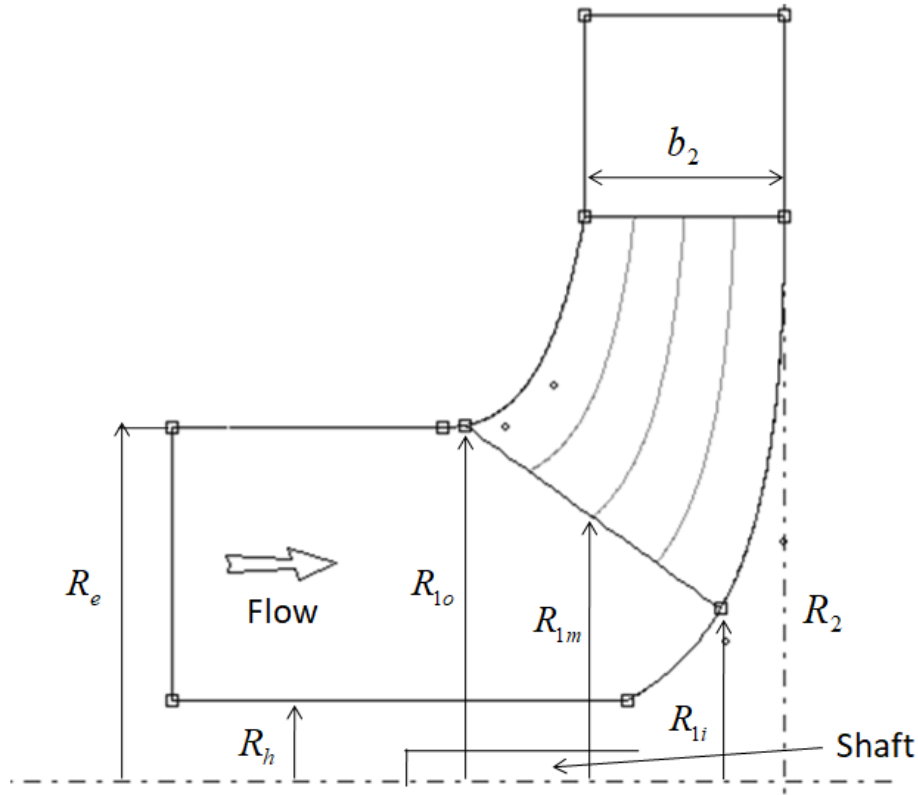


Figure 1 Geometry details for the designed impeller.

A.3 Inlet velocity triangle

The flow velocity C_{m1} before the entry to the blade is assumed to be equal to the velocity C_0 at the eye of the pump by neglecting the bend and the friction losses. The blockage factor K_1 at the inlet is not known thus has to be assumed. For initial guess of blockage factor, inlet blade angle is β_i is calculated from Eq.00. Since all the values required for the calculation of the blockage factor are known, new value of K_1 can be evaluated. With new blockage factor, the inlet velocity triangle is recalculated to get new blockage factor. This way K_1 is calculated for successive iterations (Refer Inlet Iteration 0) till the converged value is obtained. The converged value of K_1 is used for calculation of final dimensions at the inlet of the impeller blade. All the velocities are and the blade angles are calculated for the outer streamline. The blade angle β_i at the outer streamline is then interpolated by using Eq.1 for other streamlines.

$$\beta_1 = \tan^{-1} \left(\left(\frac{2.9}{D_1} \right)^3 \cdot \frac{Q}{Nk_h} \right) \quad (0)$$

$$\tan \beta_1(r) = \frac{r_{lo}}{r} \tan \beta_{lo} \quad (1)$$

Inlet Iteration 0

$$k_h = 1 - \left(\frac{D_h}{D_1} \right)^2 = 0.9423$$

$$\beta_1 = \tan^{-1} \left(\left(\frac{2.9}{D_1} \right)^3 \cdot \frac{Q}{Nk_h} \right) = 11^\circ$$

$$K_1 = \left\{ 1 - \frac{z\delta_1}{\pi D_1 \sin(\beta_1)} \right\}^{-1} = 2.2607$$

$$\beta'_1 = \tan^{-1} \left(\frac{K_1 \cdot C_{m1}}{u_1 - C_{u1}} \right) = 23.018^\circ$$

Velocity Triangle at Impeller inlet and at Outer streamline	Equation	Final Dimension
Theoretical discharge	$Q_{th} = \frac{Q}{\eta_v}$	16.52 litre per second
Axial velocity at the impeller eye	$C_0 = \frac{4Q_{th}}{\pi D_e^2}$	1.9 m/s
Blade speed	$u_1 = \frac{\pi \cdot D_1 \cdot N}{60}$	10.14 m/s
Circumferential component of absolute velocity	$C_{u1} = \frac{C_{m1}}{\tan(\alpha_1)}$	0 m/s
Relative velocity	$W_1 = \sqrt{C_{m1}^2 + (u_1 - C_{u1})^2}$	10.59 m/s
Flow angle with blockage	$\beta_1 = \arctan \left(\frac{K_1 \cdot C_{m1}}{u_1 - C_{u1}} \right)$	18.2055°
Inlet blockage multiplication factor	$K_1 = \left\{ 1 - \frac{z\delta_1}{\pi D_1 \sin(\beta_1)} \right\}^{-1}$	1.59

A.4 Outlet dimensions

For calculation of the outlet velocity triangle and the blade blockage factor K_2 , the outlet blade angle β_2 has to be assumed. Since the backward facing vanes are designed, an iterative loop is written which calculates all the outlet velocity triangle quantities for different β_2 values. The modified manometric head and the modified outlet blade velocity u_2 due to slip factor p are also included in the iterative calculations. When the slip head matches with design head, the loop is stopped and the outlet velocity triangle is calculated.

Basic calculations for initial outlet angle assumption

Pressure coefficient ψ	$\psi = 1.25 \cdot \exp(-0.3 \cdot N_s / 100)$	1.0378
Outlet blade diameter D_2	$\frac{60}{\pi N} \cdot \sqrt{\frac{2gH}{\psi}}$	171.39 mm
Dimensionless outlet width $B_2^* = \frac{B_2}{D_2}$	Ref Eq.3.26	0.0936
Outlet width B_2	$B_2 = B_2^* \cdot D_2$	17.9 mm
Inlet Area A_1	$A_1 = \pi D_1 B_1$	0.0138 mm ²
Outlet Area A_2	$A_2 = \pi D_2 B_2$	0.0086 mm ²
Outlet blade velocity u_2	$u_2 = \frac{\pi \cdot D_2 \cdot N}{60}$	16.1526 m/s
Stability Factor	$K_{stab} = \frac{u_2 - u_1}{C_{u2}}$	$K_{stab} = 1$ is assumed
Outlet tangential velocity C_{u2}	$C_{u2} = \frac{u_2 - u_1}{K_{stab}}$	6 m/s
Flow velocity at outlet C_{m2}	$C_{m2} = \frac{Q}{A_2}$	1.91 m/s
Relative velocity	$W_2 = \sqrt{C_{m2}^2 + (u_2 - C_{u2})^2}$	10.33 m/s
Outlet blade angle β_2	$\beta_2 = \sin^{-1}\left(\frac{C_{m2}}{W_2}\right)$	10.716°
Outlet blockage multiplication factor	$K_2 = \left\{1 - \frac{z\delta_2}{\pi D_2 \sin(\beta_2)}\right\}^{-1}$	1.5649

A.5 Slip factor and Head verification

There are various models given in Srinivasan[24] and Gülich[5] which are used to predict the value of the slip factor ‘p’. Slip factor calculation is done with Gülich[5] formula for the current calculation and it uses following empirical relations defined in Gülich[5].

$$\varepsilon_{\text{lim}} = \exp \left\{ -\frac{8.16 \sin \beta_2}{z} \right\}$$

$$K_w = 1 - \left(\frac{(D_{1m} / D_2) - \varepsilon_{\text{lim}}}{1 - \varepsilon_{\text{lim}}} \right)^3; \text{ for } (D_{1m} / D_2) > \varepsilon_{\text{lim}}$$

$$K_w = 1; \text{ for } (D_{1m} / D_2) < \varepsilon_{\text{lim}}$$

$$p = 0.98 \cdot \left(1 - \frac{\sqrt{\sin \beta_2}}{z^{0.7}} \right) \cdot K_w$$

Once the slip factor ‘p’ is determined, it can be used for predicting the outlet head. The outlet head is dependent on outlet blade angle β_2 and it is given by Eq.2. If the calculated verification head does not match with design head, the outlet blade angle is increased and the loop is iterated (Refer Outlet Iteration 0) till the verification head is converged to design head.

$$H_v = \frac{\eta_h u_2^2}{g} \cdot \left\{ p - \frac{Q}{A_2 u_2 \tan \beta_2} \left[K_2 - \frac{A_2 (D_{1m} / D_2) \tan \beta_2}{A_1 \tan \alpha_1} \right] \right\} \quad (2)$$

Initial values

$$p = 0.872$$

$$H_v = 19.5949 \text{ m}$$

Outlet Iteration 0

$$\beta'_2 = \beta_2 + \xi_{increment}$$

$$H_v = \frac{\eta_h u_2^2}{g} \cdot \left\{ p - \frac{Q}{A_2 u_2 \tan \beta_2} \left[K_2 - \frac{A_2 (D_{1m}/D_2) \tan \beta_2}{A_1 \tan \alpha_1} \right] \right\}$$

A.6 Outlet velocity triangle

For calculation of the outlet velocity triangle and the blade blockage factor K_2 , the outlet blade angle β_2 has to be known.

Velocity Triangle at Impeller outlet	Equations	Final Dimension
Outlet blade angle	β_2	13.1
Relative velocity ratio	$\frac{W_{1m}}{W_{2m}}$	1 is assumed
Flow velocity at trailing edge	$C_{m2} = W_2 \cdot \sin(\beta_2)$	1.71 m/s
Outlet blockage multiplication factor	$K_2 = \left\{ 1 - \frac{z \delta_2}{\pi D_2 \sin(\beta_2)} \right\}^{-1}$	1.42
Slip factor by Gülich[5]	$p = 0.98 \cdot \left(1 - \frac{\sqrt{\sin \beta_2}}{z^{0.7}} \right) \cdot K_w$	0.8605
Outlet tangential velocity C_{u2}	$C_{u2} = \frac{u_2 - u_1}{K_{stab}}$	9.68 m/s
Relative velocity	$W_2 = \sqrt{C_{m2}^2 + (u_2 - C_{u2})^2}$	7.56 m/s

A.7 Complete final dimensions

Overall Performance			
N_s	32.31	Power	2.88 kW
N_{ss}	3.1623	NPSH _r	1.5394 m

Outlet parameters				
D_2	B_2	β_2	α_2	C_{m2}
171.4 mm	17.91 mm	13.109°	10.034°	1.7134 m/s

Inlet parameters				
C_{m1}	D_s	D_h	B_1	δ
3.03 m/s	17.24 mm	25.85 mm	40.91 mm	5.14 mm
Streamline location	Diameter in mm	W in m/s	U in m/s	β_1
Outer	107.7	9.8108	10.147	18.2055°
Middle	80.7	9.71	7.610	23.68°
Inner	53.8	9.71	5.0736	33.34°

Appendix B

Design of volute

B.1 Design Specifications

Flow rate Q	: 16 litre per second
Head H	: 13.8 m
Rotation speed N	: 1800 rpm
Density of Liquid	: 1000

Volute parameter	Equations	Final Dimension
Throat diameter D_3	Eq.3.36	190.5 mm
Volute inlet width b_3	$b_3 = 1.25 \cdot b_2$	23.6 mm
Volute thickness	From Table	5 mm
Volute throat angle	From outlet velocity triangle	10.034°
Velocity coefficient K_3	From Stepanoff[25] data	0.6589
Volute velocity C_{av}	$C_{av} = K_3 \sqrt{2gH}$	10.84 m/s
Area at throat A_v	$A_v = \frac{Q}{C_{av}}$	1523.5 mm ²

B.2 Volute shaping

Areas and radial distances for various cross-sections of the volute casing are given below
(Ref. Figure 3.16 for notations)

Sr.	Area of cross section A_{vi} (mm ²)	Maximum distance ρ_{vi} (mm)
1	190.43	22.79
2	380.86	32.21
3	571.3	39.45
4	761.8	45.56
5	952.15	50.94
6	1142	55.79
7	1333	60.26
8	1523.5	64.43

Appendix C

First cell height estimation for turbulent flow

C.1 Y plus calculation

The first cell height estimation is important if the boundary layer formation, turbulence, and circulation is present in the flow. The cell height is estimated using a dimensionless number called y^+ . For obtaining the precise results through the simulation the value of y^+ should be equal to one. The y^+ formula is given by the Eq.3. The friction velocity u_* given in the Eq.3 is calculated from the shear stress τ_w on the boundary wall and is given by the Eq.4. The shear stress value is not known at the start of the simulation and thus has to be estimated by the empirical relation. The Reynolds number for the flow is calculated for estimating the shear stress.

$$Y^+ = \frac{u_* y}{\nu} \quad (3)$$

$$u_* = \sqrt{\frac{\tau_w}{\rho}} \quad (4)$$

C.2 Shear stress calculation

The estimation of the shear stress is done by using the skin friction coefficient C_f by using the Eq.5. The flat plate solution by Schlichting was used for initial estimate of the skin friction coefficient and it is given by Eq.6. The equation is valid for the Reynolds number Re less than 10^9 . The simulation is then carried out and shear stress on the surface is calculated at the end of the simulation. For the TCPF cases flat plate solution gave correct estimates. For the pump simulations, the maximum difference of 80% in value of y^+ was present. Thus for the centrifugal pump mesh, default y^+ calculation function of TurboGrid was used which gave close estimate of the y^+ .

$$\tau_w = \frac{1}{2} C_f \rho U^2 \quad (5)$$

$$C_f = [2 \log_{10}(Re) - 0.65]^{-2.3} \quad (6)$$

Appendix D

Bezier curves

D.1 Bezier polynomial

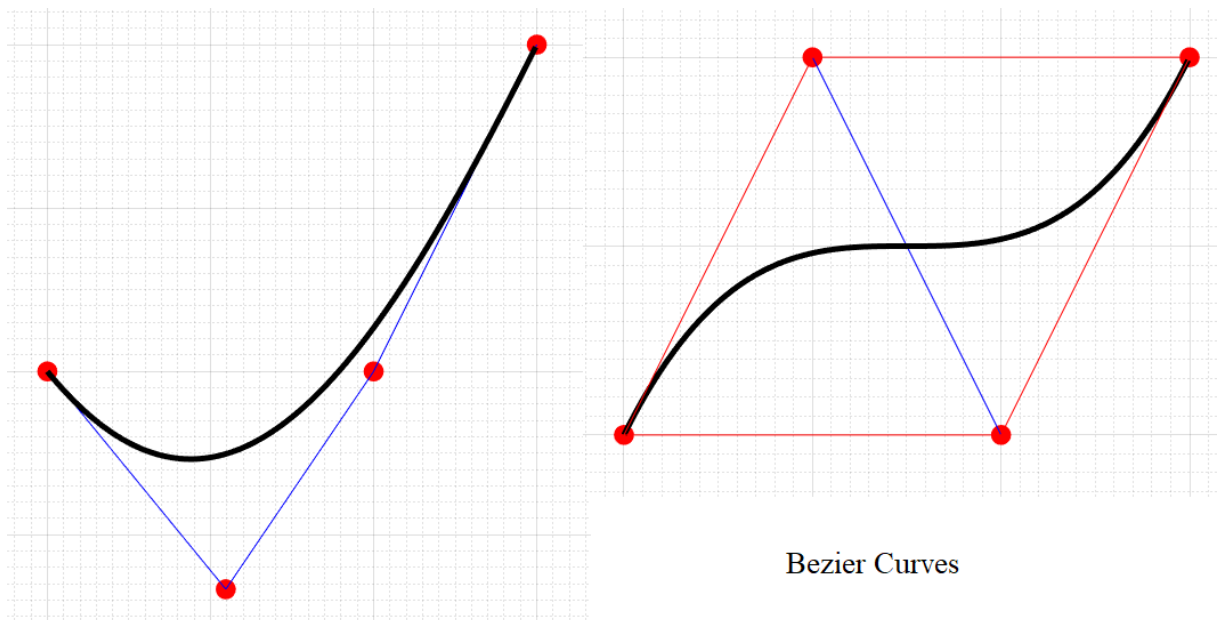


Figure 2 Bezier curves for different location of the control points

Bezier function is the polynomial expressed in terms of a parameter. The general form of Bezier function B expressed in terms of parameter u is given by Eq.7. Parameter u varies from zero to one and traces the curve. Control points $P_0 - P_n$ are required for deciding the shape and order of the polynomial. By changing the location of the control points, different shapes can be generated (Ref. Figure 2). The code published by Mugnaini[65] can be used for visualizing the effect of control points on the shape of Bezier curve.

$$B = {}_0^n C \cdot (1-u)^n \cdot P_0 + {}_1^n C \cdot (1-u)^{n-1} \cdot u \cdot P_1 + \dots$$

$$\dots + {}_{n-1}^n C \cdot (1-u)^1 \cdot u^{n-1} \cdot P_{n-1} + {}_n^n C \cdot u^n \cdot P_n \quad (7)$$

$$0 < u < 1$$

Appendix E

Numerical validation of laminar plane Couette and Poiseuille flow

E.1 Couette flow

Couette flow is the flow in the space between the two surfaces, one of which is moving relative to the other. The flow is driven by the shear force exerted by the moving surface. Figure 3 shows the schematic of the Couette flow.

E.1.1 Numerical simulation for laminar flow

Finite volume method is used for solving the plane Couette flow problem. Water is used as a working fluid. The plates are assumed to have infinite length. The gap between the plates is 5 mm and the length of the domain is 0.3 m. The comparison between numerical and analytic solution is shown in the Figure 4.

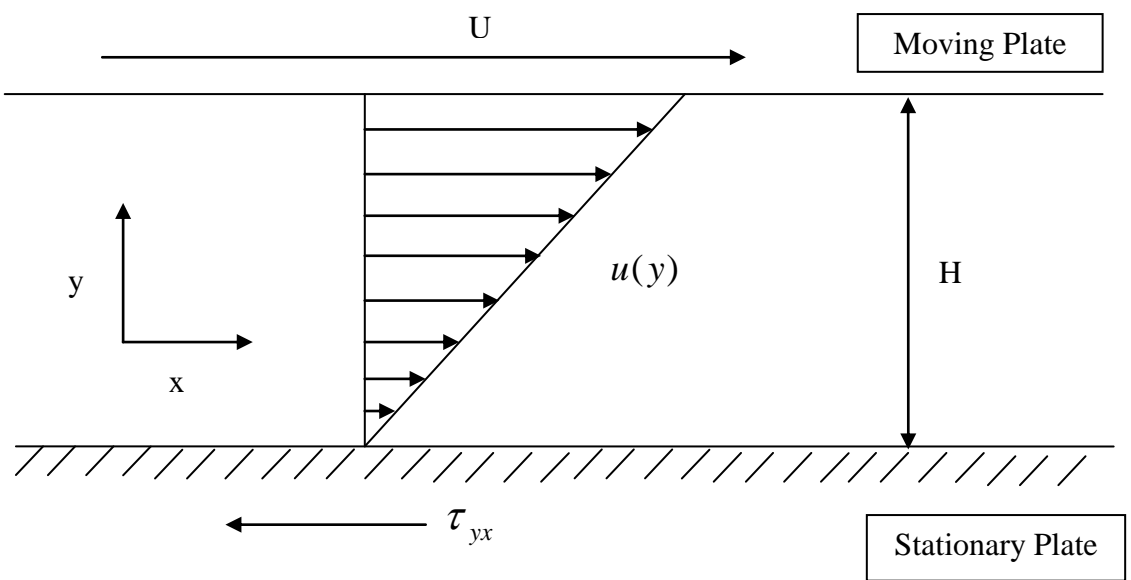


Figure 3 Couette Flow through two parallel plates

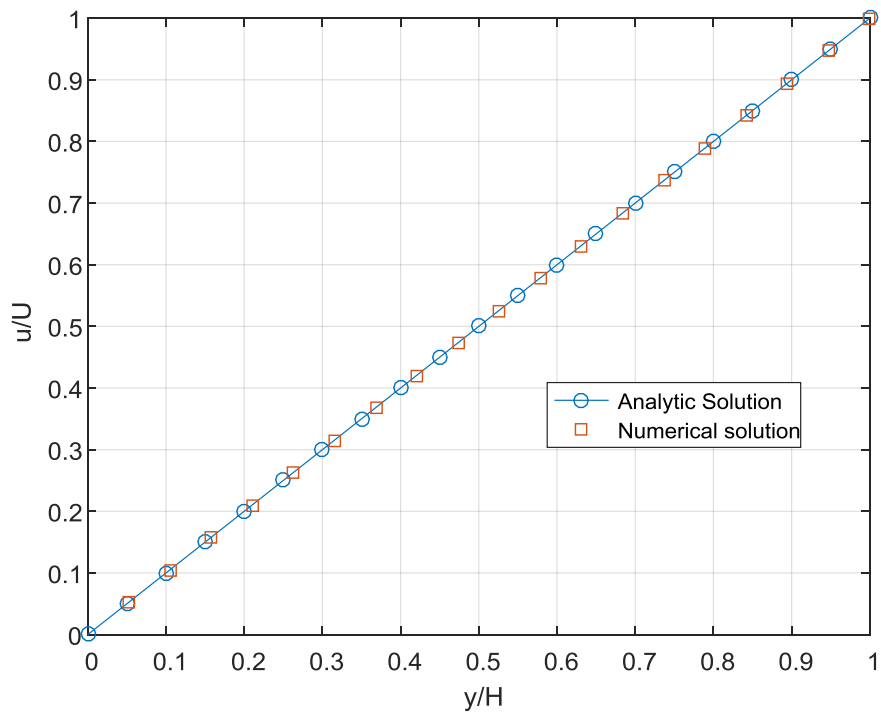


Figure 4 Comparison of Numerical and Analytic solution

E.1.2 Boundary conditions

The infinite plate assumption is achieved by defining the translational periodic boundary at the inlet and the outlet. By defining translational periodic boundary, the need for defining fully developed velocity profile is eliminated. The upper boundary of the domain moved with 0.2 m/s along the length.

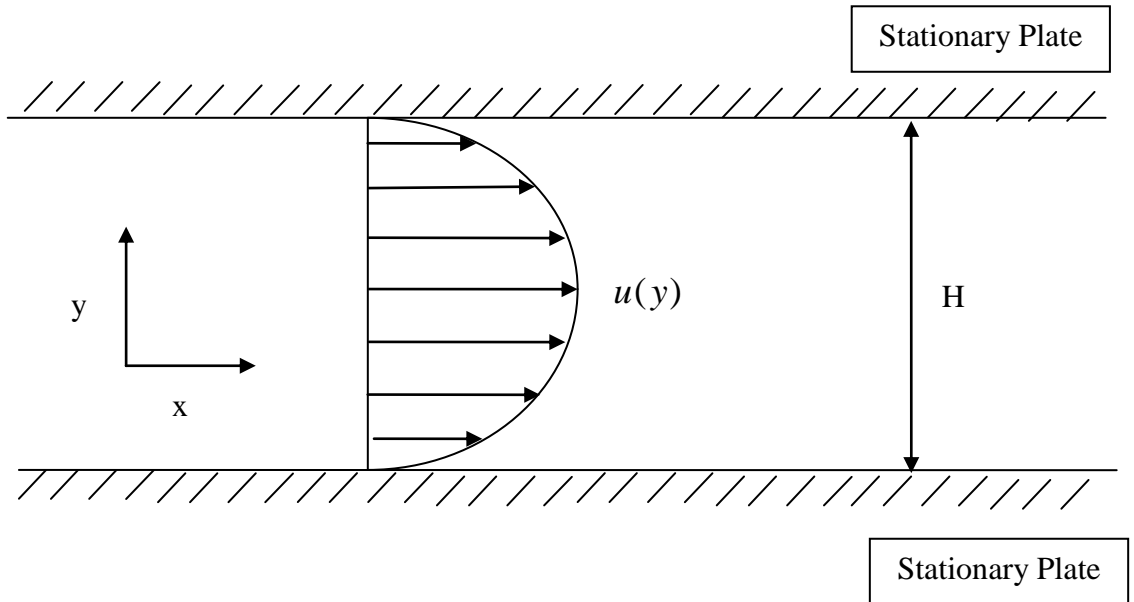


Figure 5 Schematic diagram of Plane Poiseuille Flow

E.2 Poiseuille flow

Poiseuille flow is the flow driven by the pressure gradient along the length of the domain. Schematic of the Poiseuille flow is given in Figure 5. The pressure gradient and the shear stress are balanced to get the variation of velocity profile in the lateral direction. No-slip boundaries are assumed, and shear stress is taken to be zero at the boundaries. The velocity equation of the plane Poiseuille flow is given by the Eq. 8. The comparison of the analytic and numerical simulation is given in Figure 6.

$$u(y) = \frac{1}{2\mu} \cdot \left(-\frac{dp}{dx} \right) \cdot y \cdot (H - y) \quad (8)$$

E.2.1 Numerical simulation for laminar flow

Finite volume method is used for solving the plane Poiseuille flow problem. Water is used as a working fluid. The inlet is given as velocity inlet boundary with velocity ~ 0.139 m/s. Pressure boundary is defined at the outlet of the domain. No slip condition is used for the side-wall boundaries. The comparison between numerical and analytic solution is shown in the Figure 6.

Table 22 Grid details for Poiseuille flow

Type of grid	Number of divisions along length	Number of divisions along the gap
Finest	240	40
Fine	120	20
Coarse	30	5

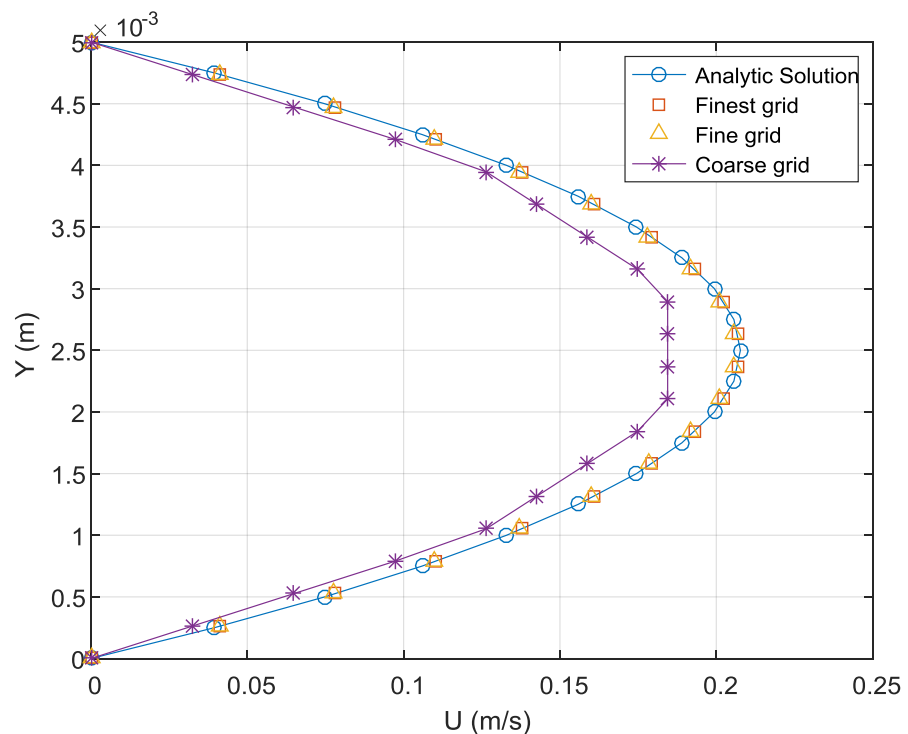


Figure 6 Numerical solution results and grid independence study for the velocity profile in plane Poiseuille flow

Appendix F

Solution for baffled piston

F.1 Acoustic radiation by a 2D ring

For any arbitrary shaped surface vibrating at the velocity $u_p = u_o \cdot e^{j\omega t}$ the pressure field at any location is given by Eq.9.

$$p(x, y, x; t) = \frac{jk\rho_o c_o u_o}{2\pi} \cdot e^{j\omega t} \cdot \int_S \frac{e^{-jkR}}{R} dS \quad (9)$$

F.1.1 Solution for 2D Annular ring

The 2D annular ring with average radius ‘a’ is vibrating at the harmonic velocity excitation. The schematic diagram is given in Figure 7. The details of the geometry and the co-ordinates can be referred from Table 23. From the geometry, the distance between the source B and the field point L can be calculated by Eq.10. The pressure field can be calculated by the Rayleigh integral given by the Eq.9 which after substituting the geometric parameters becomes Eq.11. The pressure can be evaluated by evaluating the radial distance between source and point ‘L’.

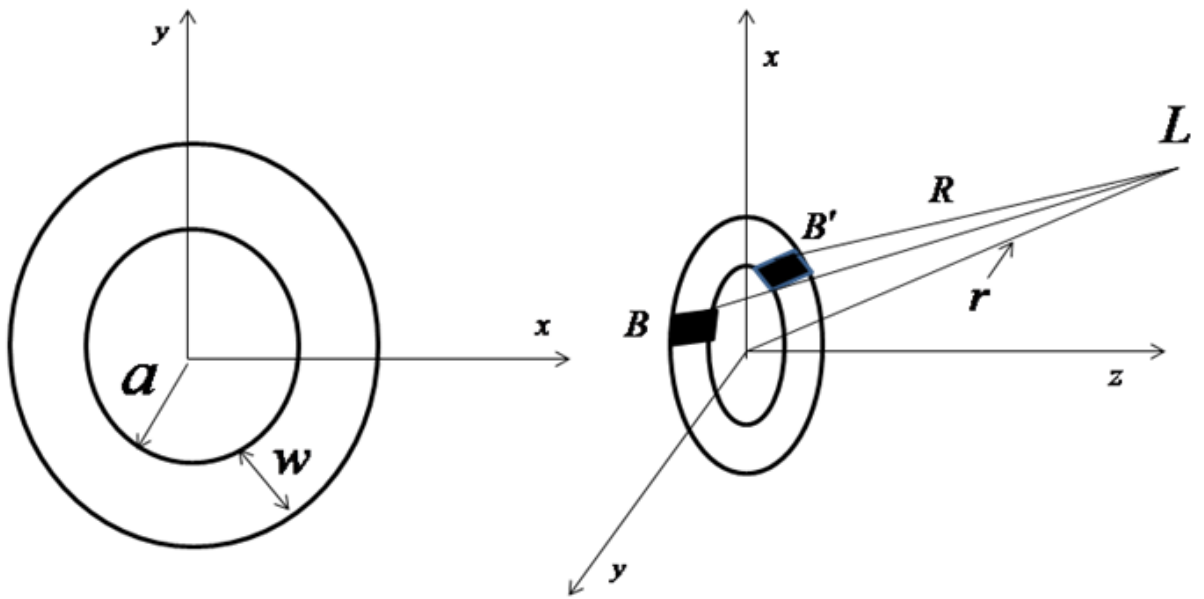


Figure 7 Schematic diagram of 2D annular ring vibrating at harmonic velocity excitation

$$R = \sqrt{(r \sin \theta - a \cos \psi)^2 + a^2 \sin^2 \psi + r^2 \cos^2 \theta} = \sqrt{r^2 + a^2 - 2ra \sin \theta \cos \psi} \quad (10)$$

$$p = \frac{jkaw\rho_o c_o u_o}{\pi} \cdot e^{j\omega t} \cdot \int_0^\pi \frac{e^{-jkR}}{R} d\psi \quad (11)$$

Table 23 Geometry and Co-ordinate details of annular ring

ψ	Angle measured from x-axis to the source point B
θ	Angle measured from z-axis to the far field point L
a	Average radius of the ring
R	Distance between L and the source point B
r	Distance between L and the origin
$L(x, 0, z)$	$x = r \cdot \sin \theta$ $z = r \cdot \cos \theta$
$B(x', y', 0)$ $B'(x', -y', 0)$	$x' = a \cdot \sin \psi$ $y' = a \cdot \cos \psi$
dS	$2awd\psi$

F.1.2 Far-field pressure solution

The radial distance of Eq.10 can be modified for $r \gg a$ into the Eq.12. For a very large distance from the origin, the radial distance R can be approximated as $R \approx r$. The far-field expression for the pressure then can be given by Eq.14.

$$R = r - a \sin \theta \cos \psi \quad (12)$$

$$p = \frac{jkaw\rho_o c_o u_o}{\pi r} \cdot e^{j(\omega t - kr)} \cdot \int_0^\pi e^{j(k a \sin \theta) \cos \psi} d\psi \quad (13)$$

$$p = \frac{jkaw\rho_o c_o u_o}{\pi r} \cdot e^{j(\omega t - kr)} \cdot J_o(ka \sin \theta) \quad (14)$$

F.1.3 Near-field pressure solution

The radial distance of Eq.10 can be modified for $r \ll a$ into the Eq.10. The near-field expression for the pressure then can be given by Eq.16.

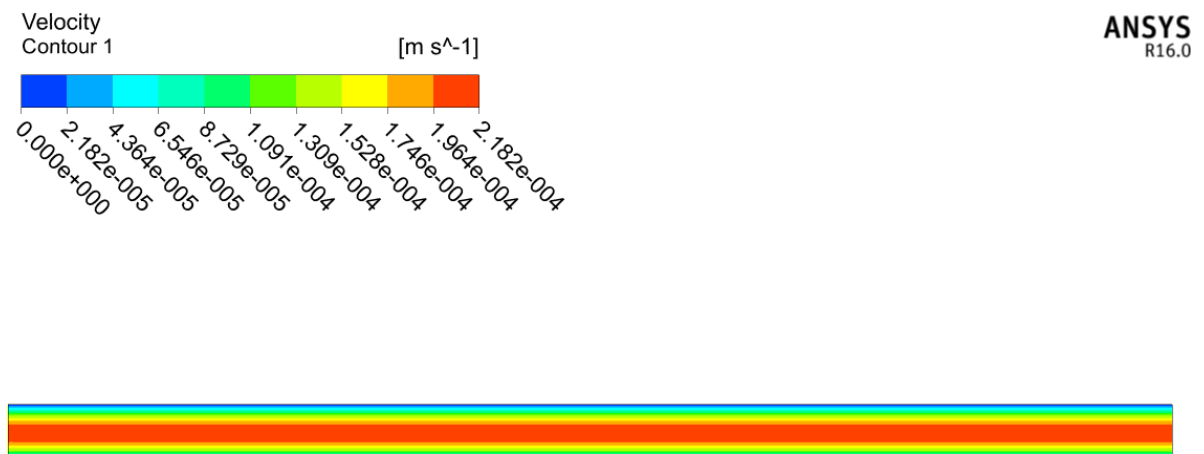
$$R = \sqrt{r^2 + a^2} \quad (15)$$

$$p = jkaw\rho_o c_o u_o \cdot \frac{e^{j(\omega t - k\sqrt{r^2 + a^2})}}{\sqrt{r^2 + a^2}} \quad (16)$$

Appendix G

UDF For Fully Developed Flow At The Inlet

Flow through concentric cylinders gives solution of the form $U(R) = A \cdot R^2 + B \cdot \ln(R) + C$. The calculation for constants A, B and C is done with excel sheet. The contour plot of the developed flow is given below.



G.1.1 UDF code

```
#include "udf.h"
DEFINE_PROFILE(inlet_x_velocity, thread, index)
{
face_t f;
real x[ND_ND]; /* this will hold the position vector */
real xx;
real y;
real a;
real b;
real c;
real r;
a=-128.7231650354290;
b=0.3646943018141680;
c=1.399441568647640;
begin_f_loop(f, thread) /*loops over all faces in the thread passed in the DEFINE macro argument*/
{
F_CENTROID(x,f,thread);
y =x[1];/*Y coordinate */
xx =x[0];/*X coordinate */
r = pow((pow(y,2)+pow(xx,2)),0.5);
F_PROFILE(f, thread, index) =( a*pow((r),2)+b*log((r))+c);
}
end_f_loop(f, thread)
}
```

Appendix H

MATLAB codes

H.1 Meanline design of the Impeller

H.1.1 Main code: Impeller_scratch.m

```
clc
clearvars

%% Input Parameters

% H = input('\nHead : ');
% Q = input('\nVolume flow rate: ');
% N = input('\nRotational speed: ');

H = 20; % Head in m
Q = 280; % Flow rate in m3/hr
N = 1450; % Rotational speed in RPM
rho = 1000; % Density of the working fluid
g = 9.81;

Q = Q/3600; % m3/hr to m3/s conversion
z = 6; % Number of blades

%% Efficiency function call

[etav, etah, etao] = efficiency(H,Q,N);
```

```

Q = Q/etav;

%% Specific speed calculation

Ns = N*Q^0.5/(H)^0.75; % Specific speed

%% Impeller eye diameter for optimum NPSH

De = 5.14*(Q/N)^(1/3); % ***** Dimension in m. Refer
derivation *****
Cme = 1.05*4*Q/(pi*(De^2)); % Flow velocity in eye of impeller
Cue = pi*De*N/60; % Tangential velocity in eye of
impeller
D1 = 1.0005*De; % Impeller shroud side diameter at
inlet

%% Dimensionless quantities

NPSHr = 1.8*(Cme^2/(2*g))+0.23*(Cue^2/(2*g)); % NPSH required
emperical formula
Nss = (2*pi*N/60)*Q^0.5/(g*NPSHr)^0.75; % Suction
specific speed
Power = rho*g*Q*H/etao; % Power
fT = 1.1;
psi = 1.21*fT*exp(-0.77*(Ns/100));

%% Impeller outlet diameter

D2 = (84.6/N)*(H/psi)^0.5;

%% Impeller balde thickness

delta1 = 0.03*D2;

%% Shaft diameter import

Ds = shaft_dia(Power,N);
% ks = input('\nShaft to hub ratio: ');
ks = 1.5; % Hub to shaft diameter ratio
Dh = ks*Ds;

%% Initial estimate of inlet blade angle at shroud

err = 1;
kh = 1-(Dh/D1)^2; % Hub to inlet blade dia ratio
alpha1 = 90; % Inlet approach angle

beta10 = round(atand((2.9/D1)^3*(Q/(N*kh)))); % Blade angle
without blockage

k1 = blockage(z,delta1,D1,beta10); % Initial guess blockage
Cm1 = k1*Cme; % Initial flow velocity
guess

[u1,C1,Cu1,W1] = triangle(N,D1,alpha1,beta10,Cm1);

```

```

beta1 = atand(Cm1/(u1-Cu1));    % Blade angle with blockage

while err>1e-6

err = abs(beta1-beta10);
beta10 = beta1;      % Blade angle without blockage

k1 = blockage(z,delta1,D1,beta10);      % Initial guess blockage
Cm1 = k1*Cme;          % Initial flow velocity
guess

[u1,C1,Cu1,W1] = triangle(N,D1,alpha1,beta10,Cm1);

beta1 = atand(Cm1/(u1-Cu1));    % Blade angle with blockage

end

% Angle exaggeration method from Gulish

beta1=atand(1.1*tand(beta1));

%% Inlet Velocity triangle values at Leading edge

% Diameters at the leading edge

D1i = max(D1/2,Dh*1.5);           % Hub streamline diameter
D1o = D1;                         % Shroud streamline diameter
D1m = (D1i+D1o)/2;               % Middle streamline diameter

beta1o = beta1;                  % Hub streamline angle
beta1i = atand((D1o/D1i)*tand(beta1o));   % Shroud streamline
angle
beta1m = atand((D1o/D1m)*tand(beta1o));   % Middle streamline
angle

b1 = 0.5*(D1-Dh);
% b1 = Q/(Cm1*pi*D1m)

%% Outlet width

b2_star = 0.017+0.262*(Ns/100)-0.08*(Ns/100)^2+0.0093*(Ns/100)^3;

b2 = b2_star*D2;                % Initial estimate of outlet
width
D1rms = (0.5*(D1i^2+D1o^2))^0.5;    % Diameter at which flow rate
is equal on both sides
D1s = D1rms/D2;

%% Initial outlet angle assumption

Cm2 = Q/(pi*D2*b2);
k_stab = 1;                      % Definition taken from ANSYS help

u2 = pi*D2*N/60;
Cu2 = (u2-u1)/k_stab;

```

```

W2 = ((u2-Cu2)^2+Cm2^2)^0.5;
beta2 = asind(Cm2/W2);

%% Head iteration loop

A1 = pi*D1*b1;
A2 = pi*D2*b2;

gamma = slip(beta2,z,D1s); % Slip factor
k2 = blockage(z,delta1,D2,beta2); % Initial guess blockage
Hv = head_veri(Q,etah,u2,beta2,k2,D1s,alpha1,A1,A2,gamma); % Head back calculation

err = abs(Hv-H); % Prediction error

while err > 0.1

    beta2 = beta2+1e-6;
    Hv = head_veri(Q,etah,u2,beta2,k2,D1s,alpha1,A1,A2,gamma);

    err = abs(H-round(Hv,12));

end

% && condition is not working for some reason
% Thus two while loops are written if code is underpredicting

if Hv < H

    while H > Hv

        beta2 = beta2+1e-6;
        Hv = head_veri(Q,etah,u2,beta2,k2,D1s,alpha1,A1,A2,gamma);

    end

end

gamma = slip(beta2,z,D1s); % Slip factor
k2 = blockage(z,delta1,D2,beta2); % Initial guess blockage
Hv = head_veri(Q,etah,u2,beta2,k2,D1s,alpha1,A1,A2,gamma); % Head back calculation

%% Outlet velocity triangle calculation

[u1m,C1m,Cu1m,W1m] = triangle(N,D1m,alpha1,beta1m,Cm1);

W2 = W1m; % No slip assumption
Cm2 = W2*sind(beta2);
b2 = Q/(pi*D2*Cm2);
Cu2 = u2-W2*cos(beta2);
alpha2 = atand(Cm2/Cu2);
[u2,C2,Cu2,W2] = triangle(N,D2,alpha2,beta2,Cm2);

```

```
% -----
```

H.1.2 Shaft diameter calculation function

```
function Ds = shaft_dia(Power,N)

%Power overload of 15%
Power = Power*1.15;
omega = (2*pi*N)/60;
Torque = Power/omega;

% fos = input('\Input factor of safety: ');
fos = 2;
Us = 35; % Ultimate stress in N/mm2
Us = Us/fos;

Ds = ((16*Torque) / (pi*Us*1e6))^(1/3);

end
```

```
% -----
```

H.1.3 Efficiency Calculation function

```
function [etav,etah,etao] = efficiency(H,Q,N)

%% Input data from user

Qref = 1;

% choice = input('\n\nChoose the option\n1.Balance hole\n2.No
balance hole\nEnter option:');

choice = 1;

%% Calculations

% Specific speed
Ns = N*sqrt(Q) / (H)^(3/4);

%% Volumetric efficiency

a = 4.1;
m = 1.6;
P = 1;
```

```

if(choice ==1)
    P = 2;
end

if(Ns<27)
    a=4.1;
    m=1.6;
end

% Seal loss prediction
L_seal = (a*P) / (Ns^m);

% Balance hole loss
L_balance = 0;

% Cooling flow in bearing
L_bearing = 0;

etav = 1/(1+L_seal+L_balance+L_bearing);

%% Hydraulic efficiency

% Empirical constant
a = 1;

if Q > 1
    a = 0.5;
end

% Exponent
m = 0.08*a*(Qref/Q)^0.15*(45/Ns)^0.06;

% Radial single stage pumps
etah = 1-0.055*(Qref/Q)^m;
etah = etah - 0.2*(0.26-log10(Ns/25))^2*(Qref/Q)^0.1;

%% Overall efficiency

% Empirical constant
a = 1;

if Q > 1
    a = 0.5;
end

m = 0.1*a*(Qref/Q)^0.15*(45/Ns)^0.06;

%% Overall Efficiecy calculation

% Radial single stage pumps
etao = 1-0.095*(Qref/Q)^m;
etao = etao - 0.3*(0.35-log10(Ns/23))^2*(Qref/Q)^0.05;

end

```

% -----

H.1.4 Blockage factor calculation function

```
function k = blockage(z,delta,D,beta)
k = 1-(z*delta)/(pi*D*sind(beta));
k = 1/k;
end
```

% -----

H.1.5 Velocity triangle calculation function

```
function [u,C,Cu,W] = triangle(N,D,alpha,beta,Cm)
u = pi*D*N/60;
C = Cm/sind(alpha);
Cu = Cm/tand(alpha);
W = Cm/sind(beta);
end
```

% -----

H.1.6 Slip factor calculation function

```
function gamma = slip(beta,z,D1s)
elim = exp(-8.16*sind(beta)/z);
kw = 1-((D1s-elim)/(1-elim))^3;
if elim >= D1s
    kw = 1;
end
f1 = 0.98;
```

```

gamma = f1*(1-((sind(beta))^0.5/(z^0.7)))*kw;
end

```

% -----

H.1.7 Head verification function

```

function Hv = head_veri(Q,etah,u,beta,k,D1s,alpha,A1,A2, gamma)
p1 = (k+(A2*D1s*tan(beta))/(A1*tan(alpha)));
p2 = (Q/(A2*u*tan(beta)));
Hv = (etah*u^2/9.81)*(gamma-p1*p2);
end

```

% -----

H.2 Meridional section

H.2.1 Main code: meridional_section.m

```

clc
clearvars

%% Impeller scratch code

Impeller_scratch

% Number of streamlines
n = 5;

%% Basic impeller dimension

Re = De/2;
Rs = Ds/2;
Rh = Dh/2;
Rlo = Dlo/2;
Rli = Dli/2;
R2 = D2/2;

```

```

%% Draft angle calculation

% Horizontal draft angle
g1 = 0.025*b1;
ehn = atand((Rlo-Re)/g1);
eh1 = 25;                                % Take user input
eslant = 15;

% eh variation loop

dehdR = (eh1-ehn) / (Re-Rh);
dR = (Re-Rh) / (n-1);
R = Rh:dR:Re;

for i = 1:n
    eh(i) = ehn+(Rlo-R(i))*dehdR;
end

% Vertical draft angle
evn = 0.2*max((Ns-20),0);
ev1 = 0;                                  % Take user input

% ev variation loop

devdb = (ev1-evn) / (b2);
db = (b2) / (n-1);
b = 0:db:b2;

for i = 1:n
    ev(i) = evn+(b2-b(i))*devdb;
end

%% Anchor point calculation

z_origin = 5e-3;

% axial extension calculation

a = 0.75;
x = -0.01;
z_ext = a*(Rlo-Rh)*(Ns)^(x);
db = b2/(n-1);

pax = zeros(n,5);
pay = zeros(n,5);

% Outer streamline points
i = n;
p1 = [z_origin,R(i)];
% p2 = [p1(1)+b1*(1+sind(eh(i))),R(i)];
p2 = [p1(1)+b1*tand(eslant)*((n-i)/(n-1))+b1,R(i)];
p2 = [p1(1)+b1*tand(eh(i))*((n-i)/(n-1))+b1,R(i)];
p5o = [p2(1)+(n-i)*db+z_ext,R2];

pax(i,1)=p1(1);

```

```

pay(i,1)=p1(2);
pax(i,2)=p2(1);
pay(i,2)=p2(2);
pax(i,5)=p5o(1);
pay(i,5)=p5o(2);

for i = 1:n-1

    % Inner streamline points
    p1 = [z_origin,R(i)];
    % p2 = [p1(1)+b1*(1+sind(eh(i))),R(i)];
    p2 = [p1(1)+b1*tand(eslant)*((n-i)/(n-1))+b1,R(i)];
    p2 = [p1(1)+b1*tand(eh(i))*((n-i)/(n-1))+b1,R(i)];
    p5 = [p5o(1)+(n-i)*db,R2];

    pax(i,1)=p1(1);
    pay(i,1)=p1(2);
    pax(i,2)=p2(1);
    pay(i,2)=p2(2);
    pax(i,5)=p5(1);
    pay(i,5)=p5(2);

end

%% Control point calculations

% Control factor
fc1 = 2/3;
fc2 = 2/3;

for i = 1:n

    p3h = (pax(i,5)-pax(i,2));
    pax(i,3)= pax(i,2)+p3h*cosd(eh(i))*(fc1);
    pay(i,3)= pay(i,2)+p3h*sind(eh(i))*(fc1);

    p4v = (pay(i,5)-pay(i,2));
    pay(i,4)= pay(i,2)+p4v*(1-cosd(ev(i))*(fc2));
    pax(i,4)= pax(i,5)-p4v*sind(ev(i))*(fc2);

end

%% Bazier curve calculation

for i = 1:n

    px = pax(i,2:end);
    py = pay(i,2:end);

    [x,y] = bez(px,py);

    xi(i,:)= x;
    yi(i,:)= y;

```

```

end

%% Matrix concatenation

xx = [pax(:,1) xi];
yy = [pay(:,1) yi];

% -----

```

H.2.2 Bezier curve calculation function

```

function [x,y] = bez(px,py)

%% Point import

% Number of control points
cp = 4;

P=zeros(3,cp);
% x co-ordinate
P(1,:) = px;
% y co-ordinate
P(2,:) = py;
% z co-ordinate
% Taken zero

%% Curve maker
idx = 1;

% Number of polynomial divisions
delta = 200;

for u = 0:(1/delta):1

    % General Bezier curve equation

    sum = [0 0 0]';
    for i = 1:cp

        % B is the Bernstein polynomial coefficients
        B = nchoosek(cp,i-1)*(u^(i-1))*((1-u)^(cp-i+1));
        % Value addition at each co-ordinate
        sum = sum + B*P(:,i);

    end

    B = nchoosek(cp,cp)*(u^(cp));
    sum = sum + B*P(:,cp);

end

```

```

    Cord(:,idx) = sum;           % Curve co-ordinates at any point Pj
in column
    idx = idx+1;                % Next point index update. Delta such
points.

end

x = Cord(1,:);
y = Cord(2,:);

end

% -----

```

H.3 Front view profile generation code Kaplan method

```

clc
clearvars

%% Beta angle variation

Impeller_final
global stream;

%% Co-ordinates of blade in meridional plane

rblade = rr(:,q*18:end);
zblade = zz(:,q*18:end);
mblade = rblade;

%% Beta variation at extremes

beta_le = zeros(stream,1);
beta_te = beta_le;

for i = 1:stream

    % At leading edge
    beta_le(i) = atand((Rlo/rblade(i,1))*tand(beta1o));
    % At trailing edge
    beta_te(i) = beta2;

end

%% y variation

px = [0,1/3,2/3,1];

```

```

py = [0,0,1,1];

%% Point import

% Number of control points
cp = 4;

P=zeros(3,cp);
% x co-ordinate
P(1,:) = px;
% y co-ordinate
P(2,:) = py;
% z co-ordinate
% Taken zero

%% Curve maker
idx = 1;

% Number of polynomial divisions
delta = length(rblade)-1;

for u = 0:(1/delta):1

    % General Bezier curve equation

    sum = [0 0 0]';
    for i = 1:cp

        % B is the Bernstein polynomial coefficients
        B = nchoosek(cp,i-1)*(u^(i-1))*((1-u)^(cp-i+1));
        % Value addition at each co-ordinate
        sum = sum + B*P(:,i);

    end

    B = nchoosek(cp,cp)*(u^(cp));
    sum = sum + B*P(:,cp);

    Cord(:,idx) = sum;           % Curve co-ordinates at any point Pj
in column
    idx = idx+1;                % Next point index update. Delta such
points.

end

x = Cord(1,:);
y = Cord(2,:);

% figure
% plot(x,y)

%% Beta_variation

```

```

bet = zeros(stream,length(rblade));

for j=1:stream

    for i = 1:length(rblade)

        bet(j,i) = beta_te(j)-y(i)*(beta_te(j)-beta_le(j));

    end
end

%% Streamline length calculation

dr = zeros(stream,(length(rblade)-1));
dz = dr;
dm = dr;
du = dr;
lm = zeros(stream,1);
lu = lm;
rublade = zeros(stream,length(rblade));
theta = 90*ones(stream,length(rblade));
rb = fliplr(rblade);

for j = 1:stream

    for i = 1:(length(rblade)-1)

        dr(j,i) = rblade(j,i+1)-rblade(j,i);
        dz(j,i) = zblade(j,i+1)-zblade(j,i);

        % Streamline distance
        dm(j,i) = (dr(j,i)^2+dz(j,i)^2)^(0.5);
        du(j,i) = dm(j,i)/tand(bet(j,i));

        % r-theta co-ordinate
        rublade(j,i+1) = rublade(j,i)+du(j,i);
        theta(j,i+1) = 90 -atand(rublade(j,i+1)/rb(j,i+1));

    end
end

%% Curve plot

% for j = 1:stream
%
%     figure (5)
%     plot(rublade(j,:),rb(j,:))
%     hold on
% end
%
% hold off

theta = theta*pi/180;
theta = theta - theta(1,end)+pi/6;

```

```

dz = 2*pi/(z);

figure (3)
tht= 0:0.01:2*pi;
polarplot(tht,(Dh/2)*ones(length(tht)), 'k')
hold on
polarplot(tht,(Ds/2)*ones(length(tht)), 'k')
hold on
polarplot(tht,rblade(1,end)*ones(length(tht)), 'k')
hold on

for k = 1:z

for j = 1:stream

    polarplot(theta(j,:),rb(j,:),'r')
    hold on

end

theta = theta+dz;

end

hold off

%% Projection plot

[xp yp]=pol2cart(theta,rb);

figure(4)
for j = 1:stream

    plot(xp(j,:),yp(j,:))
    hold on

end

hold off;
set(gca,'XTick',[], 'YTick', [])
xlabel('Theta direction')
ylabel('Radial dieraction')

figure(5)
for j = 1:stream

    plot(xp(j,:),fliplr(zblade(j,:)))
    hold on

end

hold off;
set(gca,'XTick',[], 'YTick', [])

```

```

xlabel('Theta direction')
ylabel('Axial direction')

%% Throghflow angles

betru = fliplr(bet);

% Observed from figure 5

betzu = betru*0;
zu = 30+30/stream; % For inner streamline from vertical axis
% actal angle + 30/stream

zzu = zu/stream;

for j = 1 :stream

    betzu(j,1:round(length(rblade)/2.2)) = (stream-j)*zzu ;

end

% -----

```

H.4 Vane development in front view by Srinivasan[24] method

```

clc
clearvars

%% Impeller scratch design

Impeller_scratch

%% Vane development for radial blade

%% Cm and W devlopement is assumed to be uniform

R1 = D1/2;
R2 = D2/2;
nd = 101; % Number of data points
dr = (R2-R1) / (nd-1);
dCmdR = (Cm2-Cm1) / (R2-R1);
dWdR = (W2-W1) / (R2-R1);
dBdR = (b2-b1) / (R2-R1);
R = R1:dr:R2;

%% Flow velocity linear variation

Cm = zeros(1,nd);
Cm(1) = Cm1;
Cm(end) = Cm2;

```

```

% Flow velocity Cm

for i=2:nd-1
    Cm(i)=Cm(i-1)+dCmdR*dr;
end

%% Relative velocity linear variation

W = zeros(1,nd);
W(1) = W1;
W(end) = W2;

% Relative velocity W

for i=2:nd-1
    W(i)=W(i-1)+dWdR*dr;
end

%% Width of the blade variation

B = zeros(1,nd);
B(1) = b1;
B(end) = b2;

for i = 2:nd-1
    B(i)=B(i-1)+dBdR*dr;
end

ratio1 = Cm./W;
t = 2*pi*R/z;
ratio2 = delta1./t;

zeta = asind(ratio1+ratio2);
G = R.*tand(zeta);
G = 1./G;

for i=1:(nd-1)
    x(i) = (G(i)+G(i+1))/2;
end

dtheta = x*dr;
theta = zeros(1,nd);

for i=2:nd
    theta(i) = theta(i-1)+dtheta(i-1);
end

% Theta in degrees

theta = (180/pi)*theta;

```

```

%% Plotting the graph
figure (1)
plot(R*1000,Cm, 'r+' );
hold on
plot(R*1000,W, 'k--' );
hold off
legend('Flow velocity C_{m}', 'Relative velocity W', 'location', 'best');
grid on
xlabel('Radius in mm');
ylabel('Relevant parameters');

figure (2)
plot(R*1e3,B*1e3);
grid on
xlabel('Radius in mm');
ylabel('Blade width in mm');

figure(3)

% Co-ordinates of blade

Ximp = R.*sind(theta);
Yimp = R.*cosd(theta);
figure (3)
plot(Ximp*1e3,Yimp*1e3, '-r*' );
ylm = max(Yimp)-min(Yimp);
xlm = max(Ximp)-min(Ximp);
pbaspect([xlm/xlm 2*ylm/xlm 1])
grid on
xlabel('X position in mm');
ylabel('Y position in mm');

figure(4)

tht_off = 360/z;
theta=fliplr(theta);

for i=1:z+1

polarplot((theta+(i-1)*tht_off)*(pi/180),R*1e3, 'k', 'LineWidth', 1.5)
hold on

end
theta = 0:0.01:2*pi;
polarplot(0:0.01:2*pi,R(1)*1e3*ones(length(theta)), 'k')
hold on
polarplot(0:0.01:2*pi,R(end)*1e3*ones(length(theta)), 'k')
hold off

% -----

```

H.5 Volute basic dimensions and shaping

```
clc
clearvars

%% Impeller code import

Impeller_scratch

%% Basic dimensions

% Cutwater diameter
D3 = (1.03+0.1*(Ns/40)+0.07*(H/1000))*D2;
% Volute inlet thickness
b3 = 1.25*b2;

%% Calculation of graph constants

% Volute angle
alphav = (45/(14.4*1e3))*Ns+1.875; % Stepanoff graph
alphav = round(max(alpha2,alphav)); % Condition to avoid
shock

% Velocity constant
k3 = 0.66-Ns/(30e3); % Stepanoff graph

%% Volute velocity calculation

cv = k3*(2*g*H)^(0.5);

%% Area at different sections

Avi = zeros(1,8);
Av = Q/(cv)*1e6; % Area at throat in mm2

% Area at different section
for i=1:8

    Avi(i)=Av*(i/8);

end

%% Volute shaping

rhovi = ((Avi+0.604*b3^2)./0.367).^0.5;
rvi = 0.206*rhovi;

% -----
```

H.6 Slip and Loss analysis

```
clc
clearvars

%% Recalling the designed data

Impeller_scratch

%% Basic volute dimensions

% Cutwater diameter
D3 = (1.03+0.1*(Ns/40)+0.07*(H/1000))*D2;
% Volute inlet thickness
b3 = 1.25*b2;

%% Calculation of graph constants

% Volute angle
alphav = (45/(14.4*1e3))*Ns+1.875; % Stepanoff graph
alphav = round(max(alpha2,alphav)); % Condition to avoid
shock

% Velocity constant
k3 = 0.66-Ns/(30e3); % Stepanoff graph

%% Volute velocity calculation

cv = k3*(2*g*H)^(0.5);
Av = Q/(cv)*1e6; % Area at throat in mm2

Q = Q*etav;
Qrange = 0:Q/1e3:2*Q;

itr = length(Qrange);

for m = 1:itr

%% Inlet velocity triangle calculation

Cme = 1.05*4*Qrange(m)/(pi*(De^2));
k1 = blockage(z,delta1,D1,beta1); % Inlet blockage
Cm1 = k1*Cme; % Inlet flow velocity

[u1,C1,Cu1,W1] = triangle(N,D1,alpha1,beta1,Cm1);

%% Outlet velocity triangle calculation

[u1m,C1m,Cu1m,W1m] = triangle(N,D1m,alpha1,beta1m,Cm1);

W2 = W1m; % No slip assumption
Cm2 = W2*sind(beta2);
```

```

Cu2 = u2-W2*cos(beta2);
alpha2 = atand(Cm2/Cu2);

[u2,C2,Cu2,W2] = triangle(N,D2,alpha2,beta2,Cm2);

%% Shock losses

H_shut = (u2^2-u1^2)/(2*9.81);
p1 = H_shut/Q^2;
hs(m) = p1*(Qrange(m)-Q)^2;

%% Impeller friction losses

Rh = (b2*((pi*D2/z)*sin(beta2)))/(b2+((pi*D2/z)*sin(beta2)));
hf = (b2*(D2-D1)*(W1+W2)^2)/(2*sin(beta2)*Rh*4*g);
p2 = hf/Q^2;
%
% hif(m)= p2*(Qrange(m)-Q)^2;
hif(m)= hf;

%% Volute friction losses

% hvf(m)= p2*(Qrange(m)-Q)^2; % temporary formula

v3 = Qrange(m)/(Av*1e-6);
hvf(m)= 0.1005*(v3^2/(2*9.81));

%% Disk friction losses

omega = 2*pi*N/60;
f = 0.5;

hdf(m) = (f*rho*omega^3*(D1/2)^5)/(1e9*Qrange(m));

%% Recirculation losses

hrs(m) = 1e-6*omega^3*D1*(abs(1-Qrange(m)/Q))^2.5;

%% Head calculation

H_slip(m) = (u2*Cu2-u1*Culm)/g;
H_eu(m) = (u2*(u2/gamma-Cm2*cotd(beta2))-u1*Culm)/g;
H_predicted(m) = H_slip(m)-hs(m)-hif(m)-hvf(m)-hdf(m)-hrs(m);

%% Efficiency calculation

eta(m) = rho*g*Qrange(m)*H_predicted(m)/(Power/etah);
eta(m) = rho*g*Qrange(m)*H_predicted(m)/(Power/etah);

end

%% H-Q curve prediction

figure (1)

```

```

plot(Qrange*3600,H_eu,'k.')
hold on
plot(Qrange*3600,H_slip,'-')
hold on
plot(Qrange*3600,H_predicted,'--')
hold on
idx = find(Qrange == Q);
l = plot(Qrange(idx)*3600,H_predicted(idx), 's');
l.MarkerFaceColor = l.Color;
hold off
grid on

xlim([0,1.5*Q*3600])
xlabel('Flow rate (m^3/hr)');
ylabel('Head (m)');

legend('Euler Head','Slip head','Predicted head');

figure (2)
plot(Qrange*3600,hs)
hold on
plot(Qrange*3600,hif)
hold on
plot(Qrange*3600,hvf)
hold on
plot(Qrange*3600,hdf)
hold on
plot(Qrange*3600,hrs)
hold off
grid on
xlim([0,1.5*Q*3600])
legend('Shock loss','Impeller friction','Volute friction','Disk
friction','Recirculation loss');

figure (3)

yyaxis left
plot(Qrange*3600,H_predicted)
hold on
l = plot(Qrange(idx)*3600,H_predicted(idx), 's');
l.MarkerFaceColor = l.Color;
hold on
yyaxis right
plot(Qrange*3600,eta*100)
hold on
l = plot(Qrange(idx)*3600,eta(idx)*100, 's');
l.MarkerFaceColor = l.Color;
hold off
grid on
xlim([0,1.5*Q*3600])
xlabel('Flow rate (m^3/hr)');
yyaxis left
ylabel('Head (m)');
yyaxis right
ylabel('Hydraulic Efficiency %');

```

% -----

H.7 FFT code

```
clc
clearvars

fprintf('\n----- FFT of pressure data -----')

RPM = 2900;
z = 6; % Number of impeller blades
BPF = RPM*z/60;
fprintf('\n\nBlade Passing Frequency: %f Hz',BPF);
% Time step is calculated for 0.5 degree rotation of the impeller
time_step = (60/RPM/360/2);

%% File read

filename = 'monitor point.xlsx';
p = xlsread(filename,1);
signal = p(:,9);
time = p(:,1)*time_step;

% Calculated from simulation
u = 22.258;
pref = 0;
rho = 1e3;

signal = signal-pref; % Pressure correction

% Coefficient of pressure
% signal = (signal)/(0.5*rho*u^2);

%% FFT

n = length(signal);
xdft = fft(signal);

%% Parsval verification

sum_time = 0;
sum_dft = 0;

for i=1:n

    % Time domain
    sum_time=signal(i)^2+sum_time;
    % Frequency domain
    sum_dft=abs(xdft(i))^2+sum_dft;
```

```

end

fprintf('\n\nParsval''s Theorem verification:\n');
fprintf('\nEnergy in Frequency domain: %f',sum_dft/n);
fprintf('\nEnergy in Time domain: %f',sum_time);
err=abs(sum_time-sum_dft/n)/(sum_time)*100;
fprintf('\nPercentage error: %d',err);

%% Half power spectrum calculation

% sampling interval -- assuming equal sampling
% Frequency calculations were done from MATHWORKS forum

% Copied code start

DT = time(2,1)-time(1,1);
% sampling frequency
Fs = 1/DT;
DF = Fs/size(signal,1);
freq = 0:DF:Fs/2;

if (mod(n,2) ==0)

% Even points
xdft = xdft(1:length(xdft)/2+1);

else

%Odd points
xdft = xdft(1:round(length(signal)/2));

end

xdft = (2/n)*abs(xdft);

% Copied code end

%% Coefficient of fluctuation

pbar = mean(signal);
num = signal-pbar;
num = num.^2;
num = sum(num);
Kp = (1/pbar)*((1/length(signal)*num)^(1/2))

%% Plot

figure (1)
plot(time,signal);
title('Pressure');
xlabel('Time (s)');

```

```

ylabel('Amplitude ');
grid on

figure (2)
plot(freq(2:end),abs(xdft(2:end)))
xlim([0,1400])
title('Single-Sided Pressure Spectrum of signal')
xlabel('Frequency (Hz)')
ylabel('Pressure (Pa)')
grid on

% plot(freq(2:end),abs(xdft(2:end)))
% xlim([0,1400])
% title('Single-Sided Coefficient of pressure Spectrum of y(t)')
% xlabel('Frequency (Hz)')
% ylabel('Cp')
% grid on

% -----

```

H.8 Basic sound sources (Ref. NIOT[64])

```

clc
clearvars

%% User Input

rho = 1000; % Density
c = 1500; % Speed of sound in medium
f = 20; % Frequency
Q = 1; % Volume velocity
R = 10; % Domain radius in m

w = 2*pi*f; % Angular frequency
k = w/c; % Wave number
L = 1:2:R; % Any point at distance R
h = 0.004; % Dipole distance
v = 0.005; % Quadrupole vertical
distance
theta= 0:0.01:2*pi;

choice = 2; % Type of source

%% Source Type : Monopole

if choice == 1

    figure()
    for l= 1:1: length(L)
        r= L(l);
        for m= 1:1: length(theta)

```

```

        pressure(l,m)= abs(Q*((1i*k*rho*c)/(4*pi*r)));
    end
    polarplot(theta, pressure(l,:))
    grid on
    hold on
end
hold off

end

%% Source Type : Dipole

if choice == 2
    d = h;
    figure()
    for l= 1:1: length(L)
        r= L(l);
        for m= 1:1: length(theta)
            f_theta= theta(m);
            pressure(l,m)= abs((( -1i*Q*rho*c*(k^2)*d)/(4*pi*r))*...
1i*Q*rho*c*(k^2)*d)/(4*pi*r))*...
cos(f_theta));
        end
        polar(theta, pressure(l,:))
        grid on
        hold on
    end
    hold off
end

%% Source Type : Quadrupole

if choice == 3
    d= h;
    D= v;
    figure()
    for l= 1:1: length(L)
        r= L(l);
        for m= 1:1: length(theta)
            f_theta= theta(m);
            pressure(l,m)= abs((Q*rho*c*k)*(pi*r)*(k^2*d)*D*...
cos(f_theta)*sin(f_theta));
        end
        polar(theta, pressure(l,:))
        grid on
        hold on
    end
    hold off
end

%% Source Type : Longitudial Quadrupole

```

```

if choice == 4
    d= h;
    D= v;
    figure()
    for l= 1:1: length(L)
        r= L(l);
        for m= 1:1: length(theta)
            f_theta= theta(m);

pressure(l,m)=abs(((Q*rho*c*k) / (pi*r)) * (k^2) *d*D* ...
    ((cos(f_theta)^2)));
    end
    polar(theta, pressure(l,:))
    hold on
end
hold off

```

% -----

References

- [1] J. Elsey, “A Centrifugal Pump Primer, Part 1 | Pumps & Systems,” (n.d.).
<https://www.pumpsandsystems.com/centrifugal-pump-primer-part-1> (accessed June 2, 2020)
- [2] Kirloskar, “Kirloskar Canned Motor Pumps, Kirloskar Brothers Ltd.,” (n.d.)
- [3] A.K. Sawhney, “A Course in Electrical Machine Design,” Dhanpat Rai & Sons, 1984.
<https://books.google.co.in/books?id=cYqatgAACAAJ>
- [4] J. Oilfield, “Centrifugal Pump: Principle, Parts, Types -,” (2020).
<https://joinoilfield.com/centrifugal-pump-principle-parts-types/> (accessed June 1, 2020)
- [5] J.F. GÜlich, “Centrifugal Pumps,” Springer Berlin Heidelberg, 2007.
https://books.google.co.in/books?id=eurAVC3_Pk4C
- [6] D.N. Manik, “Vibro-Acoustics: Fundamentals and Applications,” CRC Press, 2017.
<https://books.google.co.in/books?id=T5ufDgAAQBAJ>
- [7] K.H. Bech, N. Tillmark, P.H. Alfredsson, H.I. Andersson, “An investigation of turbulent plane Couette flow at low Reynolds numbers,” *J. Fluid Mech.* 286 (1995) 291–325. doi:DOI: 10.1017/S0022112095000747
- [8] H.I. Andersson, B.A. Pettersson, “Modeling plane turbulent Couette flow,” *Int. J. Heat Fluid Flow.* 15 (1994) 447–455. doi:10.1016/0142-727X(94)90003-5
- [9] M. Fénöt, Y. Bertin, E. Dorignac, G. Lalizel, “A review of heat transfer between concentric rotating cylinders with or without axial flow,” *Int. J. Therm. Sci.* 50 (2011) 1138–1155. doi:10.1016/j.ijthermalsci.2011.02.013
- [10] G.I. Taylor, “Stability of a Viscous Liquid Contained between Two Rotating Cylinders,” *Philos. Trans. R. Soc. A Math. Phys. Eng. Sci.* 223 (1923) 289–343. doi:10.1098/rsta.1923.0008
- [11] A. Davey, “The growth of Taylor vortices in flow between rotating cylinders,” (1962)

- [12] Y. Yamada, “Resistance of a Flow through an Annulus with an Inner Rotating Cylinder,” *Bull. JSME.* 5 (1962) 302–310. doi:10.1299/jsme1958.5.302
- [13] S.R.M. Gardiner, R.H. Sabersky, “Heat transfer in an annular gap,” *Int. J. Heat Mass Transf.* 21 (1978) 1459–1466. doi:10.1016/0017-9310(78)90002-9
- [14] K.M. Becker, J. Kaye, “Measurements of Diabatic Flow in an Annulus With an Inner Rotating Cylinder,” *J. Heat Transfer.* 84 (1962) 97–104. <http://dx.doi.org/10.1115/1.3684335>
- [15] S. Chandrasekhar, “Hydrodynamic and Hydromagnetic Stability,” Dover Publications, 2013. <https://books.google.co.in/books?id=Mg3CAGAAQBAJ>
- [16] W. Abassi, F. Aloui, S.B. nasrallah, J. Legrand, “Use of the PIV and Electrochemical Techniques to Experimentally Characterize the Couette-Taylor-Poiseuille Flow Instabilities,” *J. Appl. Fluid Mech.* 9 (2016) 59–68
- [17] S. Gilchrist, C.Y. Ching, D. Ewing, “HT2005-72746,” (2016) 1–7
- [18] R. Jakoby, S. Kim, S. Wittig, “Correlations of the convection heat transfer in annular channels with rotating inner cylinder,” *J. Eng. Gas Turbines Power.* 121 (1999) 670–677. doi:10.1115/1.2818524
- [19] D.H. Lim, S.C. Kim, M.S. Kim, “Thermal analysis of an electric water pump for internal combustion engine vehicles,” *Int. J. Automot. Technol.* 14 (2013) 579–585. doi:10.1007/s12239-013-0062-7
- [20] A. Nouri-Borujerdi, M.E. Nakhchi, “Optimization of the heat transfer coefficient and pressure drop of Taylor-Couette-Poiseuille flows between an inner rotating cylinder and an outer grooved stationary cylinder,” *Int. J. Heat Mass Transf.* 108 (2017) 1449–1459. doi:10.1016/j.ijheatmasstransfer.2017.01.014
- [21] I.J. Karassik, J.P. Messina, P. Cooper, C.C. Heald, “Pump handbook,” McGraw-Hill New York, 2001
- [22] J. Osterwalder, “Conference on scaling for performance prediction in rotodynamic machines. University of Stirling, 6-8 septembre 1977,” Mechanical Engineering

publications, 1977

- [23] C.A. Gongwer, “A Theory of Cavitating Flow in Centrifugal-Pump Impellers,” in: ASME Hydraul. Div. Semi-Annual Meet., 1940
- [24] K.M. Srinivasan, “Rotodynamic Pumps (Centrifugal and Axial),” New Age International Limited, 2008. <https://books.google.co.in/books?id=qWCRNLWZjscC>
- [25] A.J. Stepanoff, “Centrifugal and axial flow pumps,” J. Wiley, 1948
- [26] R.C. Worster, “The flow in volutes and its effect on centrifugal pump performance,” Proc. Inst. Mech. Eng. 177 (1963) 843–875
- [27] M. V. Casey, “A computational geometry for the blades and internal flow channels of centrifugal compressors,” Proc. ASME Turbo Expo. 1 (1982). doi:10.1115/82-GT-155
- [28] Q. Wang, X. Huang, “The use of Bezier polynomial patches to define the geometrical shape of the flow channels of compressors,” Proc. ASME Turbo Expo. 1 (1988). doi:10.1115/88-GT-60
- [29] Ansys®, “Vista CPD, Release 16.0,” (2016) ANSYS, Inc.
- [30] Ansys®, “BladeGen, Release 16.0,” (2016) ANSYS, Inc.
- [31] K.S. Cho, A.T. San, S.M. Thu, “Design of Centrifugal Pump Volute-Type Casing,” Int. J. Sci. Eng. Appl. 8 (2019) 325–330. doi:10.7753/ijsea0808.1016
- [32] N.N. Win, “Performance prediction of a centrifugal pump,” Int. J. Innov. Res. Multidiscip. F. 2 (2016) 547–557
- [33] C.-H. Wu, “A General Theory of Three-Dimensional Flow in Subsonic, and Supersonic Turbomachines of Axial, Radial and Mixed-Flow Types,” Trans. ASME. 74 (1952) 1363–1830
- [34] M. Casey, C. Robinson, “Throughflow Method for Radial,” (2013). doi:10.1115/1.3151601
- [35] Ansys®, “Vista TF, Release 16.0,” (2016) ANSYS, Inc.
- [36] Ansys®, “FLUENT, Release 16.0,” (2016) ANSYS, Inc.

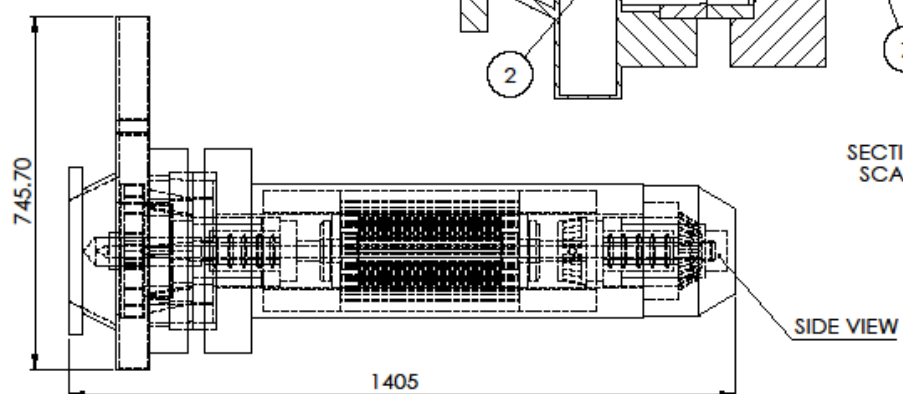
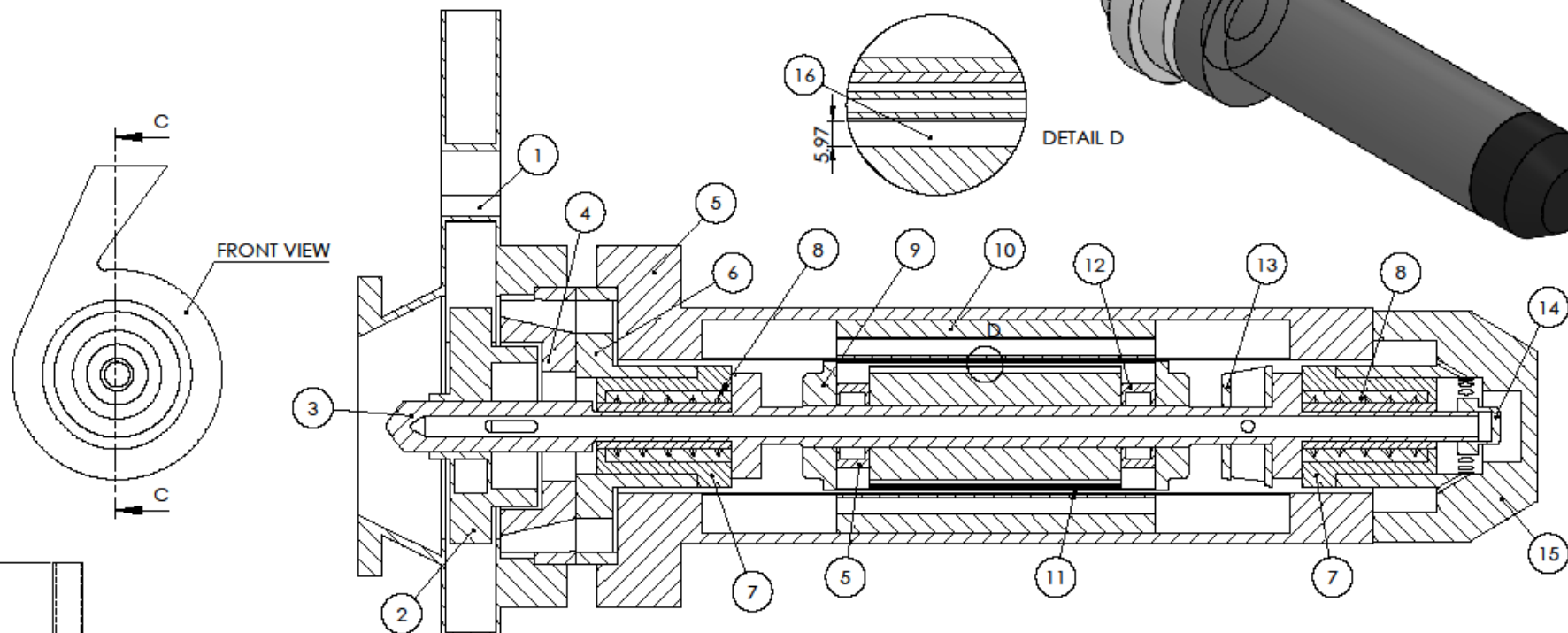
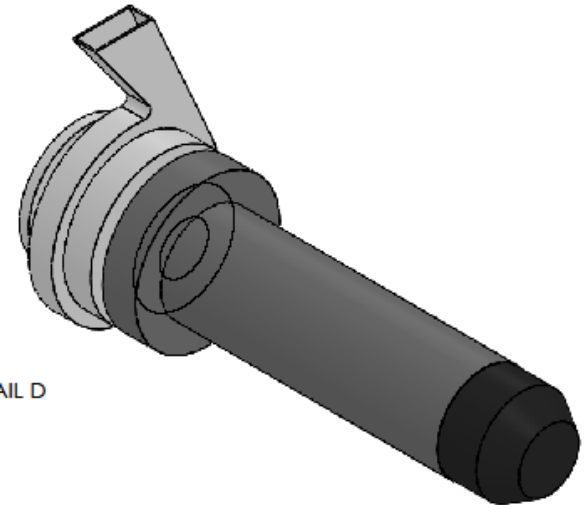
- [37] Ansys®, “CFX, Release 16.0,” (2016) ANSYS, Inc.
- [38] R.A. Novak, “Streamline Curvature Computing Procedures for Fluid-Flow problems,” Trans. ASME. (1967) 478–490
- [39] S. Kaewnai, M. Chamaoot, S. Wongwises, “Predicting performance of radial flow type impeller of centrifugal pump using CFD,” J. Mech. Sci. Technol. 23 (2009) 1620–1627. doi:10.1007/s12206-008-1106-1
- [40] M. Nataraj, R. Ragoth Singh, “Analyzing pump impeller for performance evaluation using RSM and CFD,” Desalin. Water Treat. 52 (2014) 6822–6831. doi:10.1080/19443994.2013.818924
- [41] Joon Hyung Kim, H.C. Lee, Jin Hyuk Kim, S. Kim, J.Y. Yoon, Y.S. Choi, “Design techniques to improve the performance of a centrifugal pump using CFD,” J. Mech. Sci. Technol. 29 (2015) 215–225. doi:10.1007/s12206-014-1228-6
- [42] J.C. Páscoa, F.J. Silva, J.S. Pinheiro, D.J. Martins, “Accuracy details in realistic CFD modeling of an industrial centrifugal pump in direct and reverse modes,” 19 (2010) 491–499. doi:10.1007/s11630-010-0414-9
- [43] M. Tan, X. He, H. Liu, L. Dong, X. Wu, “Mechanics Design and analysis of a radial diffuser in a single-stage centrifugal pump,” 2060 (2016). doi:10.1080/19942060.2016.1210027
- [44] B. Dürrer, F. Wurm, “Noise sources in centrifugal pumps,” Current. (2006) 203–207
- [45] S. Timouchev, J. Tourret, “Numerical Simulation of BPF Pressure Pulsation Field in Centrifugal Pumps,” Proc. 19th Pump User Symp. Houst. (2002)
- [46] K. Majidi, “Numerical Study of Unsteady Flow in a Centrifugal Pump,” Vol. 5 Turbo Expo 2004, Parts A B. 127 (2004) 805–814. doi:10.1115/GT2004-54099
- [47] Q. Si, J. Yuan, S. Yuan, W. Wang, L. Zhu, G. Bois, “Numerical investigation of pressure fluctuation in centrifugal pump volute based on SAS model and experimental validation,” Adv. Mech. Eng. 2014 (2014). doi:10.1155/2014/972081
- [48] F.A. Lu, X. Wang, D.T. Qi, J.C. Cai, “Study of the tonal casing noise of a centrifugal fan at the blade passing frequency. Part II. Vibroacoustics,” J. Low Freq. Noise Vib.

Act. Control. 30 (2011) 89–105. doi:10.1260/0263-0923.30.2.89

- [49] E. Chen, G. Zhao, G. Li, G. Nan, A. Yang, “Numerical investigation on flow-induced structural vibration and noise in centrifugal pump,” J. Vibroengineering. 18 (2016) 2448–2459. doi:10.21595/jve.2016.16803
- [50] D. Wu, Y. Ren, J. Mou, Y. Gu, “Investigation of the correlation between noise & vibration characteristics and unsteady flow in a circulator pump,” J. Mech. Sci. Technol. 31 (2017) 2155–2166. doi:10.1007/s12206-017-0411-y
- [51] J. Yang, S. Yuan, J. Yuan, Q. Si, J. Pei, “Numerical and experimental study on flow-induced noise at blade-passing frequency in centrifugal pumps,” Chinese J. Mech. Eng. (English Ed. 27 (2014) 606–614. doi:10.3901/CJME.2014.03.606
- [52] L. Cao, Z. Wang, Y. Xiao, Y. Luo, “Numerical Investigation of Pressure Fluctuation Characteristics in a Centrifugal Pump with Variable Axial Clearance,” Int. J. Rotating Mach. 2016 (2016). doi:10.1155/2016/9306314
- [53] C. Guo, M. Gao, D. Lu, K. Wang, “An experimental study on the radiation noise characteristics of a centrifugal pump with various working conditions,” Energies. 10 (2017). doi:10.3390/en10122139
- [54] A. Yang, D. Lang, G. Li, E. Chen, R. Dai, “Numerical research about influence of blade outlet angle on flow-induced noise and vibration for centrifugal pump,” Adv. Mech. Eng. 2014 (2014). doi:10.1155/2014/583482
- [55] W. Yu-qin, D. Ze-wen, “Influence of blade number on flow-induced noise of centrifugal pump based on CFD/CA,” Vacuum. 172 (2020) 109058. doi:10.1016/j.vacuum.2019.109058
- [56] I. Boldea, S.A. Nasar, “The Induction Machine Handbook,” CRC Press, 2010. <https://books.google.co.in/books?id=iQ7OBQAAQBAJ>
- [57] D.S. Adebayo, A. Rona, “Numerical Investigation of the Three-Dimensional Pressure Distribution in Taylor Couette Flow,” J. Fluids Eng. 139 (2017) 111201. doi:10.1115/1.4037083
- [58] K. Kataoka, H. Doi, T. Komai, “Heat/mass transfer in taylor vortex flow with constant axial flow rates,” Int. J. Heat Mass Transf. 20 (1977) 57–63. doi:10.1016/0017-

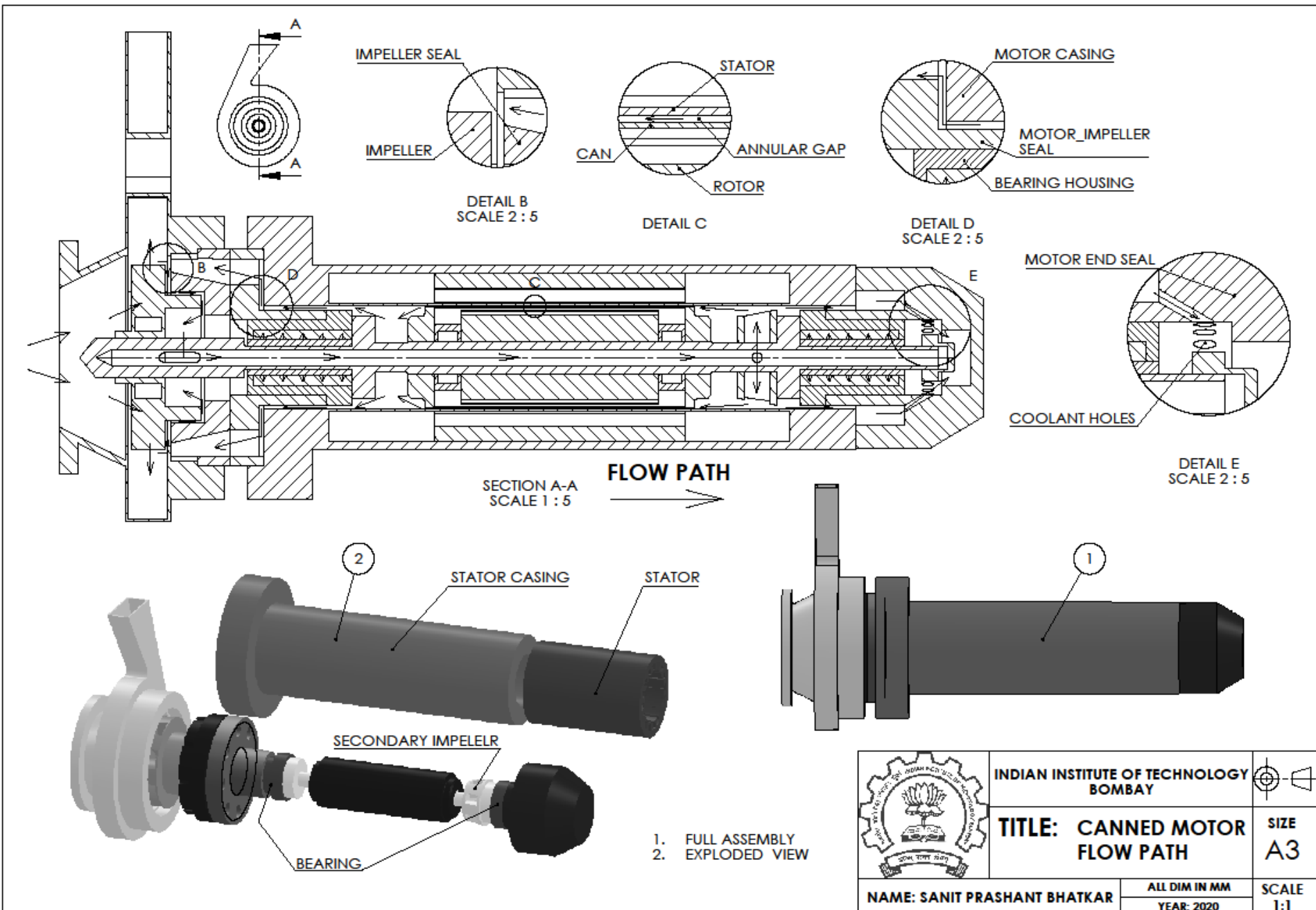
- [59] K. Kataoka, “Heat-transfer in a taylor vortex flow,” J. Chem. Eng. Japan. 8 (1975) 271–276. doi:10.1252/jcej.8.271
- [60] R. Kedia, M.L. Hunt, T. Colonius, “Numerical Simulations of Heat Transfer in Taylor-Couette Flow,” J. Heat Transfer. 120 (1998) 65. doi:10.1115/1.2830066
- [61] Institution of Mechanical Engineers (Great Britain)., “Centrifugal pumps-hydraulic design : 16 November 1982,” in: Centrif. Pumps-Hydraulic Des. 16 Novemb. 1982, London [England] : Mechanical Engineering Publications Ltd, 1982
- [62] Turbo, “Input power calculation for pump in CFD post -- CFD Online Discussion Forums,” Cfd-Online.Com. (n.d.). <https://www.cfd-online.com/Forums/cfx/183043-input-power-calculation-pump-cfd-post.html> (accessed June 6, 2020)
- [63] C. Howard, “Acoustic Analyses Using Matlab® and Ansys®,” 2014. doi:10.1201/b17825
- [64] NIOT, “RADIATION BY SIMPLE ACOUSTIC SOURCE,” n.d. https://www.niot.res.in/COAT/coat_pdf/CHAP IV- Radiation By Simple Acoustic Source.pdf?cv=1 (accessed June 2, 2020)
- [65] D. Mugnaini, “Bezier Curve with draggable control points,” MATLAB Cent. File Exch. (2020). <https://www.mathworks.com/matlabcentral/fileexchange/51046-bezier-curve-with-draggable-control-points>

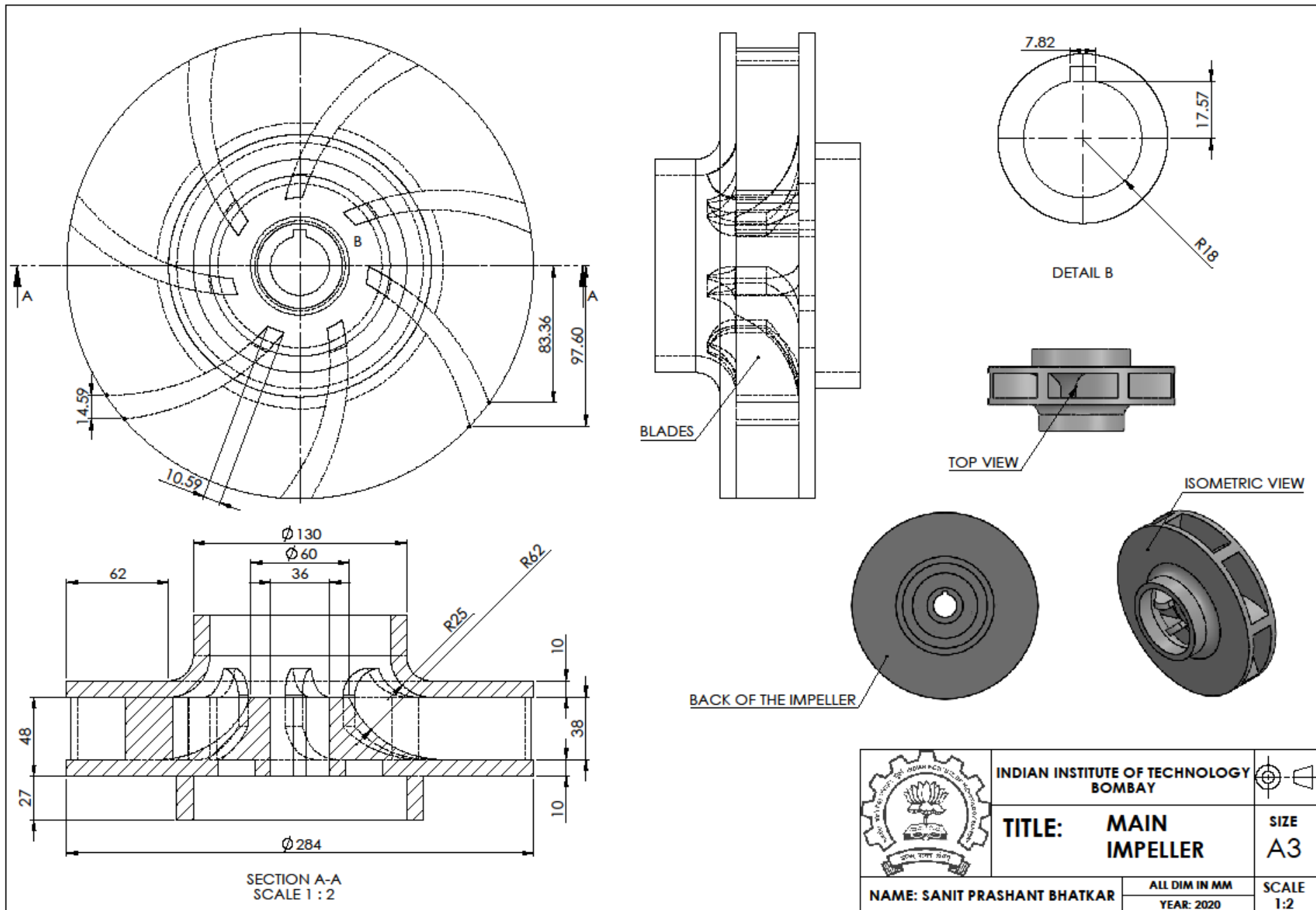
PART NUMBER	PART NAME	PART NUMBER	PART NAME
1	VOLUTE CASING	2	MAIN IMPELLER
3	SHAFT	4	MAIN IMPELLER SEAL
5	MOTOR CASING	6	MOTOR_IMPELLER SEAL
7	BEARING HUB	8	BEARING LINER
9	ROTOR CAN	10	STATOR
11	ROTOR	12	CAN SPACER
13	SECONDARY IMPELLER	14	SHAFT END NUT
15	MOTOR END SEAL	16	ANNULAR GAP

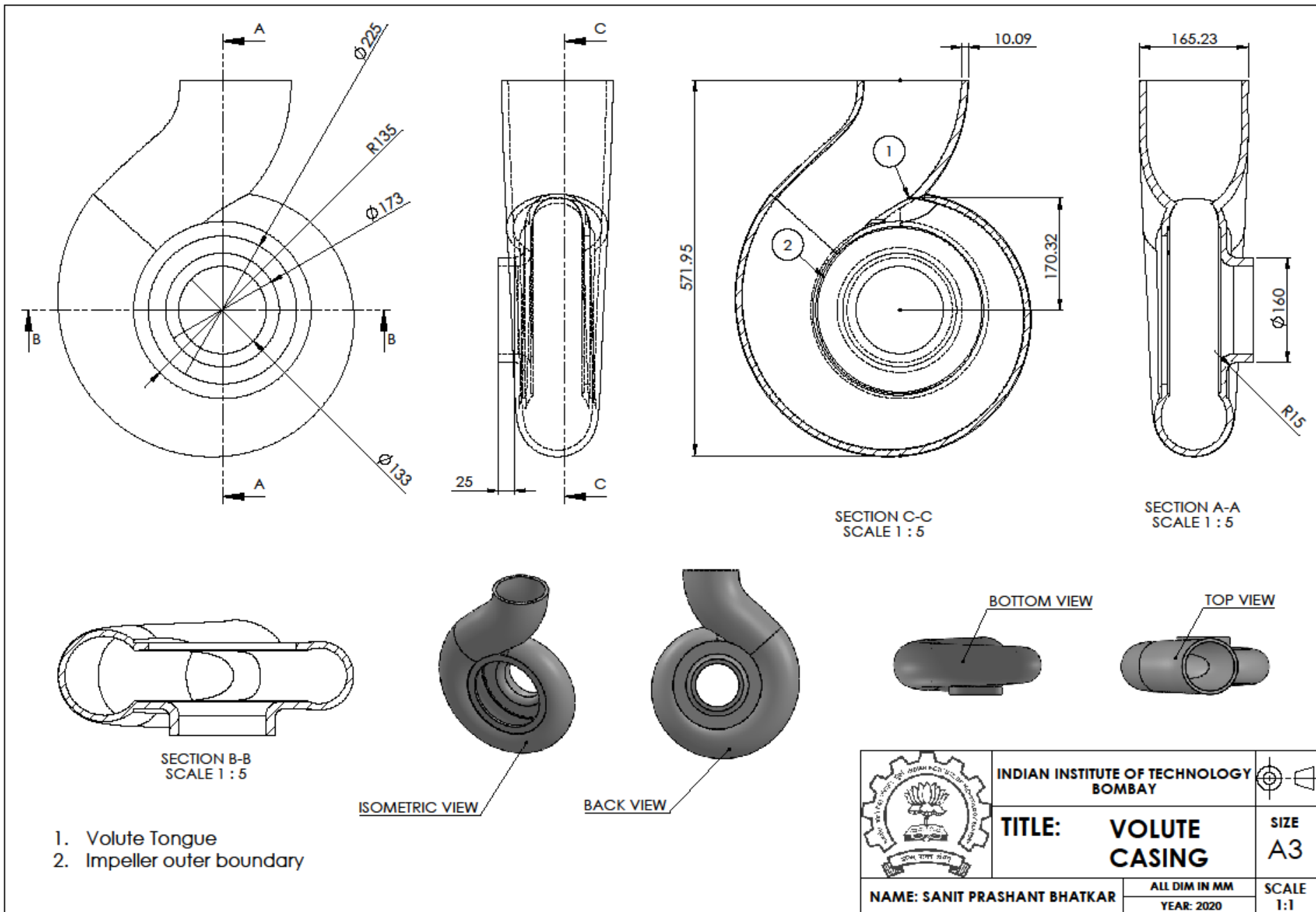


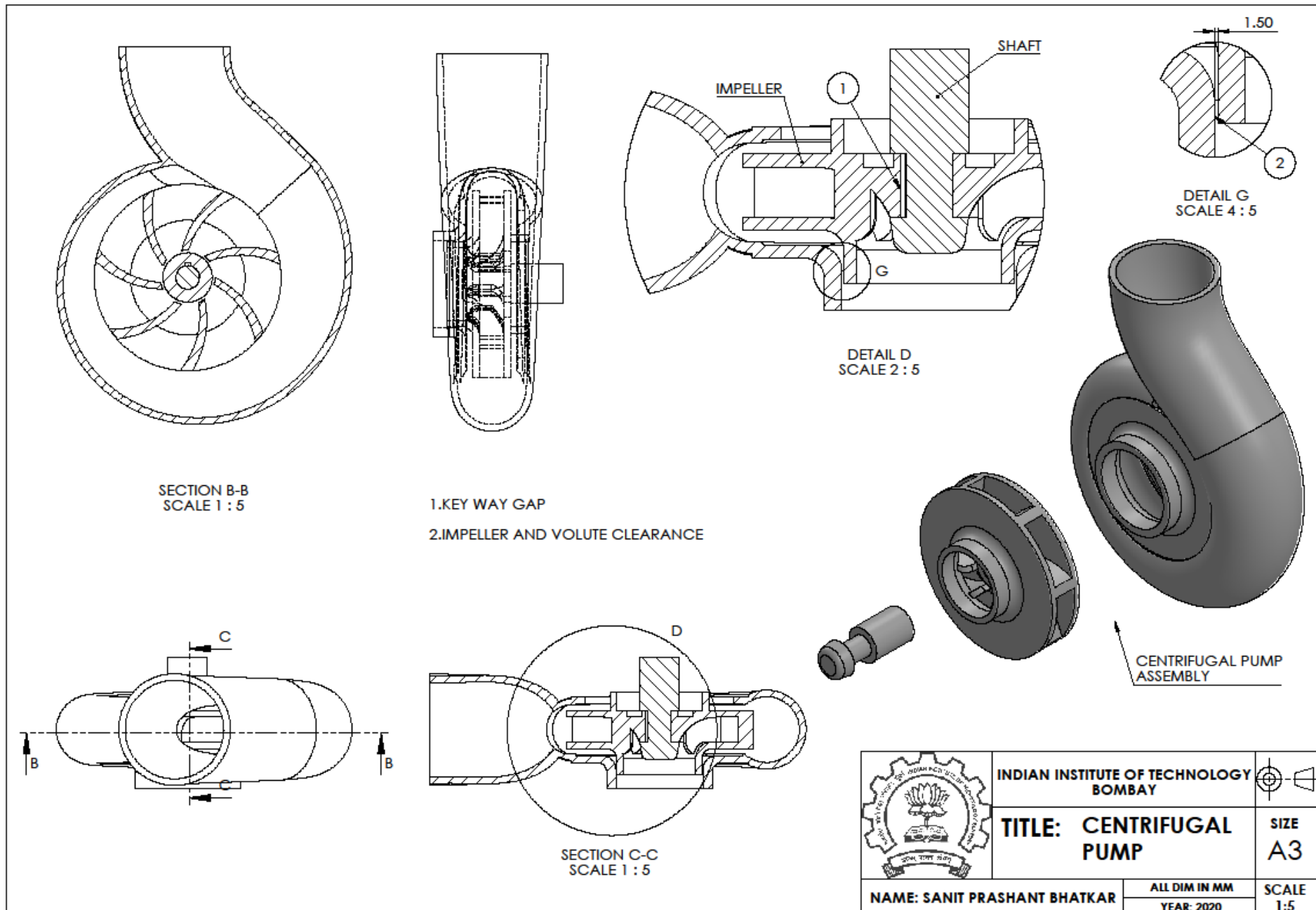
SECTION C-C
SCALE 1 : 5

	INDIAN INSTITUTE OF TECHNOLOGY BOMBAY	
TITLE: CANNED MOTOR PUMP		SIZE A3
NAME: SANIT PRASHANT BHATKAR		ALL DIM IN MM
		YEAR: 2020
		SCALE 1:1









Volute Cross Sections

For the volute cross section, a spiral is drawn such that the volute angle obtained by the design method can be maintained. Pitch of the spiral is decided from the area of the cross-sections at the inlet and outlet. The process starts with assuming the pitch equal to the center distance of the first area (47.5 mm) and developing the spiral. The pitch value is then gradually increased till the lower section of the last area touches the impeller circle. (65 mm pitch). The generated volute path is shown below.

